Fabrication and Characterization of Si Doped ZnO and $Cu_2P_2O_7$ Thin Films



Jiale Wang

St Edmund Hall

University of Oxford

Supervised by

Chris Grovenor

Susannah Speller

A thesis submitted for the degree of

Doctor of Philosophy

2019

Fabrication and Characterization of Si Doped ZnO and $Cu_2P_2O_7$ Thin Films

Jiale Wang (St Edmund Hall)

A thesis submitted to the University of Oxford for the degree of Doctor of Philosophy in Materials, Hilary Term 2019

Transparent conductive oxides (TCOs) are a group of materials that have good electrical conductivity, high visible and low near infrared (NIR, 790–2500 nm) transparencies. They are widely used in flat-panel displays, thin film solar cells and low-emissivity windows. The current material that dominates over 90% of the TCO market is tin doped indium oxide (ITO), which has superior electrical and optical properties. However, the two issues of ITO are the high cost of indium as well as its incomplete coverage of blockage in the NIR range, especially in the 790–1100 nm range that contains nearly 60% of the NIR solar irradiance. For decades, ZnO has been considered as a potentially low-cost replacement for ITO. But even after years of empirical explorations, the conductivity of the doped ZnO films are still not as good as ITO in many cases. The lack of fundamental studies such as the understandings on the relationships between processing conditions and the microstructure and the chemistries of the films is believed to be an important factor that limits further optimization. In this study, a variety of advanced microscopy techniques such as texture X-ray diffraction, transmission electron microscopy and transmission Kikuchi diffraction were used to study the Si doped ZnO films deposited and processed under different conditions. The results suggest several possible reasons for the large improvement of conductivity after the vacuum annealing and provide a few ideas on avoiding the defects observed in the thin films for future research.

In terms of the NIR properties, a more complete coverage of blockage was achieved by the production of $Cu_2P_2O_7$ thin films, which shows an absorbance of up to 66% of solar irradiance in the 790–1100 nm range while maintaining a good visible transparency (85% of transmittance at 550 nm). Given the little research reported on $Cu_2P_2O_7$, here for the first time a complete route from the analysis of powder, the production of sputtering targets to the deposition of thin films as well as further analysis on the structure and chemistry of the films is presented. These films are suitable for making low-cost and highly efficient inorganic NIR coating, which can be used in many applications such as energy efficient windows and electromagnetic shielding devices.

The work described in this thesis was carried out in the Department of Materials, University of Oxford from October 2014 until April 2019, under the supervision of Professor Chris Grovenor and Professor Susannah Speller. All of the work is my own unless otherwise stated, and has not been submitted previously for any degree at this or any other University.

Jiale Wang

April 2019

Acknowledgement

There are so many people that I would to like to thank for their helps and supports during my time in Oxford, to only some of whom it is possible to give particular mention here.

I would like to express my sincere gratitude to my supervisors Professor Chris Grovenor and Professor Susannah Speller for there guidance and supports during my Ph.D., for giving me the nearly complete freedom to choose the topics and decide what I am going to do, for providing me helps when I needed and for always believing in me even when things were not as clear as we wished. I genuinely hope the work I did here has lived up to their trust.

I would like to thank the many people who have offered technical assistance to my project. The work on growing SiZO films on glass substrates in Section 3.3 was performed in collaboration with Dr. Nazanin Rashidi from the Edwards Group in the Department of Chemistry at Oxford University, by whom some of the SiZO thin films reported on were prepared and characterized. The SiZO target was provided by the Edwards Group as well. In terms of the microstructural analysis, I am grateful to the staff at David Cockayne Centre for Electron Microscopy for their training and assistance on the SEM, TEM and FIB instruments. Other than that Prof. Susannah Speller and Dr. Sangeeta Santra operated the ZEISS Merlin SEM microscope, Dr. Jing Hu operated the ZEISS Merlin EBSD and JEOL ARM-200F TEM microscopes, while Mr Harry Orchard operated the XPS instrument on my behalf. The preparations of these microscopy samples and all the analysis and discussion of these results, though, are my own work. I am also grateful to Dr. Martin Hytch at Centre National de la Recherche Scientifique (France) for his help

with the GPA analysis.

I would like to thank Dr. Clara Barker and Mr Robert Gresham for their helps and support with the sputtering kit and the many other things happen in the lab. I also would like to thank Dr. Tayebeh Mousavi, Dr. Canan Aksoy and Mr Timothy Davies for the many useful discussions on the data and results. All of the people, past and present, in Chris and Susie's group as well as many other colleagues in the Materials department have contributed hugely to my professional and personal life at Oxford. The laughter, the pub time, the joy of finding something interesting, as well as the occasional complaints about staying whole day in the polishing or microscopy rooms that we shared will surely be a beautiful part of my memory.

The people in the Edwards Group in the Oxford University Department of Chemistry have also helped me a lot over the years. I am grateful to Prof. Peter Edwards for letting me use the instruments in their group. I am also thankful to the discussions with Prof. Peter Edwards and Prof. Jonathan Dilworth, as well as the advice given by them. It has been a pleasure of mine to work with the many brilliant researchers in their group.

I am also appreciative for the support from my college St Edmund Hall, for making me feel so much warmth and offering me the chance to meet a group of amazingly talented and friendly students.

Lastly, there really are not enough words to express my gratitude to my family and friends for their love and encouragements through out. John, Sally, AJ, dad and mom, this would not have been possible without you.

To all the helps and supports, all the friendships and loves, once again: thank you!

— Jiale Wang

April 2019, Oxford, UK

Contents

1 Introduction: A Review on Transparent Conductive Oxides 1

1.1 Introduction to transparent conductive oxides 1

1.1.1 History of TCOs 2

1.2 In_2O_3: Pros and Cons 6

1.2.1 Economic case for In_2O_3 6

1.2.2 Near-infrared properties of ITO: Are they good enough? . . . 8

1.3 Introduction to ZnO 10

1.3.1 Crystal structure 10

1.3.2 Band structure 11

1.3.3 Doping of ZnO thin films 13

1.3.3.1 P-type doping 14

1.3.3.2 N-type doping 15

1.4 Factors limiting the mobility in ZnO films 17

1.4.1 Ionized impurity scattering 17

1.4.2 Grain-boundary scattering 19

1.4.3 Neutral impurity scattering 20

1.4.4 Lattice vibration scattering 20

1.4.5 Dislocation scattering 20

1.4.6 Intragrain/inter-grain cluster scattering 21

1.5 The influence of experimental parameters on ZnO films 21

1.5.1 Substrate temperature during deposition 21

1.5.1.1 Electrical properties 21

1.5.1.2 Optical properties 24

1.5.1.3 Texture of the films 25
1.5.2 Doping level 26
1.5.3 Film thickness 31
1.5.4 Substrate choice 32
1.5.5 Post-deposition annealing 33
1.6 Transparent inorganic NIR materials 33
1.7 Aims of the thesis 36

2 Experimental Techniques **46**
2.1 Target preparation 46
2.1.1 Cold pressing 46
2.1.2 Sintering 47
2.2 Thin film preparation 47
2.2.1 RF sputtering: equipment and standard procedures 47
2.2.1.1 Principles of the technique 47
2.2.1.2 Instrumentation 49
2.2.2 Post-deposition annealing 51
2.3 Characterization of electrical and optical properties 52
2.3.1 Electrical characterization 52
2.3.1.1 Sheet resistance measurement – Four-point probe technique 52
2.3.1.2 Theory of Hall Effect 53
2.3.1.3 The van der Pauw technique 55
2.3.1.4 Instrumentation 58
2.3.2 Optical characterization (thin films) 58
2.3.2.1 Basic principles of UV-Vis-NIR spectroscopy 59
2.3.2.2 Plasma frequency 60
2.3.2.3 Instrumentation 63
2.3.3 Optical characterization (powder) 63
2.4 Microstructural characterization 64

2.4.1 X-ray diffraction (XRD) 64
2.4.1.1 Principles of the technique 64
2.4.1.2 Identification of material and its crystalline phase . . 66
2.4.1.3 Calculation of lattice parameters 67
2.4.1.4 Texture study 67
2.4.1.5 Calculation of crystallite size and internal strain . . . 69
2.4.1.6 Instrumentation 69
2.4.2 Scanning electron microscopy (SEM) 69
2.4.2.1 Principles of the technique 69
2.4.2.2 Instrumentation 73
2.4.3 Transmission Electron Microscopy (TEM) 73
2.4.3.1 Principles of the technique 73
2.4.3.2 Fresnel imaging 74
2.4.3.3 Geometric Phase Analysis (GPA) 75
2.4.3.4 Instrumentation 76
2.4.4 Focused ion beam (FIB) 76
2.4.4.1 Principles of the technique 76
2.4.4.2 Instrumentation 77
2.4.5 Transmission Kikuchi Diffraction (TKD) 78
2.4.5.1 Principles of the technique 78
2.4.5.2 Instrumentation 79
2.4.6 Profilometer 79
2.4.6.1 Principles of the technique 79
2.4.6.2 Instrumentation 79
2.4.7 Optical microscope 81
2.4.8 X-ray Photoelectron Spectroscopy (XPS) 81
2.4.8.1 Principles of the technique 81
2.4.8.2 Instrumentation 83

3 Si Doped ZnO Thin Films: Fabrication, Microstructure and Properties **86**

3.1 Introduction . . . 86

3.2 Target preparation . . . 87

3.3 Thin film preparation: growing SiZO films on glass substrates . . . 90

3.3.1 Substrate preparation . . . 90

3.3.2 Electrical property analysis . . . 90

3.3.3 Optical property analysis . . . 94

3.3.4 Structure and phase analysis . . . 95

3.4 Vacuum annealing and its influence on structure and performance of SiZO films . . . 97

3.4.1 Electrical property analysis . . . 98

3.4.2 Development of Films Structure and Chemistry during Annealing 100

3.4.2.1 Surface morphology of the films . . . 100

3.4.2.2 Phase of the films . . . 102

3.4.2.3 In-plane textures of the films . . . 103

3.4.2.4 Out-of-plane texture of the films . . . 110

3.4.2.5 Chemical composition of the films . . . 111

3.4.2.6 Lattice structure of the films and formation of nano-pores . . . 115

3.5 Discussion . . . 121

3.6 Conclusions and suggestions for future work . . . 128

4 $Cu_2P_2O_7$: from Powder to Thin Films **134**

4.1 Introduction . . . 134

4.2 Preparation of materials for sputtering . . . 135

4.2.1 Powder preparation . . . 135

4.2.2 Sputtering target preparation . . . 139

4.2.2.1 $Cu_2P_2O_7$ Target . . . 139

4.2.2.2 $Cu_2P_2O_7$ + P_2O_5 Target . . . 143

4.2.3 Substrate preparation for sputtering 144
4.3 Thin film preparation 144
4.3.1 $Cu_2P_2O_7$ target + Ar gas 145
4.3.1.1 Substrate temperature 145
4.3.1.2 Post-deposition annealing 147
4.3.1.3 RF power 149
4.3.1.4 Sputtering pressures / durations 154
4.3.2 $Cu_2P_2O_7$ / P_2O_5 target + Ar gas 155
4.3.3 $Cu_2P_2O_7$ target + Ar / O_2 gas 166
4.3.3.1 Assessment of reproducibility 174
4.3.3.2 Environmental stability 174
4.3.3.3 XPS studies of $Cu_2P_2O_7$ thin films 175
4.4 Discussion 179
4.4.1 $Cu_2P_2O_7$ + TCOs: A prototype 182
4.5 Conclusion and suggestions for future work 183

5 Conclusion and Suggestions for Future Work **188**

Appendices **194**

A SEM and XRD results of $Cu_2P_2O_7$ Thin Films **195**
A.1 Post-deposition annealing 195
A.2 RF power 196
A.3 Oxygen content 197
A.4 10% oxygen 199
A.5 15% oxygen 200
A.6 20% oxygen 201

B Quality Control Document **202**

List of Figures

1.1 Global TCF market forecasts. 1
1.2 Composition space of conventional TCOs. [2] 5
1.3 Prices of indium from 2000 to 2014. Source: metalbulletin.com 7
1.4 Optical transmittance spectrum of a commercial ITO thin film grown on glass. 9
1.5 ZnO crystal structures. [68] 10
1.6 Electronic band structure and density of states of pure wurtzite ZnO. [78] 12
1.7 Total and partial density of states of Al doped ZnO. [81] 12
1.8 Schematic band diagrams of (a) a poly-crystalline n-type doped semiconductor and (b) a degenerate n-type semiconductor.The Fermi energy level goes deep into the conduction band as the carrier concentration increases and therefore reduces the effective barrier height [105]. 18
1.9 Influence of substrate temperature on ρ, N and μ of sputtered AZO films. [121] 22
1.10 FE-SEM images of AZO films deposited at different substrate temperatures. (a) At 150 °C, (b) At 250 °C, (c) At 350 °C. [124] . . . 23
1.11 Al content increases with increasing substrate temperature. Figure adapted from [126]. 24
1.12 Influence of doping level on ρ, N and μ. [113] 27
1.13 Influence of doping level on optical transmission spectra of AZO films [113]. 28

1.14 Influence of Si content on the electrical transport properties in films made by spray pyrolysis [100]. 29
1.15 Phase diagram of SiO_2-ZnO [143]. 30
1.16 Variations of resistivity, carrier mobility and carrier concentration as a function of Si concentration for films made by sputtering [99]. . . . 30
1.17 Influence of AZO film thickness on FWHM of XRD θ - 2θ (0002) peaks and (0002) rocking curves [145]. 31
1.18 UV-Vis-NIR spectra of the powders of different copper phosphates. [67] 34
1.19 $Cu_2P_2O_7$ lattice structure. 35
1.20 Orbital correlation diagram. 35

2.1 Dies used for the manufacture of $Cu_2P_2O_7$ targets. 46
2.2 Setup of a typical sputtering kit. 47
2.3 RF discharge model. [2] 48
2.4 OAR DS500 sputter kit and its components. 50
2.5 Copper substrate holder (diameter: 6 cm) and the thermocouple. Diameter 51
2.6 Configuration of a four point probe measurement. 52
2.7 Hall Effect measurement. 53
2.8 The van der Pauw contact placements. Figure adapted from the website of National Institute of Standards and Technology 56
2.9 Voltage and current measurements for van der Pauw techniques. [6] . 57
2.10 Optical transmission. 59
2.11 Setup of UV-Vis-NIR spectrometer.[7] 60
2.12 Optical spectrum of a typical TCO [14]. 61
2.13 Calculated result of power reflection coefficient at the interface between air and a thick ITO layer as a function of free electron density for several incident wavelengths in the visible spectrum. Reflection increases drastically when the carrier concentration exceeds $10^{22}cm^{-3}$. [11] 62

2.14 Bragg reflection due to the regular arrays of atoms inside a crystal [17]. 65
2.15 XRD spectrum of a Si doped ZnO film deposited on glass. The PDF file for wurtzite ZnO (space group: P63mc) is PDF-#36-1451. 66
2.16 Schematic illustration of (a) a goniometer and (b) the measurement of a pole figure. ϕ, ψ and ω axes are shown in the above images [18]. . . 68
2.17 Schematic illustration of the setup of a typical SEM. 70
2.18 Surface morphology of a Si-doped ZnO thin film sputtered on glass substrate. 71
2.19 Schematic demonstration of electron-specimen interaction volumes [22]. 72
2.20 Schematic illustration of a TEM [24]. 73
2.21 Fresnel fringes around the edge of a hole. (a) Overfocus shows a dark fringe, (b) in focus and (c) underfocus shows a bright fringe [25]. . . . 75
2.22 Preparation of TEM lamella of SiZO thin film. 77
2.23 FIB holder and Cu grid. 78
2.24 Schematic illustration of the setup of an XPS. [39] 82
2.25 XPS spectrum (etched) of a pressed $Cu_2P_2O_7$ sample. 82

3.1 The research strategy of most previous literature (blue arrow) and the strategy of the current study (red arrows). 87
3.2 EDS maps and back-scattered electron (BSE) images of different areas of the SiZO target. Scale bar: 25 μm. 88
3.3 EDS line scans at four different areas of the target (silicon: green, zinc: red, oxygen: blue). Scales of the scans are 26 μm, 11 μm, 16 μm and 16 μm for area 1 to 4, respectively. The y axis represents the atomic percentage of the elements. 89
3.4 The phase composition analysis produced by the Aztec software. . . . 89

3.5 Ar gas pressure dependence of electrical transport properties of SiZO thin films deposited on glass substrates at power of 30 W (1.48 W/cm^2) and 40 W (1.97 W/cm^2), respectively. The substrate temperature is 200 °C. As a result of changing the sputtering pressure and the power, the thicknesses of the films also varied. The error bars are calculated from the measurements on multiple samples made under the same conditions. 91

3.6 Variations of resistivity (ρ), electron mobility (μ) and carrier (electron) concentration (n) at different Ar pressures for SiZO films sputtered on glass substrates at 200 °C and 300 °C, respectively. The sputtering power here is 30 W (1.48 W/cm^2). As a result of changing the sputtering pressure and the substrate temperature, the thicknesses of the films also changed. The error bars are calculated from the measurements on multiple samples made under the same conditions. 93

3.7 Optical transmittance spectra of SiZO thin films sputtered with various Ar pressures at 200 °C and 300 °C. 94

3.8 Variation of average visible transparency (uncorrected for glass substrate) of SiZO thin films sputtered at 200 °C and 300 °C by Ar pressure. 95

3.9 XRD spectra of SiZO thin films deposited with different Ar pressures at 300 °C. 96

3.10 Variation of thickness of SiZO films as a function of Ar pressure (300 °C). 96

3.11 Electrical transport properties of the as-deposited film (substrate temperature: 200 °C) and the films post vacuum-annealed at 400 °C and 550 °C, respectively. 99

3.12 (a) SEM micrograph of the surface of an as-deposited film (substrate temperature: 200 °C), (b) cross-sectional TEM bright field micrograph from a sample made by FIB. The red arrow represents the growth direction of the film. 100
3.13 (a) SE, (b) BSE micrographs and EDS maps (c-e) of the as-deposited film (substrate temperature: 200 °C). 101
3.14 (a) SEM micrograph of the surface of film annealed at 400 °C, (b) cross-sectional TEM micrograph from a sample made by FIB. The red arrow represents the growth direction of the film. 102
3.15 (a) SEM micrograph of the surface of film annealed at 550 °C, (b) cross-sectional TEM micrograph from a sample made by FIB. The red arrow represents the growth direction of the film. 102
3.16 XRD spectra of the as-deposited film and the annealed samples. . . . 103
3.17 TKD pattern of the cross sectional sample of the as-deposited film, including legend identifying the axes. (a) TKD inverse pole figure (IPF) map in the x direction, (b) TKD inverse pole figure (IPF) map in the y direction. The colour map of the coordinate system in this case is also shown. 104
3.18 TKD pattern of the cross sectional sample of the film annealed at 400 °C, including legend showing the axes. (a) TKD inverse pole figure (IPF) map in the x direction, (b) TKD inverse pole figure (IPF) map in the y direction. The colour map of the coordinate system in this case is also shown in the figure. 105
3.19 TKD pattern of the cross sectional sample of the film annealed at 550 °C, including legend showing the axes. (a) TKD inverse pole figure (IPF) map in the x direction, (b) TKD inverse pole figure (IPF) map in the y direction. The colour map of the coordinate system in this case is also shown in the figure. 106

3.20 Pole figures of the as-deposited doped ZnO film for different diffracting planes ({001}, {100} and {110}) calculated from the TKD data in Figure 3.17. 106
3.21 (a) Pole figures of the SiZO film annealed at 400 °C for different diffracting planes ({001}, {100} and {110}) calculated from the TKD data. (b) Pole figures of the MgO substrate for different diffracting planes ({100}, {110} and {111}) calculated from the TKD data. . . . 107
3.22 Pole figures of the SiZO film annealed at 550 °C for different diffracting planes ({001}, {100} and {110}) calculated from the TKD data. . . . 108
3.23 Distribution of grain boundary angles across the film annealed at 400 °C calculated from the TKD data. 108
3.24 Distribution of grain boundary angles across the film annealed at 550 °C calculated from the TKD data. 108
3.25 Schematic representation of the interface between MgO substrate and annealed ZnO film with two preferred in-plane relationships: $(110)_{ZnO} \parallel (110)_{MgO}$ and $(100)_{ZnO} \parallel (110)_{MgO}$. 109
3.26 Texture XRD (phi-scan) measurement of wurtzite ZnO (104) peak of sample annealed at 550 °C. 109
3.27 Rocking curve of the (002) peak of the as-deposited sample. 110
3.28 Rocking curve of the (002) peak of the sample annealed at 400 °C. . . 111
3.29 Rocking curve of the (002) peak of the sample annealed at 550 °C. . . 111
3.30 (a) STEM micrograph of the as-deposited thin film; (b) Si and (c) Zn map obtained from EDS in STEM; (d) EDS layered image in which three separate layers can be seen from top to bottom: Pt protection layer (purple), SiZO thin film (green) and MgO substrate layer (blue). 112
3.31 (a) STEM micrograph of the area around the circular feature in the 400 °C annealed sample; (b) Si map and (c) Zn map obtained from EDS in STEM. The result shows that there is no Si precipitation around the circular feature. 113

3.32 (a) STEM micrograph of the thin film annealed at 550 °C; (b) Si map (c) Zn map and (d) Pt map obtained from EDS in STEM. Layers in the STEM image are Pt protection layer (white contrast), SiZO thin film and MgO substrate layer (black contrast) from top to bottom, respectively. 114
3.33 Geometric phase analysis based on the HRTEM image of the as-deposited SiZO film (200 °C). Subfigure (a) is an HRTEM image of the grains recorded along a < 100 > zone axis of wurtzite ZnO film. The white arrow at the bottom left represents the growth direction of the film. The power spectrum (bottom right) of the grain on the right hand side is shown as an example, which shows characteristic reflections from (002) and (011) plane of wurtzite ZnO. The (002) plane in each grain is highlighted by arrows. Subfigure (b), generated by the GPA program, is the map of ω_{xy} of the rotation matrix, of which the magnitude is positively correlated to the rotation angle. Subfigure (c) is the map of rotation angle. 115
3.34 HRTEM image of grains around nanopore in the sample annealed at 550 °C. The white arrow shows the growth direction of the film. . . . 117
3.35 (a) STEM/HAADF micrograph of the 550 °C annealed sample at higher magnification and (b) annular dark-field (ADF) micrograph of the 550 °C annealed thin film. 118
3.36 STEM/HAADF map of SiZO film annealed at 550 °C. Layers from top to bottom are MgO substrate (black constrast), SiZO thin film and Pt layer (white contrast), respectively. Scale bar: 100 nm. 118

3.37 (a), (c) and (e) are underfocused TEM micrographs of the 550 °C annealed sample, the 400 °C annealed sample and the as-deposited sample respectively, in which the nano-voids show white contrast. (b), (d) and (f) are overfocused TEM micrographs of the 550 °C annealed sample, the 400 °C annealed sample and the as-deposited sample respectively, in which the nano-voids show black contrast. The red arrows point at the regions of detected nano-pores inside the film. 119
3.38 Schematic illustrations of a possible arrangement of nano-pores on the grain boundary plane in different perspectives. The red spheres represent the pores. 120
3.39 EDS spectrum of the as-deposited film, in which no Ar peak (2.957 keV) could be seen. 123
3.40 Crack like / elliptical voids on the grain boundaries of the annealed films. Scale of the TEM image: 11 × 10 nm. 124
3.41 Comparison of the films annealed at 400 °C (left) and 550 °C (right). The white arrows show the penetration depth of the voids along the grain boundaries. 125
3.42 EDS line scan across one of the voids on the grain boundary plane; (a) STEM image with the yellow line showing the scan trajectory, (b) EDS counts of Zn, Si and O, (c) the Si concentration in each nano-meter region calculated from (b), with the error bar showing the variation of Si ratio in each nano-meter region. Scale bar: 90 nm. 127

4.1 Images of $Cu_2P_2O_7$ powder. 136
4.2 XRD spectra of $Cu_2P_2O_7$ powder. 137
4.3 Absorbance spectrum of dehydrated copper pyrophosphate powder. . 138
4.4 The picture of the powder after being annealed at 500 C for 5 hrs. The retained fine powder is obvious when comparing this image with the powder annealed at 900 °C. Scale of the image: 70 × 66 mm. 138

4.5 Flow chart for target preparation. 139
4.6 Pictures of targets without heat treatment and sintered for 3 hours at 500 °C, then at 500 °C, 700 °C and 900 °C for 2 hours, respectively. . 140
4.7 Pictures of targets without heat treatment and sintered for 2 hours at 500 °C, 700 °C and 900 °C, respectively. 141
4.8 Pictures of 2-inch target after sintering at 500 °C. 142
4.9 Pictures of targets prepared from dehydrated powder without heat treatment, and annealed at 500 °C, 700 °C and 900 °C, respectively. . 143
4.10 The $Cu_2P_2O_7$ + P_2O_5 target (middle) clamped by a copper shield in the sputtering system. Scale of the image: 95 × 96 mm. 144
4.11 Properties of films deposited from pure $Cu_2P_2O_7$ target in Ar gas at different temperatures (power: 30 W). 145
4.12 XRD spectra of selected films deposited at different substrate temperatures. 146
4.13 SEM images of selected films deposited at different substrate temperatures. The films show little surface feature in the SEM, regardless of the levels of brightness and contrast. The dusts on the films were used for focusing purposes to make sure the images are in-focus, as shown in the 25 × 25 μm magnified inset in subfigure (a) as an example. 147
4.14 Properties of films deposited from pure $Cu_2P_2O_7$ target in Ar gas and post-annealed at different temperatures (power: 30 W). 148
4.15 Properties of films deposited from pure $Cu_2P_2O_7$ target in Ar gas with different powers at room temperature. 149
4.16 SEM images of the film deposited at 90 W in Ar from the $Cu_2P_2O_7$ target. 151
4.17 EDS maps of the film deposited at 90W from pure $Cu_2P_2O_7$ target in Ar gas. 152
4.18 EDS spectrum (0–9.7 keV) of the film deposited at 90W from pure $Cu_2P_2O_7$ target in Ar gas. 153

4.19 Properties of films deposited from pure $Cu_2P_2O_7$ target in Ar gas at room temperature and a power of 60 W (2.96 W/cm^2) with different sputtering pressures and durations. 154
4.20 Picture of the film deposited from $Cu_2P_2O_7$ / P_2O_5 target after 5 hrs in the air. The film was deposited at room temperature using RF power of 30 W (1.48 W/cm^2) for 1hr. Scale of the image: 36 × 18 mm. . . . 155
4.21 Optical microscopy images showing the transformation of film surface over time. The film was deposited at room temperature using RF power of 30 W (1.48 W/cm^2) for 1hr. Scales of each image: 1.8 mm × 1.3 mm. 156
4.22 Transmittance spectra of films deposited and processed at several different conditions from the $Cu_2P_2O_7$ / P_2O_5 target (substrate temperatures: 300 °C, 400 °C, post-annealing temperature: 400 °C; power: 30 W (1.48 W/cm^2) for all three samples shown here). 157
4.23 SEM images of the film deposited at substrate temperature of 300 °C from $Cu_2P_2O_7$ / P_2O_5 target in Ar gas. 158
4.24 EDS maps of the film deposited at substrate temperature of 300 °C from $Cu_2P_2O_7$ / P_2O_5 target in Ar gas. 159
4.25 SEM images of the same area in Figure 4.24(a) but shifted 10 μm after reaction with electron beam (accelerating voltage: 10 kV). 160
4.26 SEM images of the film deposited at a substrate temperature of 300 °C from $Cu_2P_2O_7$ / P_2O_5 target in Ar gas. 161
4.27 EDS maps of the film deposited at a substrate temperature of 300 °C from $Cu_2P_2O_7$ / P_2O_5 target in Ar gas. 162
4.28 EDS line scan on the film deposited at a substrate temperature of 300 °C from $Cu_2P_2O_7$ / P_2O_5 target in Ar gas. The graph includes the scan region (top), cps scan result (middle) and at% scan result (bottom). 163
4.29 SEM images of the film deposited at a substrate temperature of 300 °C after reaction with the electron beam (accelerating voltage: 10 kV). 163

4.30 EDS maps of the film deposited at a substrate temperature of 200 °C from $Cu_2P_2O_7$ / P_2O_5 target in Ar gas. 164
4.31 EDS maps (high magnification) of the film deposited at a substrate temperature of 200 °C from $Cu_2P_2O_7$ / P_2O_5 target in Ar gas. 165
4.32 SEM images of the film deposited at a substrate temperature of 200 °C after reaction with electron beam (accelerating voltage: 10 kV). . 165
4.33 Properties of films deposited from the pure $Cu_2P_2O_7$ target in Ar / O_2 gas with different amounts of O_2 (60 W, room temperature). 167
4.34 Properties of films deposited from the pure $Cu_2P_2O_7$ target in 10% O_2 / Ar gas for different times (60 W, room temperature). 169
4.35 Properties of films deposited from the pure $Cu_2P_2O_7$ target in 15% O_2 / Ar gas for different times (60 W, room temperature). 170
4.36 Properties of films deposited from the pure $Cu_2P_2O_7$ target in 20% O_2 / Ar gas for different times (60 W, room temperature). Error bars measured from the optical spectra of multiple samples are included for the 1 hr and 2 hrs sample in subfigures b and c. Some of the error bars might be too small to be easily seen in these graphs. 172
4.37 Pictures of (a) glass substrate, (b) film sputtered with 5% O_2, (c) film sputtered with 10% O_2, (d) film sputtered with 15% O_2, (e) film sputtered with 20% O_2. All of the films shown here were sputtered at RF power of 60 W (2.96 W/cm^2) at room temperature. 173
4.38 Transmittance spectra of three different samples deposited under the same conditions (20% O_2, 2 hrs, $Cu_2P_2O_7$ target). 174
4.39 Transmittance spectra of the as-deposited film and after 90 days of exposure to the air. The film was sputtered with 10% O_2 for 18 hrs from the $Cu_2P_2O_7$ target. 175
4.40 XPS spectrum of the $Cu_2P_2O_7$ target. 176
4.41 XPS spectrum of the film deposited from the $Cu_2P_2O_7$ target with 10% O_2 for 9 hrs (60 W, room temperature). 177

4.42 XPS spectrum of the film deposited from the $Cu_2P_2O_7$ target with 15% O_2 for 9 hrs (60 W, room temperature). 178
4.43 XPS spectrum of the film deposited from the $Cu_2P_2O_7$ target with 20% O_2 for 9 hrs (60 W, room temperature). 179
4.44 Solar irradiation spectra. Data originally from American Society for Testing and Materials (ASTM) [40]. Global tilt meaning the spectrum includes the radiation from not only solar disk but also sky diffusion and diffusion from ground reflection on a south facing surface tilted 37° from the horizontal. 180
4.45 Transmittance spectra of a $Cu_2P_2O_7$ film (18 hrs, 10% oxygen, pure $Cu_2P_2O_7$ target), an ITO coated glass and an ideal sample. 182
4.46 Transmittance spectrum of a double-layered coating combining a $Cu_2P_2O_7$ film (18 hrs, 20% oxygen, pure $Cu_2P_2O_7$ target) and an ITO film deposited on glass. 183

A.1 XRD spectra of films deposited from pure $Cu_2P_2O_7$ target in Ar gas and post-annealed at different temperatures. 195
A.2 SEM images of selected films deposited from pure $Cu_2P_2O_7$ target in Ar gas and post-annealed at different temperatures. 196
A.3 XRD spectra of films deposited from pure $Cu_2P_2O_7$ target in Ar gas with different powers. 196
A.4 SEM images of (selected) films deposited from pure $Cu_2P_2O_7$ target in Ar gas with different powers. 197
A.5 XRD spectra of films deposited from the pure $Cu_2P_2O_7$ target in Ar / O_2 gas with different amounts of O_2. 197
A.6 SEM images of films deposited from the pure $Cu_2P_2O_7$ target in Ar / O_2 gas with different amounts of O_2. 198
A.7 XRD spectra of selected films deposited from the pure $Cu_2P_2O_7$ target in 10% O_2 / Ar gas for different times. 199

A.8 SEM images of selected films deposited from the pure $Cu_2P_2O_7$ target in 10% O_2 / Ar gas for different times. 199
A.9 XRD spectra of selected films deposited from the pure $Cu_2P_2O_7$ target in 15% O_2 / Ar gas for different times. 200
A.10 SEM images of films deposited from the pure $Cu_2P_2O_7$ target in 15% O_2 / Ar gas for different times. 200
A.11 XRD spectra of selected films deposited from the pure $Cu_2P_2O_7$ target in 20% O_2 / Ar gas for different times. 201
A.12 SEM images of films deposited from the pure $Cu_2P_2O_7$ target in 20% O_2 / Ar gas for different times. 201

List of Tables

1.1 Selected historical TCO references. 4
1.2 Doping of TCO materials. Table modified from Minami [48]. 5
1.3 Basic properties for AZO, GZO and SiZO obtained by different techniques. 16

List of Abbreviations

ADF annular dark-field

AZO aluminum doped zinc oxide

BSE back-scattered electrons

CBM conduction band minimum

CFEG cold field-emission electron gun

CTEM conventional transmission electron microscopy

CVD chemical vapor deposition

DC direct current

DFT density functional theory

DOS density of states

DSC dye-sensitized solar cell

EDS energy dispersive X-ray analysis

EMI electromagnetic interference

FE field-emission

FEG field-mission electron gun

FIB focused ion beam

FIR far-infrared

FTO fluorine doped tin oxide

FWHM full width at half maximum

GB grain boundary

GGA generalized gradient approximation

GPA geometric phase analysis

GWA GW approximation

GZO gallium doped zinc oxide

HAADF high-angle annular dark-field

HOMO highest occupied molecular orbital

HRTEM high-resolution transmission electron microscopy

IPF inverse pole figure

IPFX inverse pole figure in the x direction

IPFY inverse pole figure in the y direction

ITO tin doped indium oxide

LCD liquid-crystal display

LDA local density approximation

low-E low emissivity

LUMO lowest unoccupied molecular orbital

NIR near-infrared

OLED organic light-emitting diode

OPV organic photovoltaic

PDC pulsed direct current

PLD pulsed laser deposition

PVD physical vapor deposition

RF radio frequency

RT room temperature

SE secondary electrons

SEM scanning electron microscope

SiZO silicon doped zinc oxide

STEM scanning transmission electron microscopy

TCF transparent conductive film

TCO transparent conductive oxide

TCOs transparent conductive oxides

TEM transmission electron microscope

TKD transmission Kikuchi diffraction

USD United States dollar

USGS United States Geological Survey

UV ultraviolet

VBM valence band maximum

Vis visible

XPS X-ray photoelectron spectroscopy

XRD X-ray diffraction

Chapter 1

Introduction: A Review on Transparent Conductive Oxides

1.1 Introduction to transparent conductive oxides

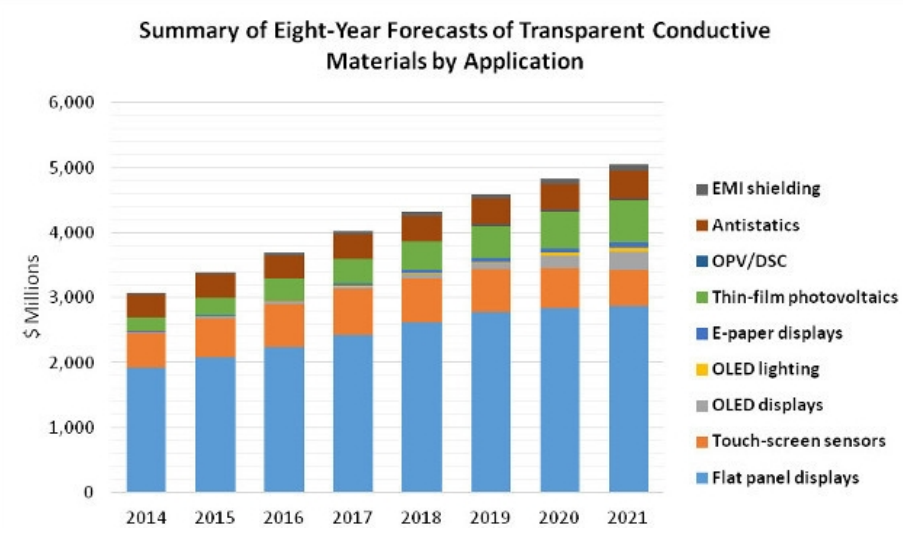


Figure 1.1: Global TCF market for sectors of display and solar cells. Figure adapted from the website of Insight Media. [1]

Transparent conductive oxides (TCOs) are materials with good electrical conductivity and comparatively high optical transparency. With the combination of these two properties, TCOs in the form of thin films are widely used as transparent electrodes or coatings in flat panel displays, opto-electrical sensors, thin film solar cells and energy efficient / low emissivity (low-E) windows [2]. According to recent market news [3] TCOs dominates more than 90% of the global transparent conductive film

(TCF) market. As shown in Figure 1.1, the market value of transparent conductor for display and solar cells in 2014 was estimated to exceed USD 3 billion, with this value expected to increase to around USD 5 billion in 2021 [1]. According to another recent report [4], the global market of low-E coated glass is projected to exceed USD 4 billion by 2024, in which TCOs such as fluorine-doped tin oxide and tin-doped indium oxide are widely adopted. The overall TCF global market is expected to cross USD 8 billion by 2024 [5].

1.1.1 History of TCOs

The first examples of transparent conductive materials were sputtered thin metal films made before the end of the nineteenth century [6]. In 1907, Baedeker, who is generally regarded as the first scientist investigating TCOs, obtained highly conductive CdO films with resistivities around $1.2 \times 10^{-3}\,\Omega\,\mathrm{cm}$ [7], only about one order of magnitude higher than the resistivity of tin doped indium oxide (ITO) films — the most conductive TCO layers today as well as the most widely used ones in industry.

The boom in TCO research and applications did not come immediately after the discovery of CdO films in 1907. However the understanding of quantum mechanics and semiconductor physics were developing with remarkable speed. Around 1908 Baedeker measured the Hall effect in copper iodide and experimentally indicated the existence of positive carriers [8]. In 1924, De Broglie generalized Planck's law from light to all particles and developed the theory of matter waves. Soon after that came the birth of modern quantum mechanics in 1925 when Heisenberg, Born and Jordan put forward matrix mechanics [9] and Schrödinger developed his theory of wave mechanics [10]. In 1928 Bloch developed his well-known theory of electrons in crystal lattices [11]. Building on the idea of filled and empty energy bands, later in 1931 Wilson put forward the band theory of solid state materials. He also confirmed that impurities inside a semiconductor would greatly improve the conductivity [12]. Understanding of the roles of dopants and intrinsic defects such as interstitial and substitutional lattice defects was significantly improved by a huge amount of

subsequent research by other scientists [13]. These investigations formed a firm foundation for the later research on TCO materials.

Accompanying the post-World War II economic expansion, the electronics industry boomed at almost the same time, including progress in the study of TCOs. In 1947, McMaster for the first time discovered chlorine doped tin oxide films (SnO_2:Cl) as good transparent conductors that could be applied to the heating of aeroplane windows [14]. This turned out to be a prototype for the later extensive use of TCO coatings on windows. The purposes of these coatings can be divided into two major categories; protecting the substrate materials from freezing or prohibiting the transmission of heat. Mochel in 1951 was probably the first scientist to try tin doped indium oxide (ITO) coatings on a series of substrates including glass [15]. ZnO, a potentially cheap and prominent ITO alternative, was initially applied for surface acoustic wave devices [16] in around 1960 as a result of its good piezoelectric properties. Today a large number of TCO materials have been discovered and studied, not only including the three major TCOs (SnO, In_2O_3 and ZnO) mentioned, but also materials such as p-type TCOs and unconventional TCO systems like $12CaO \cdot 7Al_2O_3$ ($Ca_{12}Al_{14}O_{33}$) [17]. Though not comprehensive, Table 1.1 shows the evolution of TCO research and the diversity of TCO materials.

As can be seen in Table 1.1, a variety of deposition methods have been used for the fabrication of TCO thin films. Physical deposition methods such as electron beam evaporation [18], ion assisted plasma evaporation [19], thermal evaporation [20], direct current (DC) sputtering [21], pulsed direct current (PDC) sputtering [22], radio frequency (RF) magnetron sputtering [23] and pulsed laser deposition (PLD) [24] have been used. In addition to physical vapor deposition (PVD) methods, chemical deposition methods, such as spray pyrolysis, usually produce coatings with non-uniform thickness [25]. Chemical vapor deposition (CVD) techniques like atmospheric pressure chemical vapor deposition (APCVD) and metal-organic chemical vapor deposition (MOCVD) have been used to improve the homogeneity of thickness across the film [25, 26]. Furthermore, sol-gel technology is also a widely used way to produce films chemically [27, 28].

Table 1.1: Selected historical TCO references. Table modified from Ginley *et al.*[2]

Material	Year	Process	Reference
Cd-O			
CdO	1907	Thermally Oxidation	K. Badeker. *Ann. Phys.(Leipzig)* [7]
CdO	1950	Sputtering	J.S. Preston. *P ROY SOC LOND A MAT.* [29]
CdO	1951	Spray pyrolysis	J.M. Mochel. U.S. Patent[15]
Sn-O			
SnO:Cl	1947	Spray pyrolysis	H.A. Mcmaster. U.S. Patent [14]
SnO:Sb	1947	Spray pyrolysis	J.M. Mochel. U.S. Patent [30]
SnO	1950	Sputtering	J.S. Preston. *P ROY SOC LOND A MAT.* [29]
SnO:F	1947	Spray pyrolysis	A.E. Junge *et al.* U.S. Patent [31]
In-O			
In_2O_3	1950	Spray pyrolysis	M.J. Zunick. U.S. Patent [32]
$In_2O_3 : Sn$	1951	Spray pyrolysis	J.M. Mochel. U.S. Patent [15]
$In_2O_3 : Sn$	1953	Sputtering	L. Holland *et al. Vacuum* [33]
Zn-O			
ZnO	1950	Sputtering	J.S. Preston *P ROY SOC LOND A MAT.* [29]
ZnO:Al	1971	Sputtering	T. Hada *et al. Thin Solid Films* [34]
Ti-O			
$TiO_2 : Nb$	2005	PLD	Y. Furubayashi *et al. Appl. Phys. Lett.* [35]
In-Sn-O			
$In_4Sn_3O_{12}$	1997	Sputtering	T. Minami *et al. Thin Solid Films* [36]
In-Zn-O			
$Zn_2In_2O_5$	1995	Sputtering	T. Minami *et al. Jpn. J. Appl. Phys* [37]
$Zn_3In_2O_6$	2000	PLD	N. Naghavi *et al. Thin Solid Films* [38]
Zn-Sn-O			
Zn_2SnO_4	1992	Sputtering	H. Enoki *et al. physica status solidi (a)* [39]
$ZnSnO_3$	1994	Sputtering	T. Minami *et al. Jpn. J. Appl. Phys* [40]
a - ZnSnO	2004	Sputtering	T. Moriga *et al. J. Vac. Sci. Technol.* [41]
In-Ga-Zn-O			
$InGaZnO_4$	1995	Sintering	M. Orita *et al. Jpn. J. Appl. Phys* [42]
a - InGaZnO	2001	PLD	M. Orita *et al. Philos. Mag. B.* [43]
p-type TCOs			
NiO	1993	Sputtering	H. Sato *et al. Thin solid films* [44]
$CuAlO_2$	1997	PLD	H. Kawazoe *et al. Nature* [45]
$ZnO : Ga, N$	1999	PLD	M. Joseph *et al. Jpn. J. Appl. Phys* [46]
Unconventional TCOs			
$12CaO \cdot 7Al_2O_3$	2002	Floating Zone[47]	K. Hayashi *et al. Nature* [17]

Apart from the variety of deposition technologies, the diversity of TCO materials can also be revealed from the great number of dopants that have been tried in the past. Historically TCOs have been dominated by a small set of oxide materials including CdO, Ga_2O_3, SnO_2, In_2O_3 and ZnO. In fact, the traditional TCOs can be described by the basic composition space shown in Figure 1.2. Depending on their proposed applications, this group of materials have been doped or combined with a series of

elements, listed in Table 1.2.

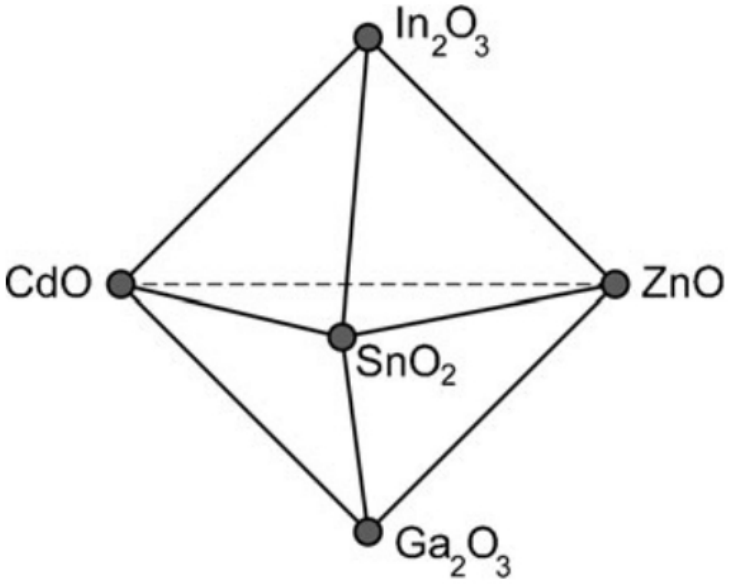


Figure 1.2: Composition space of conventional TCOs. [2]

Table 1.2: Doping of TCO materials. Table modified from Minami [48].

Material	Dopant or compound
SnO_2	Sb, F, As, Nb, Ta
In_2O_3	Sn, Ge, Mo, F, Ti, Zr, Mo, Hf, Nb, Ta, W, Te
ZnO	Al, Ga, B, In, Y, Sc, F, V, S, Ge, Ti, Zr, Hf, Si
CdO	In, Sn
Ga_2O_3	
ZnO - SnO_2	Zn_2SnO_4, $ZnSnO_3$
ZnO - In_2O_3	$Zn_2In_2O_5$, $Zn_3In_2O_6$
In_2O_3 - SnO_2	$In_4Sn_3O_{12}$
CdO - SnO_2	Cd_2SnO_4, $CdSnO_3$
CdO - In_2O_3	$CdIn_2O_4$
$MgIn_2O_4$	
$GaInO_3$, $(Ga, In)_2O_3$	Sn, Ge
$CdSb_2O_6$	Y
Zn - In_2O_3 - SnO_2	$Zn_2In_2O_5$ - $In_4Sn_3O_{12}$
CdO - In_2O_3 - SnO_2	$CdIn_2O_4$ - Cd_2SnO_4
ZnO - CdO - In_2O_3 - SnO_2	

1.2 In_2O_3: Pros and Cons

Some major goals of the TCOs industry and the reasons for trying so many different materials and dopants include the needs to achieve: 1) lower electrical resistivity, 2) higher visible transparency and 3) lower near-infrared (NIR) transparency. In terms of these three aspects, indium oxide based materials, particularly tin doped indium oxide (ITO), are the indisputable leaders. ITO is a highly degenerate n-type semiconductor that has resistivity as low as $1.5 - 2.0 \times 10^{-4}$ Ωcm for films made by electron beam (EB) evaporation or magnetron sputtering [49–52]. With a high level of Sn doping at $5 - 10$ at.%, it is possible to produce films with carrier concentrations of $1 - 2 \times 10^{21}$ cm^{-3}. Two types of electron donors are responsible for the generation of free electrons; substitutional Sn^{4+} ions and oxygen vacancies [53–56]. ITO films also show excellent transparency of typically above 85% in the visible range [53].

1.2.1 Economic case for In_2O_3

However, problems still exist when it comes to the economic side of indium oxide. The economy of indium is greatly influenced by its scarcity. Indium is a rare-earth element with an Earth crustal abundance level of 50 ppb, which is only about two-thirds that of silver [57, 58]. The fact that it rarely forms minerals of its own means it could only be produced as a by-product during the mining of other metals. The main sources of indium include sulfidic zinc ores and sulfidic copper ores [59]. Besides, according to a recent report (Mineral Commodity Summaries 2018, USGS), around 92% of global indium production was contributed by the top four national producers (China, Republic of Korea, Japan and Canada) [60].

The difficulty of extraction and the relatively centralized distribution of resources around the globe led to the volatility of the indium market, as shown in Figure 1.3. Figure 1.3 shows the fluctuation of the price of indium from 2000 to 2014. It can be seen that the price increased from around 200 USD/kg to 750 USD/kg in just 14 years owing to a rise in demand, particularly in the use of ITO for LCD computer screens and television sets that accounts for at least 50% of the total indium consumption

[60, 61]. Although following the recent trading crisis [62] the price of indium has dropped back to around 205 USD/kg, it is still well above that of zinc (∼2.5 USD/kg) [60, 63].

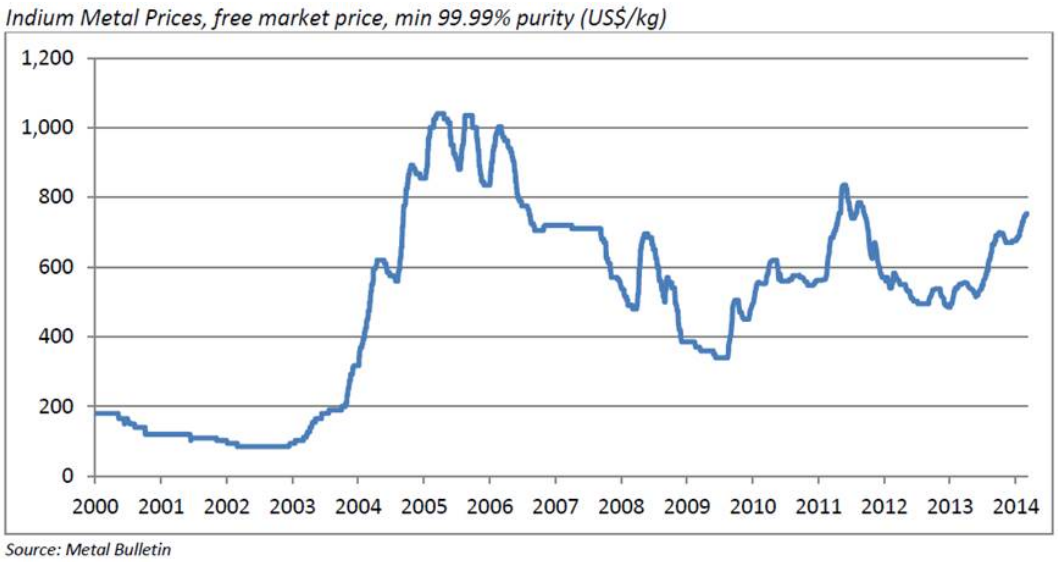


Figure 1.3: Prices of indium from 2000 to 2014. Source: metalbulletin.com

Zinc oxide is perhaps the most often quoted material when it comes to the discussion of finding cheap alternatives for ITO. Compared to indium, zinc not only has high crustal abundance, the large diversity of its applications also helps stabilize the market (between 1.7 USD/kg and 2.6 USD/kg over a six-year period since August 2009 [63]) which is a particularly valuable factor for companies buying and selling on credit. The potential that zinc oxide might replace scarce and costly indium oxide has driven an enormous amount of research over the past few decades, including active empirical exploration in the parameter space of deposition techniques, dopants and processing conditions to improve the performance of thin films, presumably influenced by the industry-driven optimization of indium oxide thin films since the early 1950s [15, 33]. As a result, a relatively small amount of focus has been put on the fundamental interpretation of the changes in properties such as detailed structural and chemical analysis, which can sometimes be challenging for companies and researchers due to its high demand in time, budget, advanced instruments and technical skills.

1.2.2 Near-infrared properties of ITO: Are they good enough?

The reason that the NIR range is of much interest is because it is the 'heat band' of the entire solar spectrum. Beyond 2500 nm into the far infrared (FIR) region, there is very little solar energy and thus the contribution to the solar heat gain is negligible. Every year huge amount of energy and resources need to be spent simply on cooling in many countries. According to the US Department of Energy [64], air conditioners in the US need to use roughly 290 terawatt hours, cost around USD 29 billion to homeowners and generate about 117 million metric tons of CO_2 annually. Because of the warming of the climate in many areas of the world as well as the growing middle class and rapid urbanization processes that are taking place in several major developing countries, the demands for air conditioning are expected to keep increasing worldwide. The electricity demand for air conditioning is estimated to increase around 35 times by 2100 [65]. Therefore, having a material that could block a major source of heat — solar irradiance, while ensuring transparency in the visible range, would certainly be beneficial to the control of needs in air conditioning, as well as the enormous pressures that might bring on emissions, costs and national infrastructure such as having to build new power plants.

As previously introduced, TCOs are used in low-E windows as a window coating to prohibit the transmission of heat due to its low transparency in the NIR region (790–2500 nm) [53]. The excellent NIR blocking properties of TCOs, particularly ITO, is due to plasma oscillation effects inside the film, which will be introduced in Chapter 2. The transmittance spectrum of a commercial ITO thin film (bought from Sigma-Aldrich ®) deposited on glass is shown in Figure 1.4.

However, as can be seen, the blocking effects mostly happen in the higher wavelength region (above 1300 nm, shown as *NIR (II)* in Figure 1.4), which is due to the characteristics of the plasma oscillations [66]. In fact, for most TCO thin films (ITO and FTO) it is difficult to block the near-infrared light close to the visible range given that there is usually a practical upper limit for the carrier

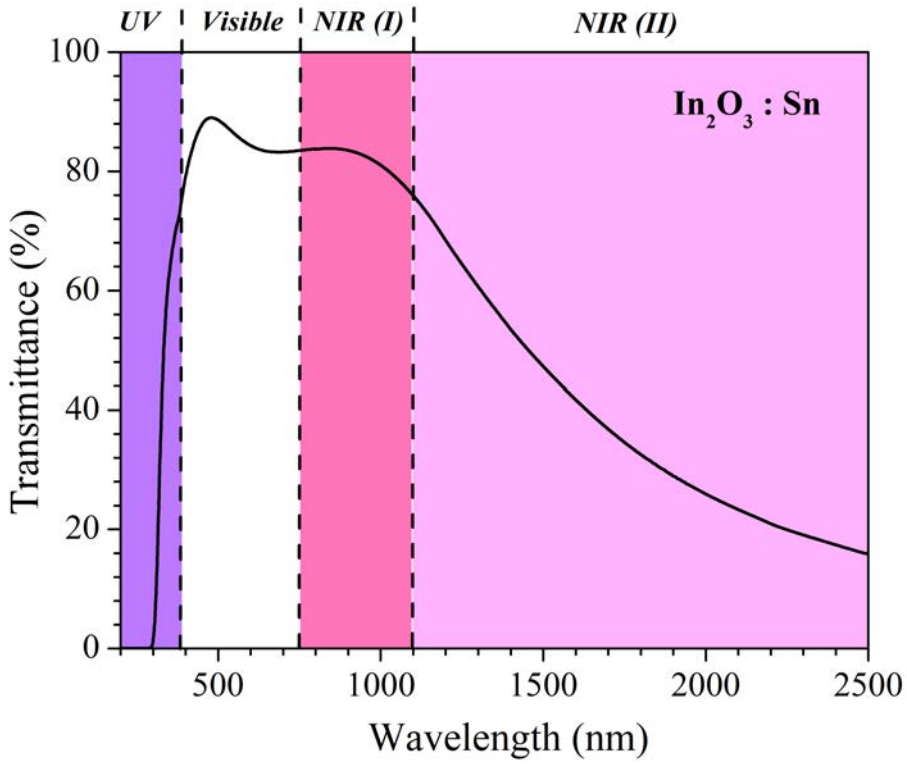


Figure 1.4: Optical transmittance spectrum of a commercial ITO thin film grown on glass.

concentration that restricts the increase of plasma frequency [2]. Yet, as will be shown later, even just the wavelength range of 790–1100 nm (*NIR(I)* in Figure 1.4) contains over 60% of the NIR solar energy, which is not excluded by traditional ITO or FTO coatings. Therefore, other kinds of NIR materials are needed to enhance the blocking of near-infrared light. In particular, visibly transparent inorganic NIR materials are desirable due to their high thermal, chemical and solar stability compared to organic materials [67]. Part of the aim of this study is to find a competent candidate for this application. Although little research has been done on the study of transparent inorganic NIR materials, a short review on some recent research will be presented in this chapter.

1.3 Introduction to ZnO

ZnO is a typical wide band gap semiconductor with high optical transparency across the visible spectrum (400–700 nm). Appropriate doping with elements from group IIIA or IVA enable the material to acquire almost metallic conductivity. As said, ZnO thin films have been regarded as one of the promising alternatives for the widely-used but expensive ITO. Here a brief introduction to ZnO will be presented, including its atomic structure, band structure and dopants that have been widely used in the past.

1.3.1 Crystal structure

ZnO has three possible crystal structures, including hexagonal wurtzite, cubic rock-salt and cubic zincblende [68]. The hexagonal wurtzite structure is the predominant form since it is thermodynamically the most stable phase under ambient conditions. In the wurtzite phase of ZnO, each cation is tetrahedrally-coordinated by four anions, and vice versa. Therefore, the coordination numbers of both Zn^{2+} and O^{2-} are four. The stick and ball representation of different ZnO crystal structures are shown in Figure 1.5.

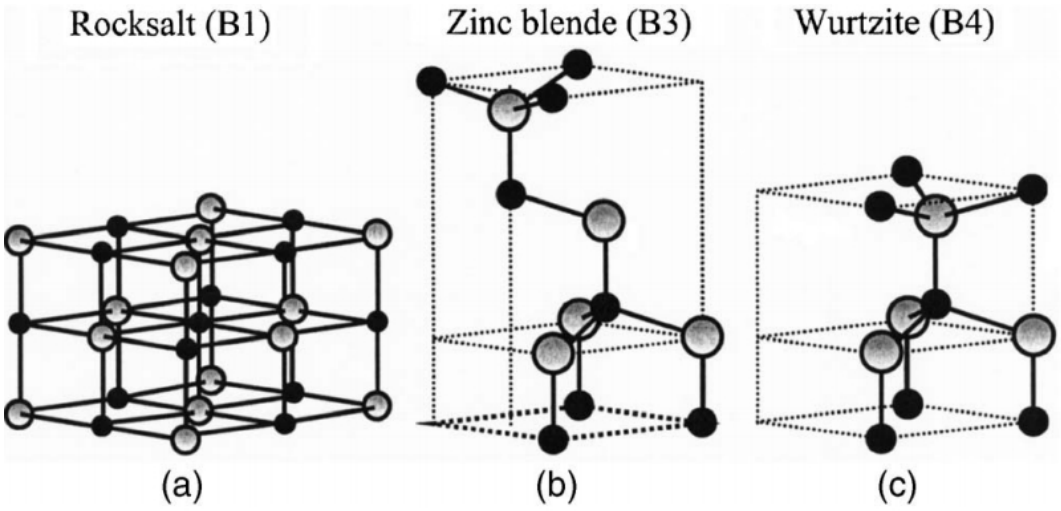


Figure 1.5: ZnO crystal structures. [68]

In general, five main factors can influence the lattice parameters of a semiconducting material: 1) the deformation of the conduction band structure that

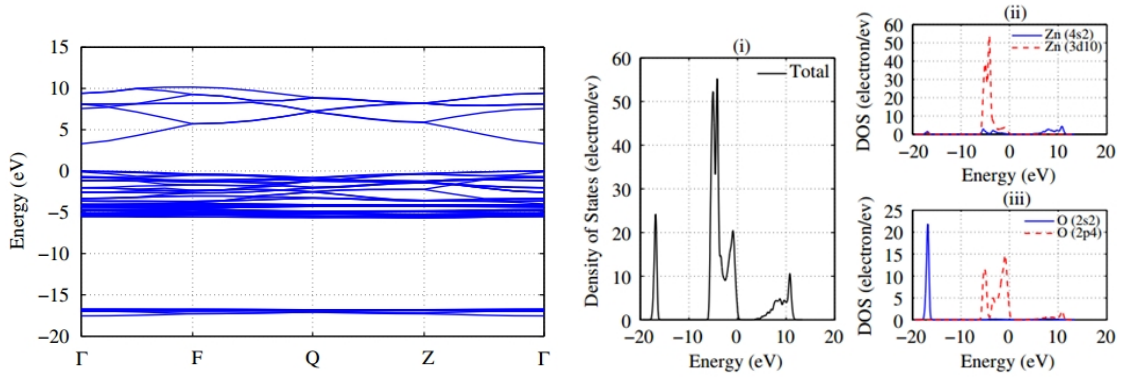
relates to the free electron density [69], 2) differences between the ionic radii of host ions and substitutional impurity atoms [70], 3) impurity atoms at interstitial sites, 4) external strain, and 5) sample temperature [68]. The wurtzite structure belongs to the space group $P6_3mc$ in the Hermann-Mauguin notation and C_{6v}^4 in the Schoenflies notation. It has lattice parameters, $a = 0.32498$ nm and $c = 0.52066$ nm, with $c/a = \sqrt{8/3} \approx 1.633$. However, the experimentally measured c/a ratio of ZnO usually has slight deviation from the ideal value [71].

Wurtzite ZnO can transform to the cubic rocksalt structure at high pressure ($\sim$ 10 GPa) [72]. Zincblende ZnO is a meta-stable phase that can only be stabilised by depositing on cubic substrates, utilizing the lattice compatibility to overcome the tendency to form the wurtzite structure. Substrates such as ZnS, Pt, Ti, Si and SiO_2 have been used for the growth of zincblende ZnO [73].

1.3.2 Band structure

ZnO has a direct band gap and the band gap energy is generally quoted as 3.4 eV [2]. Numerous calculations have been applied to determine the band structure of ZnO in the past, including highly accurate methods such as the GW approximation (GWA) [74]. Depending on the exact density functional theory (DFT) method used, various band gap energy values have been obtained from 0.4 to 3.77 eV [74–77]. In particular, the local density approximation (LDA) and the generalized-gradient approximation (GGA) significantly underestimate the value of the band gap [75, 77]. However most of the calculations confirmed that the conduction band minimum (CBM) and the valence band maximum (VBM) both occur at the Γ point where $k = 0$, as shown in Figure 1.6.

The high dispersion of the CBM indicates a small effective electron mass in ZnO. Calculated effective masses of electrons and holes are 0.28 m_e and 0.59 m_e, respectively, where m_e ($m_e = 9.11 \times 10^{-31}$ kg) represents the free electron mass [79]. Figure 1.6 illustrates the total density of states (DOS) and the partial contributions from Zn and O states. The major contribution to the CBM is from Zn $4s$ while the O $2p$ state plays a relatively minor role. The s-type character is a common feature



(a) Band structure calculated using GGA and sx-LDA functionals.

(b) Total and partial density of states.

Figure 1.6: Electronic band structure and density of states of pure wurtzite ZnO. [78]

for most of the binary TCOs including ZnO [80]. Small effective electron mass and the strong s-character of the CBM give rise to the high electron mobility ($\sim$ 200 cm^2/Vs) in pure ZnO.

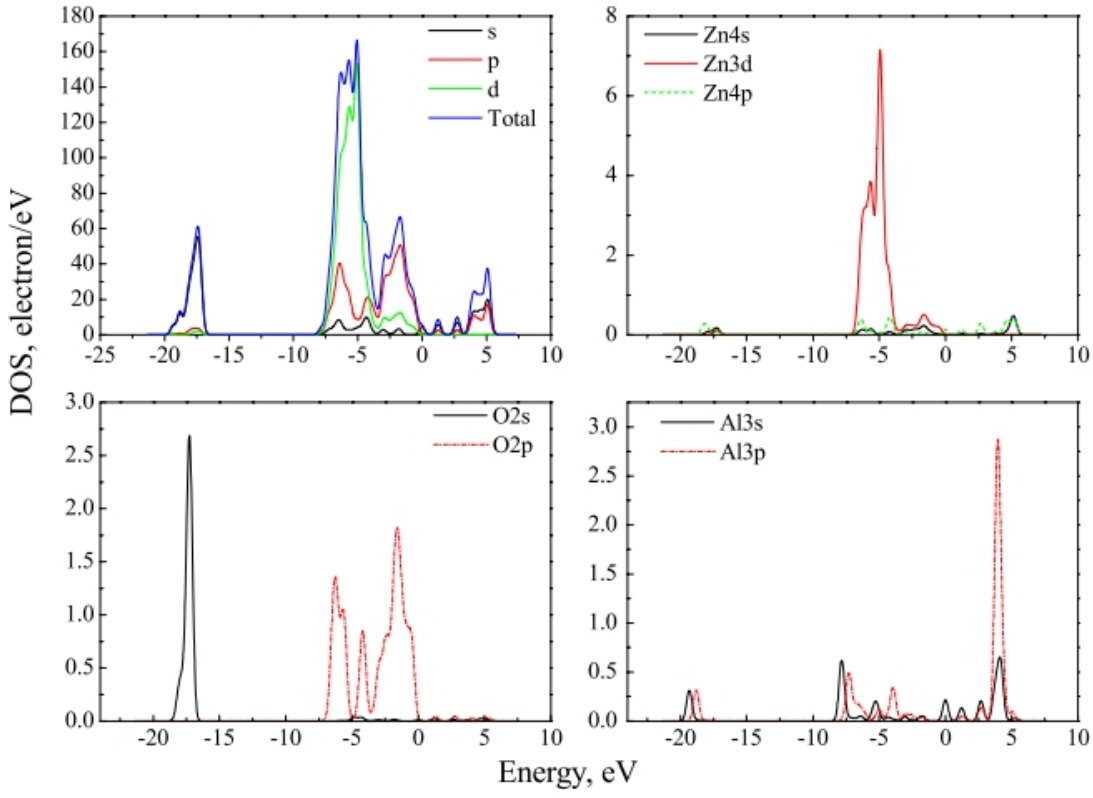


Figure 1.7: Total and partial density of states of Al doped ZnO. [81]

Figure 1.7 shows the calculated total and partial DOS of Al doped ZnO [81]. Here the concentration of Al is 3 at.%. The addition of Al introduces a large number of free electrons, which is supported by the distribution of DOS. As it can be seen, the CBM contains a clear contribution from Al $3p$ and Al $3s$ states while the Zn $4s$ states are pushed to slightly higher energies. The conduction band may be partially filled by the extra electrons owing to the incorporation of Al atoms. The VBM mainly consists of O $2p$ and Zn $3d$ states, which is similar to the case of pure ZnO.

1.3.3 Doping of ZnO thin films

Before introducing the doping in ZnO, it is helpful to know how carrier concentrations and electron mobilities contribute to the conductivity/resistivity of the films. The electrical performance of TCO materials can be described in terms of resistivity ρ (Ωcm), and its inverse, conductivity ($\Omega^{-1}\text{cm}^{-1}$). For a multi-dimensional system, the conductivity is a tensor $\sigma_{\alpha\beta}$ which is related to the internal electric field $\mathbf{E}$ and the current density $\mathbf{j}$ through the equation:

$$j_\alpha = \sum_\beta \sigma_{\alpha\beta} E_\beta \tag{1.1}$$

with the spatial indices α and β running over the entire spatial dimensions. Here j_α and E_β are the components of current density and electric field, respectively. For an isotropic system the conductivity can be simplified to:

$$j = \sigma E \tag{1.2}$$

By assuming there is only one dominant carrier type inside the material, either electrons or holes, conductivity can be given as:

$$\sigma = Ne\mu \tag{1.3}$$

where N is the concentration of free carriers, μ is the carrier mobility and e is the electronic charge (1.602×10^{-19} C). Therefore, the resistivity of the film can be written as:

$$\rho = \frac{1}{\sigma} = \frac{1}{Ne\mu} \tag{1.4}$$

It can be seen that the doping of ZnO is important because it would affect the electrical resistivity by regulating the concentration of free carriers in the thin film.

1.3.3.1 P-type doping

P-type doping in wide band gap materials such as ZnO has been found to be difficult for several reasons. In general, three major factors result in the low efficiency of p-type doping: 1) self-compensation effects, 2) low solubility of dopants and 3) the generation of deep acceptor levels [82, 83]. One of the main issues is strong self-compensation due to native low-energy n-type defects such as O vacancies or Zn interstitials [84]. ZnO is a naturally n-type semiconductor owing to the natural existence of these n-type defects correlated with deviations from ideal stoichiometry, which makes acceptor doping in ZnO very difficult.

Group IA elements (alkali metals) such as Li, Na, K and group VA elements such as N and P have been used as p-type Zn substitutions and O substitutions, respectively [82]. However, the incorporation of alkali metals is usually less efficient for two main reasons: 1) group IA elements have relatively small ionic radii which may make them take up interstitial sites rather than substitutional, and thus behave as donors, 2) the ionization energies of Li and Na are higher than those of N and P, which leads to lower carrier concentrations [85, 86]. Compared to other group VA elements, N is the most promising and widely-used p-type dopant. One of the reasons is that N has the closest ionic radii to O ($r_{N^{3-}} = 1.46$ Å and $r_{O^{2-}} = 1.38$ Å), thus the substitution of N at O sites induce a minimum lattice distortion [87]. Other group VA p-type dopants including P, As and Sb have much larger ionic radii than that of the O ion. The large ionic size decreases the dopant solubility and increases the lattice distortion [82].

1.3.3.2 N-type doping

Intrinsic N-type doping As mentioned in the previous section, ZnO contains natural donors, including interstitial Zn and O vacancies. ZnO bulk single crystals without any additional incorporation of dopants show a wide range of resistivities from $0.1 - 10^3$ Ωcm, depending on the processing conditions [88–90]. Electron generation due to oxygen vacancies can be depicted by the following equilibrium reaction [91]:

$$O_O^x \rightleftharpoons \frac{1}{2}O_{2(g)} + V_{\ddot{O}} + 2e^- \tag{1.5}$$

where $V_{\ddot{O}}$ is a doubly ionized oxygen vacancy and e^- is a free electron. This reaction not only happens in ZnO but also takes place in many other TCO materials such as In_2O_3, SnO_2 and CdO. In the 1930s Wagner and Schottky showed that the oxygen content of the crystal, varied by annealing in a series of oxygen partial pressures, could greatly influenced the conductivity through the reactions between free electrons and interstitial Zn ions or the oxygen vacancies. These processes can be described as [80]:

$$\begin{aligned} 2Zn_{(l)} + O_{2(g)} + 2V_{\ddot{O}} + 4e^- &\rightleftharpoons 2ZnO \\ 2Zn_{(i)}^{\cdot\cdot} + O_{2(g)} + 4e^- &\rightleftharpoons 2ZnO \end{aligned} \tag{1.6}$$

where l(subscript) and i(subscript) refer to lattice and interstitial positions, respectively. These films are not stable for long at ambient conditions (especially at high temperatures), owing to oxygen absorption or desorption. The best resistivity of these films is only about $10^{-2} - 10^{-3}$ Ωcm. Therefore excess Zn or oxygen vacancies cannot be used as a reliable source of donors [92].

Extrinsic N-type doping An appropriate concentration of extrinsic n-type dopants can greatly enhance the conductivity by contributing more free electrons. Known n-type elements such as Al, Ga, In from group IIIA and Si, Sn from group IVA have been used to substitute for Zn. Elements from group VIA like F, Cl and I have been substituted for O. Table 1.3 shows a collection of the basic properties for

Al doped (AZO), Ga doped (GZO) and Si doped ZnO (SiZO) achieved by different deposition techniques.

Table 1.3: Basic properties for AZO, GZO and SiZO obtained by different techniques.

TCO	Deposition techniques	N (10^{20}cm^{-3})	μ (cm^2/Vs)	ρ ($10^{-4}\Omega$cm)	T (*vis*) (%)
AZO [93]	Sputtering	15	22	1.9	> 80
AZO [94]	PLD	13.1	36.7	1.3	$89 - 95$
AZO [95]	Spray pyrolysis	0.6-0.75	38-43	20	> 80
GZO [96]	Sputtering	1-6	5-35	5.3	90
GZO [97]	PLD	64	4.9	2.6	> 90
GZO [98]	Spray pyrolysis	2.5	17	15	> 80
SiZO [99]	Sputtering	12	13.7	3.8	> 85
SiZO [79]	PLD	2.7	38	6.2	80
SiZO [100]	Spray pyrolysis	1.7	10	37	80

Here, as introduced in the previous sections, N, μ, ρ, T stand for the carrier concentration, electron mobility, resistivity and the average optical transmittance in the visible range of the film, respectively. Among all these dopants, Al is the most widely investigated due to the superior electrical and optical properties of AZO films, as shown in Table 1.3. Nevertheless, although AZO has always been regarded as a potential alternative for ITO, its electrical performance still is not as good as ITO. For ITO, either PVD methods such as PLD or chemical methods like spray pyrolysis can produce films with resistivities down to around 1.0×10^{-4} Ωcm and optical transmittance above 80% [101, 102]. Table 1.3 illustrates that chemical method like spray pyrolysis do not produce ZnO films with conductivities as high as the sputtered ZnO films. The reason for this is still not clear [103].

In contrast, there are much fewer investigations on SiZO films than that on AZO and GZO films. However, more research is worth carrying out since Si has been proven to be a promising dopant, and SiZO films may also be a potential ITO alternative in the future. The fact that Si can generate two free electrons means it may become a more effective carrier donor than other group IIIA dopants [103]. Recently, Rashidi *et al* showed that by doping ZnO with Si and F (cation-anion co-doping), it is able

to reduce the resistivity to 1.5×10^{-3} Ωcm for ZnO films made by spray pyrolysis [104], which is even lower than the minimum data that has been reported for sprayed AZO and GZO films. These experimental results indicate the great potential of Si as a dopant and SiZO as a promising ITO alternative, which is also my reason for choosing SiZO as the material for this study. However, since there is not too much data from Si doped ZnO films, the review in Section 1.5 will mainly focus on the data reported for Al doped ZnO films, which perhaps could show how much work has been done on the optimization of processing conditions for doped ZnO films.

1.4 Factors limiting the mobility in ZnO films

The mobility of carriers in ZnO films plays a crucial role not only on its electrical performance since high mobility will also reduce the needs for increasing carrier concentration that might eventually deteriorate the transparency, as will be explained more in the next chapter. In order to interpret the variation of Hall mobility observed in experiments, several scattering mechanisms have been used to fit the experimental data. According to Matthiessen's rule, the overall mobility equals:

$$\frac{1}{\mu_H} = \frac{1}{\mu_i} + \frac{1}{\mu_n} + \frac{1}{\mu_g} + \frac{1}{\mu_d} + \frac{1}{\mu_l} + \frac{1}{\mu_c} \tag{1.7}$$

where μ_i, μ_n, μ_g, μ_d, μ_l and μ_c stand for the mobilities owing to ionized impurity scattering, neutral impurity scattering, grain-boundary scattering, dislocation scattering, lattice vibration scattering and the possible dopant cluster scattering, respectively.

1.4.1 Ionized impurity scattering

The theoretical models that have been used for depicting ionized impurity scattering have been reviewed by Ellmer in 2001 [92]. For degenerate semiconductors, the model developed by Brooks, Herring and Dingle (BHD theory) [106, 107] is generally used

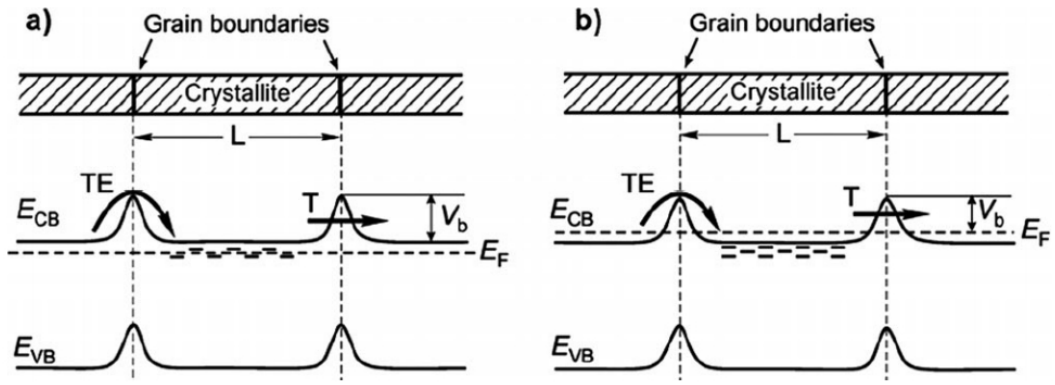


Figure 1.8: Schematic band diagrams of (a) a poly-crystalline n-type doped semiconductor and (b) a degenerate n-type semiconductor.The Fermi energy level goes deep into the conduction band as the carrier concentration increases and therefore reduces the effective barrier height [105].

for calculations. According to their theory, the mobility due to ionized impurity scattering can be expressed as:

$$\mu_i = \frac{3(\varepsilon_r \varepsilon_0)^2 h^3}{Z^2 (m^*)^2 e^3} \frac{N}{N_s} \frac{1}{F_i} \tag{1.8}$$

where ε_r, N_s, Z, F_i represent the relative static permittivity, density of the scattering centers, ion valence and the screening function, respectively. N_s in general can be regarded as the carrier concentration (N) for degenerate AZO films. The other symbols ε_0, h, e, N and m^* have their usual meaning. For highly degenerate semiconductors where the Fermi level is in the conduction band, the grain boundary potential barriers are relatively low (as shown in Figure 1.8), and thus ionized impurity scattering is sometimes regarded as the predominant scattering mechanism for films with high degeneracy. This idea is supported by the experimental observation that polycrystalline AZO films have resistivities almost as low as epitaxial AZO films with high carrier concentration [108]. The limiting effect on electron mobility caused by ionized impurities can be seen more clearly with experiments on single crystalline ZnO films. For epitaxially grown pure ZnO films, the mobility could be enhanced up to 200 cm^2/Vs [109], close to the electronic mobility in bulk ZnO. However, the highest mobility that could be achieved for

as-deposited epitaxial AZO films is only around 50 cm^2/Vs.

1.4.2 Grain-boundary scattering

Grain boundary scattering in polycrystalline silicon and TCO films is always analyzed by using the charge-trapping model proposed by Seto [110]. In this model, the investigated film is assumed to be composed of small grains separated by grain boundaries with negligible thickness. Owing to the discontinuous crystallographic arrangement, grain boundaries usually contain a high density of defects that can trap carriers from the grains. In order to achieve charge balance, the charged impurity states thus create a depletion zone on both sides accompanied by a potential energy barrier for the carriers. The barrier can be surmounted either by thermionic emission or by tunneling if the depletion width is very narrow. By assuming that thermionic emission dominates the transport of electrons, the mobility due to grain boundary scattering can be given by:

$$\mu_g = Le\left(\frac{1}{2\pi m^* kT}\right)^{1/2} \exp\left(-\frac{E_b}{kT}\right) \tag{1.9}$$

where E_b, L, k, T are the barrier height, the effective grain size, the Boltzmann constant and the sample temperature, respectively. Although ionized impurity scattering is sometimes regarded as the main scattering mechanism for highly degenerate semiconductors as said, calculations showed that the influence from the grain boundaries cannot be neglected in order to interpret the experimental data, particularly the relations between Hall mobility and carrier concentration, even at high carrier densities (about 10^{21} cm^{-3}) [108, 111]. In fact, in some cases grain-boundary scattering is considered as the dominant scattering mechanism in AZO films with carrier concentrations on the order of 10^{20} cm^{-3} [112]. A sensible explanation to this is that the grain-boundary potential barriers in these samples cannot be fully compensated by the raise of Fermi levels [112].

1.4.3 Neutral impurity scattering

Since donors such as substitutional Al or interstitial Zn create shallow states in ZnO, the concentrations of neutral impurities are generally very low at room temperature, especially when compared to the concentration of ionized impurity [113]. Therefore, the influence from neutral impurity scattering was not considered in most studies.

1.4.4 Lattice vibration scattering

The lattice vibration scattering mobility is written as:

$$\mu_l = \left(\frac{\pi}{3}\right)^{1/3} \frac{eh^3 C_l}{kT(m^*)^2 E_d^2 N^{1/3}} \propto \frac{1}{T} \tag{1.10}$$

where E_d and C_l are the deformation potential constant and the elasticity modulus, respectively [114, 115]. Lattice vibration scattering has been found to play the dominant role at high temperature [89], but its contribution at room temperature is relatively small.

1.4.5 Dislocation scattering

The dislocation scattering mobility is given by [116, 117]:

$$\mu_d = \frac{30(\varepsilon_r \varepsilon_0)^{3/2} \sqrt{2\pi N} a^2 kT}{e^3 f^2 \sqrt{m^*} N_d} \tag{1.11}$$

Here ε_r is the relative permittivity of the sample, ε_0 is the vacuum permittivity, N_d is the dislocation density, a is the spacing between acceptor centers on the dislocation line while f is the occupation rate of the acceptor states. Even though dislocation scattering exists in almost every film, it has been rarely used for the analysis of the electrical transport in TCOs [118]. More analysis on this topic is required in the future since some of the Hall mobility - carrier concentration relationships still cannot be well explained by the other scattering mechanisms [111].

1.4.6 Intragrain/inter-grain cluster scattering

As will be shown later, both the carrier mobility and carrier concentration of doped ZnO films drop after the dopant concentration exceeds a critical value, which cannot be explained solely by ionized impurity scattering or the theory of charge-trapping at the grain boundaries. Similar phenomena have been reported by other researchers [100, 113], and have been generally considered as the effect of the dopant clustering inside the grains or at the grain boundaries. Even though plenty of theoretical models [119, 120] have been set up and used by researchers to fit their experimental data [111], no clear sign of intragrain/inter-grain segregation has been detected in AZO or SiZO films so far.

1.5 The influence of experimental parameters on ZnO films

1.5.1 Substrate temperature during deposition

1.5.1.1 Electrical properties

The variation of resistivity/conductivity with substrate temperature has been studied by many researchers, and the results are in fairly good agreement. Generally the resistivity of the films decreases as the substrate temperature increases from room temperature (RT) to around 300 °C and increases again when the substrate temperature exceeds 300 °C. Moon *et al.* [121], Wang *et al.* [122] and Yang *et al.* [123] reported this behavior for sputtered AZO (ZnO:Al) films made from 2 wt% alumina doped ZnO targets. The lowest resistivity reported in these papers is 6.0×10^{-4} Ωcm for AZO film deposited on glass substrates [121]. The decrease of resistivity for temperature below 300 °C results from increases in both carrier concentration and mobility, as shown in Figure 1.9.

One reason for the increase of mobility may be the increase in the grain size that leads to the reduction in the density of grain-boundaries. As said, grain-boundary scattering can be important even in some highly-degenerate semiconductors. Both XRD data [121] and FE-SEM images [124] indicate the increase of grain size at higher

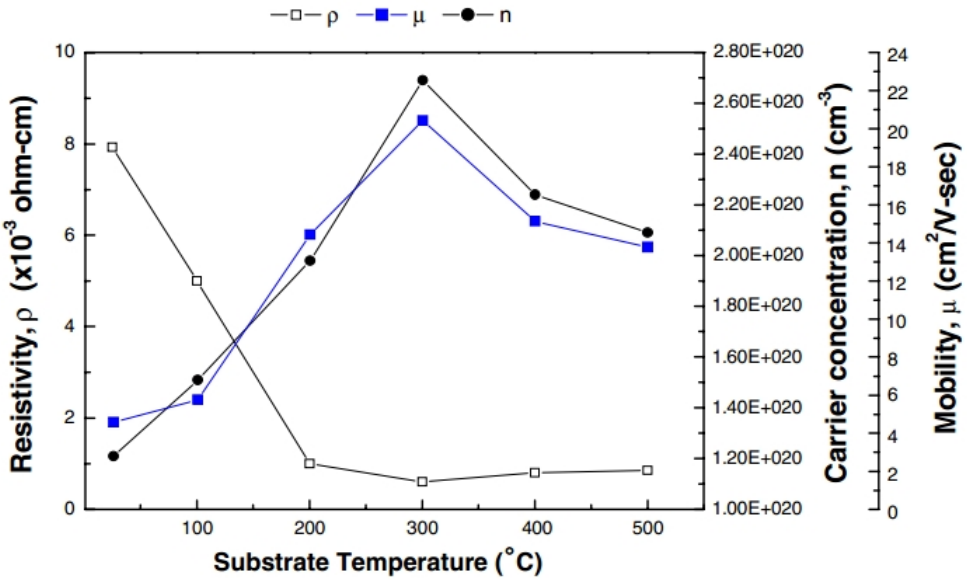


Figure 1.9: Influence of substrate temperature on ρ, N and μ of sputtered AZO films. [121]

substrate temperature. One example of larger-sized structure of films deposited at higher temperature is given in Figure 1.10.

At low substrate temperatures, the diffusivity of the atoms inside the films is relatively low, thus the average grain sizes are small in the films. If the substrate temperature goes above 300 °C, the resistivity of the films start to increase, owing to the decrease of carrier concentration and mobility.

By comparison, some other groups reported slightly different results where the resistivity starts to increase at around 150 °C, i.e. the lowest resistivity was obtained at the substrate temperature of 150 °C [125, 126]. The shift of the optimum temperatures may be because the targets used by later groups contain higher concentrations of Al (3 wt% alumina in [125]). According to electron probe micro-analyzer (EPMA) and secondary ion mass spectrometry (SIMS) studies, the content of Al inside ZnO films has been found to increase with increasing substrate temperature, as shown in Figure 1.11 [126].

The vapor pressure of Zn is relatively higher than that of Al, and the difference between their vapor pressure widens as the temperature increases [127], which may account for the increase in Al content when the temperature rises. Therefore, if this

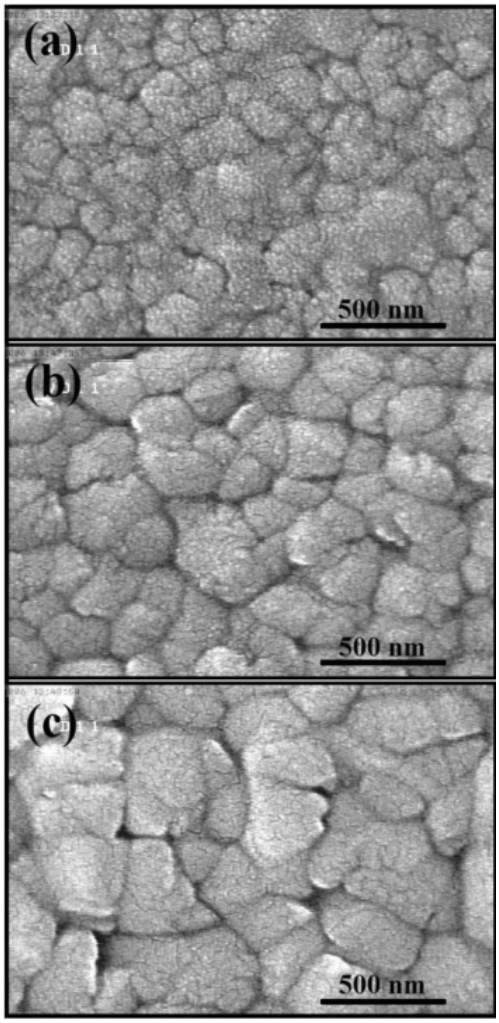


Figure 1.10: FE-SEM images of AZO films deposited at different substrate temperatures. (a) At 150 °C, (b) At 250 °C, (c) At 350 °C. [124]

temperature-Al concentration relationship can be applied generally, for films made from targets which contain higher concentrations of Al, the optimum Al concentration (as discussed later) will be reached at a lower temperature and thus cause the shift of the optimum temperature. The increase in Al concentration can also explain the increase of carrier concentration at temperatures below 150 °C. Figure 1.11 shows that films obtained at a substrate temperature of 150 °C, which is the most conducting film in this study [126], contains around 4 at.% of Al.

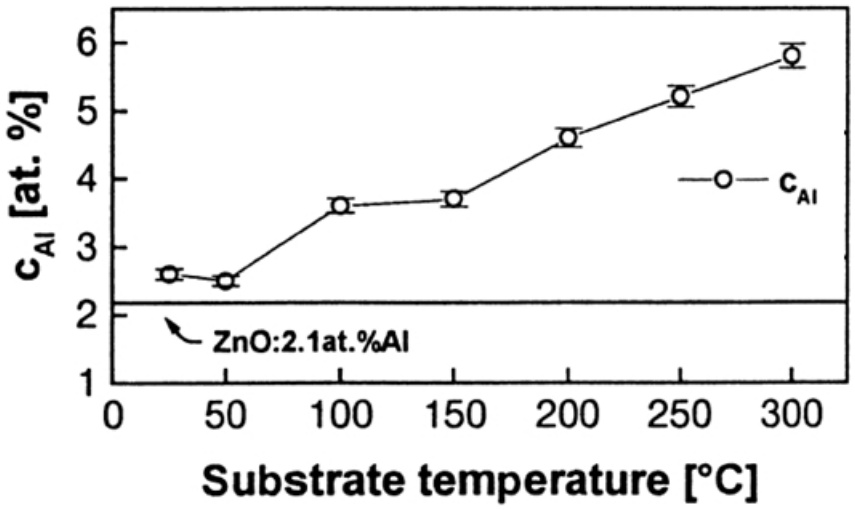


Figure 1.11: Al content increases with increasing substrate temperature. Figure adapted from [126].

1.5.1.2 Optical properties

The optical results obtained by several groups all show that the substrate temperature has little influence on the visible transmittance of deposited AZO films [122, 125]. The average transmittance across the visible spectrum is generally around or even higher than 90%, which demonstrates the good optical properties of AZO films. However, changes in optical energy band gap have been observed in the films sputtered at different substrate temperatures [122, 125]. This phenomenon is generally explained by the Burstein-Moss effect [128]. Burstein pointed out that for a degenerate semiconductor, the optical band gap (E_g) widens (blue shift) as the Fermi level in the conduction band increases. This occurs because the lower states in the conduction band are occupied and blocked. The widening ΔE_g is related to the carrier concentration N through equation:

$$\Delta E_g = \frac{h^2}{8m^*}\left(\frac{3}{\pi}\right)^{2/3} N^{2/3} \tag{1.12}$$

Therefore, when N decreases E_g becomes smaller according to the above equation. This is consistent with the experimental results [125], in which the optical band gap values were obtained from the transmittance spectrum using the Tauc relations.

It is also worth mentioning that the optical band gap of a TCO does not necessarily equal its fundamental band gap. For In_2O_3, researchers used to believe that the bulk band gap was 3.75 eV since it has been found that the optical absorption edge of the bulk sample is at 3.75 eV [129]. Yet, it has been shown later that the minimum direct band gap is in fact 2.9 eV, but is a forbidden transition [130]. According to the parity selection rules, the first permitted optical transition is 0.8 eV beneath the valence band top. Likewise, for SnO_2, of which the upper valence bands do not have the right symmetry for optical transitions to the conduction band minimum (CBM), the fundamental band gap is generally quoted as 3.6 eV and is smaller than the optical band gap measured in experiments [131–134]. Surprisingly, the band gap values obtained by all these research groups are identical — 3.76 eV. A vast number of calculations have been carried out in the past [135, 136], but almost none of them have explained accurately the origin of the experimental band gap value. Therefore, more calculations need to be done in the future in order to better understand the electronic structure of SnO_2 and other TCOs.

1.5.1.3 Texture of the films

In general, texture is an important parameter for any TCO film. It influences the scattering of electrons and electromagnetic waves in the material. Nistor *et al.* showed that for undoped ZnO films grown on MgO substrates, the variation of texture as the substrate temperature is changed can be divided into three stages: for $T < 200$ °C, the films are amorphous; for 200 °C $< T <$ 300 °C, the films are highly (002) textured without any in-plane alignment at this stage; for $T > 300$ °C, epitaxial films start to appear with the following in-plane relationships: $(1\bar{1}0)_{ZnO} \parallel (110)_{MgO}$ and $(110)_{ZnO} \parallel (110)_{MgO}$ [137]. In another study, a-axis textured ZnO thin films have been grown on MgO substrates at a substrate temperature of 500 °C [138]. The analysis of texture will also be carried out on Si doped ZnO films in this study.

1.5.2 Doping level

Doping of ZnO films not only enhances their electrical properties, but also improves other aspects of performance such as thermal and chemical stability. Major *et al.* reported that ZnO films with 3 wt% indium acquire thermal stability up to 175 °C in oxygen, and up to 375 °C in vacuum [139]. In most cases, the incorporation of dopants increase the carrier concentration yet decreases the mobility due to scattering by ionized impurities. The higher carrier concentration is generated either by dopant ions at substitutional sites of Zn^{2+} or O^{2-} ions, or by interstitial dopant ions in the ZnO lattice which are able to create a large number of free electrons in the film. However, as the dopant concentration exceeds a certain level, the resistivity starts to increase. Lu *et al.* carried out a systematic study of the variation of resistivity with dopant concentration (doping level) [113]. Figure 1.12 shows the measured resistivity, carrier concentration and mobility values for films deposited from targets with different Al atomic percentages. Here, the concentration of Al is defined as $N(\mathrm{Al})/(N(\mathrm{Al})+N(\mathrm{Zn}))$, where $N(\mathrm{Al})$ is the total number of atoms of Al and $N(\mathrm{Zn})$ is the total number of atoms of Zn.

In Lu's study, targets with $0 \sim 20$ at.% of Al were used for sputtering. The lowest resistivity ($8.21 \times 10^{-4}\,\Omega\mathrm{cm}$) and the highest carrier concentration ($6.2 \times 10^{20}\,\mathrm{cm}^{-3}$) was obtained at 4 at.% , which is also the Al concentration of the sputtered film according to the EDX analysis [113]. This value is consistent with the Al concentration of the most highly conducting films obtained in the temperature-resistivity studies we discussed in Section 1.5.1 [126]. It is also in good agreement with the optimum Al concentration obtained by Kim *et al.* [125]. Lu *et al.* suggested that for films with Al concentrations higher than this optimum value, excess Al may segregate at the grain boundaries/ or inside the grain in the form of Al-O and Al-Al clusters such as AlO_x suboxides. These clusters are electrically inactive, and will not only reduce the carrier concentration but also lead to greater scattering of carriers. Similar suggestions have been proposed by Choi *et al.* [140] and Chen *et al.* [141] for ZnO:Ga and ZnO:Al films, respectively.

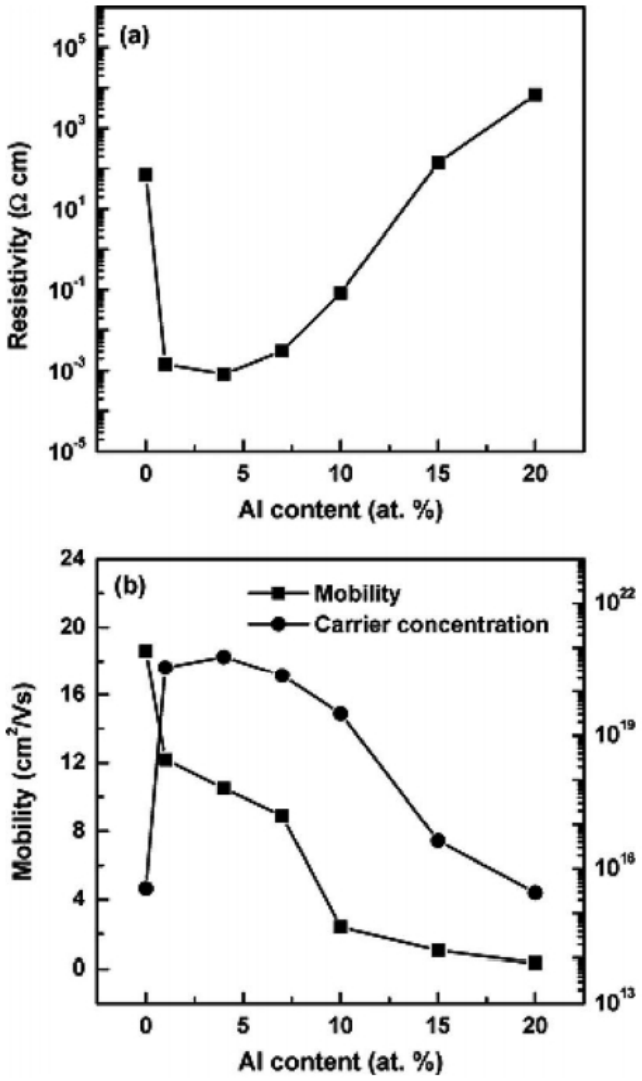


Figure 1.12: Influence of doping level on ρ, N and μ. [113]

The transmission spectra of films with different Al contents are given in Figure 1.13. The transmission was measured by UV-Vis spectrometry. In the range $0 \sim 10$ at.% Al, all films exhibit high transmittance ($\sim$ 90%) in the visible spectrum. The variation of Al concentration has not induced a huge change in optical properties. For Al contents over 15% , the absorption edges become less abrupt. This was explained by the degradation of crystal quality and the appearance of Al_2O_3 inside the ZnO [113]. For high doping levels such as 30 at.% Al, the contribution from the ZnO phase can still be seen at the edge around 345 nm. The other absorption edge is expected to be located at about 124 nm since

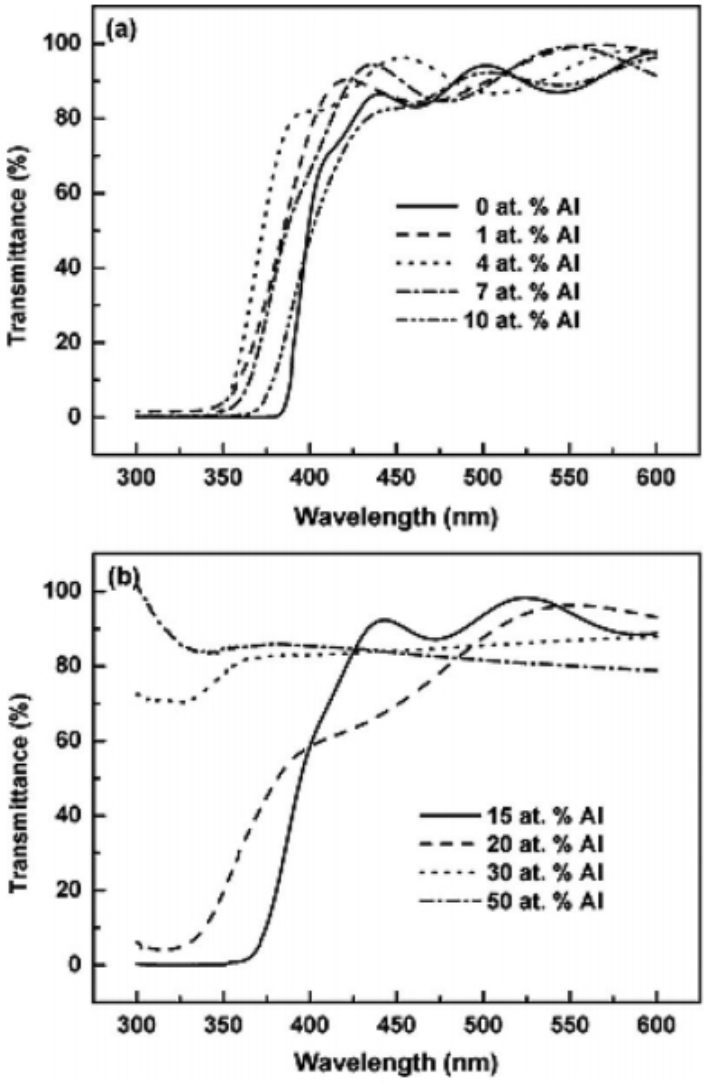


Figure 1.13: Influence of doping level on optical transmission spectra of AZO films [113].

the band gap of Al_2O_3 is 9.0 eV, higher than that of ZnO. For a doping level of 50 at.% Al, almost no sign of ZnO absorption can be seen in the transmission spectrum because the matrix has become $(Al_{1-x}Zn_x)_2O_3$ [113]. Another study conducted by Singh *et al.* [142] showed that for relatively low doping levels ($0 \sim 2$ wt% Al_2O_3 in the target), an increase of dopant concentration leads to increases of carrier concentration and greater absorption in the NIR spectrum. The result is consistent with the theory of plasma oscillations since higher carrier density will result in a blue shift of plasma frequency.

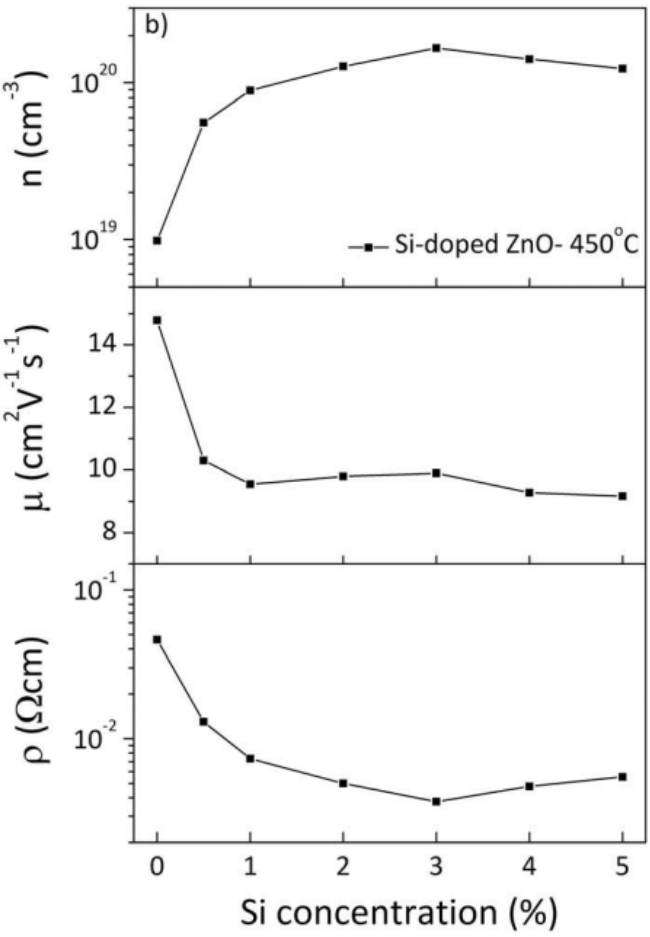


Figure 1.14: Influence of Si content on the electrical transport properties in films made by spray pyrolysis [100].

One thing that the previous research on SiZO [99, 100, 144] consist with the observations in AZO films is that conductivity increases as the dopant concentration increases only until a critical doping level. Figure 1.14 shows the variation of resistivity, carrier concentration and mobility with the nominal atomic concentration of Si in one of these publications. Here the nominal concentration is defined as N(Si)/(N(Si) + N(Zn)), where N(Si) and N(Zn) are the total number of atoms of Si and Zn in the target/precursor respectively [100]. The generation of SiO_2 and Zn_2SiO_4 impurity phase has been considered as one of the possible reasons for the decrease of conductivity at high doping levels. The phase diagram of ZnO-SiO_2 is given in Figure 1.15. It can be seen that the solubility of SiO_2 in bulk ZnO is very

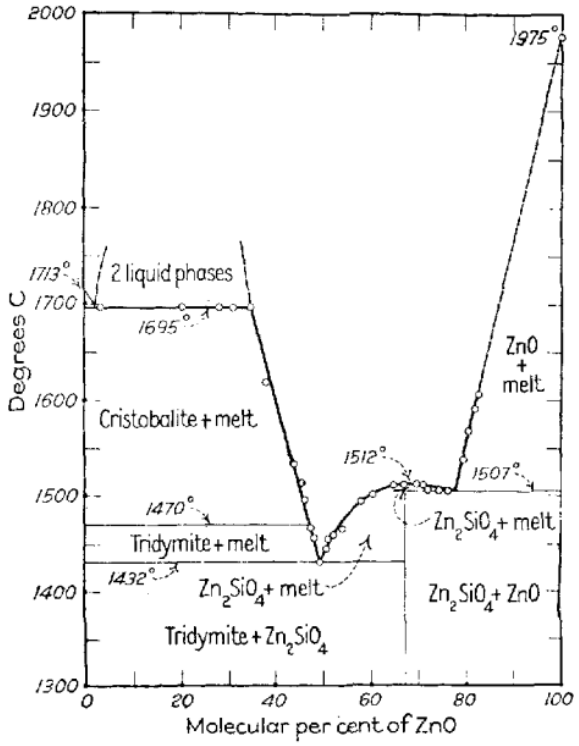


Figure 1.15: Phase diagram of SiO_2-ZnO [143].

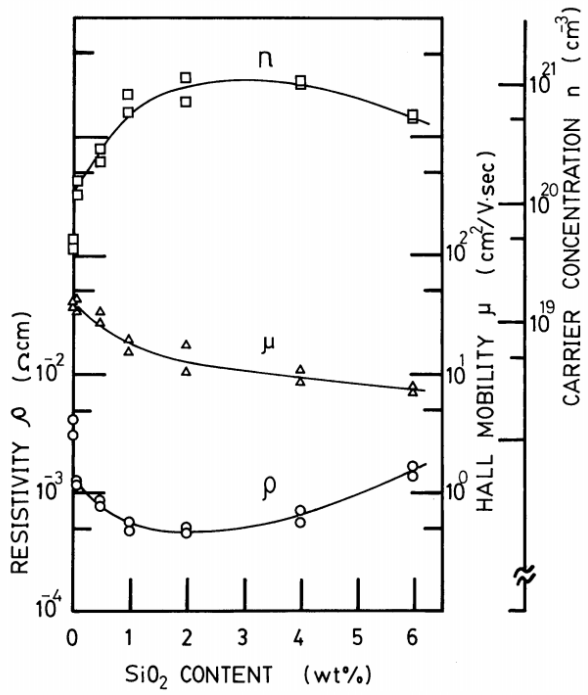


Figure 1.16: Variations of resistivity, carrier mobility and carrier concentration as a function of Si concentration for films made by sputtering [99].

low, which suggests the possibility of forming new stable phases when Si content is high. These studies of the influence of Si concentration (Figure 1.14, 1.16) also show that the optimal Si concentration range is between 3–4 at.% [99, 100], which pave the way for the choice of target Si concentration in the study shown in Chapter 3.

1.5.3 Film thickness

The relationships between resistivity and the thicknesses of polycrystalline films obtained by different researchers are qualitatively similar. Dong *et al.* showed that for their films made by pulsed laser deposition (PLD), the resistivity of the films decreased from $9.0 \times 10^{-4}\,\Omega$cm to $1.8 \times 10^{-4}\,\Omega$cm as the thickness increased from 15 to 580 nm [145]. Similar trends have been reported by Silva *et al.* for AZO films made by RF magnetron sputtering with thickness from 25 to 465 nm [146], and by Garces *et al.* for films deposited by spray pyrolysis [147].

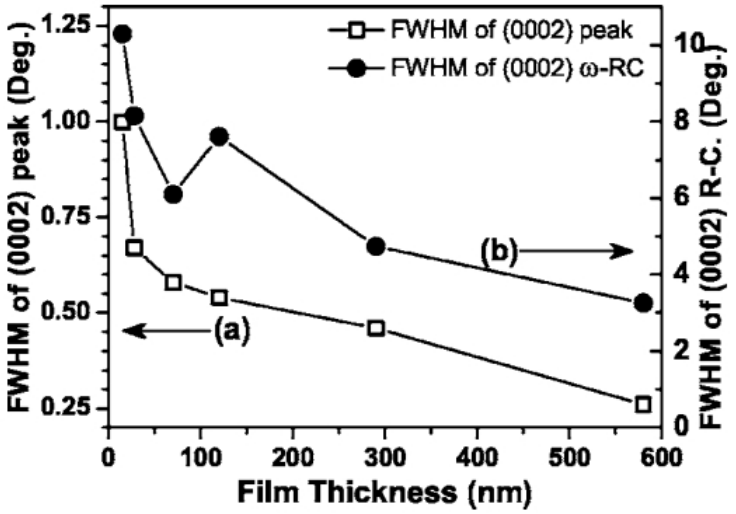


Figure 1.17: Influence of AZO film thickness on FWHM of XRD θ - 2θ (0002) peaks and (0002) rocking curves [145].

In most of these studies, the resistivity decreases rapidly with the increasing thickness when the thickness is relatively small ($<$ 250 nm), and decreases much more slowly when the thickness gets larger. The poor electrical performance for thin AZO films is generally attributed to the large stresses existing inside polycrystalline

films at low thicknesses [148, 149], which induce plenty of defects in the films. It has been shown that thicker film have better crystallinity and larger grain size compared to the thinner one [145, 150]. The relationships between the FWHM of XRD (0002) peaks, FWHM of (0002) rocking curves and the thickness are given in Figure 1.17.

1.5.4 Substrate choice

Substrate is important to the growth of ZnO films because the crystal structure of the substrate directly affects the lattice arrangements inside the film. Doped ZnO films deposited on glass or flexible substrates such as polyethylene terephthalate (PET) have been extensively investigated in the past. The films made on these substrates are either polycrystalline or amorphous [2] since the substrates do not have ordered crystal structures. The resistivity of the most conducting films made on glass substrates is around $1 \sim 2 \times 10^{-4}\,\Omega$cm and around $8 \times 10^{-4}\,\Omega$cm for coatings on PET substrates [151].

The growth of high quality epitaxial films requires the substrates to be proper single crystals. Over the last 15 years, (c-,a-,r-)sapphire (Al_2O_3), periclase (MgO), ZnO single crystals, lithium niobate ($LiNbO_3$) and scandium-aluminum-magnesium spinel (SCAM, $ScAlMgO_4$) have all been used as substrates for epitaxial deposition [80, 109, 152]. The low lattice mismatch between the substrate and the deposited material usually give rise to less mosaic misalignment in the film [108]. However, although single-crystalline films generally have higher carrier mobilities and lower resistivities, the improvement is not huge [2]. One explanation which has been mentioned is that ionized impurity scattering dominates the scattering process of electrons. The other possible reason, as pointed out by Bikowski, is that even epitaxial films may contain some small-angle grain boundaries [108]. High quality epitaxial films without any grain boundaries have recently been predicted to be able to further improve the conductivity [108], even though the improvement may not be great.

1.5.5 Post-deposition annealing

Appropriate post-deposition thermal treatments can improve the electrical and optical properties of a TCO film. A vast number of annealing experiments have been carried out for doped ZnO (predominantly AZO) in the past, with different annealing atmospheres having different or even reverse influences on conductivity. For AZO films annealed in N_2, improved conductivity has been found at annealing temperatures of 350 °C [153], whereas for temperatures of 400 °C or above a decrease in conductivity was reported [154]. Improved electrical transport has also been reported for annealing in vacuum at temperatures below 500 °C [155, 156] and for annealing in hydrogen [157] or forming gas [154] at temperatures at 400 °C or above. Yet annealing in oxygen or air usually leads to a decrease in conductivity [154, 157]. It is important to note that for annealing at high temperature the film may react with the substrate and generate new phases, leading to the degradation of the film crystallinity [158]. Ruske *et al* [159] showed that by adding a silicon capping layer to the sputtered AZO film, it is possible to enhance the electronic mobility up to $67\,\mathrm{cm^2V^{-1}s^{-1}}$, which is the highest mobility value reported for AZO thin film system so far.

This increase in conductivity is sometimes explained by the increasing concentration of oxygen vacancies, which generates more free electrons. However while excess oxygen concentration reduces the conductivity, a low oxygen concentration makes the films more metallic and deteriorates the optical transparency. Thus, the optimisation of oxygen content and the enhancement of electronic mobility seems to be necessary in order to produce highly conducting and transparent ZnO films.

1.6 Transparent inorganic NIR materials

Traditionally, industry has been focusing on the development of organic NIR materials [160, 161]. Virtually no results have been reported on the study of inorganic transparent NIR materials until recently [67]. In 2009, Norindr studied a

wide range of copper compounds and measured the optical properties of their powders. These compounds included $Cu_2P_2O_7$, $Cu_2P_4O_{12}$, $Cu_4P_2O_9$, $Cu_5P_2O_{10}$, $Cu(PO_3)_2$ and $Cu_3(PO_4)_2$. The results are summarized in Figure 1.18.

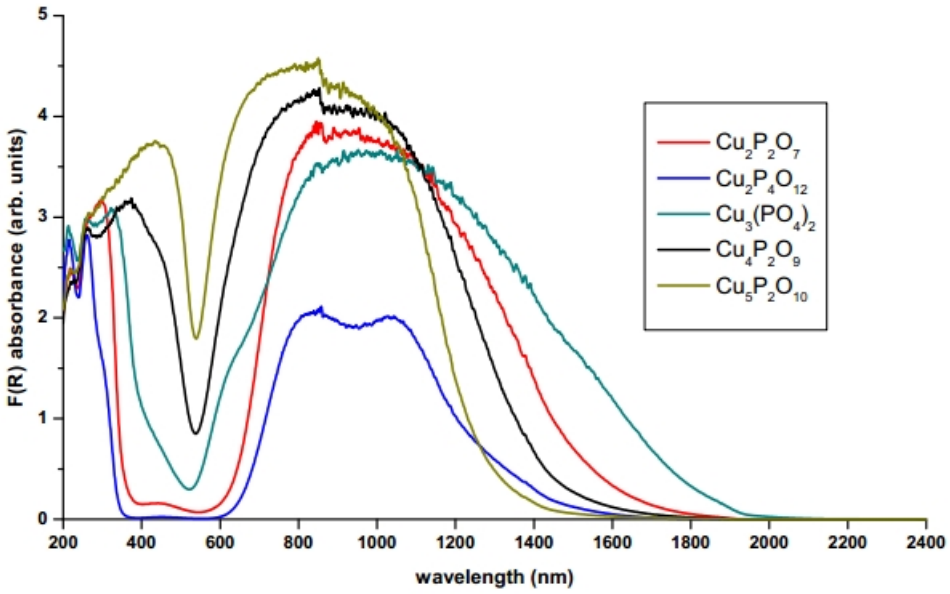


Figure 1.18: UV-Vis-NIR spectra of the powders of different copper phosphates. [67]

Among all of these compounds, copper pyrophosphate ($Cu_2P_2O_7$) was found to be a promising near-infrared absorber, yet with low absorption rate in the visible range, as it can also be seen in Figure 1.18. Apart from the Cu_xP_yO system, the work has also reported on other systems such as adding zinc phosphates or magnesium phosphates to the copper pyrophosphate system to adjust the optical properties.

Traditionally, $Cu_2P_2O_7$ has been used to supply copper ions for non-cyanide plating as a low-cost reagent [162]. However, it also possess interesting optical properties in the NIR region, due to the distortion of its molecules from regular symmetry that creates the splitting of the molecular orbitals. The lattice structure of copper pyrophosphate is shown in Figure 1.19. Cu^{2+} ions have a d^9 configuration and a distorted square pyramidal symmetry. The large atomic distance between the metal ion and apical ligand, as well as the distortion of the basal plane, lead to destabilization of the d_{xz} and d_{yz} orbitals. This special geometry enables the

material to absorb in the wavelength range of 790–1100 nm via electronic transitions between molecular bands, including $^2A_1 \leftarrow {}^2B_1$, $^2E \leftarrow {}^2B_1$ and $^2B_2 \leftarrow {}^2B_1$ (Figure 1.20). Yet, in order to use it for the purpose of this study, we must be able to manufacture uniform thin films of this material with high NIR absorption efficiency while maintaining transparency in the visible range.

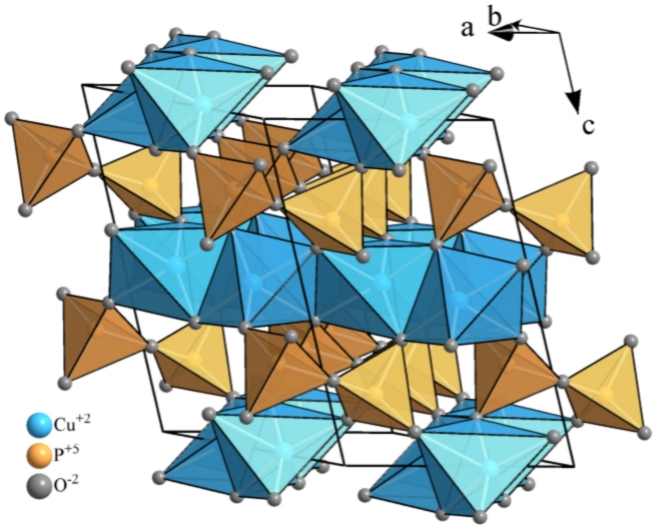


Figure 1.19: $Cu_2P_2O_7$ lattice structure. Orange tetrahedra represent the PO_4 units while the blue square pyramids show the five-fold coordination around Cu atoms [67].

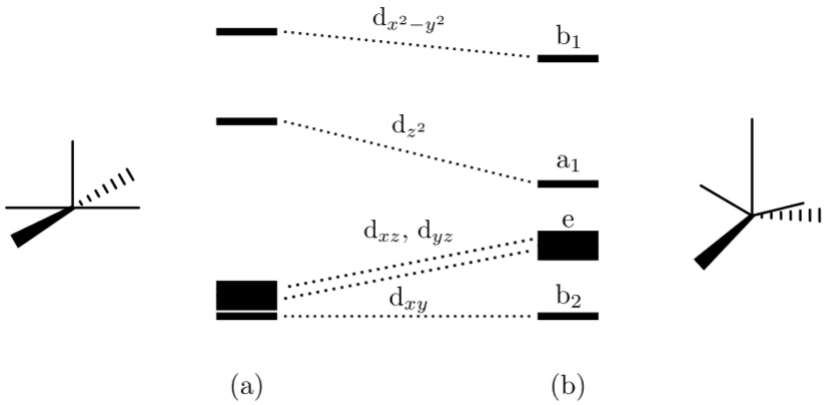


Figure 1.20: Orbital correlation diagram of (a) copper square pyramidal site and (b) distorted copper square pyramidal site [67].

Nevertheless, all of the research mentioned above for $Cu_2P_2O_7$ was carried out on powders only. Therefore, part of the goal of this study will be to try making copper pyrophosphate thin films, on which no research has been reported thus far.

1.7 Aims of the thesis

The aim of this thesis is to study how to make TCOs more attractive in terms of price, electrical conductivity and the optical properties, particularly in the NIR range. Considering the economic side, ZnO was chosen as the material of interest given its low-cost and high abundance compared to that of ITO. However, given the enormous amount of research that has been done on empirical searching for optimal parameters combination, I believe that the clues for making further improvement to the properties may lie in the fundamental studies of the films such as the careful examinations of the microstructure and chemistry. Therefore, following the introduction to a series of experimental techniques in Chapter 2, in Chapter 3 it will be shown how processing conditions affect the microstructure and chemistry of SiZO thin films and how these relate to the film properties.

Regarding the optical properties in the NIR range, it requires new materials that do not actually belong to the TCO family to develop products with wider blocking range in the NIR region, especially a part that contains a significant amount of the energy of solar irradiance. Thus, in Chapter 4 the procedure for processing copper pyrophosphate from powder to a sputtering target and to thin films will be presented. The optical properties of the produced thin films will also be discussed and compared to those of ITO. The results of this thesis will be summarized in Chapter 5, which contains a review of key discoveries, suggestions for future studies and concluding remarks.

Bibliography

[1] Insight Media, *Global TCF Market* (2014), URL `https://www.insightmedia.info/transparent-conductor-markets-report-released/`.

[2] D. Ginley, H. Hosono, and D. C. Paine, *Handbook of transparent conductors* (Springer Science and Business Media, 2010), ISBN 1441916385.

[3] K. G. Das and R., Report, IdTechEx (2014).

[4] G. M. Insights, *Low-e windows market* (2018), URL `https://www.gminsights.com/pressrelease/coated-glass-market`.

[5] MarketWatch, *Tcf global market* (2019), URL `https://www.marketwatch.com/press-release/transparent-conductive-films-market-is-projected-to-cross-us-8-billion-by-2024-2019-02-14`.

[6] A. W. Wright, American Journal of Science pp. 49–55 (1877), ISSN 0002-9599.

[7] K. Badeker, Ann. Phys.(Leipzig) **22**, 749 (1907).

[8] G. Busch, European Journal of Physics **10**, 254 (1989), ISSN 0143-0807.

[9] M. Born and P. Jordan, Zeitschrift für Physik **34**, 858 (1925), ISSN 0044-3328.

[10] E. Schrödinger, Physical Review **28**, 1049 (1926).

[11] F. Bloch, Z. Phys **52**, 555 (1928).

[12] L. Hoddeson, *Out of the crystal maze: chapters from the history of solid state physics* (Oxford University Press, 1992), ISBN 1429406925.

[13] K. Ellmer, Nature Photonics **6**, 809 (2012), ISSN 1749-4885.

[14] H. A. Mcmaster, *Conductive coating for glass and method of application*, U.S. Patent (1947).

[15] J. M. Mochel, *Electrically conducting coatings on glass and other ceramic bodies*, U.S. Patent (1951).

[16] A. Hutson, Physical Review Letters **4**, 505 (1960).

[17] K. Hayashi, S. Matsuishi, T. Kamiya, M. Hirano, and H. Hosono, Nature **419**, 462 (2002), ISSN 0028-0836.

[18] J. Sheu, Y.-K. Su, G. Chi, M. Jou, and C. Chang, Applied physics letters **72**, 3317 (1998), ISSN 0003-6951.

[19] S. Laux, N. Kaiser, A. Zöller, R. Götzelmann, H. Lauth, and H. Bernitzki, Thin Solid Films **335**, 1 (1998), ISSN 0040-6090.

[20] R.-H. Horng, D.-S. Wuu, Y.-C. Lien, and W.-H. Lan, Applied Physics Letters **79**, 2925 (2001), ISSN 0003-6951.

[21] T. Karasawa and Y. Miyata, Thin Solid Films **223**, 135 (1993), ISSN 0040-6090.

[22] Y. R. Park, E. K. Kim, D. Jung, T. S. Park, and Y. S. Kim, Applied Surface Science **254**, 2250 (2008), ISSN 0169-4332.

[23] K. Ellmer, Journal of Physics D: Applied Physics **33**, R17 (2000), ISSN 0022-3727.

[24] J.-L. Zhao, X.-M. Li, J.-M. Bian, W.-D. Yu, and X.-D. Gao, Journal of Crystal Growth **276**, 507 (2005), ISSN 0022-0248.

[25] R. N. Castellano, *Solar Panel Processing* (Archives contemporaines, 2010), ISBN 2813000167.

[26] J. Ni, H. Yan, A. Wang, Y. Yang, C. L. Stern, A. W. Metz, S. Jin, L. Wang, T. J. Marks, and J. R. Ireland, Journal of the American Chemical Society **127**, 5613 (2005), ISSN 0002-7863.

[27] T. Schuler and M. A. Aegerter, Thin Solid Films **351**, 125 (1999), ISSN 0040-6090.

[28] Y. Natsume and H. Sakata, Thin solid films **372**, 30 (2000), ISSN 0040-6090.

[29] J. Preston, in *Proceedings of the Royal Society of London A: Mathematical, Physical and Engineering Sciences* (The Royal Society), vol. 202, pp. 449–466, ISBN 0080-4630.

[30] J. M. Mochel, *Coated resistance*, U.S. Patent (1951).

[31] A. E. Junge and W. O. Lytle, *Electroconductive products and production thereof* (1951).

[32] M. J. Zunick, *Conductive coating on glass*, U.S. Patent (1950).

[33] L. Holland and G. Siddall, Vacuum **3**, 375 (1953), ISSN 0042-207X.

[34] T. Hada, K. Wasa, and S. Hayakawa, Thin Solid Films **7**, 135 (1971), ISSN 0040-6090.

[35] Y. Furubayashi, T. Hitosugi, Y. Yamamoto, K. Inaba, G. Kinoda, Y. Hirose, T. Shimada, and T. Hasegawa, Applied Physics Letters **86**, 2101 (2005), ISSN 0003-6951.

[36] T. Minami, Y. Takeda, S. Takata, and T. Kakumu, Thin Solid Films **308**, 13 (1997), ISSN 0040-6090.

[37] T. Minami, H. Sonohara, T. Kakumu, and S. Takata, Japanese journal of applied physics **34**, L971 (1995), ISSN 1347-4065.

[38] N. Naghavi, A. Rougier, C. Marcel, C. Guery, J. Leriche, and J. Tarascon, Thin Solid Films **360**, 233 (2000), ISSN 0040-6090.

[39] H. Enoki, T. Nakayama, and J. Echigoya, physica status solidi (a) **129**, 181 (1992), ISSN 1521-396X.

[40] T. Minami, H. Sonohara, S. Takata, and H. Sato, Japanese journal of applied physics **33**, L1693 (1994), ISSN 1347-4065.

[41] T. Moriga, Y. Hayashi, K. Kondo, Y. Nishimura, K.-i. Murai, I. Nakabayashi, H. Fukumoto, and K. Tominaga, Journal of Vacuum Science Technology **22**, 1705 (2004), ISSN 0734-2101.

[42] M. Orita, M. Takeuchi, H. Sakai, and H. Tanji, Japanese journal of applied physics **34**, L1550 (1995), ISSN 1347-4065.

[43] M. Orita, H. Ohta, M. Hirano, S. Narushima, and H. Hosono, Philosophical magazine B **81**, 501 (2001), ISSN 1364-2812.

[44] H. Sato, T. Minami, S. Takata, and T. Yamada, Thin solid films **236**, 27 (1993), ISSN 0040-6090.

[45] H. Kawazoe, M. Yasukawa, H. Hyodo, M. Kurita, H. Yanagi, and H. Hosono, Nature **389**, 939 (1997), ISSN 0028-0836.

[46] M. Joseph, H. Tabata, and T. Kawai, Japanese Journal of Applied Physics **38**, L1205 (1999), ISSN 1347-4065.

[47] S. Watauchi, I. Tanaka, K. Hayashi, M. Hirano, and H. Hosono, Journal of crystal growth **237**, 801 (2002), ISSN 0022-0248.

[48] T. Minami, Semiconductor Science and Technology **20**, S35 (2005), ISSN 0268-1242.

[49] Y. Shigesato, S. Takaki, and T. Haranoh, Journal of Applied Physics **71**, 3356 (1992), ISSN 0021-8979.

[50] Y. Shigesato and D. C. Paine, Applied Physics Letters **62**, 1268 (1993), ISSN 0003-6951.

[51] Y. Shigesato, D. C. Paine, and T. Haynes, Journal of applied physics **73**, 3805 (1993), ISSN 0021-8979.

[52] Y. Shigesato and D. C. Paine, Thin Solid Films **238**, 44 (1994), ISSN 0040-6090.

[53] I. Hamberg and C. G. Granqvist, Journal of Applied Physics **60**, R123 (1986), ISSN 0021-8979.

[54] G. Frank and H. Köstlin, Applied Physics A **27**, 197 (1982), ISSN 0947-8396.

[55] N. Yamada, I. Yasui, H. Li, and K. Nomura, Japanese journal of applied physics **38**, 2856 (1999), ISSN 1347-4065.

[56] N. Yamada, I. Yasui, Y. Shigesato, H. Li, Y. Ujihira, and K. Nomura, Japanese Journal of Applied Physics **39**, 4158 (2000), ISSN 1347-4065.

[57] H. Palme and H. S. C. O'Neill, Treatise on geochemistry **2**, 568 (2003).

[58] K. H. Wedepohl, Geochimica et cosmochimica Acta **59**, 1217 (1995), ISSN 0016-7037.

[59] N. T. Nassar, T. E. Graedel, and E. Harper, Science Advances **1**, e1400180 (2015), ISSN 2375-2548.

[60] U.S. Geological Survey Survey, *Mineral commodities summaries 2018* (2018), URL `https://minerals.usgs.gov/minerals/pubs/mcs/2018/mcs2018.pdf`.

[61] Indium Consumption (2018), URL `https://web.archive.org/web/20071221130320/http://geology.com/articles/indium.shtml`.

[62] Indium Trades (2018), URL https://www.reuters.com/article/us-china-metals-fanya-insight-idUSKBN0TX00K20151214.

[63] Zinc Price (2018), URL https://www.lme.com/en-GB/Metals/Non-ferrous/Zinc#tabIndex=0.

[64] U.S. Department of Energy, URL https://www.energy.gov/energysaver/home-cooling-systems/air-conditioning.

[65] Forbes, URL https://www.forbes.com/sites/judeclemente/2015/11/01/global-warming-means-more-air-conditioning-and-more-energy-demand/#535e9eb834f5.

[66] P. P. Edwards, A. Porch, M. O. Jones, D. V. Morgan, and R. M. Perks, Dalton transactions pp. 2995–3002 (2004).

[67] F. Norindr, Thesis, Southampton University (2009).

[68] Ü. Özgür, Y. I. Alivov, C. Liu, A. Teke, M. Reshchikov, S. Doan, V. Avrutin, S.-J. Cho, and H. Morkoc, Journal of applied physics **98**, 041301 (2005), ISSN 0021-8979.

[69] U. Pietsch and K. Unger, physica status solidi (a) **80**, 165 (1983), ISSN 1521-396X.

[70] N. Chen, Y. Wang, H. He, and L. Lin (1996), ISSN 0163-1829.

[71] H. Morko and m. Özgür, *Zinc oxide: fundamentals, materials and device technology* (John Wiley and Sons, 2008), ISBN 3527623957.

[72] S. Desgreniers, Physical Review B **58**, 14102 (1998).

[73] A. A. Ashrafi, A. Ueta, A. Avramescu, H. Kumano, I. Suemune, Y.-W. Ok, and T.-Y. Seong, Applied Physics Letters **76**, 550 (2000), ISSN 0003-6951.

[74] M. Usuda, N. Hamada, T. Kotani, and M. van Schilfgaarde, Physical Review B **66**, 125101 (2002).

[75] D. Vogel, P. Krüger, and J. Pollmann, Physical Review B **54**, 5495 (1996).

[76] P. Schröer, P. Krüger, and J. Pollmann, Physical Review B **47**, 6971 (1993).

[77] P. Erhart, K. Albe, and A. Klein, Physical Review B **73**, 205203 (2006).

[78] R. Chowdhury, P. Rees, S. Adhikari, F. Scarpa, and S. Wilks, Physica B: Condensed Matter **405**, 1980 (2010), ISSN 0921-4526.

[79] A. Das, P. Misra, and L. Kukreja, Journal of Physics D: Applied Physics **42**, 165405 (2009), ISSN 0022-3727.

[80] K. Ellmer, A. Klein, and B. Rech, *Transparent conductive zinc oxide: basics and applications in thin film solar cells*, vol. 104 (Springer Science and Business Media, 2007), ISBN 3540736123.

[81] X. Qu, W. Wang, S. Lv, and D. Jia, Solid State Communications **151**, 332 (2011), ISSN 0038-1098.

[82] W.-J. Lee, J. Kang, and K. Chang (2008), ISSN 0374-4884.

[83] D. Fan and Z. Lan, Journal of Wuhan University of Technology-Mater. Sci. Ed. **27**, 1184 (2012), ISSN 1000-2413.

[84] C. Park, S. Zhang, and S.-H. Wei, Physical Review B **66**, 073202 (2002).

[85] B. Meyer, J. Stehr, A. Hofstaetter, N. Volbers, A. Zeuner, and J. Sann, Applied Physics A **88**, 119 (2007), ISSN 0947-8396.

[86] K. Tamura, T. Makino, A. Tsukazaki, M. Sumiya, S. Fuke, T. Furumochi, M. Lippmaa, C. Chia, Y. Segawa, and H. Koinuma, Solid State Communications **127**, 265 (2003), ISSN 0038-1098.

[87] G. Brauer, J. Kuriplach, C. Ling, and A. Djurii, in *Journal of Physics: Conference Series* (IOP Publishing), vol. 265, p. 012002, ISBN 1742-6596.

[88] D. C. Look, D. C. Reynolds, J. Sizelove, R. Jones, C. W. Litton, G. Cantwell, and W. Harsch, Solid state communications **105**, 399 (1998), ISSN 0038-1098.

[89] A. Hutson, Physical review **108**, 222 (1957).

[90] E. Ziegler, A. Heinrich, H. Oppermann, and G. Stöver, Physica status solidi (a) **66**, 635 (1981), ISSN 1521-396X.

[91] R. M. Pasquarelli, D. S. Ginley, and R. O'Hayre, Chemical Society Reviews **40**, 5406 (2011).

[92] K. Ellmer, Journal of Physics D: Applied Physics **34**, 3097 (2001), ISSN 0022-3727.

[93] T. Minami, H. Nanto, and S. Takata, Japanese Journal of Applied Physics **23**, L280 (1984), ISSN 1347-4065.

[94] A. Suzuki, T. Matsushita, N. Wada, Y. Sakamoto, and M. Okuda, Japanese journal of applied physics **35**, L56 (1996), ISSN 1347-4065.

[95] A. Aktaruzzaman, G. Sharma, and L. Malhotra, Thin solid films **198**, 67 (1991), ISSN 0040-6090.

[96] J.-K. Sheu, M.-L. Lee, Y. Lu, and K. Shu, Quantum Electronics, IEEE Journal of **44**, 1211 (2008), ISSN 0018-9197.

[97] J. Berry, D. Ginley, and P. E. Burrows, Applied Physics Letters **92**, 193304 (2008), ISSN 0003-6951.

[98] K. R. Reddy, H. Gopalaswamy, P. Reddy, and R. Miles, Journal of crystal growth **210**, 516 (2000), ISSN 0022-0248.

[99] T. Minami, H. Sato, H. Nanto, and S. Takata, Japanese journal of applied physics **25**, L776 (1986), ISSN 1347-4065.

[100] N. Rashidi, V. L. Kuznetsov, J. R. Dilworth, M. Pepper, P. J. Dobson, and P. P. Edwards, Journal of Materials Chemistry C **1**, 6960 (2013).

[101] A. Suzuki, T. Matsushita, T. Aoki, A. Mori, and M. Okuda, Thin solid films **411**, 23 (2002), ISSN 0040-6090.

[102] Y. Sawada, C. Kobayashi, S. Seki, and H. Funakubo, Thin Solid Films **409**, 46 (2002), ISSN 0040-6090.

[103] N. Rashidi, Thesis, Oxford University (2014).

[104] N. Rashidi, A. T. Vai, V. L. Kuznetsov, J. R. Dilworth, and P. P. Edwards, Chemical Communications **51**, 9280 (2015).

[105] A. T. Vai, V. L. Kuznetsov, H. Jain, D. Slocombe, N. Rashidi, M. Pepper, and P. P. Edwards, Zeitschrift für anorganische und allgemeine Chemie **640**, 1054 (2014), ISSN 1521-3749.

[106] H. Brooks, Academic, New York **7**, 85 (1955).

[107] R. Dingle, The London, Edinburgh, and Dublin Philosophical Magazine and Journal of Science **46**, 831 (1955), ISSN 1941-5982.

[108] A. Bikowski and K. Ellmer, Journal of Applied Physics **114**, 063709 (2013), ISSN 0021-8979.

[109] T. Makino, Y. Segawa, A. Tsukazaki, A. Ohtomo, and M. Kawasaki, arXiv preprint cond-mat/0507009 (2005).

[110] J. Y. Seto, Journal of Applied Physics **46**, 5247 (1975), ISSN 0021-8979.

[111] K. Ellmer and R. Mientus, Thin solid films **516**, 4620 (2008), ISSN 0040-6090.

[112] T. Minami, T. Miyata, and H. Tokunaga, physica status solidi (a) **216**, 1700783 (2019), ISSN 1862-6300.

[113] J. Lu, Z. Ye, Y. Zeng, L. Zhu, L. Wang, J. Yuan, B. Zhao, and Q. Liang, Journal of Applied Physics **100**, 073714 (2006), ISSN 0021-8979.

[114] Z. Pei, C. Sun, M. Tan, J. Xiao, D. Guan, R. Huang, and L. Wen, Journal of Applied Physics **90**, 3432 (2001), ISSN 0021-8979.

[115] M. N. Islam, T. Ghosh, K. Chopra, and H. Acharya, Thin Solid Films **280**, 20 (1996), ISSN 0040-6090.

[116] B. Pödör, physica status solidi (b) **16**, K167 (1966), ISSN 1521-3951.

[117] K. Seeger, *Semiconductor physics: an introduction*, vol. 40 (Springer Science and Business Media, 2013), ISBN 3662026635.

[118] H. L. Hartnagel, A. Dawar, A. Jain, and C. Jagadish, *Semiconducting transparent thin films* (Institute of Physics Pub. Bristol, UK, Philadelphia, PA, 1995), ISBN 0750303220.

[119] D. Klaassen, Solid-State Electronics **35**, 961 (1992), ISSN 0038-1101.

[120] D. Klaassen, Solid-State Electronics **35**, 953 (1992), ISSN 0038-1101.

[121] Y.-K. Moon, S.-H. Kim, and J.-W. Park, Journal of Materials Science: Materials in Electronics **17**, 973 (2006), ISSN 0957-4522.

[122] Y. Wang, Y. Gu, S. Peng, W. Ding, H. Wang, and W. Chai, Applied Surface Science **257**, 8044 (2011), ISSN 0169-4332.

[123] L. Yang, S. Jie, and D. Fan, in *Advances in Optoelectronics and Micro/Nano-Optics (AOM), 2010 OSA-IEEE-COS* (IEEE), pp. 1–4, ISBN 142448393X.

[124] Z. Ghorannevis, M. Hosseinnejad, M. Habibi, and P. Golmahdi, Journal of Theoretical and Applied Physics **9**, 33 (2014), ISSN 1735-9325.

[125] K. H. Kim, K. C. Park, and D. Y. Ma, Journal of Applied Physics **81**, 7764 (1997), ISSN 0021-8979.

[126] B. Szyszka, Thin Solid Films **351**, 164 (1999), ISSN 0040-6090.

[127] D. R. Lide, *CRC handbook of chemistry and physics* (CRC press, 2004), ISBN 0849304857.

[128] E. Burstein, Physical Review **93**, 632 (1954).

[129] I. Hamberg, C. Granqvist, K.-F. Berggren, B. E. Sernelius, and L. Engström, physical Review B **30**, 3240 (1984).

[130] A. Walsh, J. L. Da Silva, S.-H. Wei, C. Körber, A. Klein, L. Piper, A. DeMasi, K. E. Smith, G. Panaccione, and P. Torelli, Physical review letters **100**, 167402 (2008).

[131] S. M. Ali, S. T. Hussain, S. A. Bakar, J. Muhammad, and N. ur Rehman, in *Journal of Physics: Conference Series* (IOP Publishing), vol. 439, p. 012013, ISBN 1742-6596.

[132] S. F. Ahmed, S. Khan, P. Ghosh, M. Mitra, and K. Chattopadhyay, Journal of sol-gel science and technology **39**, 241 (2006), ISSN 0928-0707.

[133] M.-M. Bagheri-Mohagheghi and M. Shokooh-Saremi, Physica B: Condensed Matter **405**, 4205 (2010), ISSN 0921-4526.

[134] Z. Galazka, R. Uecker, D. Klimm, K. Irmscher, M. Pietsch, R. Schewski, M. Albrecht, A. Kwasniewski, S. Ganschow, and D. Schulz, physica status solidi (a) **211**, 66 (2014), ISSN 1862-6319.

[135] A. Schleife, J. Varley, F. Fuchs, C. Rödl, F. Bechstedt, P. Rinke, A. Janotti, and C. Van de Walle, Physical Review B **83**, 035116 (2011).

[136] H. Peelaers, E. Kioupakis, and C. G. Van de Walle, Applied Physics Letters **100**, 011914 (2012), ISSN 0003-6951.

[137] M. Nistor, N. Mandache, J. Perrire, C. Hebert, F. Gherendi, and W. Seiler, Thin Solid Films **519**, 3959 (2011), ISSN 0040-6090.

[138] L. Nistor, C. Ghica, D. Matei, G. Dinescu, M. Dinescu, and G. Van Tendeloo, Journal of crystal growth **277**, 26 (2005), ISSN 0022-0248.

[139] S. Major, A. Banerjee, and K. Chopra, Thin Solid Films **125**, 179 (1985), ISSN 0040-6090.

[140] B. Choi, H. Im, J. Song, and K. Yoon, Thin solid films **193**, 712 (1990), ISSN 0040-6090.

[141] M. Chen, X. Wang, Y. Yu, Z. Pei, X. Bai, C. Sun, R. Huang, and L. Wen,

Applied Surface Science **158**, 134 (2000), ISSN 0169-4332.

[142] A. Singh, R. Mehra, A. Yoshida, and A. Wakahara, Journal of applied physics **95**, 3640 (2004), ISSN 0021-8979.

[143] E. Bunting, Journal of the American Ceramic Society **13**, 5 (1930), ISSN 1551-2916.

[144] V. L. Kuznetsov, A. T. Vai, M. Al-Mamouri, J. S. Abell, M. Pepper, and P. P. Edwards, Applied Physics Letters **107**, 232103 (2015), ISSN 0003-6951.

[145] B.-Z. Dong, G.-J. Fang, J.-F. Wang, W.-J. Guan, and X.-Z. Zhao, Journal of applied physics **101**, 033713 (2007), ISSN 0021-8979.

[146] r. P. d. Silva, M. Chaves, S. F. Durrant, P. N. Lisboa-Filho, and J. R. R. Bortoleto, Materials Research **17**, 1384 (2014), ISSN 1516-1439.

[147] F. Garcs, N. Budini, R. Arce, and J. Schmidt, Procedia Materials Science **9**, 221 (2015), ISSN 2211-8128.

[148] R. Cammarata, T. Trimble, and D. Srolovitz, Journal of Materials Research **15**, 2468 (2000), ISSN 2044-5326.

[149] B. W. Sheldon, K. Lau, and A. Rajamani, Journal of Applied Physics **90**, 5097 (2001), ISSN 0021-8979.

[150] S.-S. Lin and J.-L. Huang, Surface and Coatings Technology **185**, 222 (2004), ISSN 0257-8972.

[151] Z. Pei, X. Zhang, G. Zhang, J. Gong, C. Sun, R. Huang, and L. Wen, Thin Solid Films **497**, 20 (2006), ISSN 0040-6090.

[152] M. Novotny, J. Cizek, R. Kuzel, J. Bulir, J. Lancok, J. Connolly, E. McCarthy, S. Krishnamurthy, J.-P. Mosnier, and W. Anwand, Journal of physics. D, Applied physics **45** (2012), ISSN 0022-3727.

[153] C. Lennon, R. Kodama, Y. Chang, S. Sivananthan, and M. Deshpande, Journal of Vacuum Science and Technology B **27**, 1641 (2009), ISSN 2166-2746.

[154] B. Du Ahn, S. H. Oh, C. H. Lee, G. H. Kim, H. J. Kim, and S. Y. Lee, Journal of Crystal Growth **309**, 128 (2007), ISSN 0022-0248.

[155] Y. Igasaki, M. Ishikawa, and G. Shimaoka, Applied Surface Science **33**, 926 (1988), ISSN 0169-4332.

[156] X. Yu, J. Ma, F. Ji, Y. Wang, X. Zhang, and H. Ma, Thin solid films **483**, 296 (2005), ISSN 0040-6090.

[157] S. Ghosh, A. Sarkar, S. Bhattacharya, S. Chaudhuri, and A. Pal, Journal of crystal growth **108**, 534 (1991), ISSN 0022-0248.

[158] X. Xu, C. Guo, Z. Qi, H. Liu, J. Xu, C. Shi, C. Chong, W. Huang, Y. Zhou, and C. Xu, Chemical physics letters **364**, 57 (2002), ISSN 0009-2614.

[159] F. Ruske, M. Roczen, K. Lee, M. Wimmer, S. Gall, J. Hüpkes, D. Hrunski, and B. Rech, Journal of Applied Physics **107**, 013708 (2010), ISSN 0021-8979.

[160] Z. Y. Wang, J. Zhang, X. Wu, M. Birau, G. Yu, H. Yu, Y. Qi, P. Desjardins, X. Meng, and J. P. Gao, Pure and applied chemistry **76**, 1435 (2004), ISSN 1365-3075.

[161] G. Qian and Z. Y. Wang, Chemistry-An Asian Journal **5**, 1006 (2010), ISSN 1861-4728.

[162] D. Jensen, *Copper plating on zinc and its alloys*, U.S. Patent (1973).

Chapter 2

Experimental Techniques

This chapter introduces the background and applications of the techniques that have been used for the manufacture and characterization of SiZO and $Cu_2P_2O_7$ thin films in this thesis. These techniques are categorized into four sections: target preparation, thin film preparation, property measurement and structural characterization.

2.1 Target preparation

2.1.1 Cold pressing



(a) 30 mm die. (b) 50.8 mm die.

Figure 2.1: Dies used for the manufacture of $Cu_2P_2O_7$ targets.

Cold pressing was used to make $Cu_2P_2O_7$ targets from powder in this study. Steel dies with diameters of 50.8 mm and 30 mm were used (Figure 2.1). The cold pressing pressure used on the 50.8 mm and the 30 mm dies were 8000 psi and 3000 psi, respectively. These choices of the pressing force ensure the pressure inside both

dies are similar; around 82 MPa for the 30 mm die and 81 MPa for the 50.8 mm die, assuring the comparability between samples made by these two dies.

2.1.2 Sintering

To make the pressed targets more robust so they could be transferred into the sputtering apparatus, the targets were sintered at various temperatures after being pressed. A Carbolite RHF 1600 furnace was used to sinter the samples with the temperature controlled by an Eurotherm temperature controller (built-in). The temperatures used and other details of the sintering processes will be presented later in the thesis.

2.2 Thin film preparation

2.2.1 RF sputtering: equipment and standard procedures

2.2.1.1 Principles of the technique

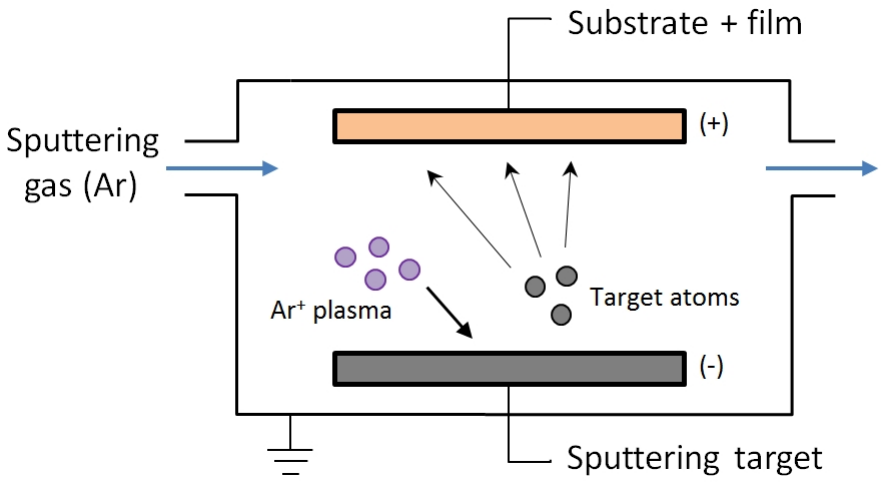


Figure 2.2: Setup of a typical sputtering kit.

Sputtering is a process in which atoms are knocked off from a solid target by energetic gas ion bombardment (Figure 2.2). The generation of gas ions is through the application of a high voltage between cathode and anode of the system to create a plasma. Typical gases that are used for sputtering include Ar, O_2 and N_2. The ejected atoms from the target travel through the gas phase and settle on the surface of

a substrate to condense into a thin layer of film. There are two kinds of power supplies that are used to generate the plasma: direct current (DC) and alternating current (AC). The sputtering processes based on these two different types of power supplies are called DC sputtering and RF sputtering, respectively. The typical voltage range for DC sputtering is 3–5 kV, and the AC frequency for RF sputtering is often set at 13.56 MHz [1]. Because sputtering is based on a continuous bombardment of the target by ions, it would lead to the accumulation of charge if the target is insulating. Thus, DC sputtering is suitable for the deposition of electrically conducting materials while RF sputtering is designed for the preparation of insulating/semiconducting thin films to avoid charging of the target.

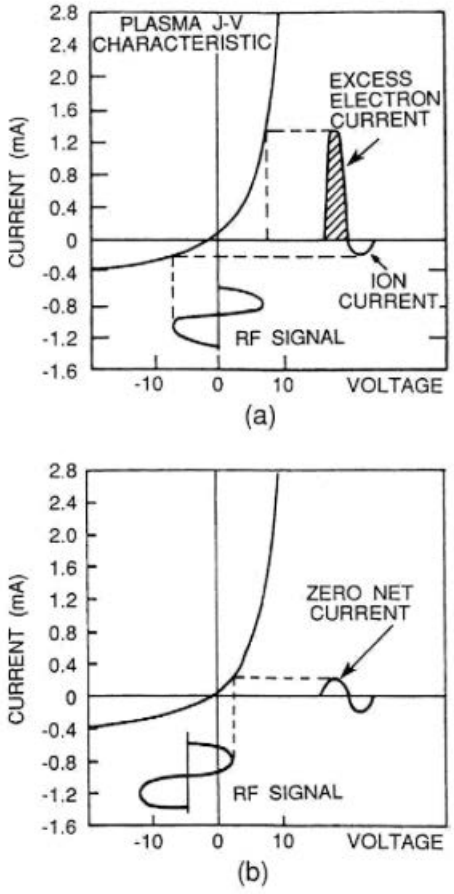


Figure 2.3: RF discharge model. [2]

In addition, the RF signal is usually biased due to the asymmetric nature of the discharge current-voltage relationship (Figure 2.3). The differential mobilities of

electrons and ions means that an isolated target with a positive charge could attract greater electron current than the ion current an isolated target with comparable amount of negative charge could sustain. Thus there is a shift of the RF signal's operating point to achieve a zero net current.

To enhance the sputtering process, one common way is to put magnet beneath the target. The magnetic field around the target confines the electrons to only spiral within a defined region near the target. The concentration and longer travelling distance of the electrons thus produces stronger plasma and increases the sputtering efficiency [3].

During the sputtering process, several parameters can influence the qualities of the deposited film. One of them is the gas used for sputtering. Sputtering is typically carried out in the ambience of inert gas such as Argon. However, reactive gases such as nitrogen and oxygen, are sometimes introduced into the system to allow reactions between target material and the plasma to happen. By altering the relative amount of the reactive gases, the stoichiometry and structure of the deposited films can be closely controlled. This process is also called reactive sputtering. In this study, oxygen is used to alter the chemical states and stoichiometries of some of the films, as an approach to produce stoichiometric thin films with desired properties. The other important parameter is the sputtering pressure, which could affect the deposition rate. When the pressure is too low, it can be difficult to generate and maintain the plasma, however, if the pressure is too high, increased collisional sputtering would happen, and thus reduce the sputter rate.

2.2.1.2 Instrumentation

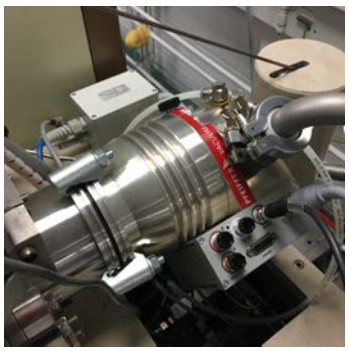
In this study, RF sputtering was carried out in an Oxford Applied Research DS500 sputter kit as shown in Figure 2.4. The sputtering happens inside the chamber shown in Figure 2.4(a), while the rotary pump (Figure 2.4(d)) and turbo pump (Figure 2.4(c)) control the base pressure of the system. The use of different types of gas can be achieved by installing multiple gas pipelines (Figure 2.4(b)). The flows of gas in the pipelines are controlled by Brooks Instrument Model 0254 mass flow controller.



(a) Overall setup of the sputter rig.



(b) Gas pipelines.



(c) Turbo pump.



(d) Rotary pump.

Figure 2.4: OAR DS500 sputter kit and its components.

During sputtering, the substrate is mounted on the stage inside the chamber, with heating unit underneath. The target to stage distance is 3.5 cm in this instrument.

For every new target made, the target was pre-sputtered to remove potential contaminants on the surface, before being used for making thin films. The chamber was always being kept under the vacuum to keep the surface of the target clean. The gas pressure was monitored by the Penning and the Pirani gauges. The gas flows were controlled by a digital Brooks 0254 flow controller. Different pressures were achieved by varying the gas flow. The film deposition rate was between 2–50 nm/min for the films made in this study, it is affected by the deposition parameters such as sputter gas, pressure, duration and power. The details of how it varies will be discussed in more details in Chapter 3 and Chapter 4.

The temperature of the stage is measured and controlled by a thermocouple inserted into the middle of the stage (Figure 2.5) with an Eurotherm temperature

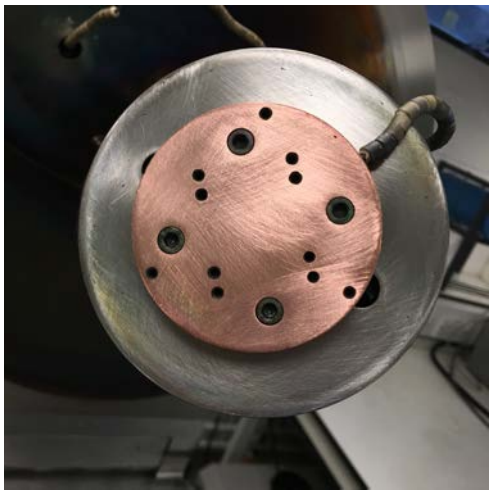


Figure 2.5: Copper substrate holder (diameter: 6 cm) and the thermocouple. Diameter

controller. The pressure of the system is measured by a Penning gauge ($<$ 1×10^{-2} mbar) and a Pirani gauge. The base pressure of the system is around 1–2$\times 10^{-6}$ mbar.

2.2.2 Post-deposition annealing

There are several different ways to anneal the films after deposition. The method used in Chapter 3 for the treatment of SiZO thin films was *in-situ* vacuum annealing. The Si doped ZnO films were first deposited at 200 °C, then the gas flow was stopped to let the chamber to be pumped down to 2×10^{-6} mbar to achieve a good vacuum level. The temperature of the stage was then raised to the annealing temperature and cooled down to room temperature after annealing. During this whole time, the chamber was not opened and the film stayed at the same place on the stage. This process enables annealing without inducing extra contamination to the surface.

The annealing method used for the copper pyrophosphate films was *ex situ* annealing in air. After deposition, the films were transferred to a furnace (Carbolite CSF1200) and heat treated in air at different temperatures.

2.3 Characterization of electrical and optical properties

2.3.1 Electrical characterization

2.3.1.1 Sheet resistance measurement – Four-point probe technique

As has been introduced in Chapter 1, resistivity is generally used to represent the electrical performance of TCO materials (it is also the parameter used to characterize the electrical properties of films in this work), but sheet resistance, R_s (in Ω/sq), of a film is sometimes a more important industrial parameter and thus it is worthwhile to present some background information here. Resistance (Ω) of a thin film is a physical quantity that includes sample shape and thickness, and is defined by $R = \rho(L/Wd)$, where L, W, d are the sample length, the sample width and the sample thickness respectively. The conventional technique used to measure the sheet resistance of a film is called the four-point in-line probe technique. In this technique, four probes are lined up with equal spacing (s) as shown in Figure 2.6. The outer pair of probes provide the current while the inner pair measure the voltage dropped over the distance separating them [4].

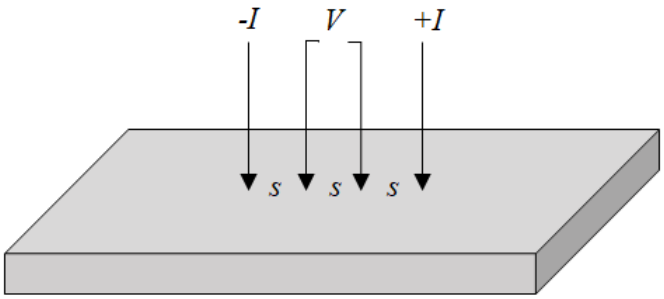


Figure 2.6: Configuration of a four point probe measurement.

By assuming that the sample lateral dimension is infinite (i.e. $W \gg s$, $L \gg s$), the sheet resistance of the sample can be obtained using [4]:

$$R_s = \frac{\pi}{\ln 2}\frac{V}{I} \approx 4.532\frac{V}{I} \tag{2.1}$$

The resistivity is therefore given as:

$$\rho = R_s d = \frac{\pi}{\ln 2}\frac{Vd}{I} \tag{2.2}$$

For small tested area, where the sample size is not that large compared to the probe spacing, edge effects cannot be ignored. In order to get accurate measurements a correction factor needs to be included. In general then:

$$R_s = C\frac{V}{I} \tag{2.3}$$

where C is the correction factor. Note that for $D/s > 40$, $C = 4.53$, which approximates to the value of the multiplier in Equation (2.1). Here D is the length of the side of a square sample.

2.3.1.2 Theory of Hall Effect

The Hall Effect is a fundamental phenomenon in solid state physics as well as an important diagnostic tool for the characterization of materials — particularly semiconductors. It allows direct determination of the sign of the charge carriers (electrons or holes), the density of the carriers and the average mobility of the carriers in a given sample. The basic setup of a Hall Effect experiment is shown in Figure 2.7.

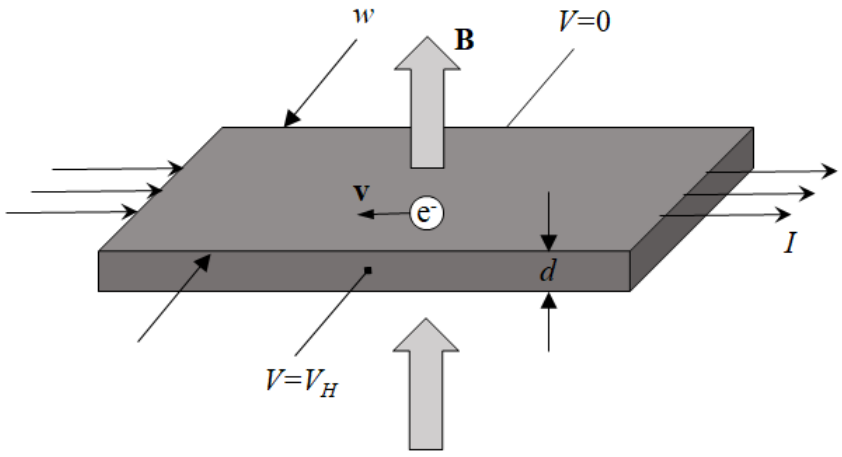


Figure 2.7: Hall Effect measurement.

In Figure 2.7, the sample to be studied is lying perpendicular to a constant magnetic field **B**, with current I flowing through the sample from left to right along the x axis. According to classical electrodynamics, when a carrier moves through a non-parallel magnetic field it experiences the magnetic Lorentz force **F** ($\mathbf{F} = q\mathbf{v} \times \mathbf{B}$), where q is the charge of the carrier and **v** is the velocity of the carrier), perpendicular to both the velocity of the carrier and the field. From a microscopic perspective, the current I is the result of holes moving in the direction of I, or electrons moving in the opposite direction. However, in either case, the carriers experience a Lorentz force along the negative y-direction, generating an internal E-field. Steady-state is achieved when the electrostatic force due to this E-field counteracts the Lorentz force. The transverse potential difference over the two sides of the sample is called the Hall Voltage, V_H. It can be written as:

$$V_H = \frac{IB}{Ned} \tag{2.4}$$

where I is the current, B is the magnitude of the magnetic field, N is the bulk density of carrier and d is the thickness of the sample. In Equation (2.4), the only spatial dimension that is related to the Hall voltage is the sample thickness (the dimension in the direction of the magnetic field). Therefore, with given values of I, B, d, one can obtain the density of charge carriers easily by measuring the Hall voltage:

$$N = \frac{IB}{edV_H} \tag{2.5}$$

In some circumstances, it is more convenient to use sheet density N_s ($N_s = Nd$) rather than using bulk density, N.

Hall mobility, μ, can be calculated from the values of V_H, I, B and the sheet resistance R_s through:

$$\mu = \frac{V_H}{IBR_s} = \frac{1}{eN_sR_s} \tag{2.6}$$

Here the sheet resistance is measured by the van der Pauw technique which will be introduced later. This method is used in most Hall measurement set-ups. Given the sheet resistance value and the thickness of the sample, one can easily calculate the resistivity.

The sign of the Hall voltage varies with the sign of the charge carriers. Therefore the sign of the Hall coefficient is also determined by the sign of the carriers according to its definition:

$$R_H = \frac{V_H d}{IB} = \frac{1}{Nq} \tag{2.7}$$

where $q = e$ for holes and $q = -e$ for electrons. The Hall coefficient is determined only by the intrinsic properties of the material being tested. With this coefficient, the relationships between carrier mobility, carrier concentration and sample resistivity can be simply written as:

$$\begin{aligned} N &= \frac{1}{R_H e} \\ \mu &= \frac{R_H}{\rho} \end{aligned} \tag{2.8}$$

2.3.1.3 The van der Pauw technique

Since the four-point probe technique requires the sample size to be much larger than the spacing of the probes, for some relatively small samples it cannot provide very accurate results. Another method which is widely used in the semiconductor industry for both resistivity and Hall measurements is the van der Pauw technique [5]. This method allows electrical measurements on arbitrarily shaped two-dimensional sample simply by making four small ohmic contacts at the periphery. Some van der Pauw configurations, contact placements and their preferences are shown in Figure 2.8.

In general, their are four preliminary conditions for the van der Pauw technique: 1) The sample is a flat two-dimensional sample with uniform thickness. 2) No isolated holes or nonconducting islands or inclusions are on/in the sample. 3) The average size of the contacts and sample thickness (d) are much smaller than the spacing of the

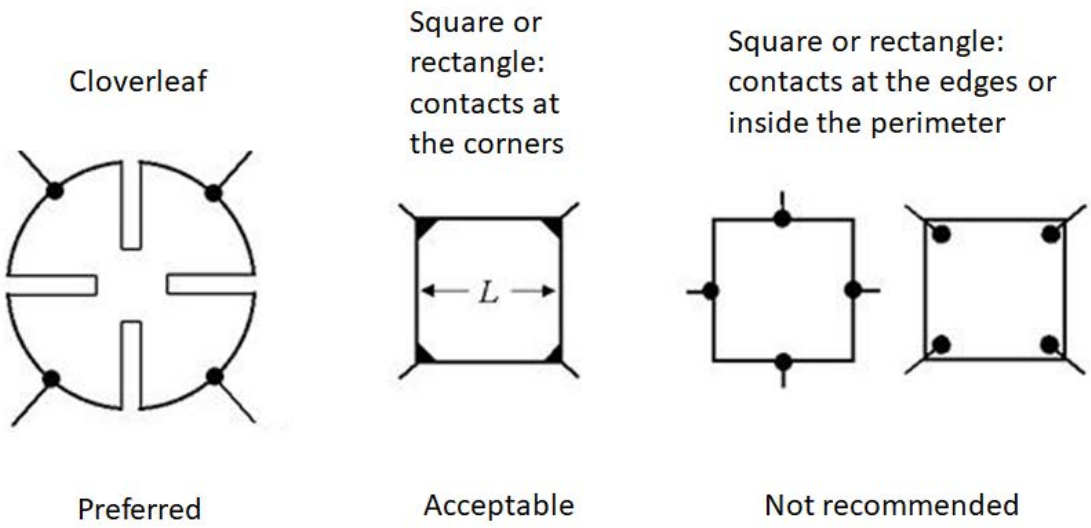


Figure 2.8: The van der Pauw contact placements. Figure adapted from the website of National Institute of Standards and Technology .

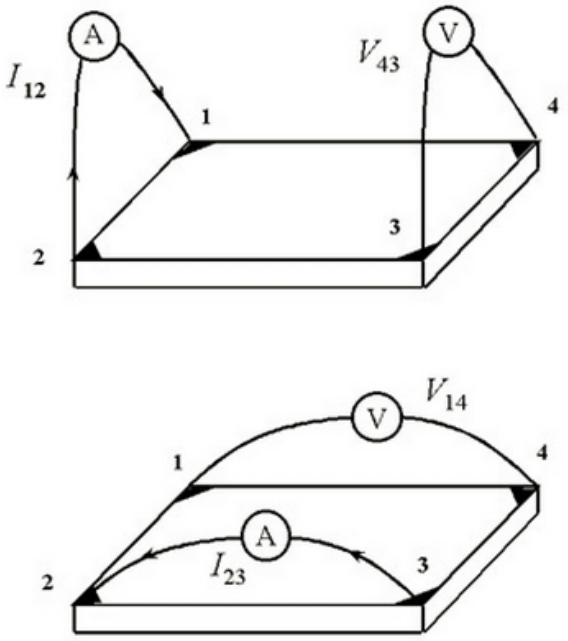
contacts. 4) The four contacts are at the very periphery of the sample. In addition, all four contacts should be ideally made of the same material and all four leads should come from the same batch of wire.

In this measurement, a DC current flows from one contact to the adjacent contact and the current is recorded by an ammeter, while the corresponding voltage drop is measured by a voltmeter across the other two contacts on the opposite side. Each measurement like this needs to be repeated twice by switching the polarity. Thus the eventual resistivity result should be derived from a total of eight measurements. The basic setup of a van der Pauw resistivity measurement is shown in Figure 2.9(a).

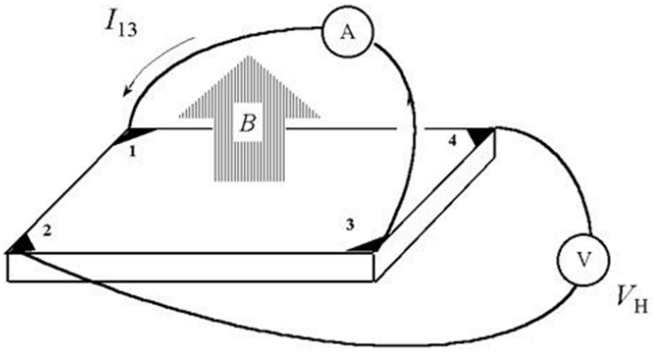
Once all voltage and current measurements are taken, two characteristic resistances can be defined as:

$$\begin{aligned} R_X &= (R_{14,23} + R_{41,32} + R_{23,14} + R_{32,41})/4 \\ R_Y &= (R_{12,43} + R_{43,12} + R_{21,34} + R_{34,21})/4 \end{aligned} \tag{2.9}$$

where $R_{ab,cd} = V_{cd}/I_{ab}$. For instance, $R_{23,14} = V_{14}/I_{23}$ and $R_{12,43} = V_{43}/I_{12}$, as shown in Figure 2.9(a). These two resistances relate the sheet resistance R_s through the Van der Pauw equation [9]:



(a) Van der Pauw resistivity measurement.



(b) Hall voltage measurement.

Figure 2.9: Voltage and current measurements for van der Pauw techniques. [6]

$$e^{-\frac{\pi R_X}{R_S}} + e^{-\frac{\pi R_Y}{R_S}} = 1 \tag{2.10}$$

For the usual case in which the sample is square and homogeneous, where $R_X \approx R_Y$, the expressions of the sheet resistance and the resistivity can be written as:

$$\begin{aligned} R_s &= \frac{\pi}{\ln 2}\frac{(R_X + R_Y)}{2} f \\ \rho &= \frac{\pi d}{\ln 2}\frac{(R_X + R_Y)}{2} f \end{aligned} \tag{2.11}$$

where d is the thickness of the sample and f is a correction factor which is a

function of sample symmetry. For the measurement of Hall voltage, the setup of the experiment is different. The current flows from one contact to the opposite contact (e.g. $3 \rightarrow 1$, as shown in Figure 2.9(b)), and the Hall voltage is measured across the other opposing pair of contacts (2 and 4 in Figure 2.9(b)). Once the Hall voltage is obtained, one can easily calculate the bulk carrier density and the carrier mobility from the known values of d, I, B and R_s.

2.3.1.4 Instrumentation

In this study, electrical properties of SiZO films were measured at 300K using an Ecopia Hall Effect Measurement System HMS3000, in a 0.55 T magnetic field. A 5 mm $\times$ 5 mm section from the original film was mounted on a specifically designed circuit board. The current of the Hall measurement could be adjusted in the range of μA to mA, depending on the resistivity of the sample. Ohmic contacts were prepared by indium soldering. The results of the measurements will be presented in Chapter 3 for the SiZO films.

The main source of the error in this measurement is usually from the dimension of the sample, particularly the thickness. From Equation (2.5), it could be seen that the error of the measured thickness would lead to the error in carrier concentration thus generates an error in the measured resistivity. The method used to reduce and control the errors of thickness measurement and the scale of the errors will be discussed later in Section 2.4.6.

2.3.2 Optical characterization (thin films)

One way to measure the transmittance, reflectance and absorbance of a material is by using Ultraviolet-visible-near infrared (UV-Vis-NIR) absorption spectroscopy. UV-Vis-NIR spectroscopy is the measurement of the decay of a beam of light after it is transmitted through a sample or after reflecting from a sample surface. This technique allows the measurement over a wavelength range from approximately 200 nm to 3300 nm. It is widely used for optical studies of a wide range of materials, including

semiconductors for electronics, lasers and detectors, materials for photovoltaic cells, optical fibers and transparent or partially transparent chemical solutions.

2.3.2.1 Basic principles of UV-Vis-NIR spectroscopy

When light passes through a sample, it interacts with the sample in various ways, including reflection, transmission, absorption and scattering. In general, scattering is a much weaker interaction compared to the others and therefore usually only the first three processes are considered, as shown in Figure 2.10.

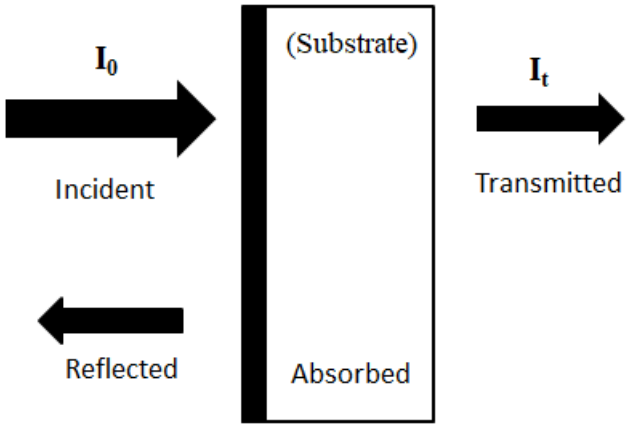


Figure 2.10: Optical transmission.

Figure 2.10 shows a typical schematic for a beam of light passing through a TCO thin film with its substrate. Transmittance T can be calculated from the measured I_0 and I_t values by using equations:

$$T = \frac{I_t}{I_0} \tag{2.12}$$

where I_0 is the initial light intensity and I_t refers to the light intensity after passing through the sample. T is dimensionless and often presented versus wavelength. In this thesis, the intensity of the beam transmitted through a blank substrate was also measured as a reference.

A typical spectrophotometer consists of 1) a light source; 2) sample holder; 3) wavelength selector used to isolate a particular region of the spectrum for measurement (generally it is made up of a diffraction grating); 4) radiation detector

that converts beam intensity into an electrical signal; and 5) signal processor and readout which displays the translated signal on a computer screen, a digital meter or any other recording equipment. A schematic of a dual-beam UV-Vis-NIR spectrometer is demonstrated in Figure 2.11.

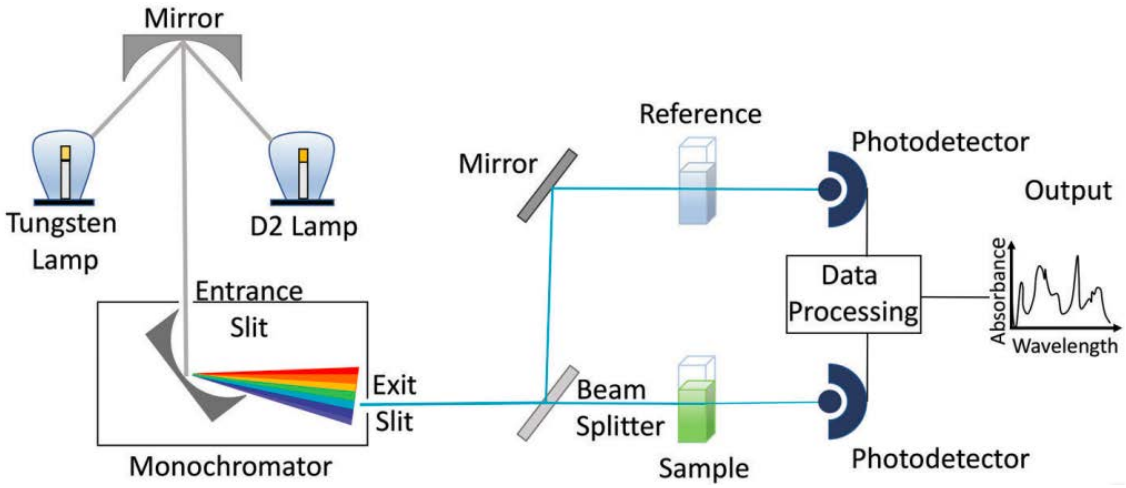


Figure 2.11: Setup of UV-Vis-NIR spectrometer.[7]

In a dual-beam spectrometer, a beam of light emitted by a deuterium arc lamp (190-400nm) or tungsten filament lamp (300-2500nm) is split into two beams when it passes through the beam splitter. One beam is used for reference since scattering from the air and the sample holder need to be excluded. The other beam with the same initial intensity passes through the sample. The instrument automatically swaps lamps while scanning across the UV and Vis-NIR regions. A complete and continuous spectrum of the absorption can be generated at the end of the measurement.

2.3.2.2 Plasma frequency

The optical spectrum of a typical transparent conductor is shown in Figure 2.12. As we have mentioned, the transmission window has two edges, the one at the longer wavelength is caused by the charge density oscillations, also called plasma oscillations. The frequency of these oscillations is called the plasma frequency, ω_p.

One way to characterize the plasma oscillations is by using the Drude model. However, this model is valid only within the free electron framework, which requires

the sample to be a degenerate semiconductor. The critical carrier concentration set by the Mott criterion [10] for ITO is $N_c \approx 10^{19}\text{cm}^{-3}$ [11], above which the ITO can be considered to have a full valence band with a conduction band partially filled by a degenerate free electron gas going up to the Fermi energy, $E_F = \hbar^2(3\pi^2 N)^{2/3}/2m^*$, where m^* is the effective electron mass [12, 13]. For typical TCOs, the carrier concentration is at least one order of magnitude greater than N_c, therefore the Drude model can be used for most practical TCOs.

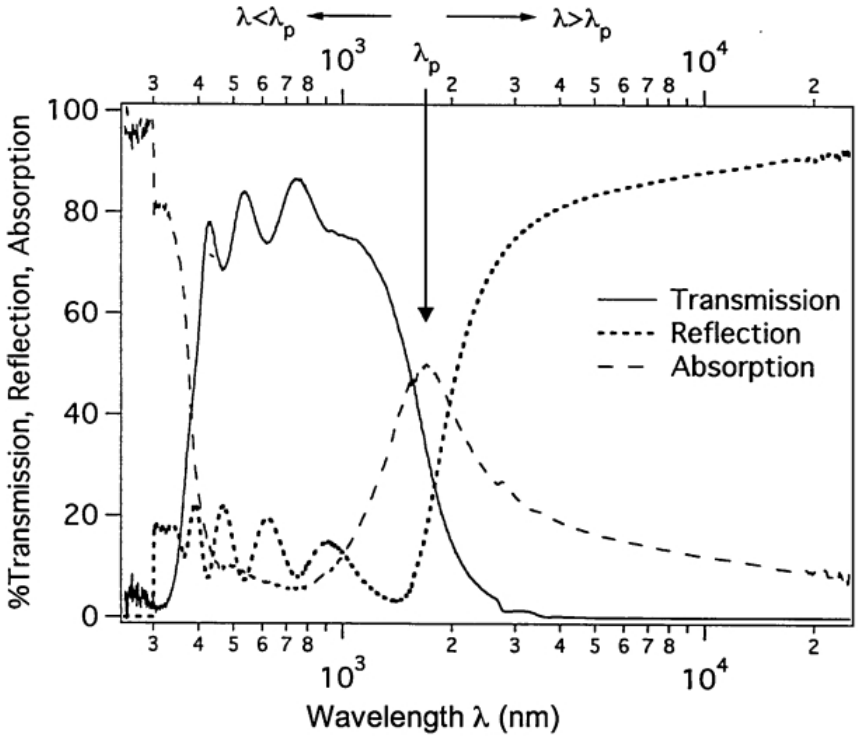


Figure 2.12: Optical spectrum of a typical TCO [14].

Since the light can be treated as a electromagnetic waves, we can assume that the electric field of the electromagnetic wave can be written as:

$$E(t) = \text{Re}(\mathbf{E}(\omega)e^{i\omega t}) \tag{2.13}$$

where ω is the angular frequency of the incoming beam. For high quality TCO films in the limit of high mobilities, one can obtain the expression for dielectric constant as [11]:

$$\varepsilon(\omega) = 1 - \frac{\omega_p^2}{\omega^2} \tag{2.14}$$

where the plasma frequency is defined as:

$$\omega_p = \left(\frac{4\pi N e^2}{m^*}\right)^{1/2} \tag{2.15}$$

Here, all the symbols represent their usual meanings. For $\omega < \omega_p$, ε is real and negative. According to the theory of electrodynamics, **E** decays exponentially inside the metal, which means no radiation can propagate and the sample is highly reflective in this region of the spectrum. Yet, for $\omega > \omega_p$, ε is real and positive, which enables the radiation to be transmitted freely through the sample.

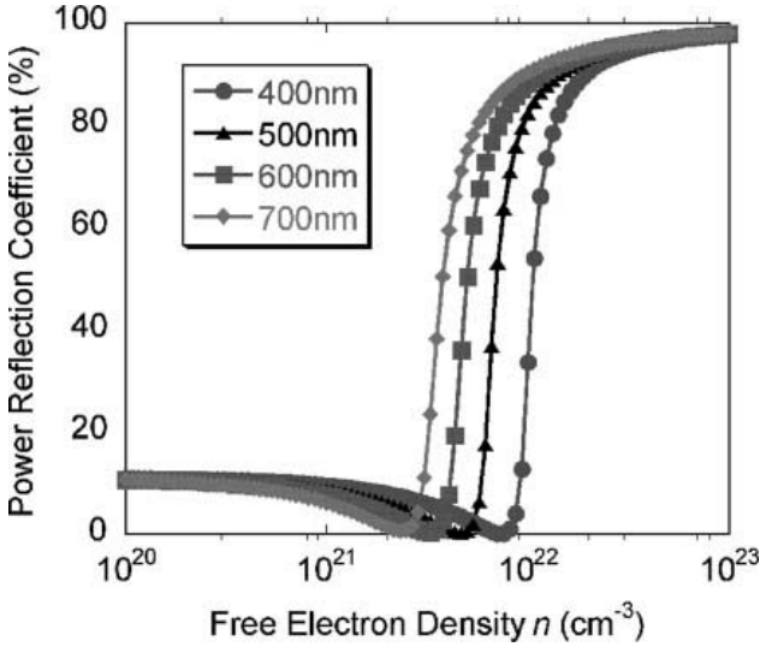


Figure 2.13: Calculated result of power reflection coefficient at the interface between air and a thick ITO layer as a function of free electron density for several incident wavelengths in the visible spectrum. Reflection increases drastically when the carrier concentration exceeds 10^{22}cm^{-3}. [11]

As the number of conduction band electrons increases, as a result of substitutional doping or oxygen vacancies, the plasma wavelength, $\lambda_p \propto 1/\omega_p \propto 1/\sqrt{N}$, shifts to shorter wavelength and thus will narrow the transmission window. At very high carrier concentrations, plasma oscillations may even reduce the transmittance in the

visible spectrum. The calculated reflectance-carrier concentration relationships are given in Figure 2.13 using an ITO film as an example.

Therefore the priority of a lot of TCO research has been focusing on the enhancement of carrier mobilities rather than carrier concentrations. However for materials like ZnO, there is still great potential for further improvements, which requires the deeper understanding of the factors that are limiting the electronic properties [15].

2.3.2.3 Instrumentation

Optical transmission spectra of SiZO and $Cu_2P_2O_7$ films between 250 nm and 2500 nm was obtained on a Cary 5000 UV-Vis-NIR spectrometer and a Perkin Elmer Lambda 19. Both of the machines are dual-beam UV-Vis-NIR spectrometers that contain a tungsten quartz Vis-NIR source, a deuterium arc UV source, a photomultiplier tube UV-Vis detector (175–800 nm) and a PbS photocell NIR detector (800–3300 nm). The interval of the data collection is 1 nm for the Cary 5000 and 2 nm for the Lambda 19.

2.3.3 Optical characterization (powder)

In this study, reflectance spectra of powder were also measured. Reflectance measurements were carried out using an Ocean Optics ISP-REF Integrating Sphere connected to a LR1 spectrometer [16]. For an integrating sphere, the light scattered by the inside surface of the sphere is distributed evenly over all angles. The interior is assumed to have a diffuse reflectivity of approximately 100% (>95% for our device for wavelength in between 250–2000 nm). During the measurement, the sample was backed with a mirror so that the total reflectance could be measured. The sample port diameter is 10.3 mm. Because here the signal obtained is the total reflectance of the specimen, the absorbance of the sample (A) can thus be written as

$$A = C - R_p \tag{2.16}$$

where R_p is the measured reflectance for the powder and C is the reference signal collected by the detector when there is no sample and is independent of wavelength. The results of the measurement will be shown and discussed in Chapter 4 for results on copper pyrophosphate.

2.4 Microstructural characterization

2.4.1 X-ray diffraction (XRD)

X-ray diffraction is a technique than can provide information on the physical structure of materials based on diffraction from the crystalline structure. This is a non-destructive technique that can be applied to the study of many materials including powders, solid-state bulk materials and thin films deposited on a substrate. Plenty of information can be extracted from the measurement of the angles and intensities of the diffracted beams. The main applications of this technique are summarized as: 1) Identifying an unknown material by comparing its θ-2θ scan peaks to the XRD database of known materials, 2) Determining the crystal structure from the XRD spectrum, 3) Obtaining the texture information and preferred orientations of the grains, if there is any, 4) Measuring grain size and internal strain.

2.4.1.1 Principles of the technique

To produce the incoming X-ray beam, electrons are first generated by heating up a filament (generally tungsten) in a vacuum tube beyond its work function. The electrons are then accelerated under high voltage (20–50 kV) and bombard metal cathode (Cu, Mo, etc.). Inner shell ionizations are generated by the collision of the electrons and produce X-ray of various wavelengths as a result of electrons dropping down to fill the vacant shells. For X-ray diffraction, it is ideal to have monochromatic light, thus for Cu X-rays source a nickel plate is typically used to filter out other X-rays.

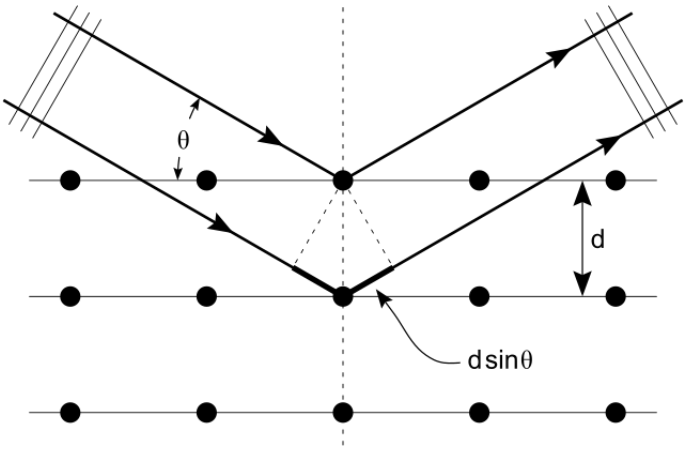


Figure 2.14: Bragg reflection due to the regular arrays of atoms inside a crystal [17].

When an X-ray hits on an atom it is scattered in multiple directions. For a crystallite that consists of regular lattice planes (hkl), only when the scattered X-rays from each lattice plane are in-phase can diffracted X-rays generate a single beam with intensity high enough to form a detectable peak. This constructive interference would only happen when the wavelength of the incident beam (λ), incident angle (θ) and the spacing between (hkl) crystal planes ($d_{(hkl)}$) meet the following requirement:

$$n\lambda = 2d_{(hkl)} \sin\theta \tag{2.17}$$

where n is an integer. This relationship between these parameters to generate constructive interference is called Bragg's law, as shown schematically in Figure 2.14. The reflection is called first order when $n = 1$, second order when $n = 2$, and so on, a higher order reflection have much smaller intensity. Therefore traditionally only the first order reflection is considered in Bragg's relationship and Equation (2.17) can be re-written as:

$$\lambda = 2d_{(hkl)} \sin\theta \tag{2.18}$$

It can be seen from Bragg's law that different set of (hkl) crystal planes with various d-spacings would result in different peak positions in an XRD spectrum. For instance, the highest angle peak represents the diffraction from crystal planes of

smallest spacing. This important characteristic of X-ray diffraction is the foundation for many of its applications.

2.4.1.2 Identification of material and its crystalline phase

The most common application is to determine the phase of the materials via fingerprinting. In this study, the phase of Si doped ZnO thin films, $Cu_2P_2O_7$ powder and $Cu_2P_2O_7$ films have been examined by XRD. In order to know the exact phase of the material, the measured spectra were compared to the XRD spectrum data gathered by International Centre for Diffraction Data (ICDD). ICDD is one of the largest and most widely referred centers in the world that gathers diffraction information for most inorganic and plenty of organic crystalline materials. The gathered data is saved in individual Powder Diffraction Files (PDF) with an unique serial number for each substance.

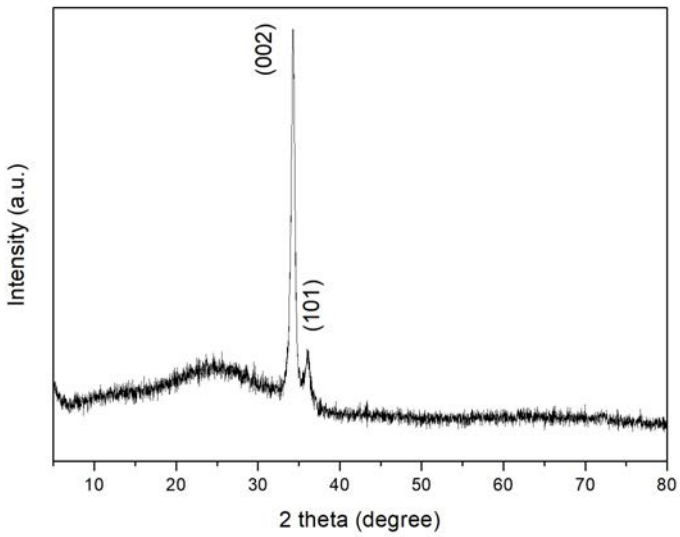


Figure 2.15: XRD spectrum of a Si doped ZnO film deposited on glass. The PDF file for wurtzite ZnO (space group: P63mc) is PDF-#36-1451.

Figure 2.15 shows the XRD spectrum of a Si doped ZnO thin film grown on a glass substrate. It can be seen that because the glass substrate does not have long-range order at the atomic level, it contributes an amorphous background to the spectrum

consisting of a very broad peak of low intensity. The sharp peaks in the spectrum can be identified by comparing the measured data to the PDF-#36-1451 file for wurtzite ZnO in the ICDD database. The two peaks were generated by the diffraction from the (002) and (101) planes of ZnO, respectively.

2.4.1.3 Calculation of lattice parameters

Once the material and peak positions are determined, one can calculate the lattice parameters, i.e. spacing of a set of (hkl) planes that the peak represents by using Equation 2.19, which is an adaptation from Bragg's law (Equation 2.18).

$$d_{(hkl)} = \frac{\lambda}{2\sin\theta} \tag{2.19}$$

In fact, there are many applications of this calculation. For instance, by comparing the lattice parameters of a series of samples that were prepared under different conditions, one can understand how the processing parameters affect the material's crystalline structure.

2.4.1.4 Texture study

Theta-2theta XRD scans can tell one information on the sample phase. Yet, sometimes it is important to also know the texture of the material. The general setup of XRD for texture measurements is shown in Figure 2.16a. The sample can rotate around three different axes ϕ, ψ and ω. Based on the different texture information one wants to obtain, different axis will be chosen as the rotation axis for the measurement.

For the examination of *out-of-plane texture*, also known as rocking curve measurements, the sample will be rotated around the ω axis while the detector is fixed at a 2θ angle and the source at the incident angle of θ so that they meet the Bragg condition for a target hkl plane. For instance, if one wants to know the out-of-plane texture of wurtzite ZnO thin film the (002) plane could be used and the detector should be positioned at a fixed 2θ angle of 34.4° for (002) ZnO while the sample is rocked around the ω axis. The curve that is obtained from such

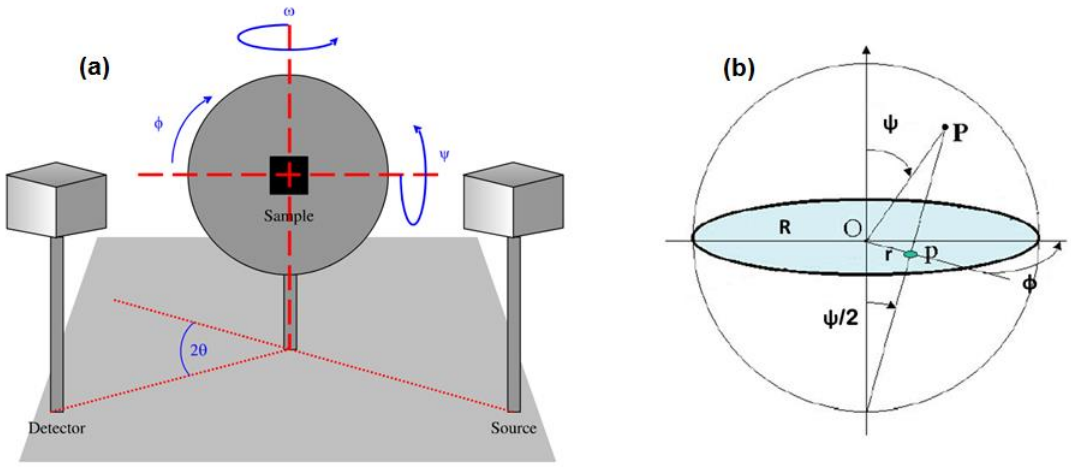


Figure 2.16: Schematic illustration of (a) a goniometer and (b) the measurement of a pole figure. ϕ, ψ and ω axes are shown in the above images [18].

measurement is called a rocking curve. The full-width at half maximum intensity (FWHM) of the rocking curve represents how good the out-of-plane alignment of the sample is.

In terms of the measurement of *in plane texture*, the sample can be rotated around the ϕ axis. The detector will still be positioned at a fixed 2θ angle and the source at the incident angle of θ, while the ω and ψ will also be in chosen places so that the positions of the target plane and the detector satisfy the Bragg's law. Taking a (001)-oriented MgO single crystal as an example, if one wants to measure the in plane texture of its (101) plane, ψ should be 45° while $\omega = 0°$. The obtained curve (scan range of ϕ: ±180°) should show four evenly distributed peaks with 90° spacing given the MgO single crystal possesses a four-fold symmetry (space group: $Fm\bar{3}m$).

Instead of positioning ψ at a fixed angle, one can also measure the pole figure of a particular hkl plane by measuring the ϕ scan curve at different ψ angles with step size of usually 1–2° (0–88°). The construction process is illustrated in Figure 2.16b. Pole figures can be used to show the 3D orientation distribution of selected lattice planes inside the material.

2.4.1.5 Calculation of crystallite size and internal strain

For materials with relatively small crystallites (<200 nm), the average crystallite size can be calculated from the broadening of XRD peaks by using Scherrer equation [19]:

$$\tau = \frac{K\lambda}{\beta \cos\theta} \tag{2.20}$$

where τ is the mean size of crystallites, K is the shape factor ($\sim$0.9, varies with the shape of the crystallite), λ is the wavelength of the X-rays, β is the peak broadening at the FWHM and θ is the Bragg angle. The broadening of the peaks can be obtained by software like X'Pert HighScore or MDI Jade. In this study, the Scherrer equation is used to calculate the crystallite size of the SiZO films sputtered on MgO substrate. The θ positions in the measured spectra were pre-calibrated using the (200) peak of the single crystalline MgO at 2θ angle of 42.9°.

In some cases, the broadening of the peak has other causes such as inhomogeneous strain inside the specimen. In that case, more sophisticated method needs to be used to separate the broadening generated by different mechanisms [20].

2.4.1.6 Instrumentation

The theta-2theta XRD experiments in this study were carried out in a Panalytical MRD X-ray Diffractometer (SiZO thin films), Panalytical Empyrean X-ray Diffractometer ($Cu_2P_2O_7$ powder) and a Rigaku Miniflex XRD system ($Cu_2P_2O_7$ thin films). Omega-scans of the SiZO thin films were carried out in a Panalytical MRD X-ray Diffractometer. Phi-scans of the SiZO thin films were carried out in Panalytical Empyrean X-ray Diffractometer. These systems all use Cu K_α X-rays ($\lambda = 0.15406$ nm) as sources with a tube voltage of 40 kV.

2.4.2 Scanning electron microscopy (SEM)

2.4.2.1 Principles of the technique

A scanning electron microscope (SEM) is a device that creates the magnified image of a specimen by scanning a focused electron beam over the surface of the sample.

Traditionally people use light to illuminate the sample and magnify the detailed structures. However, the resolution of a light microscope is limited by wavelength of light (550 nm is the average wavelength of white light). Meanwhile, electrons can have much smaller wavelengths (12.2 pm at 10 keV and 2.5 pm at 200 keV) that enables a much higher imaging resolution. Since it was firstly constructed in the 1930s [21], SEM has been extensively used in the studies of almost all kinds of materials. The typical setup of a SEM is illustrated in Figure 2.17.

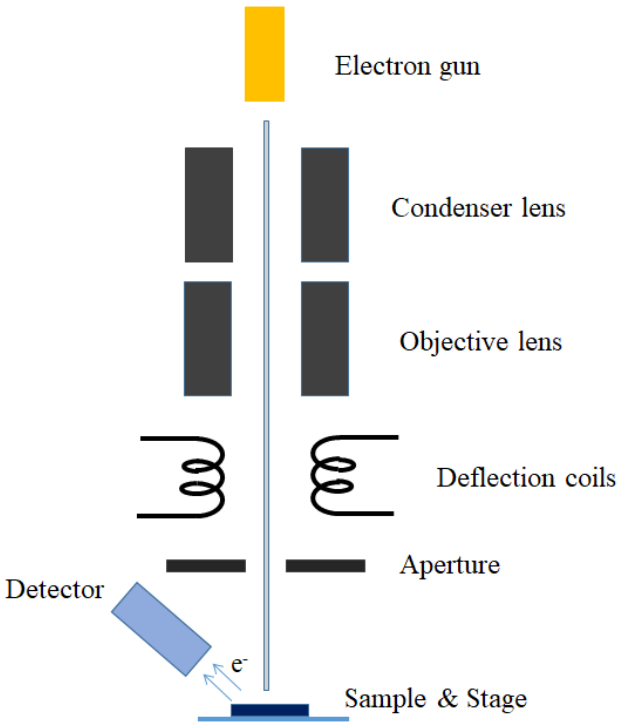


Figure 2.17: Schematic illustration of the setup of a typical SEM.

Components of SEM include source of the electron beam (electron gun), a series of electromagnetic lenses that control the radius of the beam as well as the focus, apertures that adjust the beam size and its coherence, the stage and the electron detector. Two types of electron gun can be used for imaging; thermionic electron guns (TEG) and field emission guns (FEG). For TEG, electrons are generated by heating up a piece of solid such as tungsten wire or a LaB_6 crystal. Regarding FEG, electrons are emitted from a tip by using a strong electric field. The electron beam generated by FEG can achieve higher intensity and smaller diameter compared to

that of TEG. The operation of both of the guns requires high vacuum levels (FEG: $\sim 10^{-10}$ mbar, LaB_6: $\sim 10^{-6}$ mbar).

The uses of SEM can be summarized into two categories: 1. Morphology studies and 2. Composition studies. By collecting the secondary electrons (SE) that are generated by the interaction between the beam and the sample, SEM is able to show the surface features of a specimen, including the shape and size of the particles/crystallites that make up the sample. For instance, Figure 2.18 shows the surface morphology of a Si-doped ZnO film deposited on glass substrate.

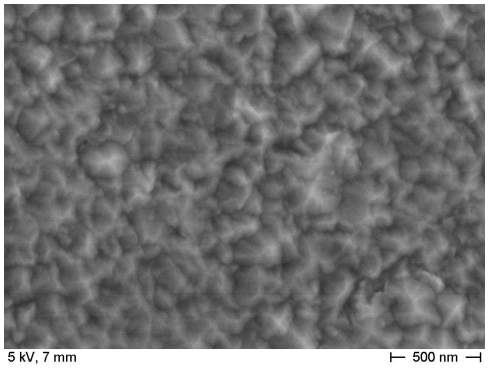


Figure 2.18: Surface morphology of a Si-doped ZnO thin film sputtered on glass substrate.

Composition studies can be achieved by either collecting backscattered electrons (BSE) or X-rays emitted from the specimen; the latter one can give quantitative information about the relative content of each element in the sample. Unlike secondary electrons, backscattered electrons are made up of high-energy electrons that are reflected or back-scattered via elastic scattering from atomic nuclei in the interaction volume (Figure 2.19). The higher the atomic number of the element, the greater the backscattered signal, owing to stronger backscattering effect. Therefore, one can obtain the compositional uniformity from contrast in the BSE image.

The method that uses characteristic X-rays for compositional analysis is called Energy Dispersive X-ray (EDS) analysis. In order to perform EDS analysis, a special detector needs to be attached to the SEM chamber. The intensities of the signal are measured by counting photons of different energies. Information on the composition of the sample can be obtained by comparing the intensities of different elemental

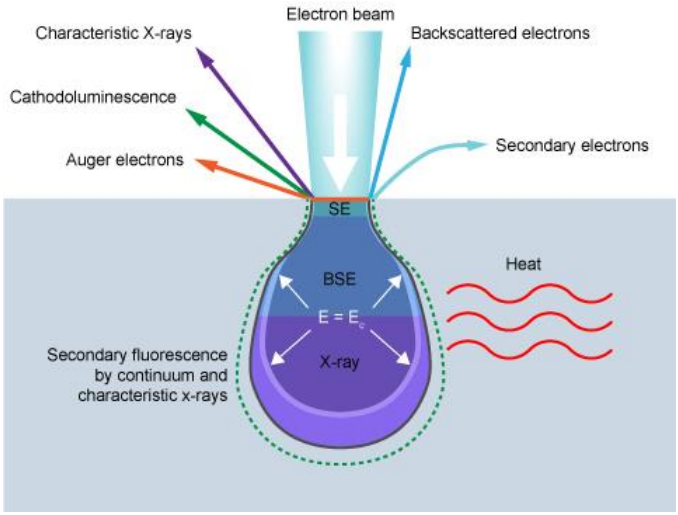


Figure 2.19: Schematic demonstration of electron-specimen interaction volumes [22].

peaks. However it can be seen in Figure 2.19 that the interaction volume for X-ray generation is a lot bigger than that of secondary electrons. The volume depends on the atomic number of the element, accelerating voltage and angle of incidence for the beam. For instance, for copper (atomic number: 29), the depth of the interaction volume is about 5 μm at an accelerating voltage of 20 kV, which is bigger than the thicknesses of the copper pyrophosphate films discussed in this thesis. That means the measured signal will not only contain chemical information on the film but also that of the substrate, which is why it is important to choose a substrate that does not contain the elements of interest.

For most of the commercial EDS softwares nowadays, the method they used for the calibration of the relations between the X-ray intensity and the concentration of a certain element is called 'Remote standards' [23], which is based on a library suite of standard intensities carefully collected from standard samples such as pure elements and stoichiometric binary compounds at multiple beam energies. The remotely obtained database is then adapted to the EDS photon efficiency of the local instrument using a detector efficiency transfer calculation.

2.4.2.2 Instrumentation

SEM imaging and EDS analysis in this thesis were carried out in Zeiss EVO MA10, Zeiss Merlin, JEOL JSM-840F and JEOL JSM-5510 instruments. Most of the EDS signals were collected using accelerating voltage of 20 kV.

2.4.3 Transmission Electron Microscopy (TEM)

2.4.3.1 Principles of the technique

A transmission electron microscope (TEM) is a device that creates a magnified image of a specimen by detecting electrons transmitted through it. The core components of a TEM microscope are shown in the schematic diagram (Figure 2.20) below.

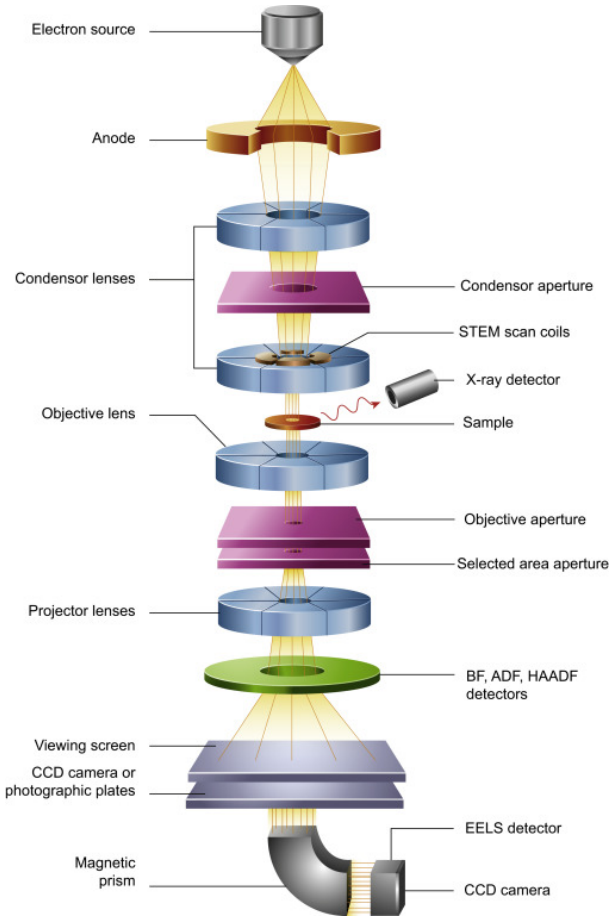


Figure 2.20: Schematic illustration of a TEM [24].

The source of a TEM can be either TEG or FEG like that in SEM. Three lens systems from the top to the bottom are the condenser lens system that controls

the illumination on sample, the objective lens system that focuses the beam coming through the specimen and the projection lens system that expands the beam and projects the image onto the imaging surface. The condenser lens aperture that sits near the top of the column is used to adjust the spot size and the beam coherence. The objective aperture that located beneath the objective lens is primarily used to control the image contrast.

There are generally two types of imaging mode, Conventional Transmission Electron Microscopy (CTEM) imaging in which the beam is close-to-parallel, and Scanning Transmission Electron Microscopy (STEM) imaging where images are formed by scanning a finely focused beam over the specimen (typical spot size: 0.05–0.2 nm). This raster illumination in STEM allows it to be used for analytical techniques like annular dark-field (ADF) imaging, electron energy loss spectroscopy (EELS) and energy dispersive X-ray spectroscopy (EDS) mapping. Another mode of imaging is called High Resolution Transmission Electron Microscopy (HRTEM) which allows the imaging of the structure of the sample on the atomic scale. It can be operated under both CTEM and STEM modes. For HRTEM imaging, calibration of the scale is required to accurately calculate the lattice spacing and determine the zone axis of the imaging area. This is usually done by measuring the lattice constants of a standard sample right before or after the session.

2.4.3.2 Fresnel imaging

For TEM imaging, the contrast of the image is at its minimum when the sample is in focus. When the sample is out of focus, contrast began to show due to the interference of out-of-phase waves. For different focus conditions, the Fresnel fringes around a hole also show different contrast, as shown in Figure 2.21.

The detailed explanation and wave function calculations for Fresnel fringes can be found in previous publications [26, 27]. Fresnel imaging is a useful technique for the identifying small holes in materials, and will be used in this thesis to demonstrate porosity in some of the specimens.

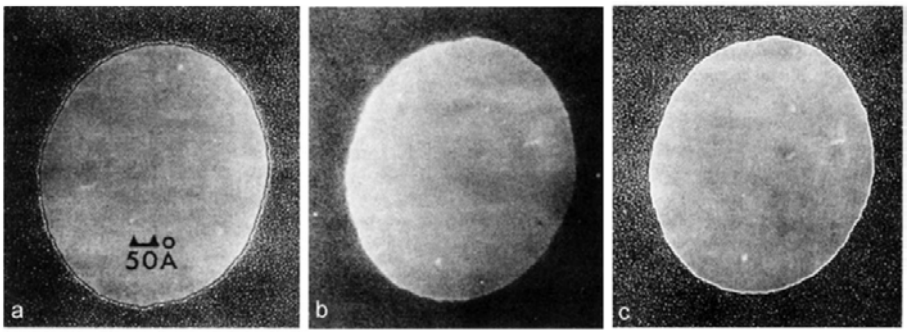


Figure 2.21: Fresnel fringes around the edge of a hole. (a) Overfocus shows a dark fringe, (b) in focus and (c) underfocus shows a bright fringe [25].

2.4.3.3 Geometric Phase Analysis (GPA)

As useful and powerful as HRTEM is, sometimes it can be difficult to directly study the HRTEM image given the subtle differences between parts that can be challenging for visual inspection or quantification. Algorithms have been developed to extract geometric phase information from the image by using methods including Fourier transformations, and can help quantify and map local displacements and strain fields in lattices, with resolution down to the nano-scale [28, 29]. This method is called Geometric Phase Analysis (GPA) which will be used in Chapter 3.

According to Hytch [28], the local distortion of the lattice is defined by the gradient of the displacement field and can be written as a 2×2 matrix, d, defined as follows:

$$d = \begin{pmatrix} d_{xx} & d_{xy} \\ d_{yx} & d_{yy} \end{pmatrix} = \begin{pmatrix} \frac{\partial u_x}{\partial x} & \frac{\partial u_x}{\partial y} \\ \frac{\partial u_y}{\partial x} & \frac{\partial u_y}{\partial y} \end{pmatrix} \tag{2.21}$$

where $\boldsymbol{u}(\boldsymbol{r})$ is the displacement field [28]. This matrix can be divided into two terms, ε (symmetric) and ω (anti-symmetric):

$$\varepsilon = \frac{1}{2}\left\{d + d^{\mathrm{T}}\right\} \tag{2.22}$$

$$\omega = \frac{1}{2}\left\{d - d^{\mathrm{T}}\right\} \tag{2.23}$$

where T denotes the transpose operation of matrix. Here, ε represents the strain while ω gives the local rigid rotation. The magnitude of ω_{xy} is positively correlated

with the rotation angle, and the angle can be calculated from the diagonal components (ω_{xy}, ω_{yx}) of the rotation matrix [28].

2.4.3.4 Instrumentation

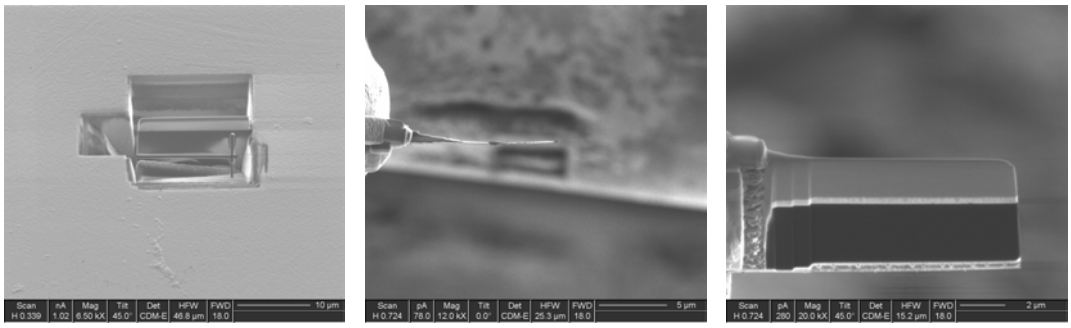
TEM analysis was carried out in JEOL 3000F FEG-TEM (300 kV), JEOL ARM-200F Cs probe corrected CFEG-TEM (200 kV) and Zeiss Merlin (STEM mode) instruments. EDS analysis was done on JEOL 3000F FEG-TEM (300 kV) and Zeiss Merlin (STEM mode). Calibrations of the scales were carried out by measuring the (200) and (220) planes of an oriented single crystal gold foil purchased from Agar Scientific ®[30].

2.4.4 Focused ion beam (FIB)

2.4.4.1 Principles of the technique

In order for the sample to have the right thickness to be imaged in TEM, a technique called Focused Ion Beam (FIB) can be used to prepare TEM lamellae from the original specimen. Focused ion beam instruments operate in a way similar to the SEM, but with a primary Ga^+ ion beam instead of the electron beam. The high energy gallium ions allow the milling of holes/trenches in the specimen, while the generated secondary electrons are collected for imaging purpose. Some systems nowadays combine a SEM and FIB column, which is called 'Dual Beam', 'Cross Beam' or 'Multi Beam' depending on the vendor of the instrument. Usually the ion beam is used for milling and the electron beam is used for high magnification imaging of the sample preparation.

The process of preparing TEM lamellas varies slightly depending on the material and the instrument. For thin film material, a layer of Pt (thickness: 1-2 μm) is first deposited on the surface as a protection layer against beam damage. A high current gallium ion beam (voltage: 30 kV) is then used to mill several trenches (typically 3) around the sample as a preparation for lift-out (Figure 2.22(a)). Lift out in FIB can be either *ex-situ* or *in-situ*. The samples introduced in this thesis were made by the *in-situ* approach. To carry out the *in-situ* lift-out, a micro-manipulator is required to



(a) Trench made by FIB before sample being lifted out (tilt angle: 45°). Scale bar: 10 µm.

(b) The top perspective of the TEM lamella after thinning. Scale bar: 5 µm.

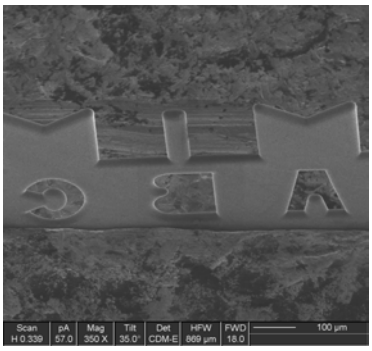
(c) 45° tilted perspective of the TEM lamella. Scale bar: 2 µm.

Figure 2.22: Preparation of TEM lamella of SiZO thin film.

move the lamella (thickness at this stage: $\sim$ 1 µm) from the thin film to the copper grid. The Cu grid used here is the half grid that could stand in the specially made holder. The lamella is then attached to the Cu grid for further thinning. In order to be properly imaged by TEM, the thickness of the lamella must be smaller than 200 nm for most materials. The samples made in this study were thinned down to $\sim$ 50 nm (Figure 2.22(b), 2.22(c)). Different current values are required at different stages to minimize the beam damage to the sample. Low energy (voltage: 5 kV) cleaning is carried out at the end of the thinning process to reduce the impurities (Ga penetration) and to remove the disrupted structure on the surface of the lamella caused by the ion beam bombardment.

2.4.4.2 Instrumentation

The FIB machine used in this study is FEI FIB 200. The used Cu grids were the 3 post lift-out grids from Agar Scientific ®. The grid contains multiple indexed mounting locations, including the vertical bar (B) and V-shaped surfaces (A, C) (Figure 2.23(a)). The specially designed holder (Figure 2.23(b)) allows the lift-out and the thinning to be carried out continuously without opening the chamber, which increases both the time efficiency and the safety of the delicate lamella.



(a) 3 post lift-out Cu grid.



(b) Sample holder for FIB experiment. Scale of the image: 126 × 94 mm.

Figure 2.23: FIB holder and Cu grid.

2.4.5 Transmission Kikuchi Diffraction (TKD)

2.4.5.1 Principles of the technique

Transmission Kikuchi Diffraction (TKD) is a high-resolution orientation mapping technique that has received plenty of interest recently for the characterization of nano-structured materials [31]. It is also known as transmission electron forward scatter diffraction (t-EFSD) or transmission electron backscatter diffraction (t-EBSD). EBSD analysis is based on the capture and analysis of Kikuchi patterns [32]. Kikuchi patterns, also known as Kikuchi bands, are pairs of parallele lines generated when the crystalline sample interacts with the incoming electron beam and scatter electrons at the right diffraction angles [32]. A CCD camera then records the patterns from a phosphor screen for further use in automated indexing. The fundamental principles of TKD is similar to that of EBSD. Yet, the introduction of TKD by Keller and Geiss greatly improved the spatial resolution of EBSD. Compared to traditional EBSD, the sample is required to be thin enough to be electron transparent, similar to that in TEM. The spatial resolution improved from $\sim$ 20 nm for traditional EBSD to 2 nm for TKD [33]. This makes the technique particularly useful, in fact necessary, for the orientation mapping of the sputtered thin films discussed here with nano-sized grains.

2.4.5.2 Instrumentation

TKD analysis in this study was carried out on a ZEISS Merlin SEM (30 kV) and an FEI Magellan FEG-SEM XHR 400L. The TKD samples are the same samples used for TEM imaging made by FIB.

2.4.6 Profilometer

2.4.6.1 Principles of the technique

The thickness of the films made in this study was measured by a stylus profilometer. A profilometer is a device that can measure the profile of a surface and quantify the roughness. There are two different types of profilometer: contact and non-contact. The one used in this study is the contact type. It has a diamond-tip stylus moving vertically to stay in contact with the sample while moving horizontally across the specimen for a selected distance. The height position of the diamond stylus produces an analog signal which is then converted into a digital signal for storage, analysis and display. The advantages of this method can be summarized as: 1) Wide measuring acceptance for most of the surface, 2) Non-sensitivity to surface reflectance or color which can be a problem for non-contact (optical) profilometer, 3) High resolution with vertical resolution down to 1 Angstrom while the horizontal resolution depends on the radius of the diamond stylus, 4) Direct measurement that does not require additional modeling.

2.4.6.2 Instrumentation

The profilometer used in this study is Bruker (Veeco) Dektak 6M contact profilometer. The instrument has a vertical resolution from 1 to 200 Angstroms depending on the measured step height. The sharp step for thickness measurement was created by covering part of the substrate with Kapton tape or a copper shield before sputtering and removing it afterwards.

In fact, the measurement of the thickness is important not only because it offers correct information on the dimensions of the samples, it also impact the accuracy of

the measured Hall carrier concentration and resistivity (Equation (2.5)). However, given that for most of the thin film deposition techniques, there could be an uneven distribution of the thickness across the deposited film that leads to an inaccurate evaluation of the film thickness, a few actions were implemented to increase the accuracy: 1) The sputtering stage was always pre-calibrated before depositions to make sure its surface is parallel to the target surface, 2) The Kapton tapes were stuck on the left and right sides of the films to create sharp steps on both sides of the films before sputtering. After sputtering, measurements were then carried out on each side on three evenly spaced points: top, middle and bottom, and the thickness was calculated as an average of the values measured at these six positions for each film. However, the resolution of the instrument would still induce a certain degree of instrumental error. The resolution of Dektak 6M profilometer is a function of the step height, in this study the resolution is around 4 nm given the thickness range (200–1000 nm) of the SiZO films made here [34]. This means for films with thicknesses of 200–400 nm, there could be an instrumental error of 1–2% in the measured thickness, creating an ∼1–2% error in the carrier concentration and resistivity. Therefore, only two significant figures were kept for the electrical results reported in this thesis. The thickness variation in multiple measurements (5 times) on a 320 nm step is within ±10 nm.

Other potential sources of error exist when it comes to measurement by a stylus profilometer. The finite dimensions of any stylus tip can cause distortion in the traced profile compared with the actual surface profile. This includes the exaggeration of the magnitude of peak curvature and the reduction of the depth of valleys [35]. Another potential source for contact stylus measurement is the possible lift-off of a tip as it scans across the surface at a relatively high scanning velocity [36]. When this happens, a sharp peak could usually be seen in the traced profile. Moreover, the stylus load could potentially lead to undesired surface distortion if the load is too high for a particular surface type. Plastic deformation could happen and lead to measurement error at a high load, especially for metallic samples [37]. The choices of

stylus dimension, scanning speed and stylus load are important for the minimisation of these potential error sources.

2.4.7 Optical microscope

A ZEISS Axioskop 2 MAT optical microscope was used in this study for imaging the thin films. The principles of the optical microscope can be found in many previous publications [38].

2.4.8 X-ray Photoelectron Spectroscopy (XPS)

2.4.8.1 Principles of the technique

XPS is a surface sensitive technique often used to study the elemental composition and chemical state of elements in a material. To achieve that, a beam of X-rays is irradiated onto the sample while the electron detector and the hemispherical energy analyzer (Figure 2.24) measure the counts and kinetic energy of the electrons escaped from the surface of the sample. The electrons are generated as a result of the photoelectric effect.

Once the kinetic energy of the escaped electrons are known, one can calculate the binding energy of the electron ($E_{binding}$) by using the following relationship:

$$E_{binding} = h\nu - (E_{kinetic} + \phi_s) \tag{2.24}$$

where h is the Planck constant, ν is the frequency of the X-ray photon, $E_{kinetic}$ is the measured kinetic energy of the photo-ejected electron and ϕ_s is the work function of the spectrometer. Since binding energy is a characteristic value of the shell that emits the electrons, the obtained energy spectrum shows resonance peak characteristics of the electronic structure of the surface atoms. The peaks are generated at energies where photo-excitation occurs. Since the binding energies of the orbits of an atom are influenced by factors such as chemical bonding, XPS can also provide information about bonding. The usual measuring depth of XPS measurement is the top 1-10 nm of the sample, and the machine needs to be

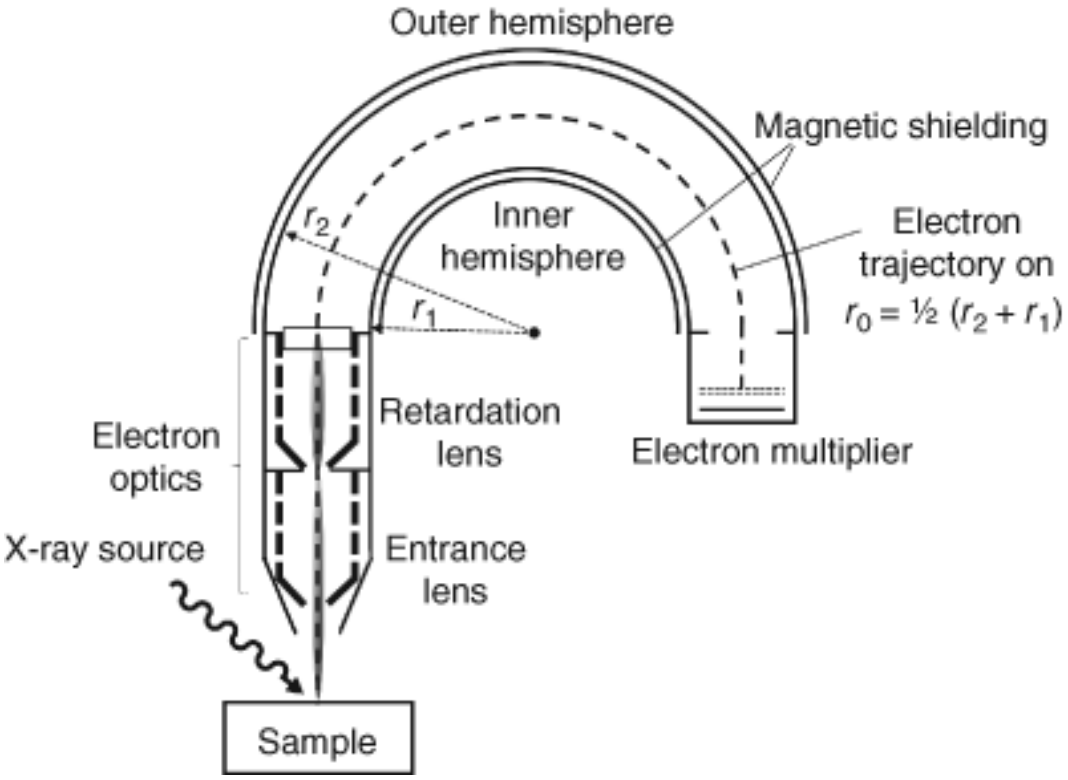


Figure 2.24: Schematic illustration of the setup of an XPS. [39]

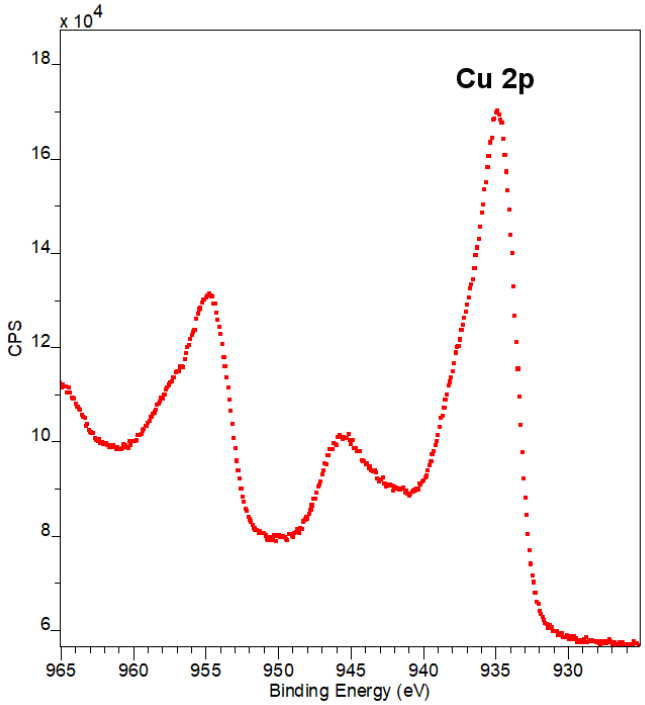


Figure 2.25: XPS spectrum (etched) of a pressed $Cu_2P_2O_7$ sample.

operated under high vacuum ($\sim 10^{-8} - 10^{-10}$ torr). An example of XPS spectrum obtained on a pressed $Cu_2P_2O_7$ sample is shown in Figure 2.25, in which the peak of Cu $2p_{3/2}$ can be seen. More detailed discussion will be illustrated in Chapter 4.

2.4.8.2 Instrumentation

XPS analysis was carried out on a Thermo K-Alpha XPS System. The source of the system is Al K-alpha (monochromatic) X-rays. The measurements were run at constant analyser energy (CAE) with a pass energy of 200 eV and 5 scans used for the survey scans, while the detailed scans used a pass energy of 50 eV and 10 scans. The step size of the measurement is 0.1 eV. The surfaces of the samples have been etched by Argon ion to remove any contaminants with a beam voltage of 2kV. The etch time is 30 s each time.

Bibliography

[1] J. E. Mahan, Physical Vapor Deposition of Thin Films, by John E. Mahan, pp. 336. ISBN 0-471-33001-9. Wiley-VCH, January 2000. p. 336 (2000).

[2] M. Ohring, *Materials science of thin films* (Academic press, 2001), ISBN 0080491782.

[3] D. L. Smith, *Thin-film deposition: principles and practice* (McGraw Hill Professional, 1995), ISBN 0070585024.

[4] F. Smits, Bell System Technical Journal **37**, 711 (1958), ISSN 1538-7305.

[5] L. Van der Pauw, Philips technical review **20**, 220 (1958).

[6] NIST, URL `https://www.nist.gov/pml/`.

[7] F. S. Rocha, A. J. Gomes, C. N. Lunardi, S. Kaliaguine, and G. S. Patience, The Canadian Journal of Chemical Engineering **96**, 2512 (2018).

[8] N. Rashidi, Thesis, Oxford University (2014).

[9] T. Matsumura and Y. Sato, Journal of Modern Physics **1**, 340 (2010).

[10] P. P. Edwards and M. J. Sienko, Physical Review B **17**, 2575 (1978).

[11] P. P. Edwards, A. Porch, M. O. Jones, D. V. Morgan, and R. M. Perks, Dalton transactions pp. 2995–3002 (2004).

[12] I. Hamberg and C. G. Granqvist, Journal of Applied Physics **60**, R123 (1986), ISSN 0021-8979.

[13] J. Bellingham, W. Phillips, and C. Adkins, Journal of Materials Science Letters **11**, 263 (1992), ISSN 0261-8028.

[14] R. M. Pasquarelli, D. S. Ginley, and R. O'Hayre, Chemical Society Reviews **40**, 5406 (2011).

[15] K. Ellmer and R. Mientus, Thin solid films **516**, 4620 (2008), ISSN 0040-6090.

[16] M. Law, M. C. Beard, S. Choi, J. M. Luther, M. C. Hanna, and A. J. Nozik, Nano letters **8**, 3904 (2008), ISSN 1530-6984.

[17] X-ray Crystallography, URL `https://en.wikipedia.org/wiki/X-raycrystallography`.

[18] S. Speller, Thesis, Oxford University (2003).

[19] L. E. Smart and E. A. Moore, *Solid state chemistry: an introduction* (CRC press, 2016), ISBN 1439847924.

[20] P. Bindu and S. Thomas, Journal of Theoretical and Applied Physics **8**, 123 (2014), ISSN 1735-9325.

[21] B. Breton, Retrieved October **7**, 2007 (2006).

[22] AMMRF (2018), URL `http://www.ammrf.org.au/myscope/`.

[23] D. E. Newbury and N. W. Ritchie, Scanning **35**, 141 (2013), ISSN 0161-0457.

[24] B. Inkson, *Scanning electron microscopy (SEM) and transmission electron microscopy (TEM) for materials characterization* (Elsevier, 2016), pp. 17–43.

[25] B. Fultz and J. M. Howe, *Transmission electron microscopy and diffractometry of materials* (Springer Science & Business Media, 2012), ISBN 3642297609.

[26] K. Fukushima, H. Kawakatsu, and A. Fukami, Journal of Physics D: Applied Physics **7**, 257 (1974), ISSN 0022-3727.

[27] D. B. Williams and C. B. Carter, *The transmission electron microscope* (Springer, 1996), pp. 3–17.

[28] M. Hÿtch, E. Snoeck, and R. Kilaas, Ultramicroscopy **74**, 131 (1998), ISSN 0304-3991.

[29] M. J. Hÿtch, J.-L. Putaux, and J.-M. Pnisson, Nature **423**, 270 (2003), ISSN 1476-4687.

[30] Agar Scientific, *Gold foil for tem* (2019), URL `http://www.agarscientific.com/plane-spacing-0-204-0-143-and-0-102-nm.html`.

[31] G. C. Sneddon, P. W. Trimby, and J. M. Cairney, Materials Science and Engineering: R: Reports **110**, 1 (2016), ISSN 0927-796X.

[32] A. J. Schwartz, M. Kumar, B. L. Adams, and D. P. Field, *Electron backscatter diffraction in materials science* (Springer, 2000), ISBN 030646487X.

[33] P. W. Trimby, Ultramicroscopy **120**, 16 (2012), ISSN 0304-3991.

[34] Cornell University (2011), URL `https://www.cnfusers.cornell.edu/sites/default/files/Equipment-Resources/Veeco%20Dektak%206M%20protocol%20102011.pdf`.

[35] B. Bhushan, *Modern tribology handbook, two volume set* (CRC press, 2000), ISBN 0849377870.

[36] P. Pawlus and M. Smieszek, Precision Engineering **29**, 272 (2005), ISSN 0141-6359.

[37] M. A. Davinci, N. Parthasarathi, U. Borah, and S. K. Albert, Measurement **48**, 368 (2014), ISSN 0263-2241.

[38] E. Hecht, *Optics* (Pearson Education, 2016), ISBN 1292096934.

[39] Z. Wang, U. Wille, and E. Juaristi, eds., *Encyclopedia of physical organic chemistry* (John Wiley & Sons, 2017), ISBN 9781118468586.

Chapter 3

Si Doped ZnO Thin Films: Fabrication, Microstructure and Properties

3.1 Introduction

Silicon is an attractive dopant in ZnO because it is cheap and abundant, which accords with the major motivation for most of the industrial or academic interest in ZnO. In a simple view of the Si doping process, each Si^{4+} replaces a Zn^{2+} ion and also generates 2 extra conduction band electrons due to the charge neutrality requirement. These ionisation electrons thus increase the carrier concentration and enhance the electrical conductivity. As mentioned earlier in Chapter 1, recent research showed that with a fluorine-assisted doping strategies, the resistivity of Si doped ZnO (SiZO) film made by spray pyrolysis can be smaller than the reported resistivities of most, if not all, of the sprayed indium-free doped ZnO films [1]. This suggests that there is perhaps a great potential of SiZO being a highly competitive indium-free candidate, which is yet not fully unveiled, given the relatively small amount of research published on this topic.

This chapter has six sections. Following the introduction, the second section is about the preparation of sputtering targets including the analysis of morphology and chemical content. After that, films deposited under different conditions onto glass substrates will be discussed. In the fourth section, detailed examination of the microstructure and chemistry of films before and after vacuum annealing will be

presented. The purpose of this section is to see if the route of investigating TCO thin film taken here, which is quite 'unusual' compared to many previous researches, would offer us any new insight (Figure 3.1). The fifth section is a discussion of my results, followed by conclusions and suggestions for future work.

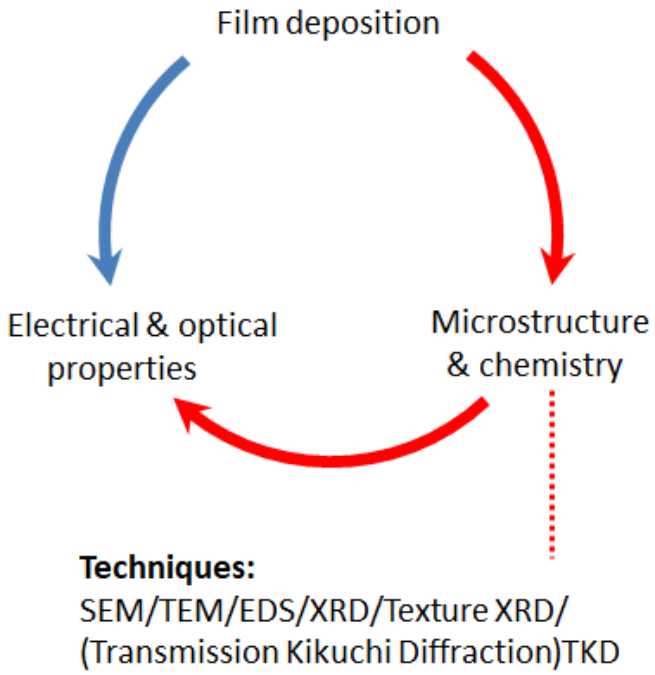


Figure 3.1: The research strategy of most previous literature (blue arrow) and the strategy of the current study (red arrows).

3.2 Target preparation

The target was made by our collaborators from the Chemistry Department of Oxford University by slip casting. After obtaining the target, it was studied by SEM/EDS prior to any sputtering. Pieces of target were mounted in epoxy and polished to obtain a smooth surface for SEM/EDS study. The microscopy results are shown in Figure 3.2.

As can be seen, the surface of the four different target areas all showed non-uniform chemical distribution. The elemental maps show phase separation of Si-rich phase and Si-poor phase in all the areas (green map, Si K line). In order to know exactly what phase each area represents, line scans were carried out as presented in

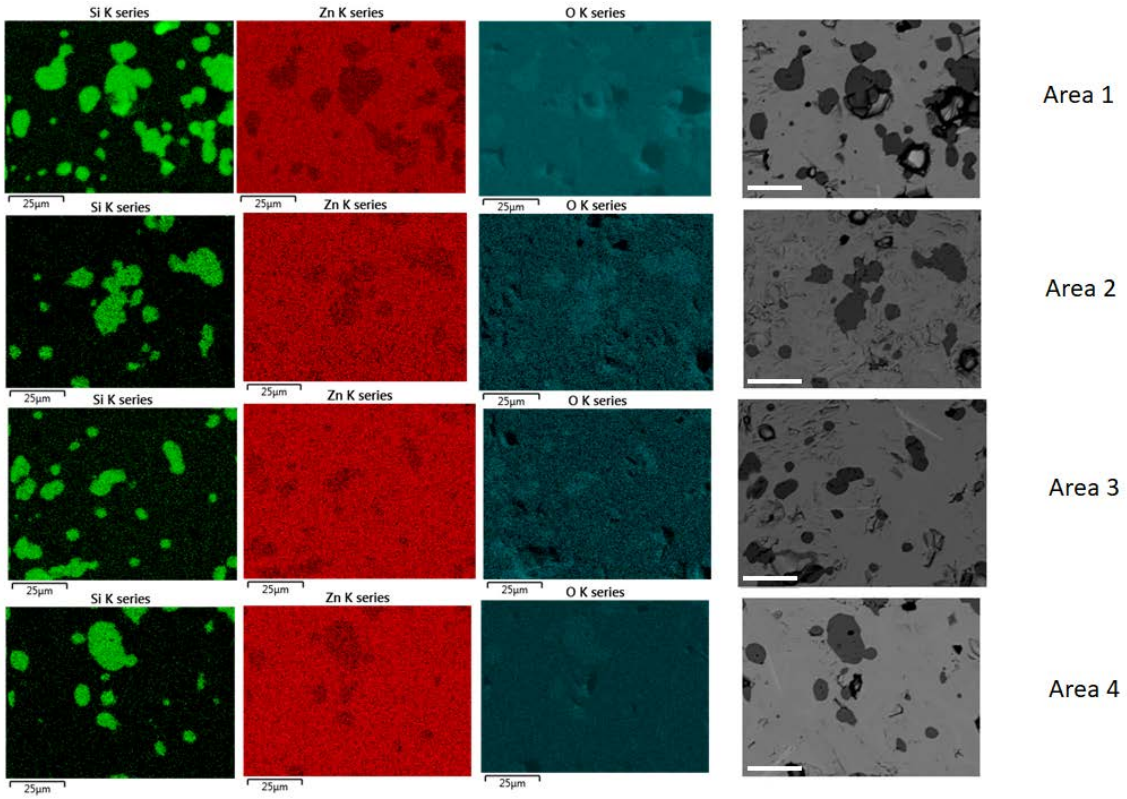


Figure 3.2: EDS maps and back-scattered electron (BSE) images of different areas of the SiZO target. Scale bar: 25 µm.

Figure 3.3. In the light grey area, only zinc and oxygen could be detected with almost no silicon signal. Regarding the darker area, zinc, oxygen and silicon signals could all be detected and the silicon to zinc ratio is roughly 0.5.

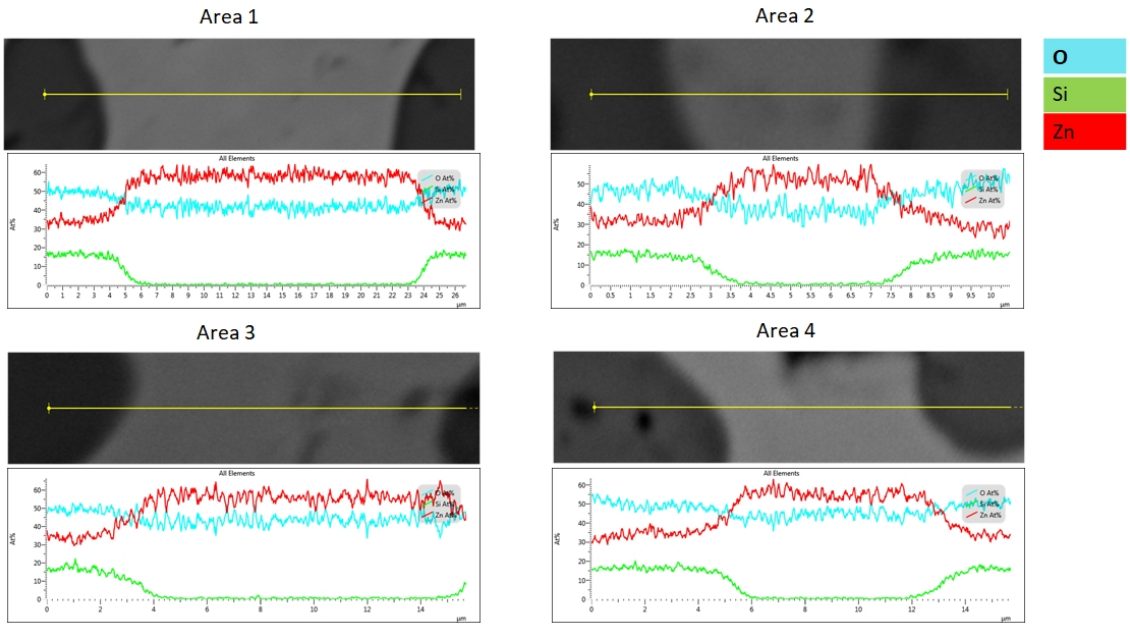


Figure 3.3: EDS line scans at four different areas of the target (silicon: green, zinc: red, oxygen: blue). Scales of the scans are 26 µm, 11 µm, 16 µm and 16 µm for area 1 to 4, respectively. The y axis represents the atomic percentage of the elements.

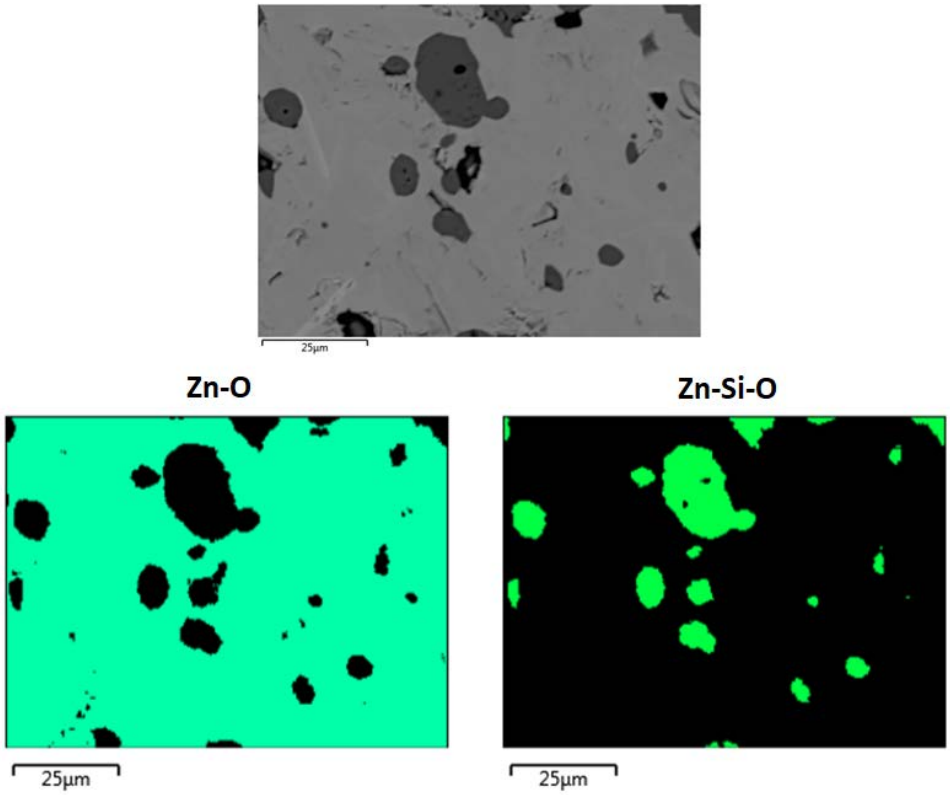


Figure 3.4: The phase composition analysis produced by the Aztec software.

This indicates that the two phases might be ZnO and Zn_2SiO_4, which is also consistent with the ZnO-SiO_2 phase diagram (Figure 1.15). Similar results were found in other line scans as well in different areas (Figure 3.3). Phase analysis has also been carried out using the built-in software component of the Aztec software which gave the same result (Figure 3.4). To obtain the average Si/(Zn+Si) atomic ratio in the target, EDS mapping over a larger area was applied and the result it gave was 3.4 at.%, which falls in between the optimal concentration region (3–4 at.%) as shown above.

3.3 Thin film preparation: growing SiZO films on glass substrates [i]

3.3.1 Substrate preparation

Schott D263T borosilicate glass substrates (Menzel-Gläser ®, 32 mm×24 mm, 0.13–0.17 mm thick) were ultrasonically cleaned in acetone (99.8+%) for 5 mins and ethanol (99.8+%) for 5 mins to remove the dust and chemical contamination on the surface of the substrates. During sputtering the substrate was mounted firmly on a copper stage with heating block beneath. More details of the sputter kit can be found in Chapter 2.

3.3.2 Electrical property analysis

In order to investigate how the properties of the films respond to changes in processing conditions, as well as to find the optimal deposition parameters, a series of films were deposited at various parameters including different Ar pressures, sputtering powers and substrate temperatures. Figure 3.5 shows the relationships of resistivity (ρ), electron mobility (μ) and carrier (electron) concentration (n) as a function of Ar pressure during sputtering, for films sputtered at substrate temperature of 200 °C

[i]The work in this section was performed in collaboration with Dr. Nazanin Rashidi from the Edwards Group in the Department of Chemistry at Oxford University, by whom some of the SiZO thin films reported on were prepared and characterized. However, all analysis and discussion of these is my own work.

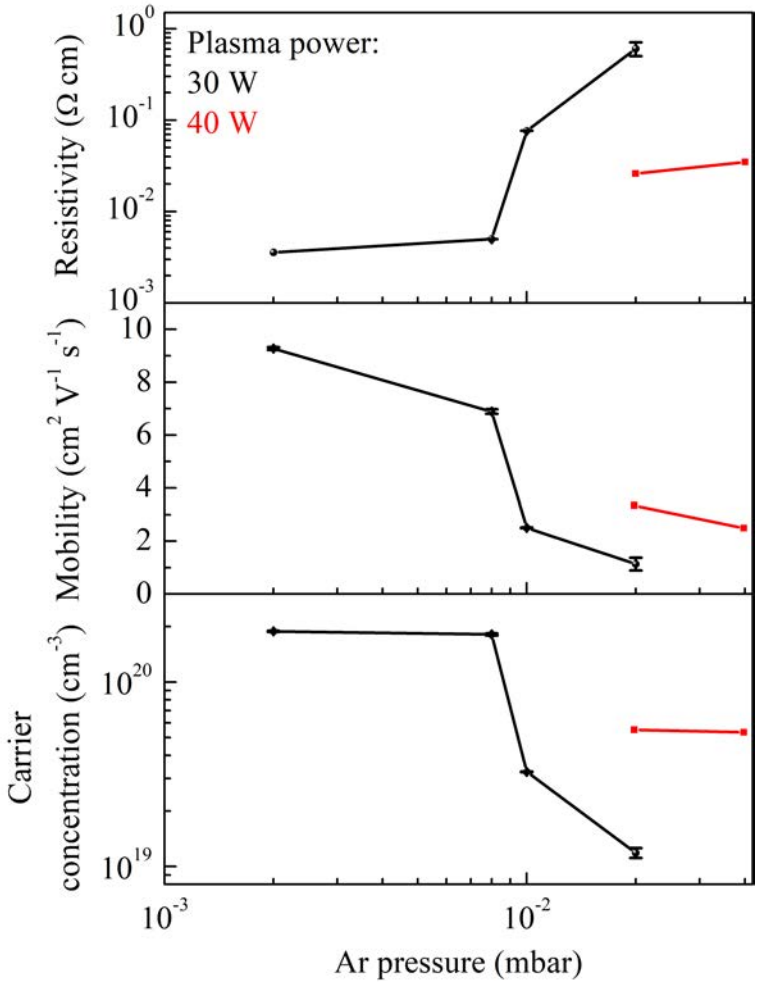


Figure 3.5: Ar gas pressure dependence of electrical transport properties of SiZO thin films deposited on glass substrates at power of 30 W (1.48 W/cm^2) and 40 W (1.97 W/cm^2), respectively. The substrate temperature is 200 °C. As a result of changing the sputtering pressure and the power, the thicknesses of the films also varied. The error bars are calculated from the measurements on multiple samples made under the same conditions.

with RF powers of 30 W (power density: 1.48 W/cm^2) and 40 W (power density: 1.97 W/cm^2) respectively. The sputtering duration for each film is 135 mins. The reason that a substrate temperature of 200 °C was initially used instead of room temperature is because it has been observed in AZO films before that films made at higher substrate temperature tend to show lower resistivity (Chapter 1). For the films deposited at 30 W, the results show that the resistivity decreased from 6.1×10^{-1} Ωcm to 3.6×10^{-3} Ωcm as the Ar pressure decreased from 2×10^{-2} mbar to 2×10^{-3}

mbar. At the same time, the electron mobility increased from 1.1 $cm^2V^{-1}s^{-1}$ to 9.3 $cm^2V^{-1}s^{-1}$ correspondingly, while the carrier concentration increased from 1.2×10^{19} cm^{-3} to 1.9×10^{20} cm^{-3}. For thin films sputtered at 40 W, the resistivity also showed a small decrease as the Ar pressure decreased from 4×10^{-2} mbar to 2×10^{-2} mbar. The film sputtered at 2×10^{-2} mbar, 40 W possessed a much lower resistivity than the one deposited at 2×10^{-2} mbar, 30 W, showing an improvement in electrical performance due to higher power. Nevertheless, the power control was a bit unstable at the time this study was carried out, meaning that it was difficult to make thin films with power higher than 40 W, which is also the reason that we did not pursue further on the 40 W series at other pressures. All of the films discussed in the current section were made with power of 30 W unless otherwise stated. The electrical properties were measured by the Van der pauw technique discussed in Section 2.3.1.3.

The small error bars in the graph, calculated from the measurements on multiple samples made under the same conditions, confirm the high reproducibility of the properties of these sputtered films and the reliability of the presented results. In terms of other potential contributors to the measurement errors, the error from the thickness measurement was discussed in Section 2.4.6.2. Besides, parameters, such as atmosphere, light exposure and humidity, can also have an impact on the measured conductivity, thus contributing to some of the experimental scatter. Other potential sources, such as variability in deposition conditions and purity of sputtering gas, was mitigated by process controls.

The pressure dependence of electrical performance of thin films deposited at 300 °C has also been studied. Figure 3.6 shows the variations of transport properties of thin films sputtered at 200 °C and 300 °C as a function of Ar pressure. As the Ar pressure decreased from 2×10^{-2} mbar to 1×10^{-3} mbar, the resistivity decreased from 1.2×10^{-1} Ωcm to 2.6×10^{-3} Ωcm, while the carrier concentration and mobility increased from 4.0×10^{19} cm^{-3}, 1.3 $cm^2V^{-1}s^{-1}$ to 2.7×10^{20} cm^{-3} and 8.8 $cm^2V^{-1}s^{-1}$, respectively. The electrical properties were measured by the Van der pauw technique discussed in Section 2.3.1.3.

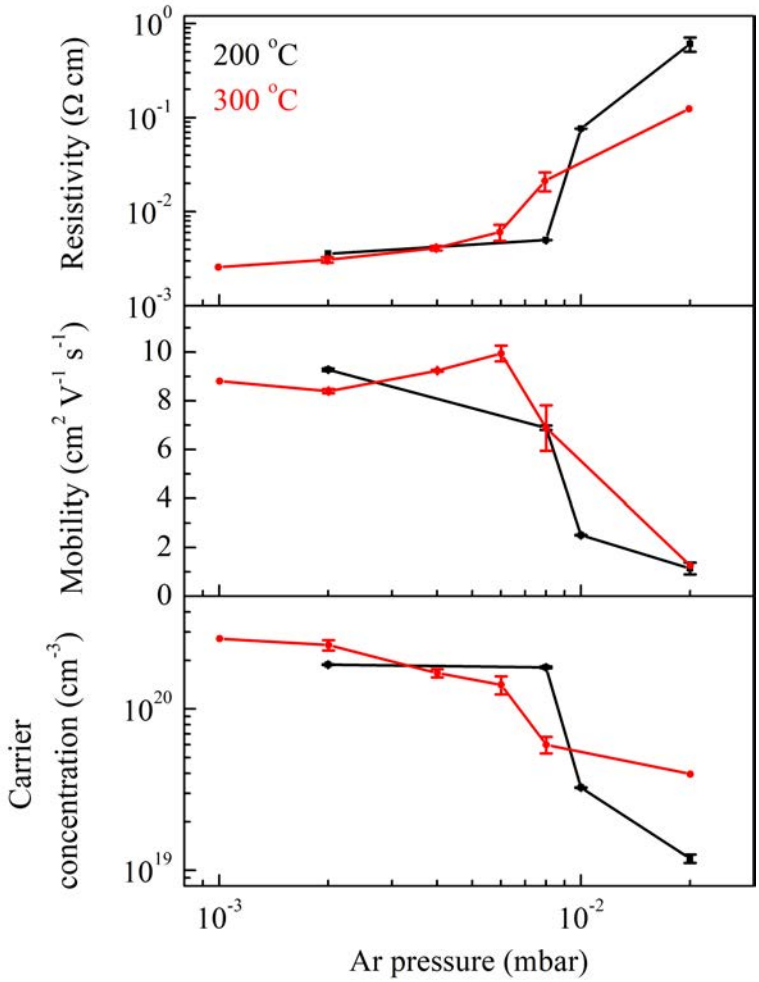
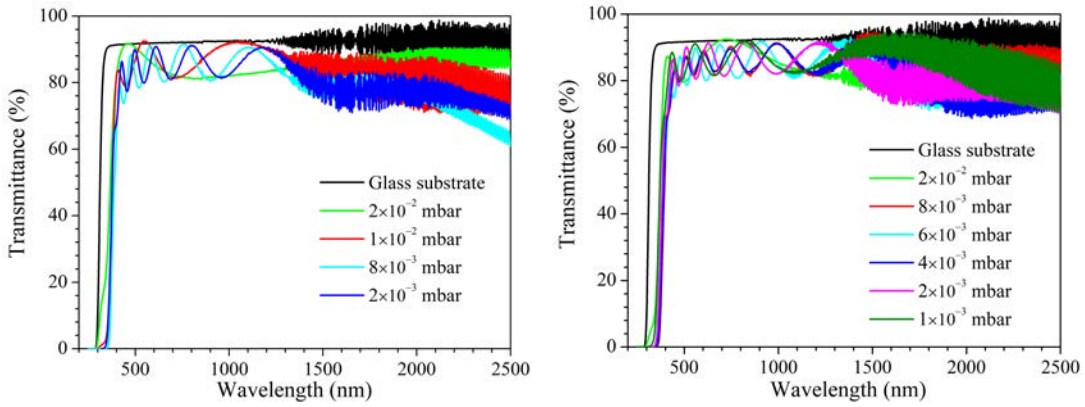


Figure 3.6: Variations of resistivity (ρ), electron mobility (μ) and carrier (electron) concentration (n) at different Ar pressures for SiZO films sputtered on glass substrates at 200 °C and 300 °C, respectively. The sputtering power here is 30 W (1.48 W/cm^2). As a result of changing the sputtering pressure and the substrate temperature, the thicknesses of the films also changed. The error bars are calculated from the measurements on multiple samples made under the same conditions.

The results show that for films made at deposition temperatures of 200 °C and 300 °C, the lower the pressure the better the conductivity. In general, most of this improvement happens at pressure above 6×10^{-3} mbar, but this does not necessarily mean that lower pressure is always better. As it will be shown below, lower sputter gas pressure leads to a lower deposition rate and thus would make it more time-consuming to make a thin film. Moreover, if the Ar pressure is too low, it can even be difficult to generate and maintain the plasma.

3.3.3 Optical property analysis

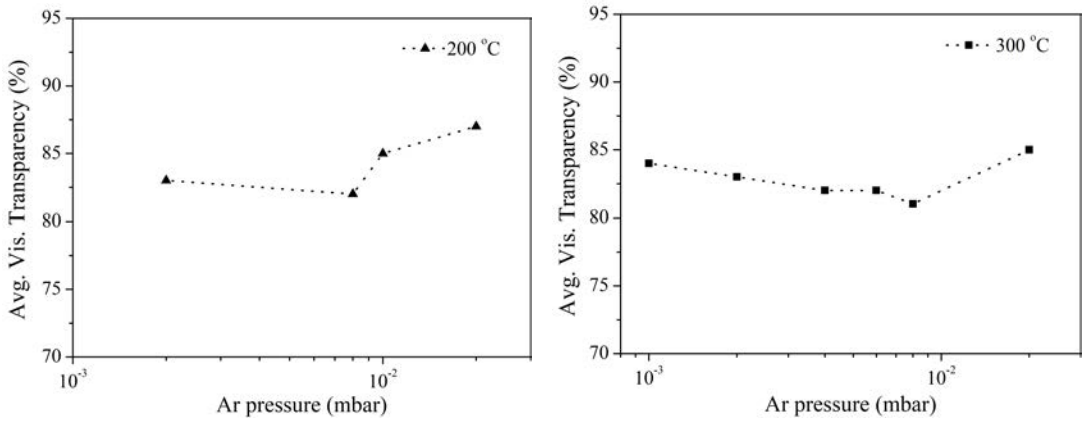
The optical transmittance spectra of the thin films shown in Figure 3.6 were measured by UV-Vis techniques. It can be seen in Figure 3.7(a) that the transmittance of the films made with Ar pressures of 8×10^{-3} mbar and 2×10^{-3} mbar both showed reduction in the wavelength region above 1300 nm, especially when the wavelength is closer to 2500 nm. This is due to plasma oscillations inside the films. As introduced in Section 2.3.2.2, the higher the carrier concentration, the smaller the plasma oscillation wavelength would be and the reflectance range would shift closer to the visible wavelength region. It has previously been seen that these two films have the highest carrier concentration among the 200 °C batch (Figure 3.6), thus they would be expected to have the strongest reflectance in the near-infrared wavelength region.



(a) 200 °C. (b) 300 °C.

Figure 3.7: Optical transmittance spectra of SiZO thin films sputtered with various Ar pressures at 200 °C and 300 °C.

Figure 3.8 shows the change of average transmittance of SiZO thin films in the visible wavelength region (390–700 nm) deposited at different Ar pressures (uncorrected for the glass substrate which has an average visible transparency of 91%). There is little fluctuation in transparency as the Ar pressure is increased. The minimum transparency of the deposited films is 83% in both graphs. The result is close to the transmittance value reported previously for SiZO films made by both



(a) 200 °C. (b) 300 °C.

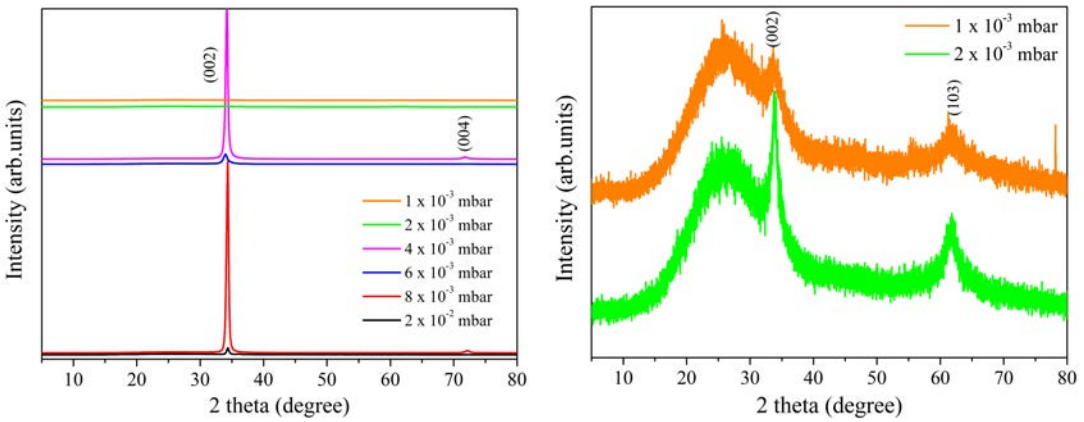
Figure 3.8: Variation of average visible transparency (uncorrected for glass substrate) of SiZO thin films sputtered at 200 °C and 300 °C by Ar pressure.

PVD and CVD methods, which is between 80% and 90% [2–4]. This high transparency of SiZO films is ideal for many opto-electronic applications of TCOs [5].

3.3.4 Structure and phase analysis

In order to understand the phase of these thin films, XRD spectra of the samples deposited at 300 °C were recorded as shown in Figure 3.9. The results show that most of the films are preferentially c-axis oriented with the only appreciable peak being the (002) wurtzite ZnO peak. The films deposited at lower pressure (1×10^{-3} mbar, 2×10^{-3} mbar) have stronger background relative to peak height, which is either due to smaller thicknesses or worse crystallinity compared to samples made at higher pressures. Besides, the spectra of the films made at low pressure (Figure 3.9(a)) also show the existence of (103) peaks in addition to the (002) texture. (103) orientations have been reported previously as well in the ZnO films deposited on glass and Si substrates [6–8].

The relationship between the Ar pressure and the thickness of deposited films has also been studied. The results show that the thickness of the film gradually increased from around 460 nm to 960 nm as the pressure increased from 1×10^{-3} mbar to 8×10^{-3} mbar, but decreased to 225 nm as the pressure continued to



(a) XRD spectra showing the preferred orientation of (002) in the films.

(b) (103) peaks of ZnO shown in the spectra of samples deposited at low pressures.

Figure 3.9: XRD spectra of SiZO thin films deposited with different Ar pressures at 300 °C.

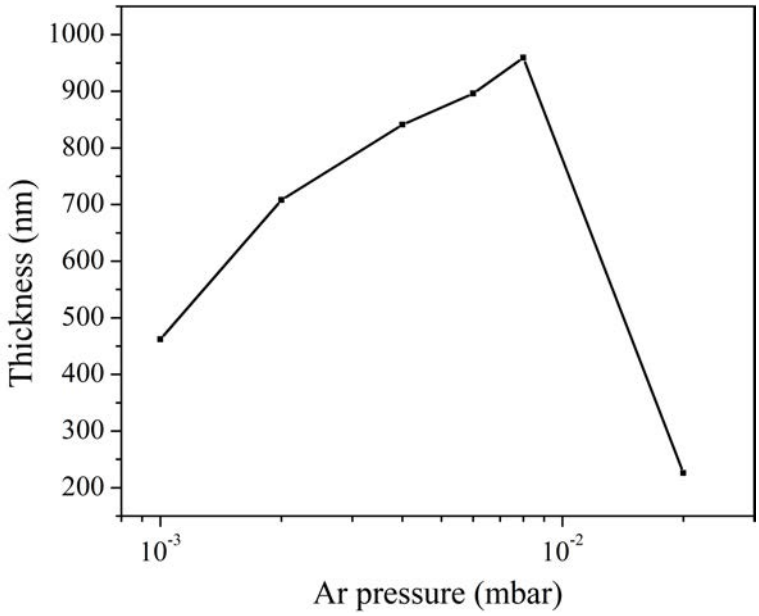


Figure 3.10: Variation of thickness of SiZO films as a function of Ar pressure (300 °C).

increase to 2×10^{-2} mbar. This is because at low pressure, not enough Ar ions were generated so the sputtering efficiency was low, but if the pressure became too high, increased collisional scattering would happen among sputtered atoms and thus reduce the deposition efficiency. Although it has mentioned earlier that lower pressure gave films with better electrical transport properties, there is a trade-off that needs to be made between the electrical performance and deposition efficiency.

Given the fact that most of the improvement of resistivity happened at pressure above 6×10^{-3} mbar, it is sensible to choose 6×10^{-3} mbar as an optimal pressure value.

3.4 Vacuum annealing and its influence on structure and performance of SiZO films

Traditionally, the main procedure in TCO research is to try different deposition parameters, attempting to obtain a film with good electrical transport properties and optical transparency, like in the previous section. Yet more and more studies show that the performance of doped ZnO thin films seems to hit a 'glass ceiling' and the traditional way of trying various processing conditions and hoping it might suddenly make a remarkable step-change in conductivity is unlikely to work anymore. In order to produce doped ZnO thin films as good as ITO, or even just better than the current performance, it is important to first understand what *intrinsic* factors are affecting the electrical and optical properties, and what are the parameters that might limit its performance. Although this is a multi-aspects problem that requires studies taken from different perspectives, the structure and chemistry of the film must play some crucial, if not determining roles in this. Thus, in this section the results and analysis obtained by using a variety of advanced microscopy techniques will be introduced to try and shed some light on these issues.

In order to carry out this kind of in-depth microstructural study, the strategy here is to focus on a smaller set of samples rather than all the films prepared. Here, the films before and after post-deposition vacuum annealing at various temperatures were studied. As mentioned in Chapter 1, vacuum annealing is an approach that has been used by researchers to improve the electrical conductivity of TCO thin films [9, 10]. Nevertheless, *how* and *why* that happened is not completely clear. The fact that the annealing happened after the deposition means it is particularly suitable for the goal of the current study, which is to investigate how processing conditions change the films intrinsically and how would that lead to the change of properties. In this

study, the films were first deposited at 200 °C for 1 hr at a RF power of 30 W (1.48 W/cm^2) and pressure of 6×10^{-3} mbar from the SiZO target onto (100)-oriented single-crystalline MgO substrates. MgO is a substrate that has been widely used for the growth of thin films due to its low cost and simple structure [11–14]. More importantly, MgO provides an ideal base for studying the elemental concentrations of the SiZO film since it does not contain any Si, compared to other commonly used substrates like borosilicate glass or silicon dioxide. After deposition the films were annealed in vacuum for another 1 hr at 400 °C and 550 °C, respectively.

As has been shown earlier, most of the films discussed in the previous section possess high visible transparency. In fact, as long as the average visible transparency of the films is over 80%, they should be good enough for most TCO-related applications [15, 16]. It is therefore of more interest of this industry to focus on the improvement of electrical performance of doped ZnO thin films. Thus the following discussion will focus on the change of electrical transport properties and the reasons behind that.

3.4.1 Electrical property analysis

The electrical transport properties of the as-deposited and annealed films are summarized in Figure 3.11. The resistivity of the film decreased from 3.6×10^{-1} Ωcm to 6.7×10^{-3} Ωcm and 3.9×10^{-3} Ωcm after being annealed at 400 °C and 550 °C, respectively. Meanwhile, the carrier concentration and mobility increased from 4.8×10^{19} cm^{-3}, 0.5 cm^{2}V^{-1}s^{-1} to 1.2×10^{20} cm^{-3}, 7.7 cm^{2}V^{-1}s^{-1} and 1.8×10^{20} cm^{-3}, 8.7 cm^{2}V^{-1}s^{-1}. The electrical properties were measured by the Van der pauw technique discussed in Section 2.3.1.3.

The results show that the annealing process greatly improved the electrical performance of the films by increasing both the carrier concentration and electron mobility. Yet, the simultaneous increase in both factors after a single process step is uncommon. According to Matthiessen's rule introduced in Chapter 1, an increase in carrier concentration will usually sacrifice part of the mobility due to increased ionized impurity scattering. Therefore, if we consider the classical model where

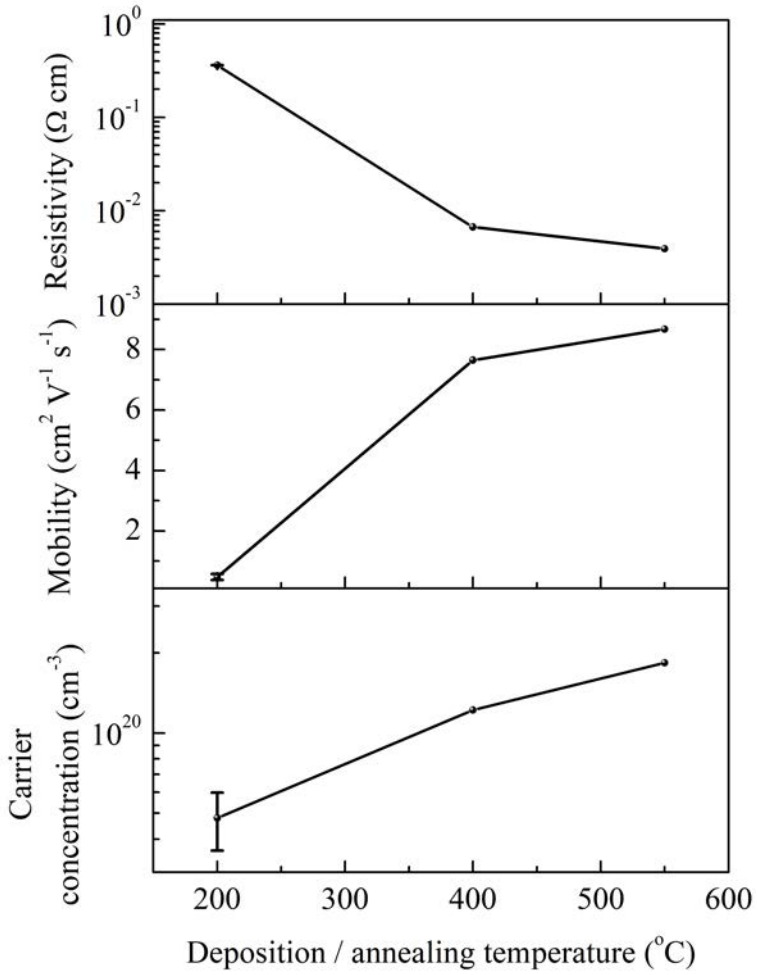


Figure 3.11: Electrical transport properties of the as-deposited film (substrate temperature: 200 °C) and the films post vacuum-annealed at 400 °C and 550 °C, respectively.

scattering is predominantly from ionized impurities, dislocations and grain boundaries, there must be a distinctive change in crystallinity and defects to compensate for the influence of increased ionized impurities. In order to confirm that, the samples were carefully examined using both structural and chemical approaches.

3.4.2 Development of Films Structure and Chemistry during Annealing

3.4.2.1 Surface morphology of the films

The as-deposited films show relatively uniform surfaces under electron microscopy study. In Figure 3.12(a), the SEM image shows that there are crystals with white contrast distributed on the surface, but these bumps did not show much detectable difference in terms of their composition in neither the EDS point/local studies nor the EDS maps (Figure 3.13). In fact, the phase uniformity could be seen if one compares the secondary-electron (SE) image with the back-scattered electron (BSE) image. The bright features do not appear in the BSE image, thus they could be just topographical contrast produced during film growth.

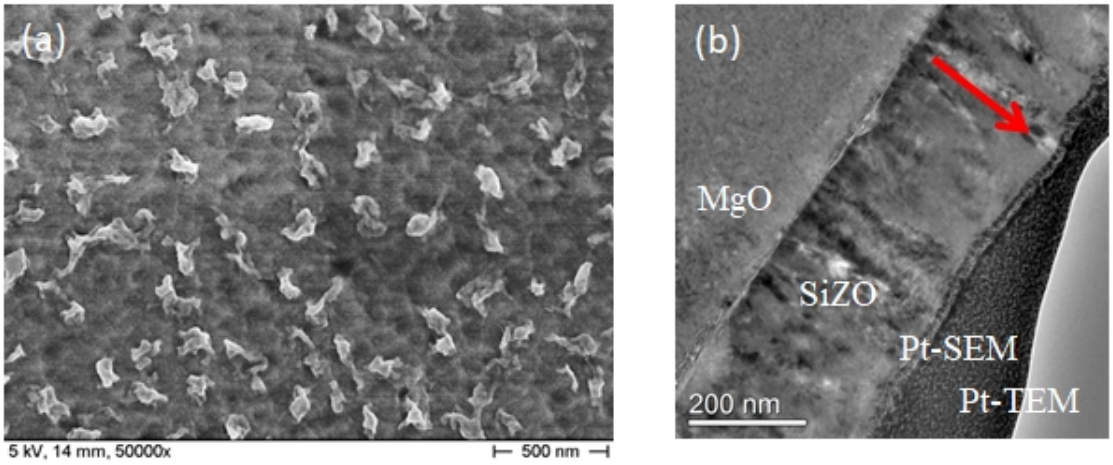


Figure 3.12: (a) SEM micrograph of the surface of an as-deposited film (substrate temperature: 200 °C), (b) cross-sectional TEM bright field micrograph from a sample made by FIB. The red arrow represents the growth direction of the film.

In Figure 3.12(b), four layers can be seen in the cross-sectional TEM image of the as-deposited sample. One is the Pt layer used in FIB to protect the thin film, and one is the Pt layer coated before the high-resolution SEM study to avoid charging, the other two include the SiZO thin film layer and the MgO substrate layer. The TEM image shows the high uniformity of the sputtered film in this area. The bright and dark contrast in the bright field TEM image of the SiZO layer is mostly diffraction contrast due to the different orientations of grains.

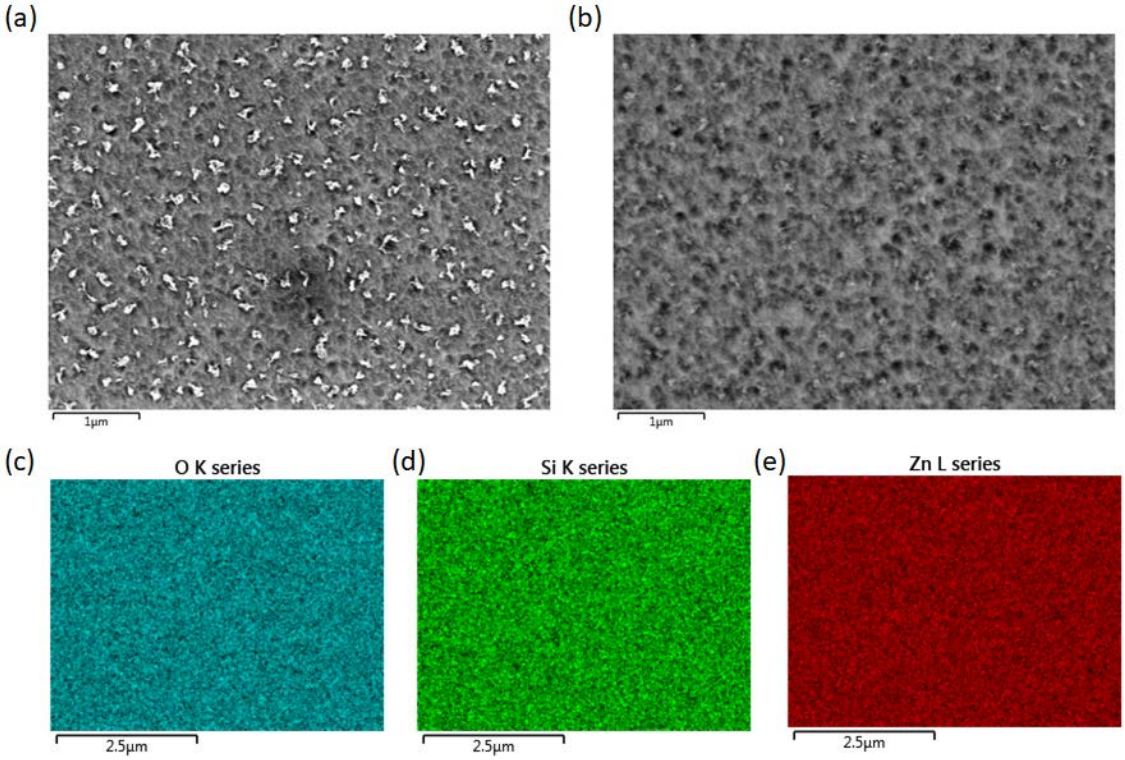


Figure 3.13: (a) SE, (b) BSE micrographs and EDS maps (c-e) of the as-deposited film (substrate temperature: 200 °C).

Similar techniques were applied to study the surface morphology of the film annealed at 400 °C. The SEM image (Figure 3.14(a)) shows that the density of the particles with white contrast on the film's surface decreased compared to the 200 °C sample, which could be a result of surface diffusion of atoms at 400 °C. The TEM micrograph of the sample shows the highly uniform surface of the film after annealing. Similar to that of the 200 °C specimen, the TEM image shows four layers, including the Pt layer for TEM sample, Pt layer for SEM imaging, SiZO thin film layer and the MgO single crystal substrate.

For the sample annealed at 550 °C, it can be seen in the SEM micrograph (Figure 3.15(a)) that the density of the particles, with white contrast on the film surface, is smaller than that of the 400 °C annealed sample. This could be due to the fact that the diffusion rates of atoms are generally higher at greater temperature, which leads to a better incorporation of the film and the particles at 550 °C than that at 400 °C, thus fewer visible SiZO particles on top of the film. In fact, very few particles with

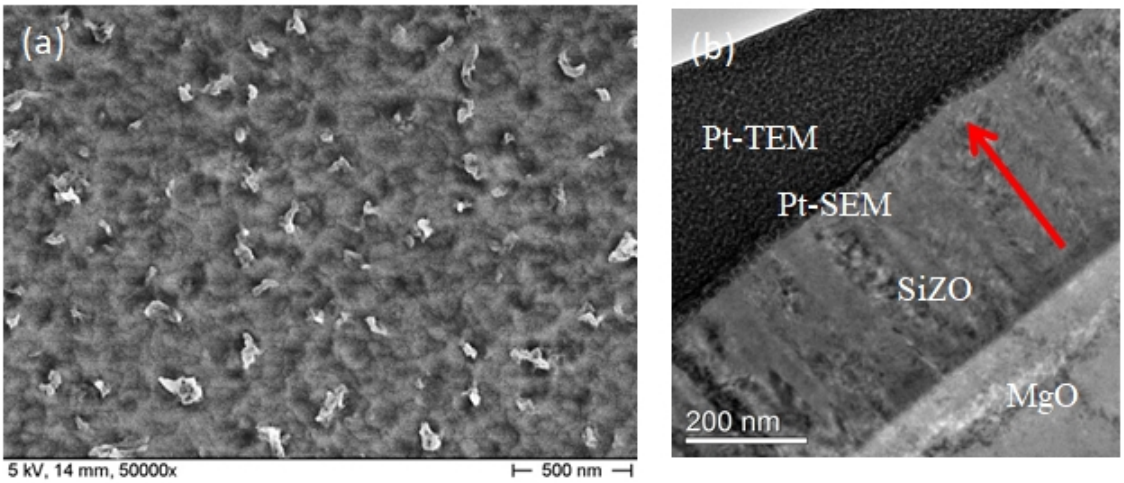


Figure 3.14: (a) SEM micrograph of the surface of film annealed at 400 °C, (b) cross-sectional TEM micrograph from a sample made by FIB. The red arrow represents the growth direction of the film.

white contrast could be seen in Figure 3.15(a). The TEM image of the film shows the highly uniform surface of the annealed film Figure 3.15(b).

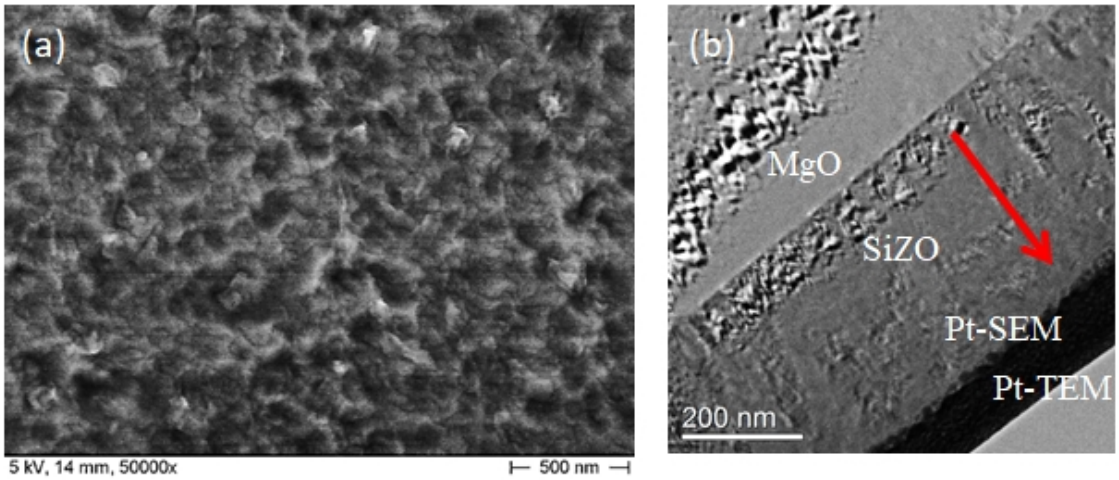


Figure 3.15: (a) SEM micrograph of the surface of film annealed at 550 °C, (b) cross-sectional TEM micrograph from a sample made by FIB. The red arrow represents the growth direction of the film.

3.4.2.2 Phase of the films

XRD was carried out to study the phases in the thin films. The results are shown in Figure 3.16. For the as-deposited film, the XRD result shows only the (002) peak of

the hexagonal wurtzite ZnO phase, suggesting that the film is c-axis oriented. The results of the 400 °C and 550 °C samples show that the films also possess strong c-axis (002) orientation after annealing, yet, with much higher (002) peaks than that of the as-deposited film. A reason for the stronger (002) peaks and comparatively smaller backgrounds could be the improvement of the film crystallinity, i.e. a sharper distribution of the lattice orientations, which will be shown by the omega-XRD measurement.

According to the XRD results, the (002) peaks of the as-deposited film and the films annealed at 400 °C and 550 °C are at 2θ degrees of 34.2°, 34.2° and 34.3°, calibrated using the MgO substrate peak for each sample. The crystallite size can be calculated using the Scherrer equation (shape factor: 0.9) introduced earlier. The calculated crystallite sizes for the as-deposited samples and the 400 °C and 550 °C annealed samples are 83 nm, 93 nm and 82 nm, respectively, showing a relatively small variation.

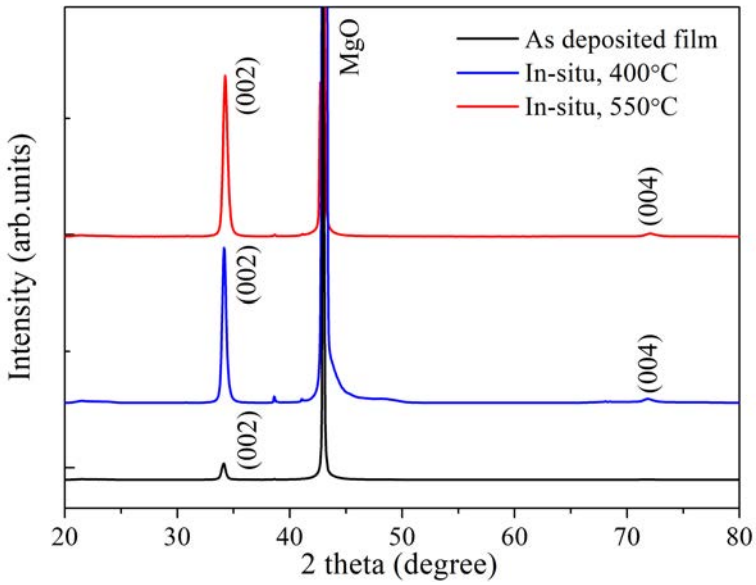


Figure 3.16: XRD spectra of the as-deposited film and the annealed samples.

3.4.2.3 In-plane textures of the films

In order to have a better understanding of the crystallinities of the films, transmission Kikuchi diffraction (TKD) analyses were performed on the films. The results are

shown in Figures 3.17, 3.18 and 3.19 for the as-deposited film, the films annealed at 400 °C and 550 °C, respectively. The pole figures generated automatically from the TKD data, showing the texture of each film, are shown in Figures 3.20 (as-deposited film), 3.21 (400 °C sample) and 3.22 (550 °C sample).

Here, the ZnO phase that the software used to match the TKD data is the one with hexagonal wurtzite structure, which has been introduced before as the most thermodynamically stable ZnO phase under ambient conditions and the most commonly-seen one. Inverse pole figure maps (IPF) in both the x and the y directions show the polycrystallinity of all of the studied films and the columnar structures of the grains. The columnar growth observed in these films is consistent with the results reported by other researchers on ZnO films [17–19]. It can be seen that, for all the as-deposited and annealed films, the IPFY maps have an almost single colour (red) across the films and that the {001} pole figures have only one peak in the centre, which confirms (002) as the preferred growth orientation for most grains in the y direction.

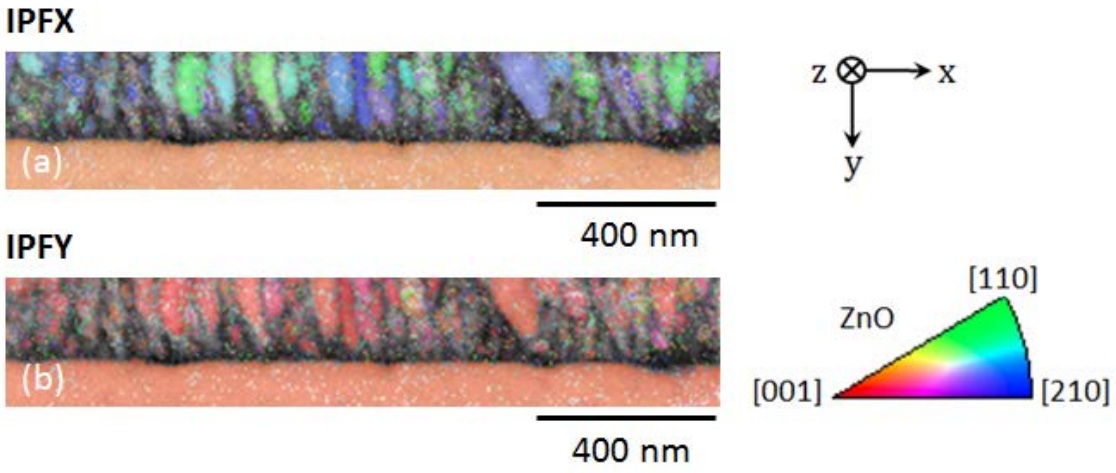


Figure 3.17: TKD pattern of the cross sectional sample of the as-deposited film, including legend identifying the axes. (a) TKD inverse pole figure (IPF) map in the x direction, (b) TKD inverse pole figure (IPF) map in the y direction. The colour map of the coordinate system in this case is also shown.

In contrast, the IPFX maps show different crystallographic orientations of grains in the x direction. For the as-deposited film, the {100} and {110} pole figures in

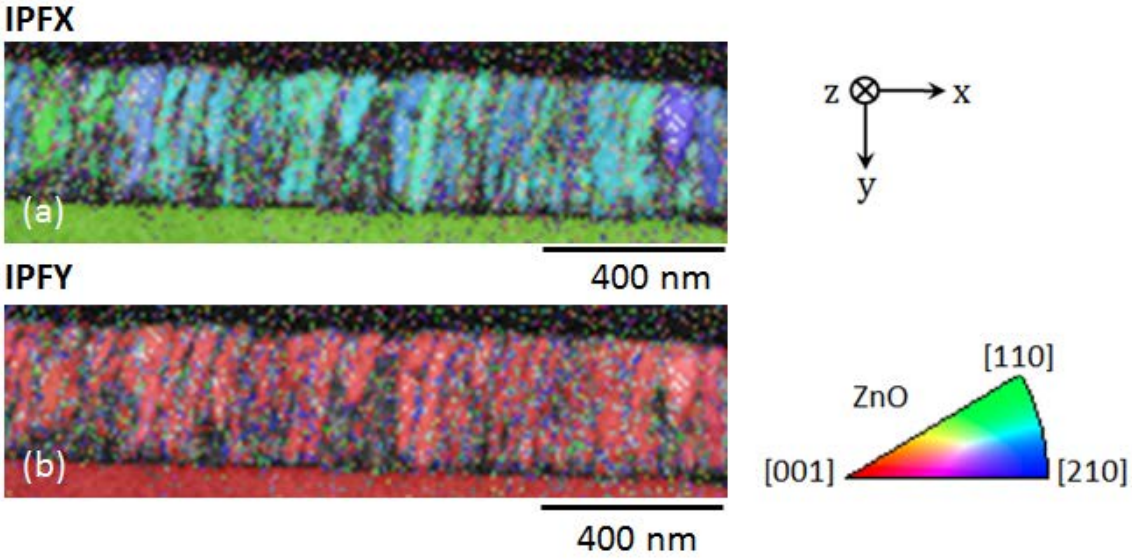


Figure 3.18: TKD pattern of the cross sectional sample of the film annealed at 400 °C, including legend showing the axes. (a) TKD inverse pole figure (IPF) map in the x direction, (b) TKD inverse pole figure (IPF) map in the y direction. The colour map of the coordinate system in this case is also shown in the figure.

Figure 3.20 demonstrate its mosaic in-plane film texture. Compared to the mosaic in-plane alignment of the as-deposited sample (Figure 3.20), the {100} and {110} pole figures of the annealed films (Figure 3.21, 3.22) show that the film developed preferred in-plane orientations after heat treatment. The bar charts of the distribution of grain boundary angles in Figure 3.23 and Figure 3.24 affirm that the distribution of grain boundary angles is centralized around 30°. Since the structure of wurtzite ZnO is hexagonal with six-fold symmetry ($P6_3mc$), it can be deduced that there are two preferred in-plane orientations in the annealed sample. By comparing the pole figures of ZnO and the pole figures of the MgO substrate (Figure 3.21) along different orientations, the preferred orientations between film and substrate can be worked out as $(110)_{\mathrm{ZnO}} \parallel (110)_{\mathrm{MgO}}$ and $(100)_{\mathrm{ZnO}} \parallel (110)_{\mathrm{MgO}}$, as shown in Figure 3.25. For the sample annealed at 550 °C, texture XRD (phi-scan) of the wurtzite ZnO (104) peak was carried out over an area of the sample bigger than the TEM lamella. The result further confirms the 30° misalignment between grains (Figure 3.26) in the annealed films.

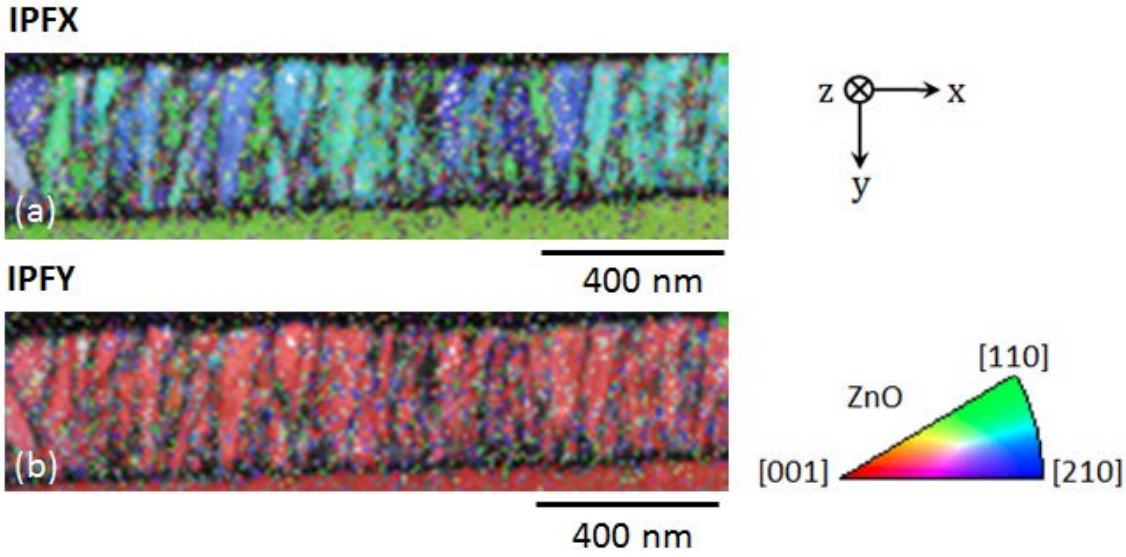


Figure 3.19: TKD pattern of the cross sectional sample of the film annealed at 550 °C, including legend showing the axes. (a) TKD inverse pole figure (IPF) map in the x direction, (b) TKD inverse pole figure (IPF) map in the y direction. The colour map of the coordinate system in this case is also shown in the figure.

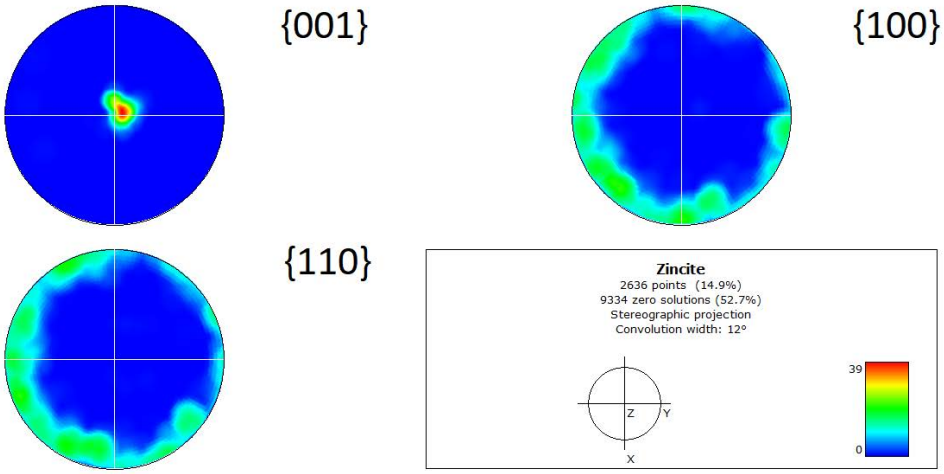


Figure 3.20: Pole figures of the as-deposited doped ZnO film for different diffracting planes ({001}, {100} and {110}) calculated from the TKD data in Figure 3.17.

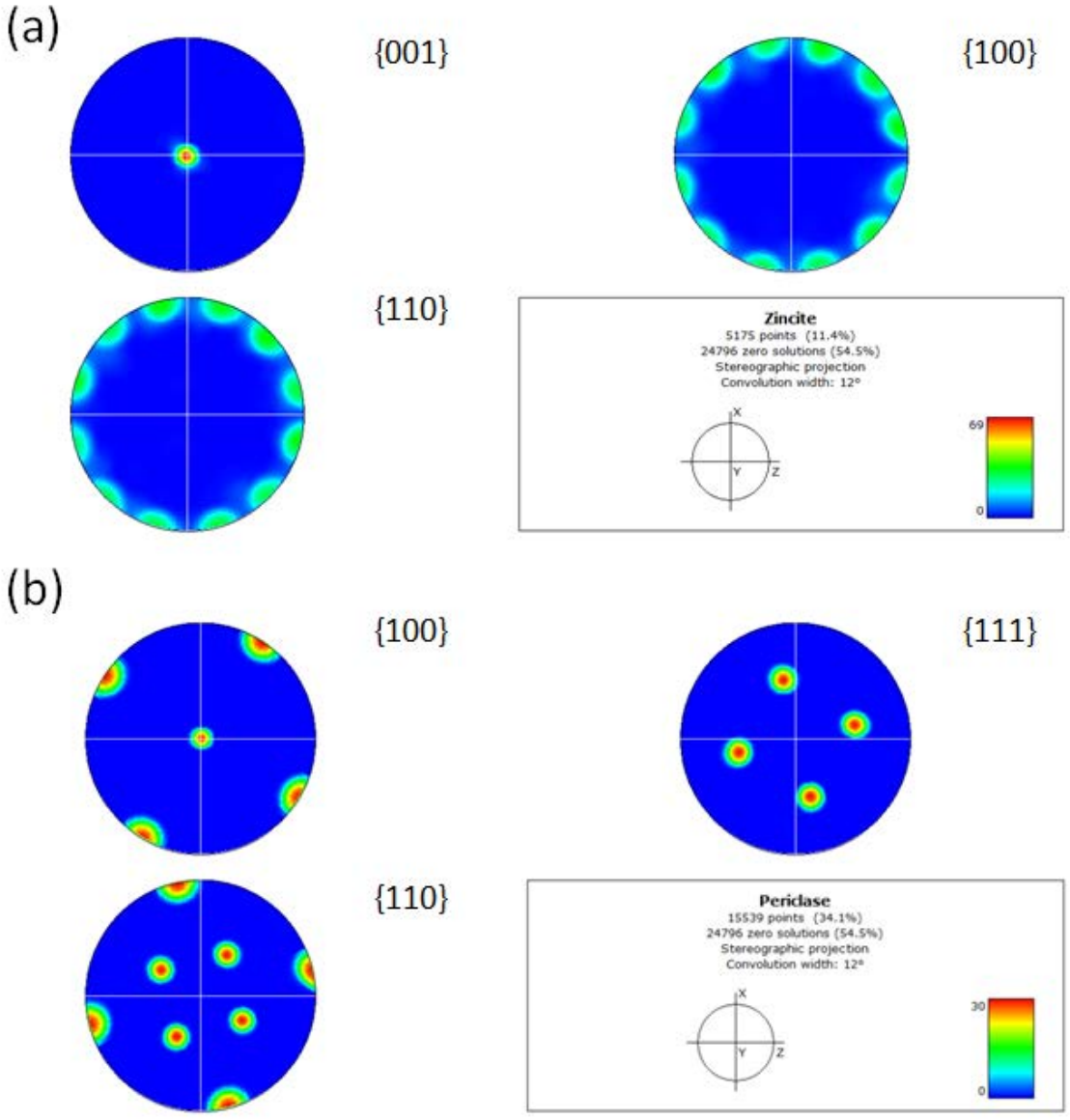


Figure 3.21: (a) Pole figures of the SiZO film annealed at 400 °C for different diffracting planes ({001}, {100} and {110}) calculated from the TKD data. (b) Pole figures of the MgO substrate for different diffracting planes ({100}, {110} and {111}) calculated from the TKD data.

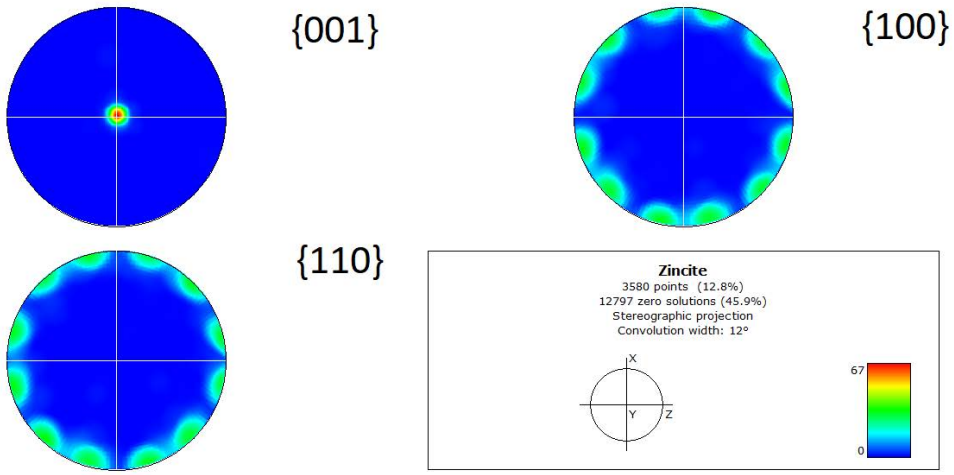


Figure 3.22: Pole figures of the SiZO film annealed at 550 °C for different diffracting planes ({001}, {100} and {110}) calculated from the TKD data.

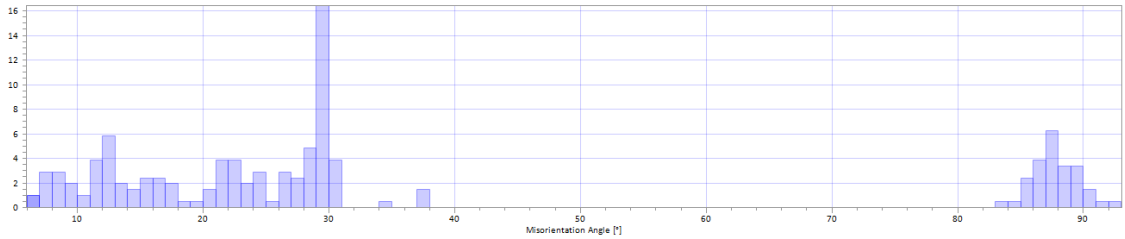


Figure 3.23: Distribution of grain boundary angles across the film annealed at 400 °C calculated from the TKD data.

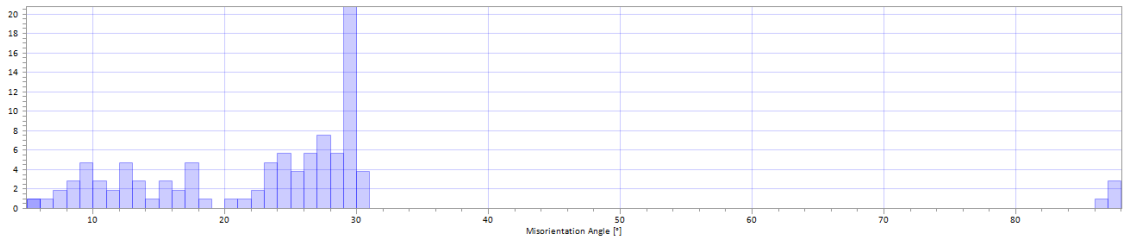


Figure 3.24: Distribution of grain boundary angles across the film annealed at 550 °C calculated from the TKD data.

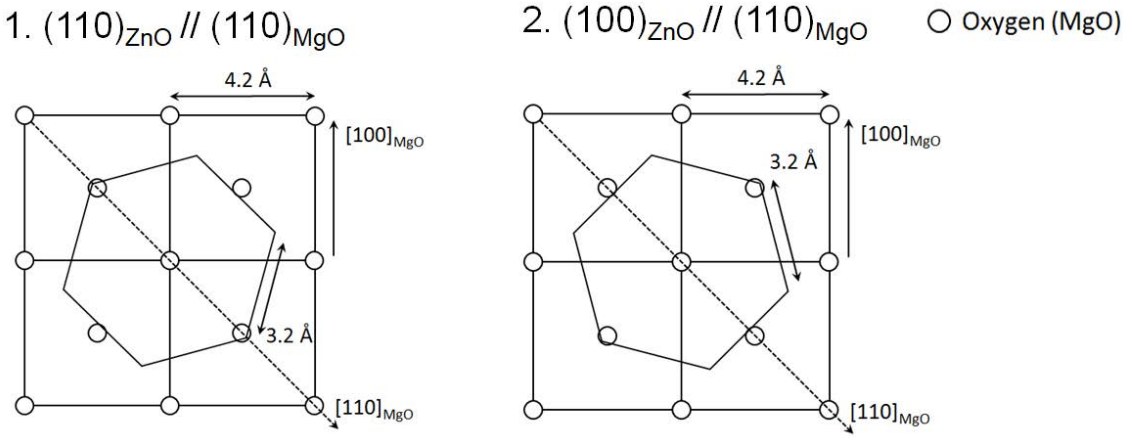


Figure 3.25: Schematic representation of the interface between MgO substrate and annealed ZnO film with two preferred in-plane relationships: $(110)_{\mathrm{ZnO}} \parallel (110)_{\mathrm{MgO}}$ and $(100)_{\mathrm{ZnO}} \parallel (110)_{\mathrm{MgO}}$.

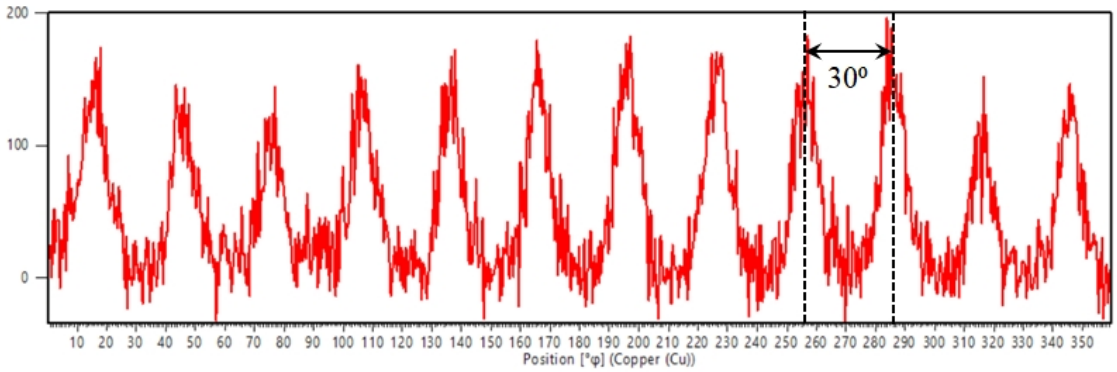


Figure 3.26: Texture XRD (phi-scan) measurement of wurtzite ZnO (104) peak of sample annealed at 550 °C.

3.4.2.4 Out-of-plane texture of the films

In order to determine the uniformity of c-axis orientation across the film, texture XRD has been performed for the measurements of rocking curves. More details of the method can be found in Section 2.4.1.4. The full width at half maximum (FWHM) of the curve represents the average out-of-plane alignment over a large number of grains. The rocking curve of the as-deposited sample is shown in Figure 3.27, with a FWHM value of 9°. For the film annealed at 400 °C, the omega scan gave a narrower rocking curve (Figure 3.28) than that of the as-deposited one, with FWHM value of 5°, suggesting an improved out-of-plane alignment of the ZnO grains after annealing. For the film annealed at 550 °C, the FWHM of the rocking curve futher reduced to 3° (Figure 3.29), showing that the film has a better out-of-plane alignment than both the as-deposited sample and the one annealed at 400 °C. According to the model developed by Ayers [20], the broadening of the rocking curve is positively correlated to the density of threading dislocations when assuming there is little influence from the specimen curvature and the instrument. Thus, the smaller FWHMs of the rocking curves of the annealed thin films could suggest lower densities of threading dislocations than that of the as-grown sample.

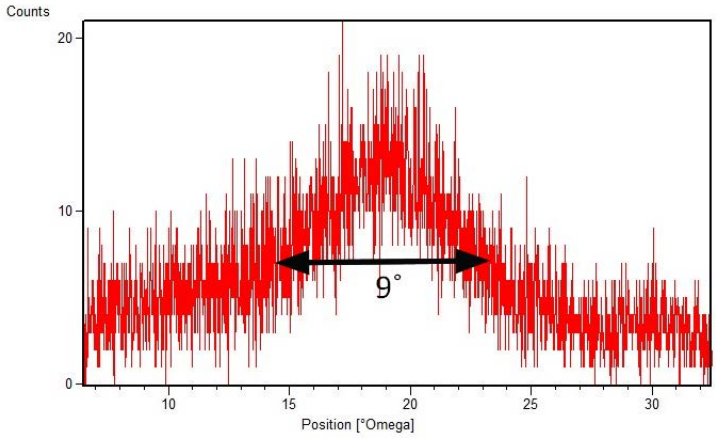


Figure 3.27: Rocking curve of the (002) peak of the as-deposited sample.

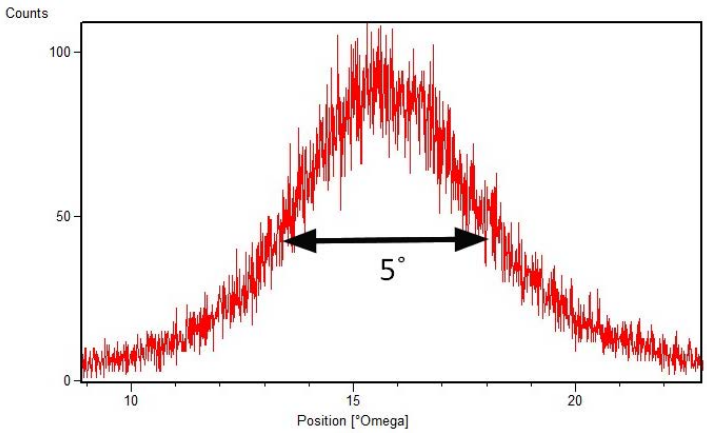


Figure 3.28: Rocking curve of the (002) peak of the sample annealed at 400 °C.

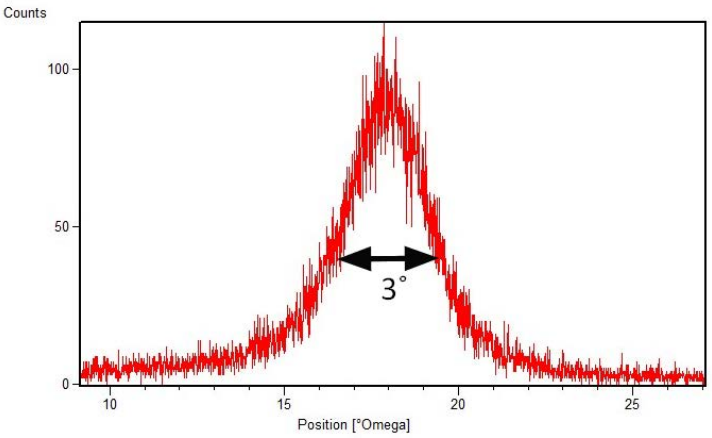


Figure 3.29: Rocking curve of the (002) peak of the sample annealed at 550 °C.

3.4.2.5 Chemical composition of the films

The elemental distributions inside the film were studied by EDS. The results of the chemical analysis are shown in Figure 3.30, 3.31 and 3.32. The overall Si concentration (Si/(Si+Zn)) obtained from EDS in SEM is 5.6% in the as-deposited sample. The value has been double checked by the cross sectional EDS in the TEM which gave an almost identical value of 5.7%. The Si concentration of the film annealed at 400 °C and 550 °C are 5.5% and 5.7% respectively which showed very little difference compared to the as-grown sample. However, this value is higher than the Si concentration in the target, suggesting the preferred depositions of Si over Zn, which are probably due to the higher sputter rate of SiO_2 than that of ZnO [21]. This value is also well above

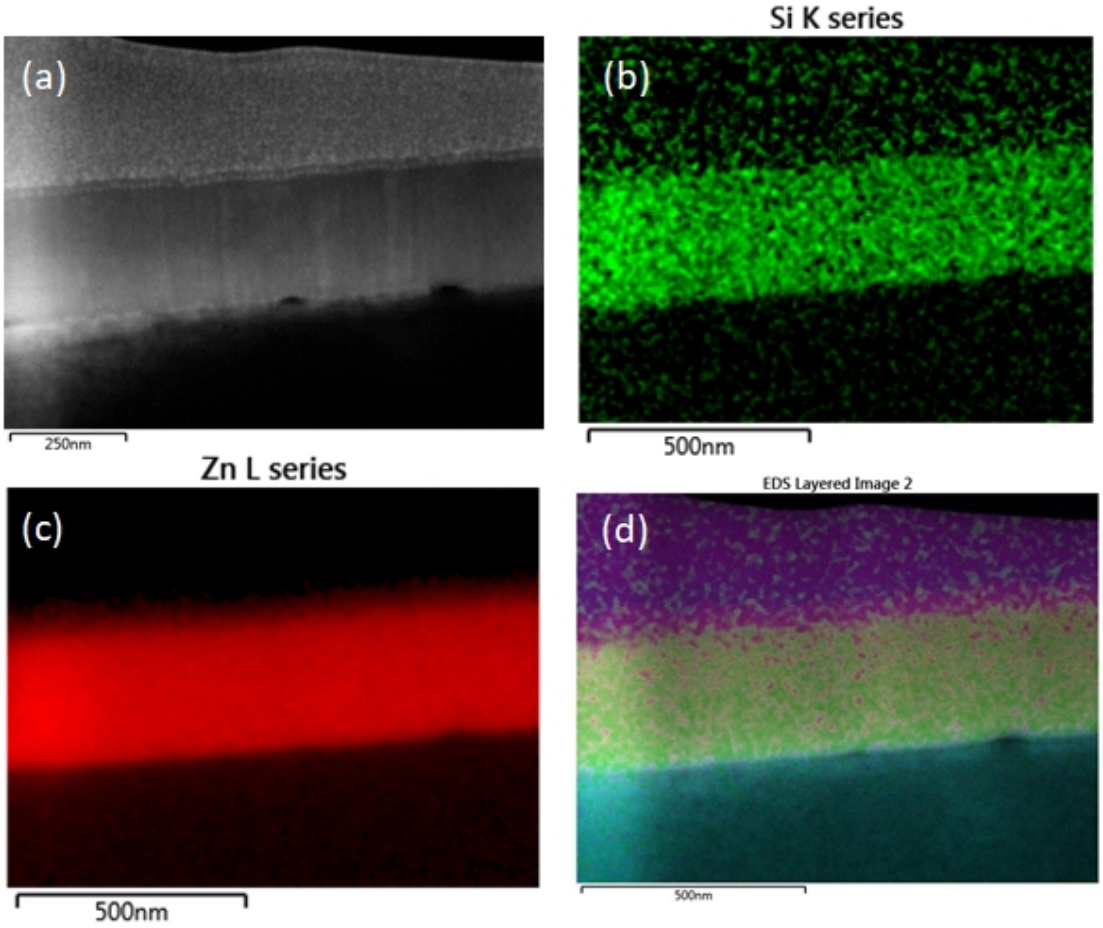


Figure 3.30: (a) STEM micrograph of the as-deposited thin film; (b) Si and (c) Zn map obtained from EDS in STEM; (d) EDS layered image in which three separate layers can be seen from top to bottom: Pt protection layer (purple), SiZO thin film (green) and MgO substrate layer (blue).

the saturation level of Si shown in the SiO_2-ZnO equilibrium phase diagram (Figure 1.15 in Section 1.5.2), but no Si segregation could be observed in the EDS maps in all of the studied films, which suggests that the solubility of Si in the thin film might be greater than that in the bulk system.

For the annealed films one could see some dark circular features in the STEM images. EDS mapping was carried out around one of the features (Figure 3.31) in the sample annealed at 400 °C. The result shows no distinct elemental precipitation/second phase. More careful analysis based on the TEM and EDS results will be shown in Section 3.4.2.6, in order to study what these features are

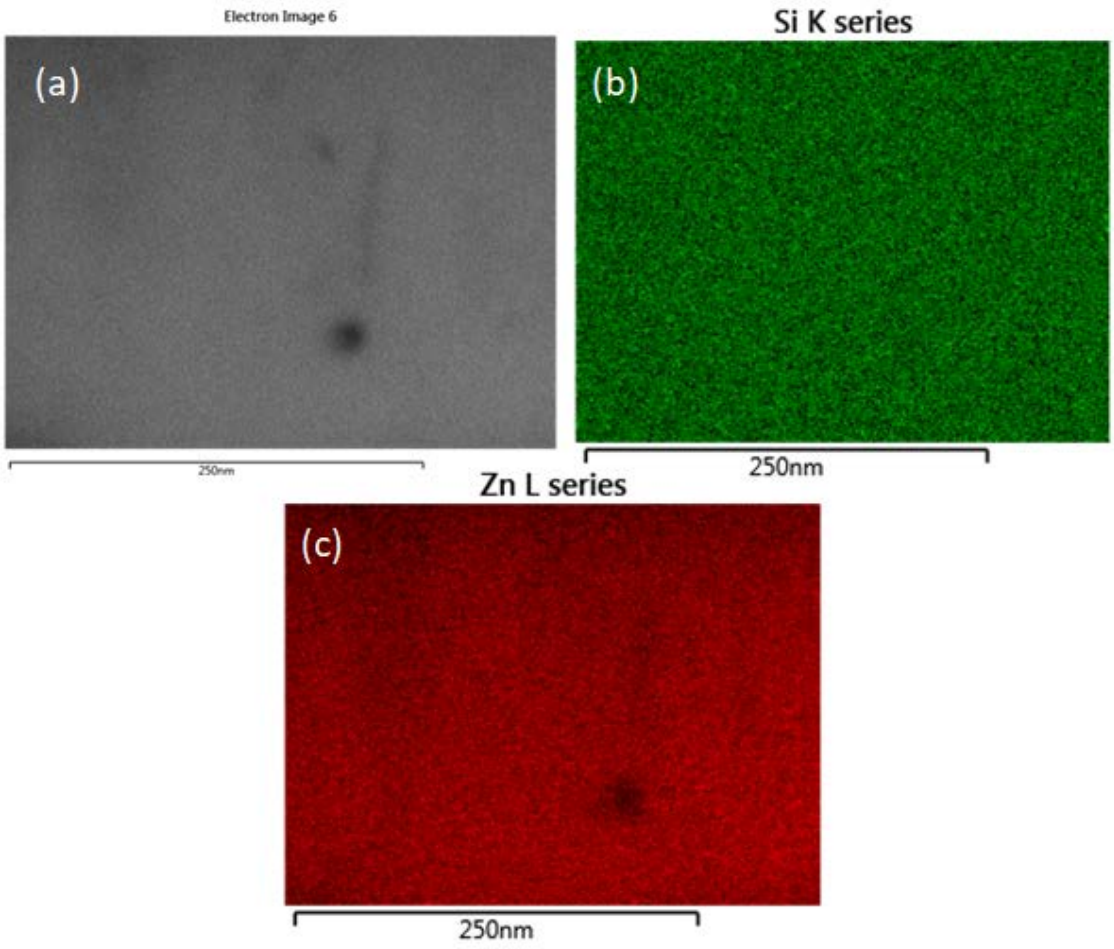


Figure 3.31: (a) STEM micrograph of the area around the circular feature in the 400 °C annealed sample; (b) Si map and (c) Zn map obtained from EDS in STEM. The result shows that there is no Si precipitation around the circular feature.

and the mechanism of their formation.

The EDS mapping of the sample annealed at 550 °C is shown in Figure 3.32. Again, no Si or Zn precipitation could be observed. It can be seen that the Pt protection layer on the top also contain Si. This is because at the time of the experiments, the Pt source in the FIB instrument was contaminated by Si. The amount of Si measured in the Pt layer is around 3%. Another possible reason for the observation of Si in Pt is that during the FIB thinning process, the sample was milled with high-energy ions which could generate local sputtering. Some of the SiZO films could be sputtered onto the Pt layer and thus be detected in EDS. However, no Zn peak could be detected in the Pt layer, making this unlikely to be

the reason.

When looking at Matthiessen's rule, the observation that there is no precipitation in any of these films means that the term for scattering by precipitates can be excluded in this case. In terms of other factors that influenced the carrier mobility, better out-of-plane and in-plane texture could be the two major reasons for the increase of electron mobility, which will be further discussed later.

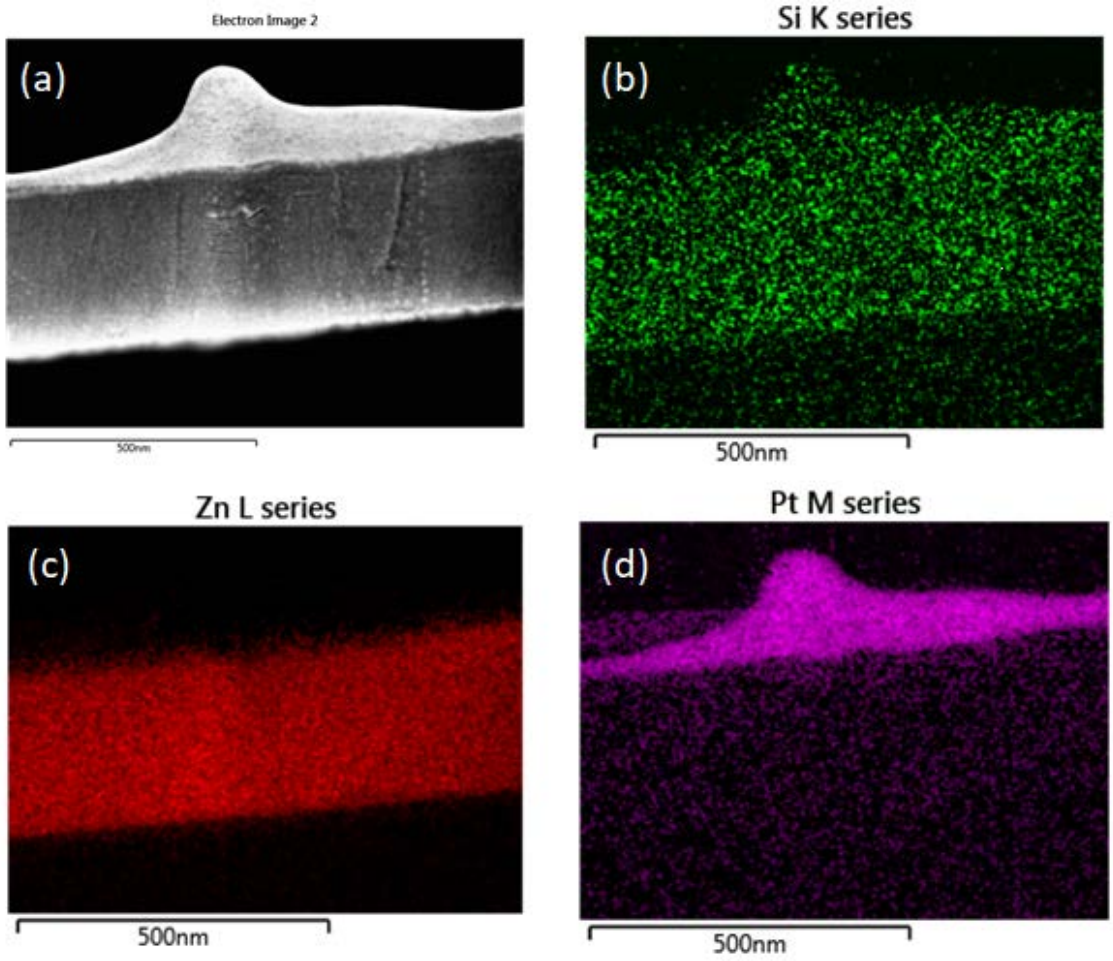
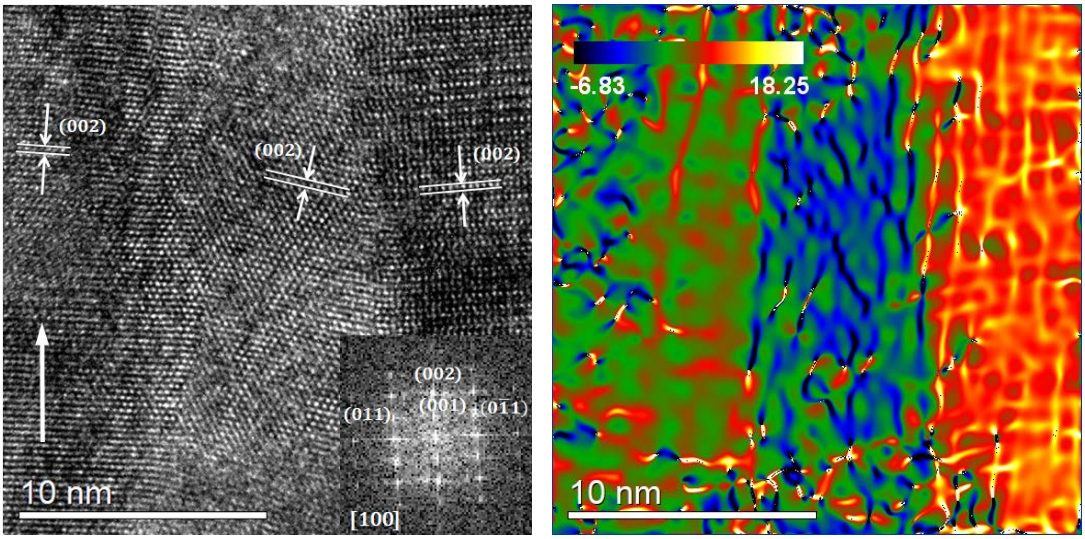


Figure 3.32: (a) STEM micrograph of the thin film annealed at 550 °C; (b) Si map (c) Zn map and (d) Pt map obtained from EDS in STEM. Layers in the STEM image are Pt protection layer (white contrast), SiZO thin film and MgO substrate layer (black contrast) from top to bottom, respectively.

3.4.2.6 Lattice structure of the films and formation of nano-pores



(a) HRTEM image of the grains.

(b) Map of ω_{xy} of the rotation matrix.

(c) Map of rotation angle.

Figure 3.33: Geometric phase analysis based on the HRTEM image of the as-deposited SiZO film (200 °C). Subfigure (a) is an HRTEM image of the grains recorded along a $<$ 100 $>$ zone axis of wurtzite ZnO film. The white arrow at the bottom left represents the growth direction of the film. The power spectrum (bottom right) of the grain on the right hand side is shown as an example, which shows characteristic reflections from (002) and (011) plane of wurtzite ZnO. The (002) plane in each grain is highlighted by arrows. Subfigure (b), generated by the GPA program, is the map of ω_{xy} of the rotation matrix, of which the magnitude is positively correlated to the rotation angle. Subfigure (c) is the map of rotation angle.

In order to further understand the micro-structure of the films, TEM were used to study the samples. High-resolution TEM (HRTEM) imaging (Figure 3.33(a)) of the as-deposited film again confirms its poly-crystallinity. A Geometric Phase Analysis (GPA) program compatible with Digital Micrograph was used to visualize the degree of rotation around the grain boundaries. Details of this method can be found in Section 2.4.3.3. One of the advantages of GPA is that it could isolate the different components of local distortion (horizontal, vertical, dilatation, shear and rotation) and carry out mapping on the individual one [22, 23]. The mapping of the local rigid rotation (ω_{xy}) and the mapping of rotation angle are shown in Figure 3.33(b). Here, the grain in the middle is used as the reference lattice. It can be seen that the grain on the right hand side has greater rotation compared to the one on the left hand side. The average rotation angle of the left grain is 10° while that of the right grain is 15°. The positive values mean that the rotation directions of both grains are anti-clockwise versus the reference grain. These misalignment values are consistent with the ones measured manually in the DigitalMicrograph ® software across the two grain boundaries (left-middle, middle-right).

These results show that the grains in the film are not strictly parallel to each other, which is consistent with what the omega-XRD result suggests. In fact, by indexing the HRTEM image, it could be found that the plane normal of the (002) plane has different degrees of rotation in different grains versus the growth direction of the film (Figure 3.33(a)).

However, HRTEM and high-angle annular dark-field (HAADF) imaging show some different features around the grain boundaries in the annealed samples. Figure 3.34 is an HRTEM image of the film annealed at 550 °C, showing the lattice arrangement at the two sides of the grain boundaries with an elliptical-shaped nano-defect in the middle. The size of it, as it can be seen, is about 5 nm in length (direction along the grain boundary) and 2 nm in width. At lower magnification, one can see lines of nano-circles along the grain boundaries with individual size of less than 10 nm (Figure 3.35). The growth patterns of these features can be seen more clearly in a HAADF map across a larger area, as shown in Figure 3.36. In

order to tell whether these are second phase/precipitation or voids, Fresnel imaging was applied to examine all the as-deposited and annealed samples. In Figure 3.37, it can be seen that in both of the annealed samples (400 °C and 550 °C) the contrast of the nano-features changed from white to black as the focus condition changed from underfocus to overfocus. This affirms that the black features in the HAADF and ADF images are nano-pores rather than a second phase. In contrast, similar features could not be observed in the as-deposited sample (Figure 3.30(a), Figure 3.37), suggesting that there are no nano-voids formed during deposition, or at least they must be of a size below the resolution limit of the Fresnel imaging technique.

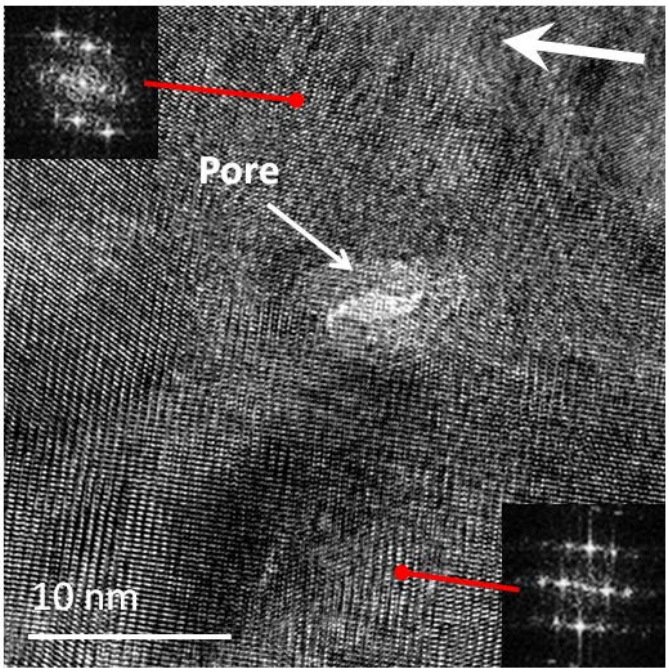


Figure 3.34: HRTEM image of grains around nanopore in the sample annealed at 550 °C. The white arrow shows the growth direction of the film.

Figure 3.38 shows a schematic of a sensible arrangement of nano-voids on the grain boundary plane. Because TEM imaging is the two-dimensional projection of a three dimensional sample, the actual positions of the apparently linked-up pores can have variations in height (direction along the electron beam) as demonstrated in the image.

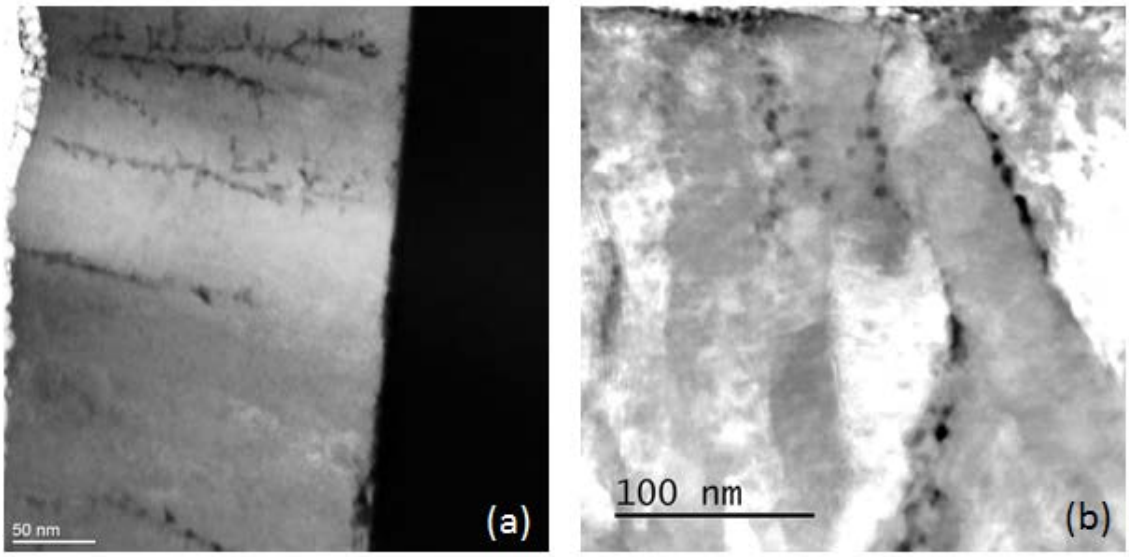


Figure 3.35: (a) STEM/HAADF micrograph of the 550 °C annealed sample at higher magnification and (b) annular dark-field (ADF) micrograph of the 550 °C annealed thin film.

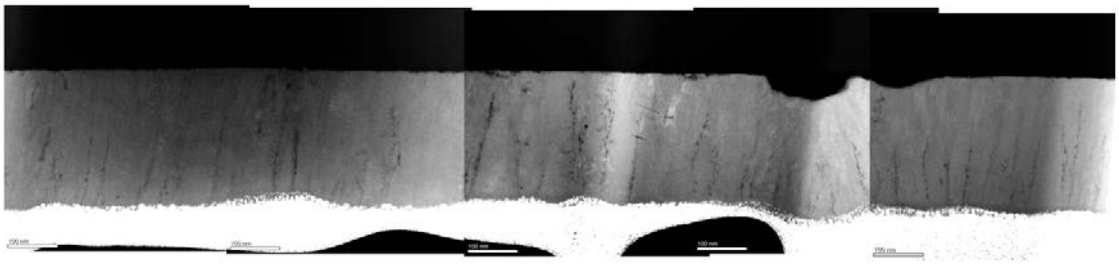


Figure 3.36: STEM/HAADF map of SiZO film annealed at 550 °C. Layers from top to bottom are MgO substrate (black constrast), SiZO thin film and Pt layer (white contrast), respectively. Scale bar: 100 nm.

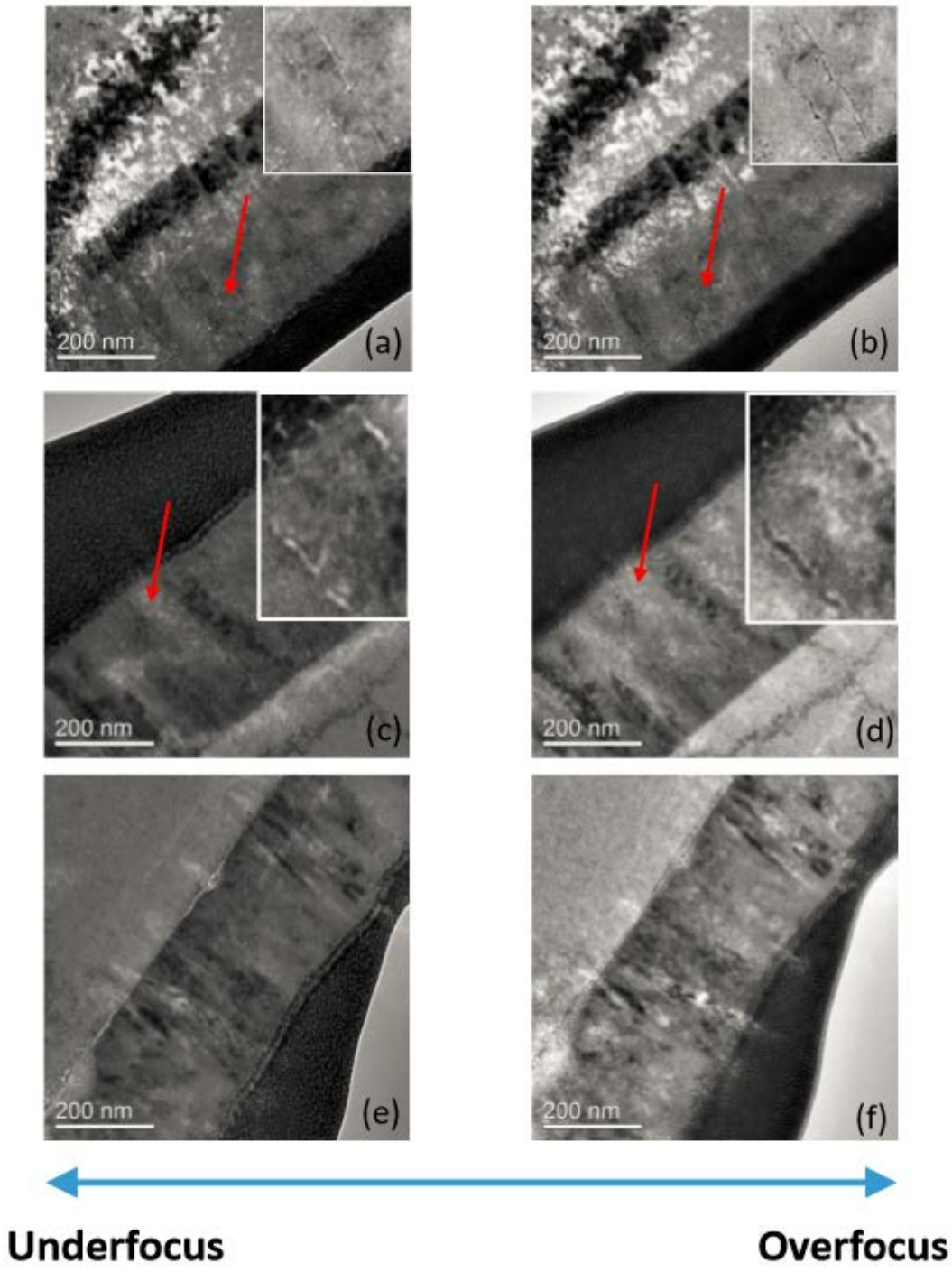


Figure 3.37: (a), (c) and (e) are underfocused TEM micrographs of the 550 °C annealed sample, the 400 °C annealed sample and the as-deposited sample respectively, in which the nano-voids show white contrast. (b), (d) and (f) are overfocused TEM micrographs of the 550 °C annealed sample, the 400 °C annealed sample and the as-deposited sample respectively, in which the nano-voids show black contrast. The red arrows point at the regions of detected nano-pores inside the film.

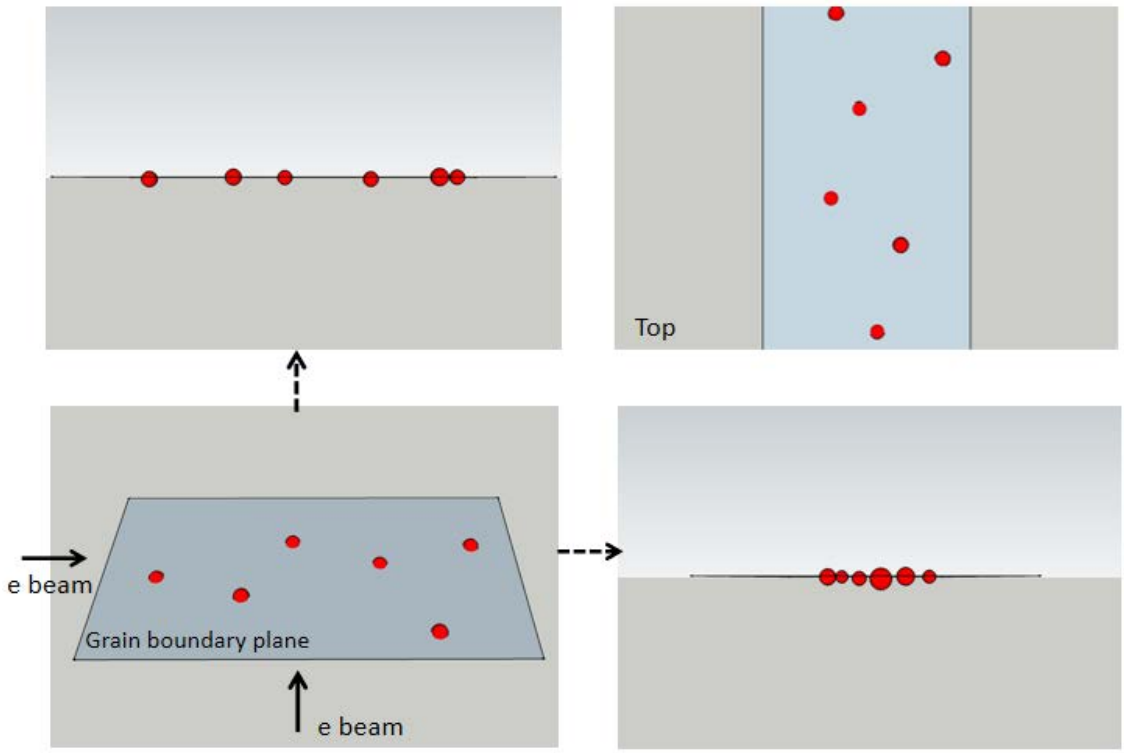


Figure 3.38: Schematic illustrations of a possible arrangement of nano-pores on the grain boundary plane in different perspectives. The red spheres represent the pores.

3.5 Discussion

Compared to other techniques that have been used for preparing Si doped ZnO thin film such as spray pyrolysis [24], sputtering was able to generate highly uniform thin films. All the films discussed above show n-type electrical conduction according to the Hall measurement. For the films deposited on glass, the lowest resisitivity reported here is 2.6×10^{-3} Ωcm. For the films deposited on MgO, the film annealed at 550 °C exhibited the best electrical performance ($\rho = 3.9 \times 10^{-3}$ Ωcm), while the as-deposited one showed a relatively high resistivity with the lowest electron mobility. From the results, one could notice that the resistivity of the as-deposited SiZO film on the MgO substrate is higher than that of the film on the glass substrate deposited at a similar pressure and substrate temperature. One reason for this could be that the optimal pressure for depositing films on MgO substrates is different from that for depositing films on glass substrates. In Figure 3.6, it could be seen that the resistivity of the films is very sensitive to the sputtering pressure, especially between 6×10^{-3} mbar and 1×10^{-2} mbar. Besides, a previous study suggests that doped ZnO films deposited on glass substrates tend to contain more oxygen vacancies than other single crystal substrates [25], thus contributing to the higher carrier concentration of the films. Moreover, the films on glass substrates are thicker because of the longer sputtering duration, which could also affect resistivity, though this impact is usually small for films thicker than 250 nm (see Section 1.5.3).

The resistivity report in this thesis is close to the results obtained on SiZO films made by spray pyrolysis [4] with resistivity value of 3.7×10^{-3} Ωcm. The results reported by Minami *et al.*, show lower resistivity of 3.8×10^{-4} Ωcm of SiZO films made by off-axis RF sputtering (substrates in which are suspended perpendicular to the target surface). However, there are many challenges for off-axis RF sputtering when it comes to large-scale industrial productions [26], including uniformity of thickness across the film, variation of target-substrate distance across the film etc. In another study, Faure *et al.* made SiZO thin films, using co-sputtering from ZnO and SiO_2 targets, with resistivity of 3.5×10^{-3} Ωcm [27]. Compared to ITO, it is still not as good

in terms of mobility and carrier concentration. In fact, most of the results reported for ZnO-based films are still not as good and the 'processing window' is known to be much narrower than that of ITO [28]. A good amount of papers have been published in the past trying to understand why the difference exist [28, 29]. However it is worth mentioning that even though the resistivity reported here is around one order of magnitude higher than that of the best ITO value, according to the previous model built by Vai [29], the cost of producing a ZnO film with the same sheet resistance of an ITO film is still a lot lower, considering material and labour cost etc. The only problem is that in that case the thickness of the ZnO film will be bigger than the ITO film which might not be ideal for some TCO-related devices that has thickness requirement (e.g. touch panel).

Previous research on Al doped ZnO thin film grown on MgO substrate has also shown that films deposited at low temperature possess comparatively poor electrical performance [12]. At lower processing temperatures, the atoms in the film did not have enough energy to bond and form crystallites with good in-plane alignment, giving a distribution of randomly oriented grains (Figure 3.20), containing some large grain boundary angles according to the TKD results ($> 30°$, up to $90°$). By contrast, for the films treated by vacuum annealing, the grain boundary angles are predominantly around $30°$ as shown in Figures 3.23 and 3.24. It has been reported that the potential barriers at the grain boundaries are related to the grain boundary angle in ZnO films [30], the larger the grain boundary angle, the greater the potential barrier. Therefore according to the Matthiessen's rule, in which grain boundary is one of the factors limiting the mobility, it is not difficult to understand that the formation of the preferred in-plane orientations would lead to a higher electron mobility in the film. Besides, as mentioned earlier, the decreases in the FWHM of the rocking curve suggests smaller amount of threading dislocations in the annealed films which may contribute to the improvement of carrier mobility as well.

Another feature that appeared after annealing is the arrays of voids on the grain boundary planes. One plausible explanation for the void formation would be the evaporation of Ar atoms which were originally trapped inside the as-deposited film.

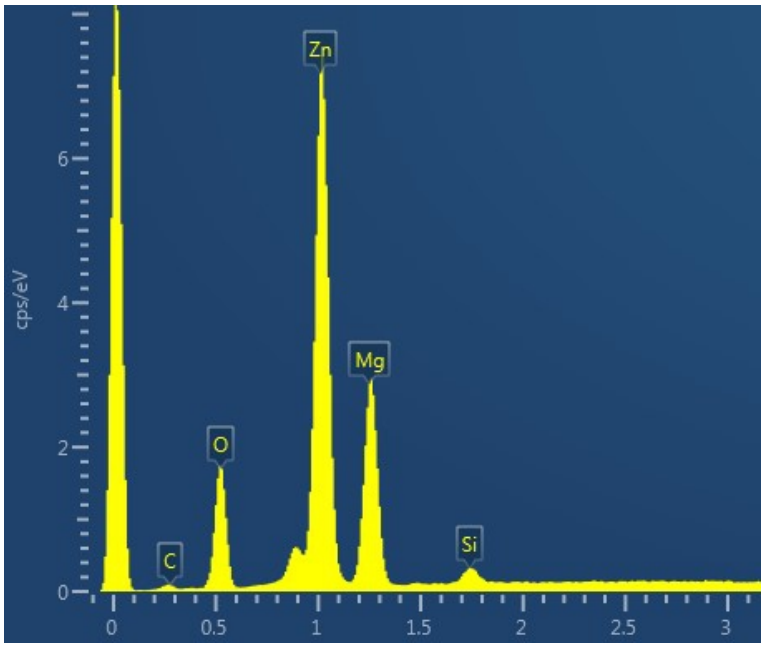


Figure 3.39: EDS spectrum of the as-deposited film, in which no Ar peak (2.957 keV) could be seen.

Nevertheless, no Ar signal (2.96 keV for the Kα line) could be detected in the as grown film in the EDS study that thus excludes this explanation.

Previous studies on ZnO thin films made from aqueous solution found pores in the films after annealing as well, though not particularly at grain boundaries [31]. The mechanism for pore formation that the researcher suggested is the expelling of water vapor following the combination of zinc vacancies to compensate for the hydrogen vacancies. This is unlikely to be the mechanism for pore formation in films made by sputtering which had very little contact with water molecules.

Other research on powder-pressed bulk ZnO materials also reported the existence of pores in their materials [32], but those pores were from the space between the starting powder particles and incomplete sintering which also could not explain the pore formation here.

Another possible explanation for the pore formation mechanism is the aggregation of oxygen vacancies in the film. However, it has been reported before that isolated oxygen vacancies are unlikely to aggregate in ZnO due to the large lattice relaxations the aggregation would induce and the existence of directed bonds that would result

in the instability of dimer vacancy [33–35].

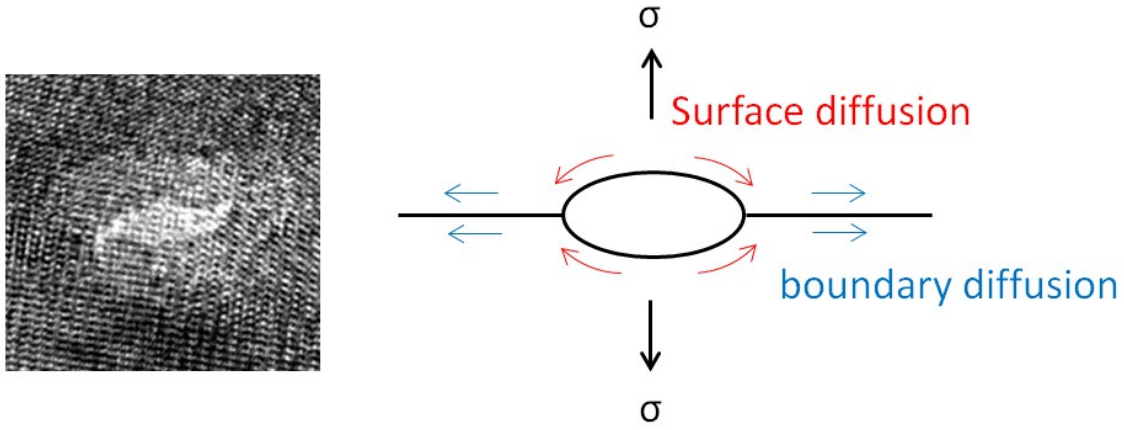


Figure 3.40: Crack like / elliptical voids on the grain boundaries of the annealed films. Scale of the TEM image: 11 × 10 nm.

Therefore it seems like the voids are more likely to be an outcome of stress and exposure to high temperatures . Although mostly studied in metal and alloy systems, creep damage has been reported and investigated in ZnO bulk material previously as well [36]. Research on creep voids in bulk materials [37] has reported two different kinds of voids; spherical-shaped void and crack like (elongated) void. When boundary diffusion is the controlling factor for void growth, i.e. the surface diffusion rate is bigger than the boundary diffusion rate, the voids become spherical given the surface diffusion rate is high enough to redistribute atoms on the surface of the void rapidly. Nevertheless, the voids become flatter when the surface diffusion is slow, until a surface flux generated by the differential curvature between the equators and poles of the void is strong enough to counteract the flux leaving from the void by boundary diffusion. Here the voids in the annealed SiZO thin films are predominantly the elongated ones according to the HRTEM image (Figure 3.40), suggesting that surface diffusion is the prevailing rate-limiting factor. The stress field that leads to creep damage can be generated by the differential thermal expansion of the SiZO thin film and the MgO substrate during annealing. By comparing the films annealed at 400 °C and 550 °C (Figure 3.41), it can be seen that the 550 °C sample has a higher density of voids and the defect seems to go deeper (shown by the white arrows) into the

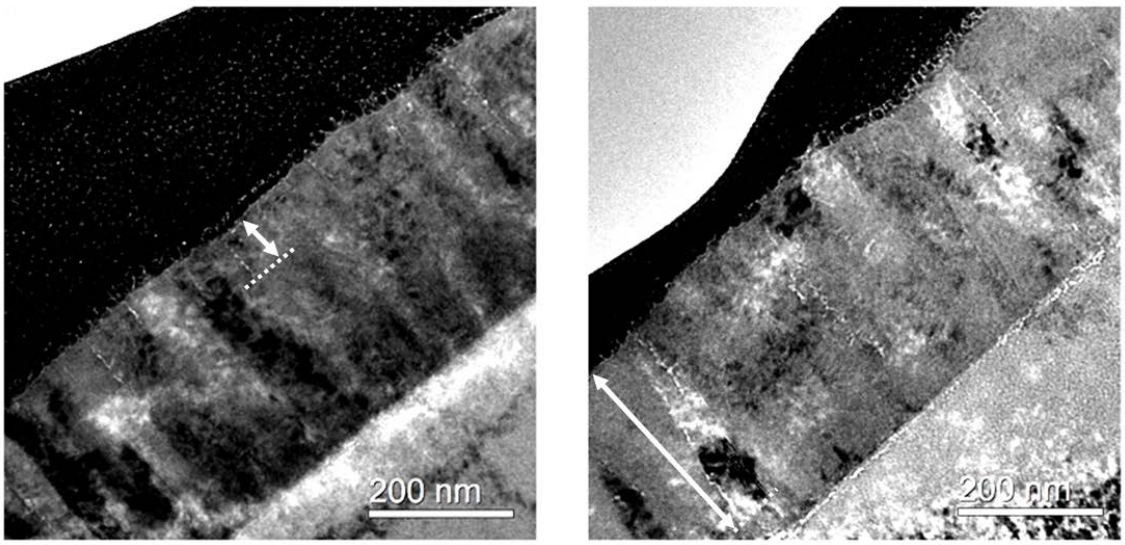


Figure 3.41: Comparison of the films annealed at 400 °C (left) and 550 °C (right). The white arrows show the penetration depth of the voids along the grain boundaries.

film as the voids generally started from the surface of the films (Figure 3.36). This on one hand could be due to the greater diffusion rate of atoms at higher annealing temperature, thus generating bigger fluxes from voids to grain boundaries. On the other hand, if one considers a linear thermal expansion model, the stress field would get bigger at higher temperature owing to the larger difference of thermal expansion between the SiZO thin film and the MgO substrate, and thus will also increase the flux.

According to previous research on bulk materials [37], voiding happens when there is a presence of tensile stress field. Therefore, by comparing the thermal expansion coefficients of ZnO ($\alpha_{\mathrm{ZnO},\perp} = 4.31 \times 10^{-3}$ K^{-1} [38], which is the coefficient of wurtzite ZnO normal to the c-axis) and that of MgO ($\alpha_{\mathrm{MgO}} = 10.5 \times 10^{-6}$ K^{-1}, rock salt type structure [39]), it could be known that the creep happened during the heating stage of the annealing when a tensile stress field normal to the grain-boundary is developed.

To avoid the creep damage, films with larger grain size could be used given that the strain rate in diffusional creep is negatively correlated to the grain size. In fact, no creep damage cases have been reported in epitaxial ZnO thin films given they are mostly single crystals. Another thing that one could do is to choose a substrate

that has smaller lattice mismatch with the ZnO film and thus will generate smaller internal stress field that would lead to a reduction in creep. If annealing is going to be performed on the film, it is better to choose a substrate which has thermal expansion coefficient close to that of the film.

EDS line scans in TEM have also been used to study the chemical variation around the pore, and especially any segregation of Si. The results are presented in Figure 3.42. The EDS counts decreased substantially when the electron beam moved across the pore, but the atomic percentage of Si did not show any obvious peak but a rather even distribution of Si considering the range of the error bars (Figure 3.42(c)). The difference in the signal intensity (Figure 3.42(b)) here is due to the variation of thickness in different regions. The thickness at the void is smaller and thus generated weaker X-ray signal. No Ar signal was detected here, which further confirms that the voids are not from Ar gas trapped during sputtering.

As previously stated, it is unusual for the simultaneous improvement of electron mobility and carrier concentration. There are several possible reasons for the improvement of carrier concentration after annealing: 1. Generation of oxygen vacancies, 2. The enhancement in the amount of effective dopants., 3. Reduction of electron acceptor states (i.e. defects that localize electrons). The concept of effective dopants means the Si atoms that actually contributed the generation of free electrons in SiZO thin film. In general, these are the Si^{4+} ions that substitute the Zn^{2+} ions and generate 2 free electrons per ion. However, other forms of Si in the lattice include Si (non-ion form), SiO_2 would also present in the thin films and have no contribution to the generation of free electrons. A thermodynamic explanation to this is that the more the free electrons, the higher the Fermi level (E_F) / electron chemical potential of the sample would be. According to Le Châtelier' s principle, the tendency for the donors to generate electrons would thus reduce. Besides, deep donor states might form depending on the bonding environment of the Si ions which will also reduce the amount of effective donors. Annealing is therefore a process that might be able to turn the inactive dopants into active ones, which is likely to be an outcome of rearrangement of atoms in the thin film. In terms of the electron

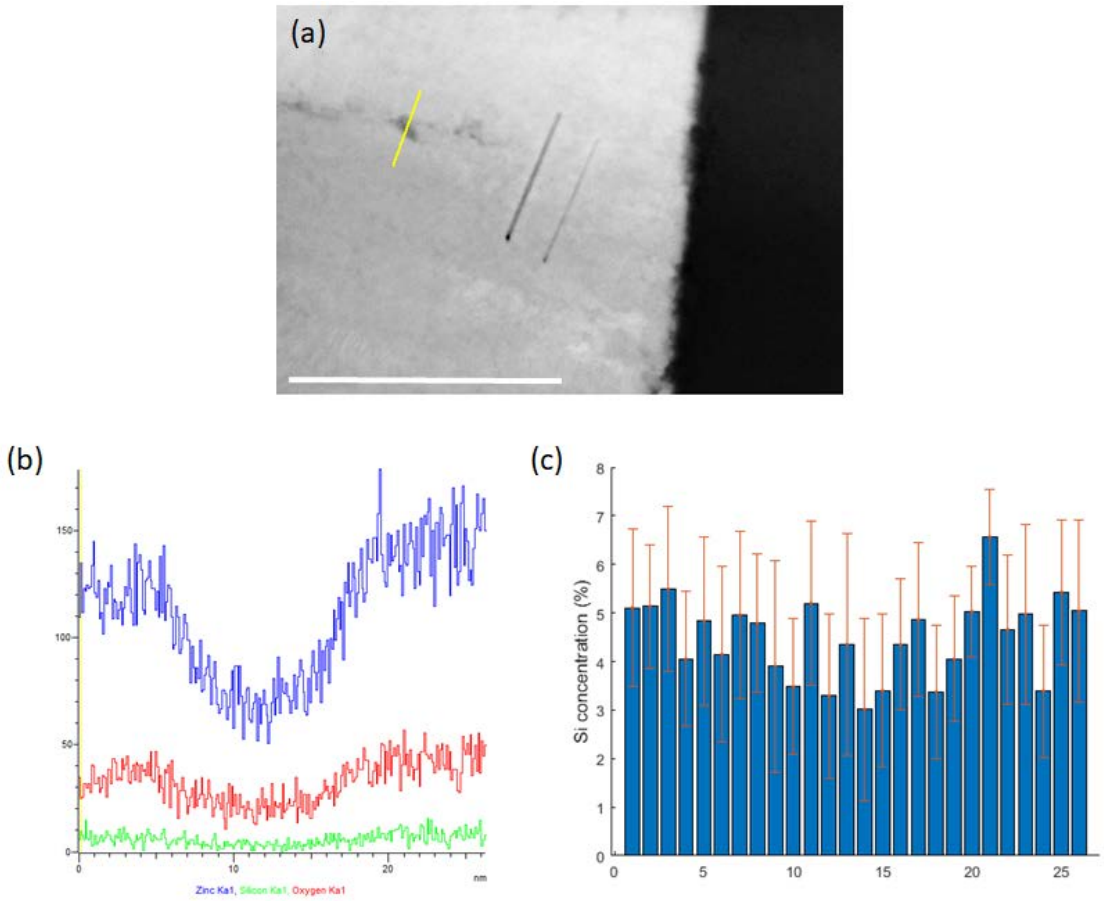


Figure 3.42: EDS line scan across one of the voids on the grain boundary plane; (a) STEM image with the yellow line showing the scan trajectory, (b) EDS counts of Zn, Si and O, (c) the Si concentration in each nano-meter region calculated from (b), with the error bar showing the variation of Si ratio in each nano-meter region. Scale bar: 90 nm.

localizing defects, it has been reported for ZnO that the grain boundaries with bigger angles and random orientations are more likely to trap electrons than the ones with smaller angles [40]. According to our previous discussion, vacuum annealing changed the mosaic in-plane alignment of the film to an alignment with GB angles of 0–30° (Figures 3.23, 3.24). The improvement in in-plane alignment thus could help reduce the amount of electron acceptor states and increase the carrier concentration.

However, to accurately understand which factor is the dominant reason behind the increase of carrier concentration, careful measurement of the density of oxygen

vacancies need to be carried out, using techniques such as photoluminescence (PL) spectroscopy and electron paramagnetic resonance (EPR) [41, 42]. This is currently beyond the scope of this thesis, yet it would be an interesting topic for future researchers and would bring valuable insights to the study of SiZO.

3.6 Conclusions and suggestions for future work

Here, highly conducting polycrystalline Si-doped ZnO thin films have been made by RF sputtering on glass and MgO substrates. Various deposition parameters were explored to find the optimal conditions. Regarding the films deposited on MgO substrates, a variety of advanced microscopy techniques have been used to study the change of microstructure and nano-chemistry of the film in order to understand the improvement of electrical transport properties of the SiZO films after annealing in vacuum. All the films show preferred growth orientations in the c-axis. The out-of-plane-alignment was studied with omega-XRD, and the FWHM of the rocking curve shows a decrease after annealing. Two preferred in-plane alignments, $(110)_{\mathrm{ZnO}} \parallel (110)_{\mathrm{MgO}}$ and $(100)_{\mathrm{ZnO}} \parallel (110)_{\mathrm{MgO}}$, between the SiZO film and the MgO substrate were observed in the annealed films using TKD and texture XRD. The increase in mobility was ascribed to the improvement in in-plane and out-of-plane alignments of the grains inside the film. The EDS results show that the Si/(Si+Zn) ratio is around 5%–6% in the as-deposited and annealed films. The Si/(Si+Zn) ratios in these films are higher than that of the target, showing the preferred deposition of Si. Although the Si contents in the films are well above the equilibrium level shown in the SiO_2-ZnO phase diagram, no precipitation/phase separation could be detected. Arrays of nano-pores were found near the grain boundaries of the annealed samples, which suggests creep damage may have happened during annealing at high temperatures. Some advice has been given for future researchers to avoid the formation of creep defects in their thin films.

Because of cost reasons, in many technical applications, such as touch panel displays, polycrystalline films on glass/plastic substrates have to be used. However,

the study of SiZO films on single crystal substrates would deepen our understanding of the relationships between microstructure, grain boundaries and the properties of doped ZnO films. Studies with such purpose have been carried out in the past on doped ZnO films deposited on other single crystal substrates, such as r-sapphire, c-sapphire and a-sapphire [43]. In our present work, studies of ZnO films on MgO substrates also show that annealing is a reliable approach to increase both the mobility and the carrier concentrations of the films. It allows the study of Si content in the films, which is difficult for films deposited on borosilicate glass substrates. The studies show that the films have higher Si content than the target, but no Si-rich precipitation could be detected. Moreover, the results could offer some useful guidelines for integrating wurtzite ZnO films with more complicated cubic perovskite materials, which have recently been discussed in a few reports, in attempts to produce high-efficiency perovskite solar cells [44–46].

Despite the high conductivity of the SiZO films reported here, these values are still not as good as the class-leading TCO performer—ITO. In fact, even after decades of study, there is still a long way for ZnO thin film to catch up in terms of not only opto-electronic performances but also environmental stability and the ability to deposit high quality films using all kinds of techniques, which has already been carefully investigated in the past [47]. However, this does not mean that finding a better recipe to make doped ZnO thin film more attractive is impossible, it is just important to be aware that it will not be an easy or straightforward path. That is why more fundamental studies like those presented in this chapter are crucial for improving ZnO performance or any other TCO systems including ITO itself. With the help of greater computer processing power and the development of machine learning algorithms, one might even be able to predict the needs for a highly conducting and easy-to-produce ZnO thin film in the future. If that can be achieved one day, the data from microstructural studies like this could perhaps contribute to the database for the learning algorithm, which is also part of the goal of the global Materials Genome Initiatives (MGI) [48] that are currently being studied in many countries of the world.

In terms of suggestions for future studies, several things would potentially be very helpful including the in-depth structural examination of ZnO films grown on other single crystal substrates to see if similar defects exist. Studies of single crystal substrates would not only be a topic of scientific interest but would also offer some useful guidelines for making devices that require high-quality ZnO films deposited on single crystals, such as surface acoustic wave devices [49] and blue/UV light-emitting diodes [50]. A deeper understanding of the doping mechanism and the conditions for forming *effective* dopants would also be critical in terms of increasing the electron concentration. Lower amounts of inactivated dopants would also improve the electron mobility by reducing the concentration of neutral impurities. To better control the Si concentration, co-sputtering from independent ZnO and Si/SiO_2 targets could be used. Last but not least, finding the right applications for Si doped ZnO thin film is crucial given the wide range of TCO applications. For instance, touch panels which do not require remarkably high conductivity can make use of the SiZO's advantages of low-cost, high transparency and excellent scalability.

Bibliography

[1] N. Rashidi, A. T. Vai, V. L. Kuznetsov, J. R. Dilworth, and P. P. Edwards, Chemical Communications **51**, 9280 (2015).

[2] T. Minami, H. Sato, H. Nanto, and S. Takata, Japanese journal of applied physics **25**, L776 (1986), ISSN 1347-4065.

[3] A. Das, P. Misra, and L. Kukreja, Journal of Physics D: Applied Physics **42**, 165405 (2009), ISSN 0022-3727.

[4] N. Rashidi, V. L. Kuznetsov, J. R. Dilworth, M. Pepper, P. J. Dobson, and P. P. Edwards, Journal of Materials Chemistry C **1**, 6960 (2013).

[5] D. Ginley, H. Hosono, and D. C. Paine, *Handbook of transparent conductors* (Springer Science and Business Media, 2010), ISBN 1441916385.

[6] S. Nandi, S. Chakraborty, M. Bera, and C. Maiti, Bulletin of Materials Science **30**, 247 (2007), ISSN 0250-4707.

[7] N. Jahed, M. Mahmoudysepehr, and S. Sivoththaman, Materials Research Express **3**, 116402 (2016), ISSN 2053-1591.

[8] A. Taabouche, M. BOUAFIA, C. BENAZZOUZ, T. KERDJA, Y. BOUACHIBA, S. MENAKH, F. HANINI, F. KERMICHE, A. BOUABELLOU, and S. Amara, Advances in Materials Physics and Chemistry **3**, 209 (2013).

[9] Y. Igasaki, M. Ishikawa, and G. Shimaoka, Applied Surface Science **33**, 926 (1988), ISSN 0169-4332.

[10] X. Yu, J. Ma, F. Ji, Y. Wang, X. Zhang, and H. Ma, Thin solid films **483**, 296 (2005), ISSN 0040-6090.

[11] M. Nistor, N. Mandache, J. Perrire, C. Hebert, F. Gherendi, and W. Seiler, Thin Solid Films **519**, 3959 (2011), ISSN 0040-6090.

[12] H. Li, H. Qiu, M. Yu, and X. Chen, Materials Chemistry and Physics **126**, 866 (2011), ISSN 0254-0584.

[13] H. Zhou, H.-Q. Wang, L. Wu, L. Zhang, K. Kisslinger, Y. Zhu, X. Chen, H. Zhan, and J. Kang, Applied Physics Letters **99**, 141917 (2011), ISSN 0003-6951.

[14] L. Nistor, C. Ghica, D. Matei, G. Dinescu, M. Dinescu, and G. Van Tendeloo, Journal of crystal growth **277**, 26 (2005), ISSN 0022-0248.

[15] Sigma Aldrich (2019), URL `https://www.sigmaaldrich.com/catalog/product/aldrich/703192?lang=en&region=GB`.

[16] FTO (2018), URL `https://www.techinstro.com/fto-coated-glass/`.

[17] J. Wienke and A. Booij, Thin Solid Films **516**, 4508 (2008), ISSN 0040-6090.

[18] D. Damjanovic, Reports on Progress in Physics **61**, 1267 (1998), ISSN 0034-4885.

[19] A. Rosli, M. Marbie, S. H. Herman, and M. Ani, Journal of Nanomaterials **2014**, 92 (2014), ISSN 1687-4110.

[20] J. Ayers, Journal of Crystal Growth **135**, 71 (1994), ISSN 0022-0248.

[21] Sputter rate (2019), URL `http://www.semicore.com/reference/sputtering-yields-reference`.

[22] M. Hÿtch, E. Snoeck, and R. Kilaas, Ultramicroscopy **74**, 131 (1998), ISSN 0304-3991.

[23] M. J. Hÿtch, J.-L. Putaux, and J.-M. Pnisson, Nature **423**, 270 (2003), ISSN 1476-4687.

[24] N. Rashidi, Thesis, Oxford University (2014).

[25] J. Ding, H. Chen, X. Zhao, and S. Ma, Journal of Physics and Chemistry of Solids **71**, 346 (2010), ISSN 0022-3697.

[26] E. Alfonso, J. Olaya, and G. Cubillos, *Thin film growth through sputtering technique and its applications* (IntechOpen, 2012).

[27] C. Faure, J. Clatot, L. Teul-Gay, G. Campet, C. Labrugre, M. Nistor, and A. Rougier, Thin Solid Films **524**, 151 (2012), ISSN 0040-6090.

[28] K. Ellmer and R. Mientus, Thin solid films **516**, 4620 (2008), ISSN 0040-6090.

[29] A. T. Vai, Thesis, Oxford University (2015).

[30] Z. Yu-Ming, H. Yi-Gang, L. Ai-Xia, and W. Qing, Chinese Physics B **18**, 3966 (2009), ISSN 1674-1056.

[31] J. J. Richardson, G. K. Goh, H. Q. Le, L.-L. Liew, F. F. Lange, and S. P. DenBaars, Crystal Growth & Design **11**, 3558 (2011), ISSN 1528-7483.

[32] J. Choi, N. Hwang, and D. Kim, Journal of the American Ceramic Society **84**, 1398 (2001), ISSN 0002-7820.

[33] J. Carrasco, N. Lopez, and F. Illas, The Journal of chemical physics **122**, 224705 (2005), ISSN 0021-9606.

[34] J. Carrasco, N. Lopez, and F. Illas, Physical review letters **93**, 225502 (2004).

[35] E. G. Seebauer and M. C. Kratzer, *Charged Semiconductor Defects: Structure, Thermodynamics and Diffusion* (Springer Science & Business Media, 2008), ISBN 1848820593.

[36] M. Bahaman and L. De Jonghe, Journal of materials science **22**, 4326 (1987), ISSN 0022-2461.

[37] A. Cocks and M. Ashby, Progress in materials science **27**, 189 (1982), ISSN 0079-6425.

[38] H. Iwanaga, A. Kunishige, and S. Takeuchi, Journal of Materials Science **35**, 2451 (2000), ISSN 0022-2461.

[39] H. Morkoc, S. Strite, G. Gao, M. Lin, B. Sverdlov, and M. Burns, Journal of Applied physics **76**, 1363 (1994), ISSN 0021-8979.

[40] F. Greuter and G. Blatter, Semiconductor Science and Technology **5**, 111 (1990),

ISSN 0268-1242.

[41] H. Kaftelen, K. Ocakoglu, R. Thomann, S. Tu, S. Weber, and E. Erdem, Physical Review B **86**, 014113 (2012).

[42] C. Drouilly, J.-M. Krafft, F. Averseng, S. Casale, D. Bazer-Bachi, C. Chizallet, V. Lecocq, H. Vezin, H. Lauron-Pernot, and G. Costentin, The Journal of Physical Chemistry C **116**, 21297 (2012), ISSN 1932-7447.

[43] A. Bikowski and K. Ellmer, Journal of Applied Physics **114**, 063709 (2013), ISSN 0021-8979.

[44] H. Zhou, H.-Q. Wang, Y. Li, K. Li, J. Kang, J.-C. Zheng, Z. Jiang, Y. Huang, L. Wu, and L. Zhang, ACS applied materials & interfaces **6**, 13823 (2014), ISSN 1944-8244.

[45] F. Yang, D.-W. Kang, and Y.-S. Kim, RSC Advances **7**, 19030 (2017).

[46] J. Luo, Y. Wang, and Q. Zhang, Solar Energy **163**, 289 (2018), ISSN 0038-092X.

[47] T. Minami, T. Kuboi, T. Miyata, and Y. Ohtani, physica status solidi (a) **205**, 255 (2008), ISSN 1862-6300.

[48] A. Jain, S. P. Ong, G. Hautier, W. Chen, W. D. Richards, S. Dacek, S. Cholia, D. Gunter, D. Skinner, and G. Ceder, Apl Materials **1**, 011002 (2013), ISSN 2166-532X.

[49] T. Mitsuyu, S. Ono, and K. Wasa, Journal of Applied Physics **51**, 2464 (1980), ISSN 0021-8979.

[50] Y. Chen, D. Bagnall, Z. Zhu, T. Sekiuchi, K.-t. Park, K. Hiraga, T. Yao, S. Koyama, M. Shen, and T. Goto, Journal of Crystal Growth **181**, 165 (1997), ISSN 0022-0248.

Chapter 4

$Cu_2P_2O_7$: from Powder to Thin Films

4.1 Introduction

Near-infrared (NIR) materials are materials that interact with light of wavelengths from 750 to 2500 nm by absorption, reflection or emission. In particular, NIR-absorbing materials have long been of interest for optical recording [1], heat shielding [2] and camouflage schemes [3]. To date the majority of this research was focused on organic NIR-absorbing materials which have the disadvantages of high vulnerability to heat, light radiation and attack by chemical compounds [4, 5]. A few inorganic NIR materials such as WO_3, IrO_x (absorbing) [6] and transparent conducting oxides (reflecting) [7] are either electro-chromatic and have low transparency in the visible range when reduced, or only block waves of wavelength above 1300 nm. Therefore, an inorganic NIR material that could absorb light in the wavelength range of 790–1100 nm yet be transparent in the visible range would be ideal for many applications.

Recently, researchers have reported on the light absorbing capabilities of $Cu_2P_2O_7$ powder in the near-infrared range [5]. An introduction to the absorbing mechanism of the material has been shown in Section 1.6. No previous study could be found in the literature on making thin films from this material, so in this chapter a complete route from powder and sputtering target preparation/characterization to thin film production, as well as detailed property and microstructural analysis will

be reported for the first time. This chapter has five sections. After this introduction, the second section is about the preparation of materials for sputtering, including the pre-processing of commercial powder, preparation of sputtering targets and substrates. The third section gives details of thin film preparation, and films deposited under different conditions will be studied. The fourth section is a discussion of my results, followed by conclusions and suggestions for future work.

4.2 Preparation of materials for sputtering

4.2.1 Powder preparation

Powder analysis was carried out as a preliminary examination of the NIR absorbing capability of this material in the as delivered form. Almost all of the materials available on the market are the hydrated form of copper pyrophosphate — $Cu_2P_2O_7 \cdot xH_2O$ [8, 9], given the material is generally produced from a solution-based route:

$$2CuSO_4 \cdot 7H_2O + Na_4P_2O_7 \xrightarrow{\text{In a liquid solution environment}} 2Na_2SO_4 + Cu_2P_2O_7 + 14H_2O$$

The powder used in this study was bought from Alfa Aesar ®[9]. The XRD spectrum of the copper pyrophosphate hydrate powder is shown in Figure 4.2(a), the position of the peaks match relatively well with the PDF data file of $Cu_2P_2O_7 \cdot 3H_2O$ (PDF-#51-0202). However, there are still peaks that cannot be assigned because the exact amount of water the powder ($Cu_2P_2O_7 \cdot xH_2O$, $x \approx 3$ to 4) contains is unknown. Since it has been reported that H_2O could have an impact on deposition of thin films [10, 11], in order to better control the deposition process dehydrated copper pyrophosphate would be a better starting material.

In order to obtain dehydrated copper pyrophosphate powder, the powder was first baked at 900 °C for 5 hrs. This temperature was chosen because it is only slightly below the decomposition temperature of the compound [12], which enabled the dehydration efficiency to be maximized while retaining the material at a stable



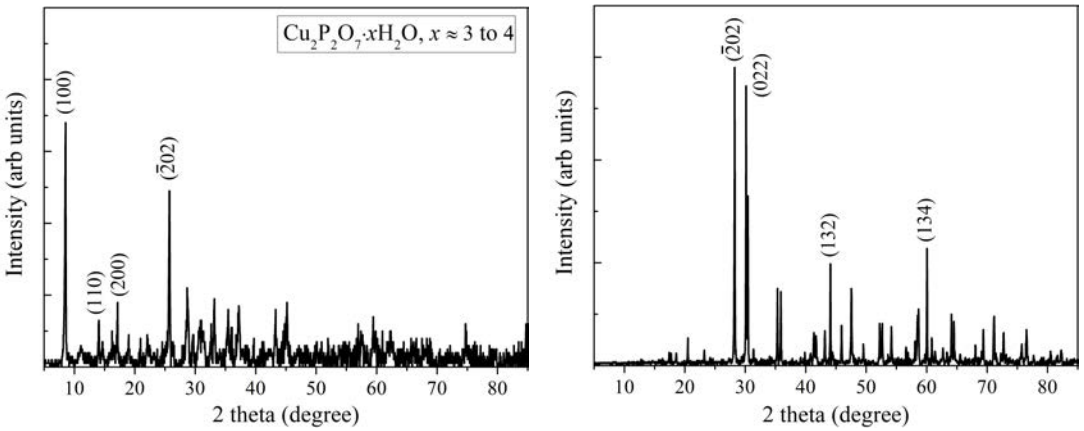
(a) As-delivered powder. Scale: 55 × 54 mm.

(b) The result of annealing as delivered $Cu_2P_2O_7$ powder at 900 °C for 5hrs. Scale: 51 × 51 mm.

Figure 4.1: As delivered sample and the annealed sample (900 °C).

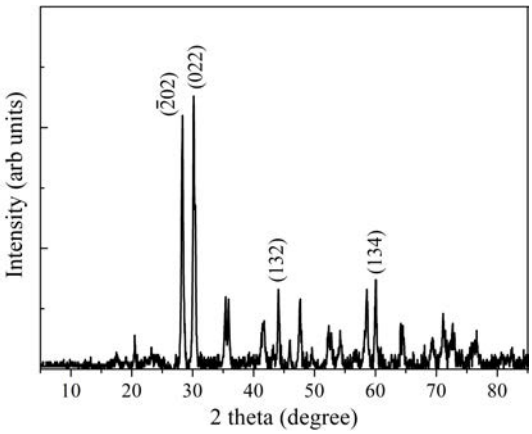
phase. The result is shown in Figure 4.1(b). It can be seen that the powder clustered due to sintering and becomes darker blue than that the initial material (Figure 4.1(a)). The XRD spectrum (Figure 4.2(b)) only shows peak characteristic of pure copper pyrophosphate (PDF-#44-0182). This confirms that the as-delivered powder can be dehydrated through high temperature annealing in ambient environment, but it also shows that the deepening of the color is not from the generation of any new chemical phase, instead it could be due to the increase of grain size during annealing. The mechanism of this colour change has been well-studied over the past few decades [13]. The absorbance spectrum of the dehydrated powder is shown in Figure 4.3. The spectrum confirms the high NIR absorbing ability of copper pyrophosphate powder reported by Norindr [5].

The hydrated powder was also annealed at 500 °C for 5hrs, and shows a lighter blue colour (Figure 4.4) compared to the one annealed at 900 °C. The XRD spectrum in Figure 4.2(c) shows a good match with the pure copper pyrophosphate phase (PDF-#44-0182). However, given that the agglommerated powder after 900 °C requires another round of grinding before the following cold pressing procedure, in order to facilitate the target making, 500 °C was used to dehydrate the powder for the rest of the study.



(a) XRD spectrum of the as-delivered $Cu_2P_2O_7 \cdot xH_2O$ powder shows characteristic peaks of $Cu_2P_2O_7 \cdot 3H_2O$ (PDF-#51-0202).

(b) XRD spectrum of powder annealed at 900 °C shows characteristic peaks of pure $Cu_2P_2O_7$ (PDF-#44-0182).



(c) XRD spectrum of powder annealed at 500 °C shows characteristic peaks of pure $Cu_2P_2O_7$ (PDF-#44-0182).

Figure 4.2: XRD spectra of the as-delivered sample and samples processed under different conditions.

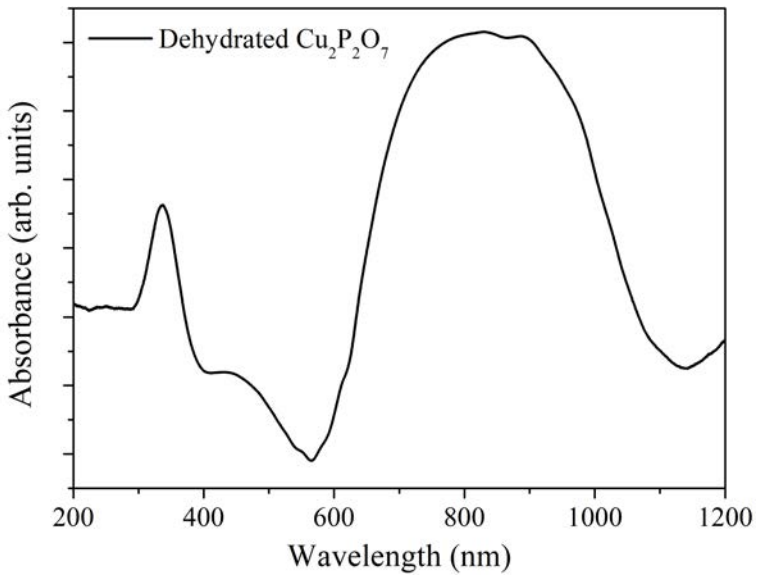


Figure 4.3: Absorbance spectrum of dehydrated copper pyrophosphate powder.



Figure 4.4: The picture of the powder after being annealed at 500 C for 5 hrs. The retained fine powder is obvious when comparing this image with the powder annealed at 900 °C. Scale of the image: 70 × 66 mm.

4.2.2 Sputtering target preparation

4.2.2.1 $Cu_2P_2O_7$ Target

It is known that the quality of the sputtering target can greatly affect the thin film deposition process and the quality of the films produced [14, 15]. The preparation of crack-free targets of the correct dimensions is important for industrial manufacturing processes [16]. Thus, a great amount of effort has been made in this study to find the best approach for preparing the target. Figure 4.5 shows the selection process for the right parameters.

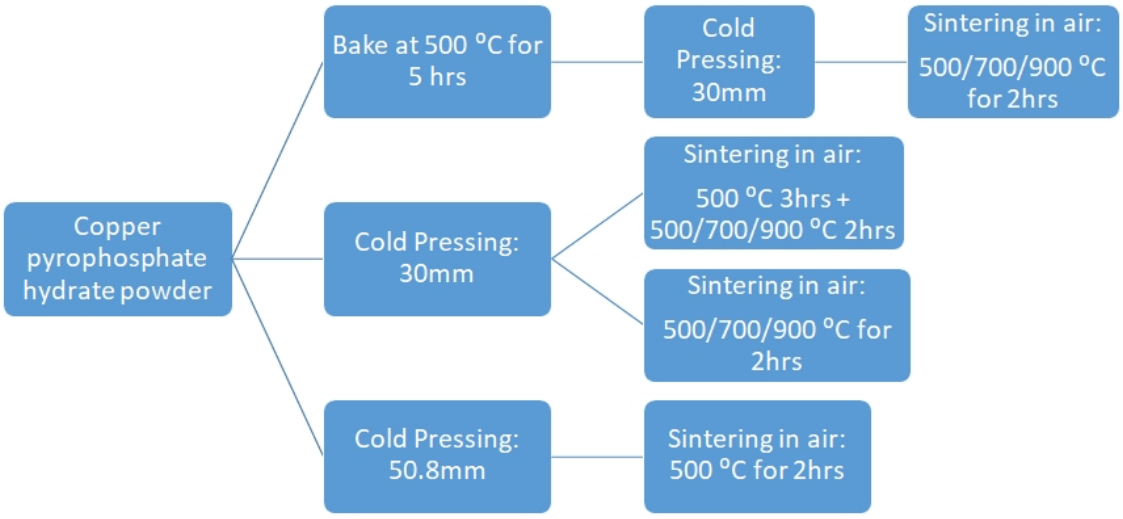


Figure 4.5: Flow chart for target preparation.

In the first set of experiments, as delivered hydrated copper pyrophosphate powder was used for cold pressing directly. The reason that no dehydration was used is because the water content makes the powder stickier and thus makes the pressed disk more robust after cold pressing. The powder was cold pressed in a steel 30 mm die, and three pressed copper pyrophosphate disks were sintered in air at 500 °C for 3 hrs, and then at 500 °C, 700 °C and 900 °C. The results are shown in Figure 4.6. The figure shows that the target shrank significantly and formed cracks (700 °C, 900 °C) after high temperature sintering. The shrinkage may be due to the grain growth and densification [17], and also because of the loss of water molecules. The cracks

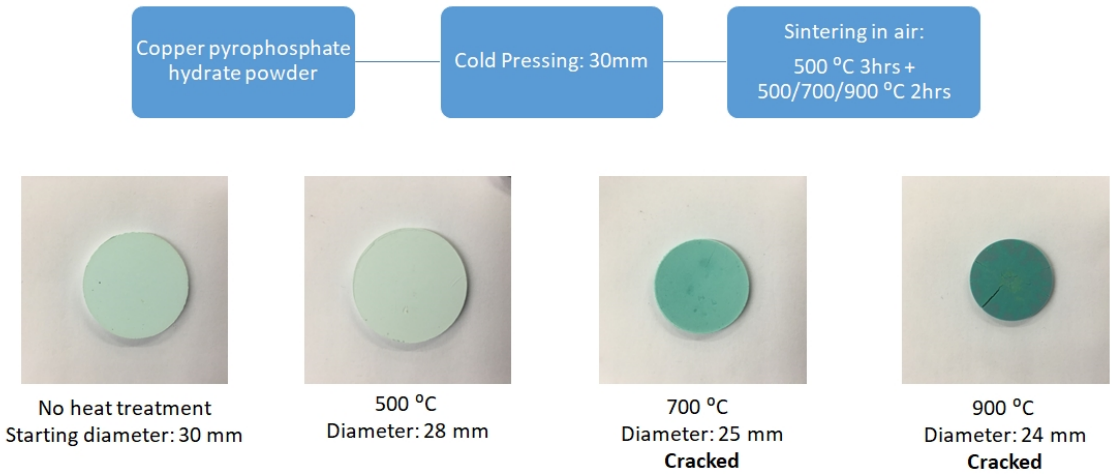


Figure 4.6: Pictures of targets without heat treatment and sintered for 3 hours at 500 °C, then at 500 °C, 700 °C and 900 °C for 2 hours, respectively.

happened perhaps due to the different shrinkage rate in different areas. It can also be seen that the higher the sintering temperature, the bigger the shrinkage was (7%, 17% and 20% for 500 °C, 700 °C and 900 °C, respectively).

In large-scale industrial manufacturing, it is important to have a process for making targets for which the size is controllable and preferably crack-free. Being able to control the size of the target could help manufacturers produce targets with exactly the right diameter and thickness for different sputtering tools. Cracks on the surface could get bigger and deeper during high-power sputtering due to the bombardment of active gas ions such as Ar and oxygen ions and the thermal strain created due to the temperature imbalance between the top surface and the inside of the target. Eventually this would lead to an accelerated degradation of the target and could even cause short-circuits between electrodes. It is therefore part of the goal of this thesis to find the right set of parameters for making a robust, non-shrunk and crack-free copper pyrophosphate target.

The reason that 30 mm die is used initially instead of the 50.8 mm die designed to produce targets for the 2-inch magnetrons in the sputtering tools I was using is for the exploration of the optimization of parameters. It is both more economical on materials and the resulted pressed-disk is easier to handle if a smaller die was used. Yet, as demonstrated above, it also works well to show the effect of temperature

on phenomena such as shrinkage and cracking. Meanwhile, the color of the target deepened as the sintering temperature increased. This is similar to what is previously described in the powder section.

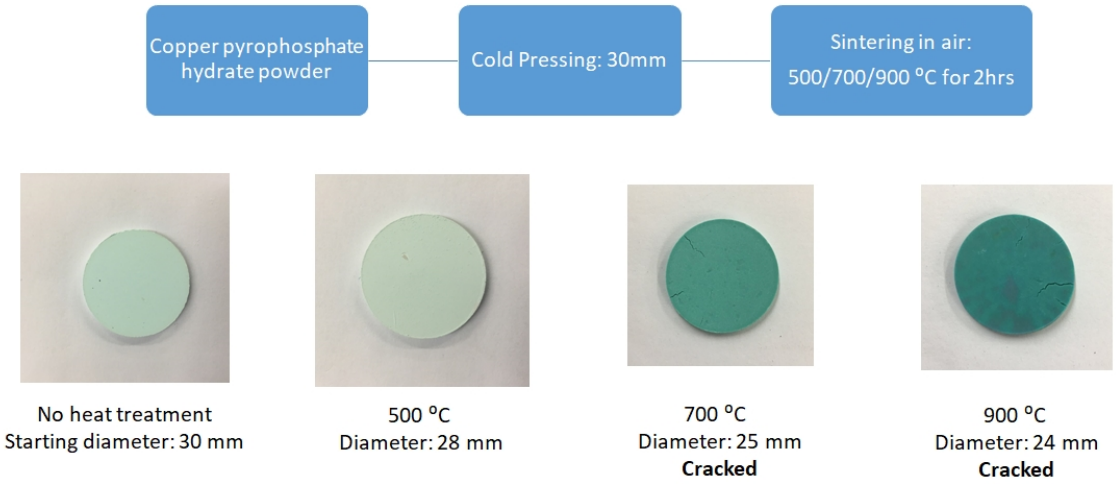


Figure 4.7: Pictures of targets without heat treatment and sintered for 2 hours at 500 °C, 700 °C and 900 °C, respectively.

In order to try to reduce the thermal impact, shorter sintering periods were used to process the targets. Here the targets were sintered at 500 °C, 700 °C and 900 °C for 2 hours, respectively. However, the results in Figure 4.7 show that shorter sintering duration does not solve the issues of shrinkage and cracking. The targets shrank 7%, 17% and 20% for sintering at 500 °C, 700 °C and 900 °C, respectively. As before, the colour deepened as the sintering temperature increased.

A 2-inch target formed from the as-delivered powder was also sintered at 500 °C to further observe the development of cracks on the surface. The results are shown in Figure 4.8.

As it can be seen, the diameter of target reduced from 50.8 mm to 47 mm, by 8%, after heat treatment. Cracks were generated not only on the top surface but also on the side.

Since losing the water content could potentially be one of the driving forces for shrinkage and cracking, dehydrated powder was then used for cold pressing using the procedure described in the previous powder section. One drawback for

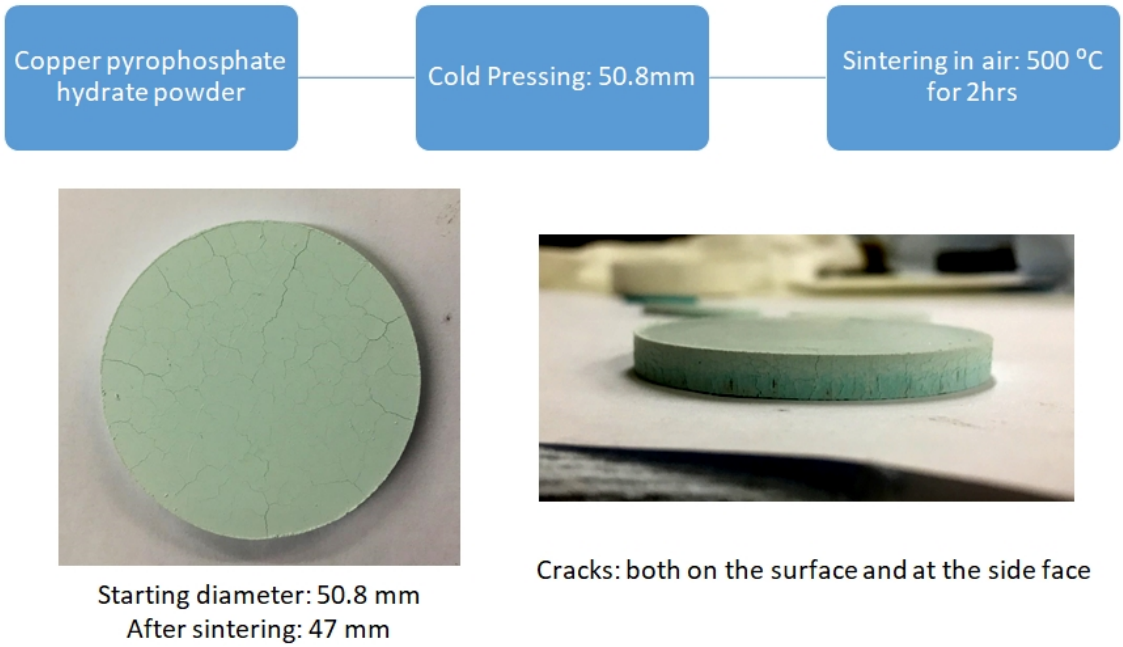


Figure 4.8: Pictures of 2-inch target after sintering at 500 °C.

dehydrated powder is that it is not as sticky as the hydrated one and therefore makes the cold pressed disk more vulnerable against external forces/vibrations, and difficult to transfer from the pressing die to the sintering furnace.

Here, the disks made of dehydrated powder were sintered in air at 500 °C, 700 °C and 900 °C for 2 hrs, respectively. The results presented in Figure 4.9 show that the target sintered at 500 °C did not show any shrinkage and also did not have any cracks on the surface. The targets sintered at 700 °C and 900 °C shrank from 30 mm to 26 mm, by 13%, but neither of them developed any visible cracks.

This shows that by baking the powder prior to cold pressing, it is possible to produce crack-free targets, meaning that the loss of water may be the major driving force for cracking instead of the densification during sintering. Using a low enough temperature such as 500 °C also restricts this shrinkage during heat treatment.

Thus a promising route has been found to produce crack-free and robust copper pyrophosphate targets that maintain their original diameter. These targets were used for the following sputtering experiments in this study.

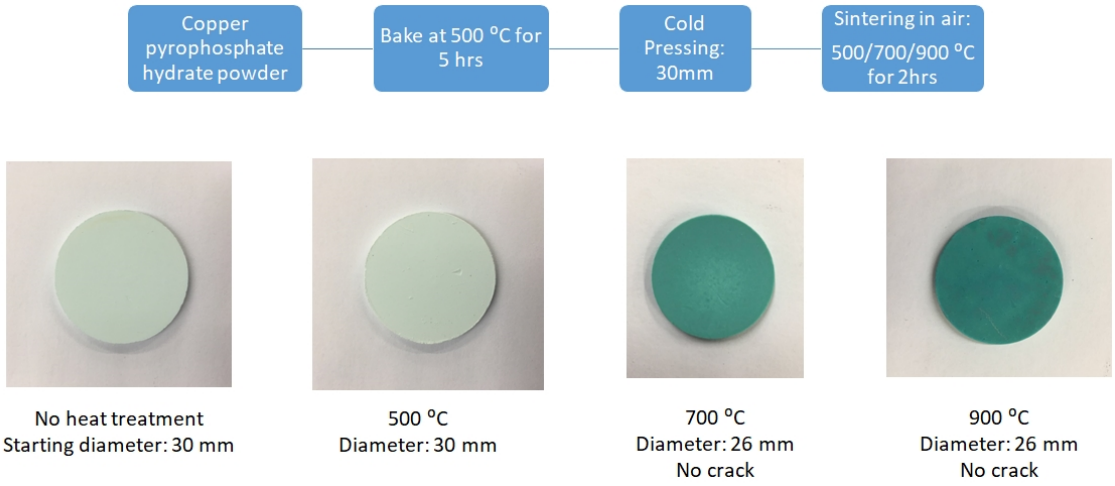


Figure 4.9: Pictures of targets prepared from dehydrated powder without heat treatment, and annealed at 500 °C, 700 °C and 900 °C, respectively.

4.2.2.2 $Cu_2P_2O_7 + P_2O_5$ Target

One distinctive feature of sputtering is that it does not always produce thin films with the same stoichiometry as the target. Non-stoichiometric transfer during sputtering of systems such as ZnO and $Ca_2P_2O_7$ (hydroxyapatite) have been extensively studied in the past [18–20]. In order to have more leeway in terms of adjusting the composition especially the Cu/P ratio of the films, a $Cu_2P_2O_7 + P_2O_5$ target was also made and used in this study.

The reason that extra phosphorous was added in this case is because it is likely that phosphorous is a more volatile element compared to copper during sputtering. It has lighter atomic mass of 31 u than 63.5 u of copper and its vapor pressure is also higher than that of copper [21]. This means that thin films in this case were likely to lose phosphorous during deposition, which was indeed found in some of my films as will be discussed below.

The overall procedure is similar to that described above except the baked copper pyrophosphate powder was first mixed with phosphorous pentoxide powder (mol ratio of 1:1) before cold pressing. The phosphorous pentoxide powder was bought from Sigma Aldrich ®[22]. The mixed powder was then transferred to the 2-inch die and sintered at 500 °C for 2 hrs. The target did not show any shrinkage or cracking after

heat treatment (Figure 4.10).



Figure 4.10: The $Cu_2P_2O_7$ + P_2O_5 target (middle) clamped by a copper shield in the sputtering system. Scale of the image: 95 × 96 mm.

4.2.3 Substrate preparation for sputtering

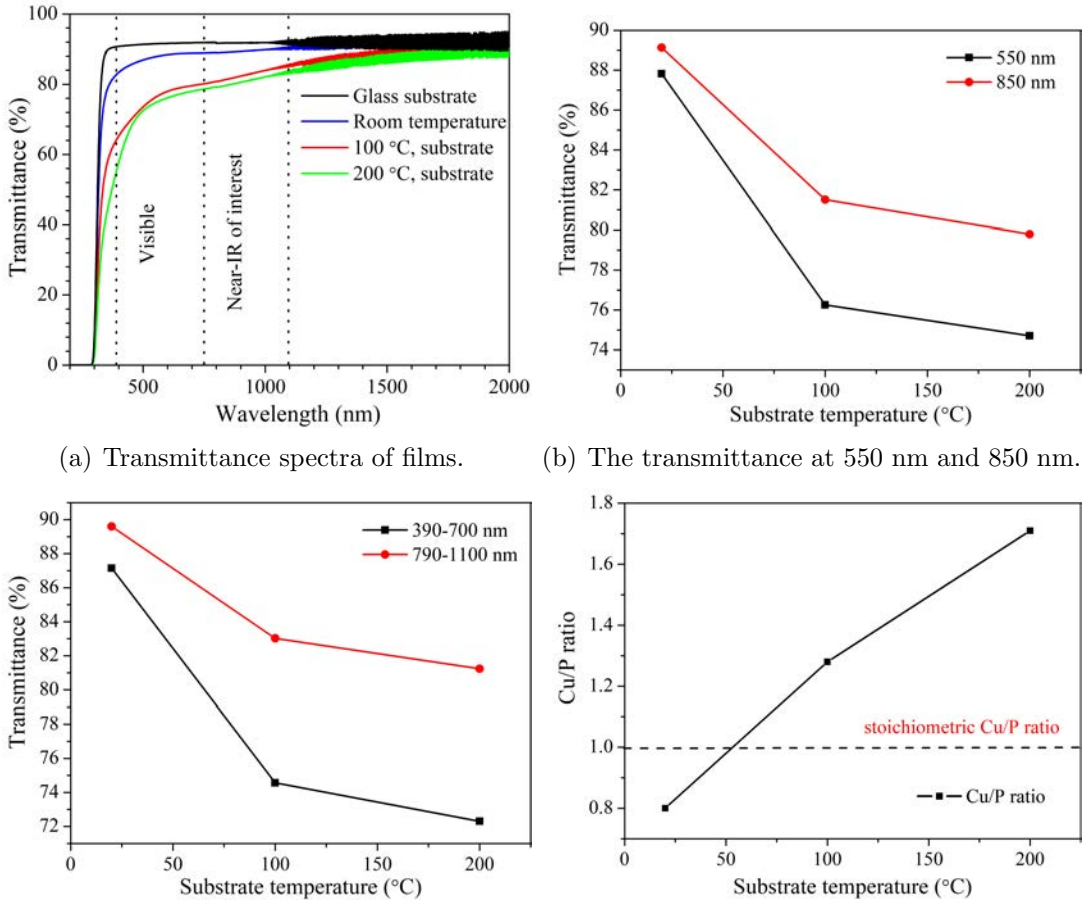
The glass substrates and sapphire substrates were ultrasonically cleaned in acetone (99.8+%) for 5 mins and ethanol (99.8+%) for 5 mins to remove the dust and chemical contamination on the surface of the substrates. The sapphire substrates are C-plane oriented and are used for compositional analysis in this study given that they do not contain either copper or phosphorus. Many glasses contain some phosphorous that could interfere with the analysis of Cu/P ratios in the deposited thin films.

4.3 Thin film preparation

As no previous research could be found on the preparation of copper pyrophosphate thin films, in order to produce films with desirable properties and stoichiometry, a variety of typical deposition parameters have been tested as a part of the empirical approach, including target composition, sputtering gas composition, substrate temperature, post-deposition annealing, sputtering power, pressure and duration. The results will be introduced as follow.

4.3.1 $Cu_2P_2O_7$ target + Ar gas

4.3.1.1 Substrate temperature



(a) Transmittance spectra of films.

(b) The transmittance at 550 nm and 850 nm.

(c) The average transmittance in the ranges of 390–700 nm and 790–1100 nm.

(d) Cu/P ratios of films.

Figure 4.11: Properties of films deposited from pure $Cu_2P_2O_7$ target in Ar gas at different temperatures (power: 30 W).

To start with, the pure copper pyrophosphate target was sputtered in Ar gas. The relationship between the temperature of substrate and the composition, structure and properties of films was studied first. Films were deposited onto a substrate mounted on the copper holder showed previously in Chapter 2. The copper holder was either at room temperature (unheated) or heated to 100 °C or 200 °C before deposition took place. These films were all sputtered at 30 W (power density: 1.48 W/cm^2) for 0.5 hr. Their transmittance spectra are shown in Figure 4.11(a). The spectrum of the glass substrate is also shown as a reference. The average visible transparency

for the borosilicate glass substrate is 91.3%. Optical fringes at higher frequency was detected in the infrared region of the spectra are generated by multiple reflections within the glass substrate (thickness: ∼0.17 mm). All of the films showed relatively high transparency in both the visible and 790–1100 nm regions. The film deposited at room temperature showed the highest transparency in both regions, 87.8% at 550 nm and 89.1% at 850 nm, and has an average transparency of 87.2% in the visible range (390–700 nm). For the samples deposited on preheated substrates, the transparency decreased to 76.3% (550 nm) / 81.5% (850 nm) for the 100 °C sample, and to 74.7% (550 nm) / 79.8% (850 nm) for the 200 °C sample. The visible transparency (average) decreased to 74.6% for the 100 °C sample and 72.3% for the 200 °C sample. However, although the visible transparency was good, the films did not show any absorption in the target NIR range (790–1100 nm). The reproducibility of the results will be tested later in this chapter.

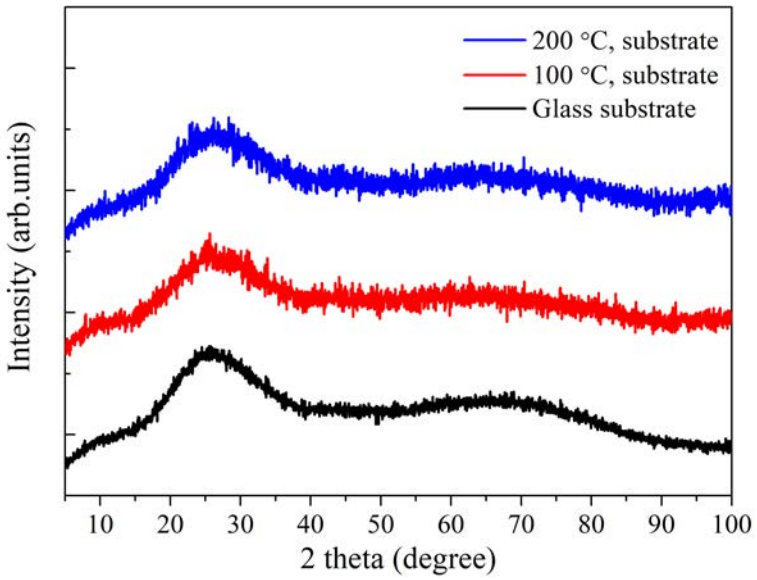
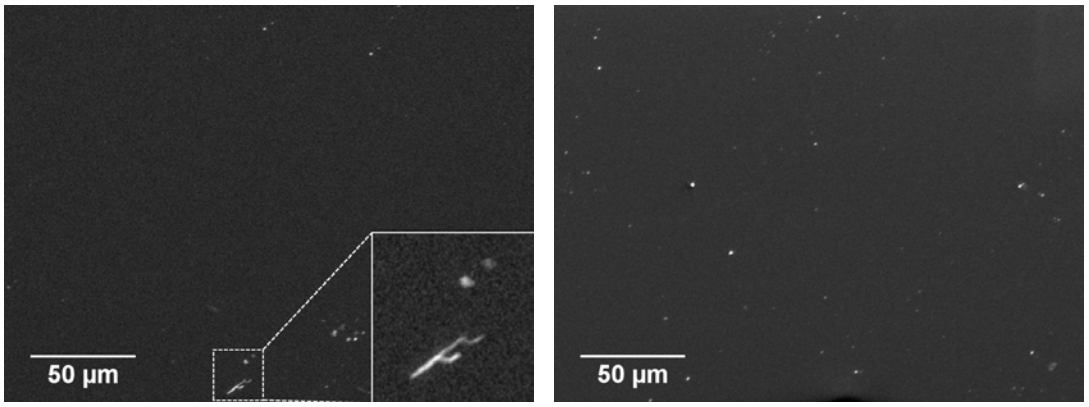


Figure 4.12: XRD spectra of selected films deposited at different substrate temperatures.

The XRD results (Figure 4.12) show that all these films are amorphous. This is probably due to the low substrate temperatures used that did not provide enough energy for atoms to migrate across the substrate surface and for the crystalline phase to nucleate. The films showed yellow-ish/brown-ish colour resembling that of



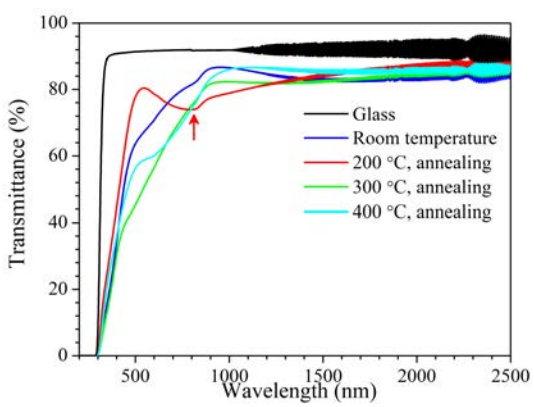
(a) Thin film deposited at room temperature. (b) Thin film deposited at 100 °C.

Figure 4.13: SEM images of selected films deposited at different substrate temperatures. The films show little surface feature in the SEM, regardless of the levels of brightness and contrast. The dusts on the films were used for focusing purposes to make sure the images are in-focus, as shown in the 25 × 25 µm magnified inset in subfigure (a) as an example.

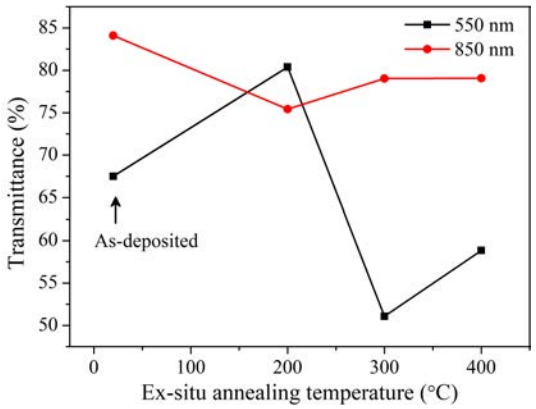
CuO/Cu_2O thin films [23, 24]. The SEM micrographs in Figure 4.13 show that the films have smooth surfaces, which is ideal for applications like window coating or multi-layer device. The EDS results show that the film deposited at room temperature has an Cu/P ratio of 0.8 while the films deposited at 100 °C and 200 °C have Cu/P ratios of 1.3 and 1.7 respectively. The increase in Cu/P ratio is probably due to the different dependence of sticking coefficient on substrate temperature between Cu and P. Another reason could be the difference between the vapor pressures of these two elements gets bigger as temperature increases (P > Cu) [25].

4.3.1.2 Post-deposition annealing

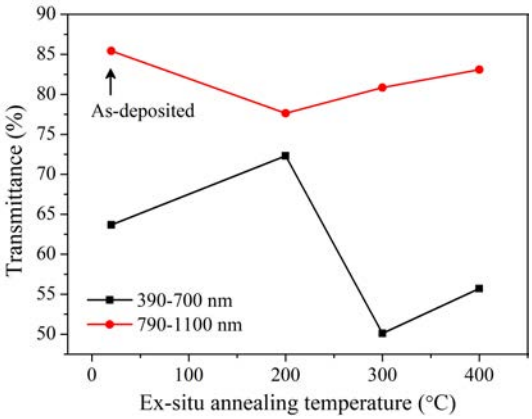
Post-deposition annealing has also been applied to investigate how this could affect their optical properties. These films were first deposited at room temperature for 1 hr at a power of 30 W (power density: 1.48 W/cm^2) and then transferred to a box furnace for heat treatment in air at 200 °C, 300 °C and 400 °C for 1 hr, respectively. Their optical properties are presented in Figure 4.14. It shows that after annealing at 300 °C and 400 °C both of the visible and infrared transmittance decreased.



(a) Transmittance spectra of films.



(b) The transmittance at 550 nm and 850 nm.



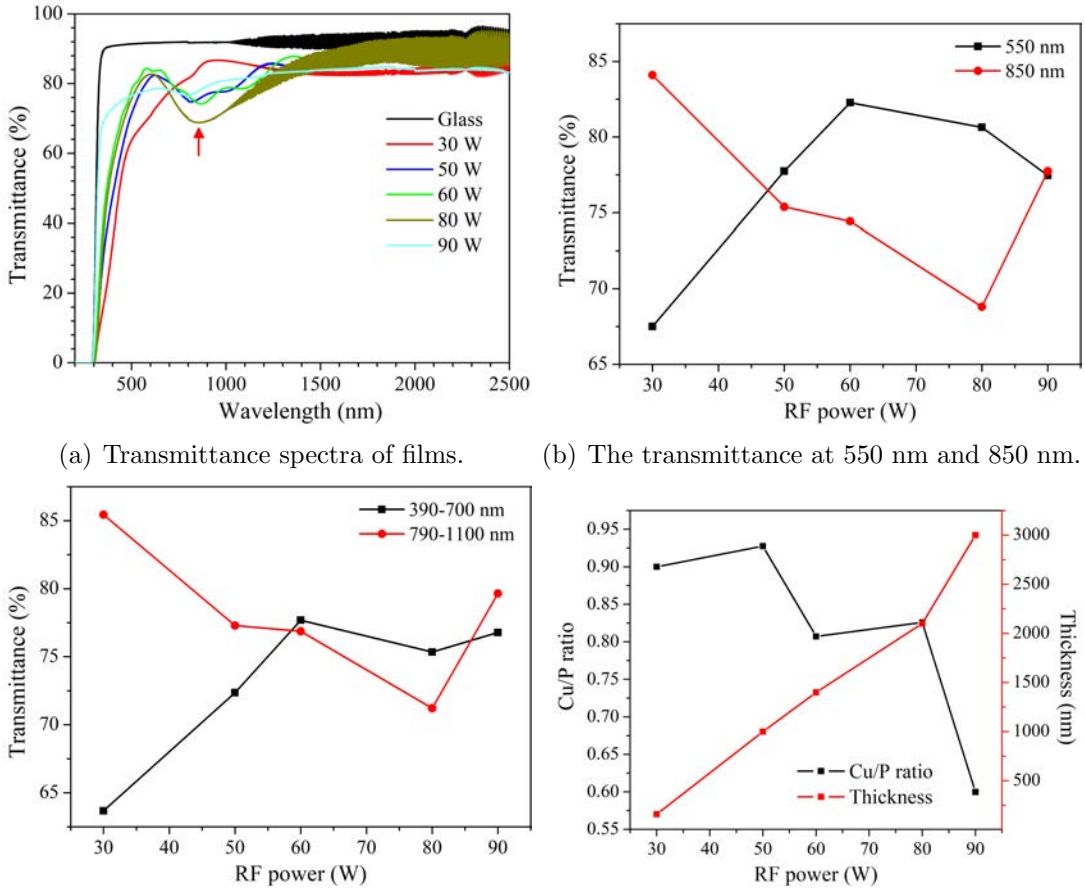
(c) The average transmittance in the ranges of 390–700 nm and 790–1100 nm.

Figure 4.14: Properties of films deposited from pure $Cu_2P_2O_7$ target in Ar gas and post-annealed at different temperatures (power: 30 W).

However, the film annealed at 200 °C showed a different change in optical properties. The transmittance at 550 nm increased from 67.5% to 80.4% while at 850 nm it decreased from 84.1% to 75.4%. The average transmittance in the 390–700 nm range also showed an increase from 63.7% to 72.3%, yet the average transmittance in the 790–1100 nm range decreased from 85.4% to 77.6%. This was the first time that I observed a transmittance at 550 nm greater than the transmittance at 850 nm, and the spectrum in Figure 4.14(a) shows a shallow absorption peak (arrowed). The XRD results (Figure A.1) show that these films are still amorphous and the SEM micrographs (Figure A.2) show that the films are also highly uniform. Since the features of the XRD spectra and the SEM micrographs

here are similar to the ones shown previously (Figures 4.12 and 4.13), the results are put in the Appendix A.

4.3.1.3 RF power



(a) Transmittance spectra of films.

(b) The transmittance at 550 nm and 850 nm.

(c) The average transmittance in the ranges of 390–700 nm and 790–1100 nm.

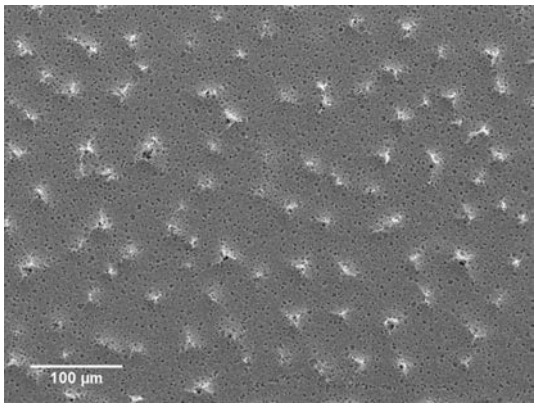
(d) Cu/P ratios and thicknesses of films.

Figure 4.15: Properties of films deposited from pure $Cu_2P_2O_7$ target in Ar gas with different powers at room temperature.

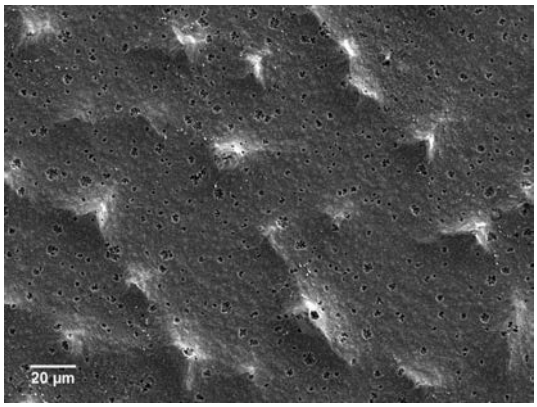
Sputtering power is one of the key parameters that can affect the properties of the deposited films. The relationship between the sputtering power and the structure, chemistry and properties of copper pyrophosphate films was studied by depositing films at room temperature for 1 hr using RF powers of 30 W (1.48 W/cm^2), 50 W (2.47 W/cm^2), 60 W (2.96 W/cm^2), 80 W (3.95 W/cm^2) and 90 W (4.44 W/cm^2), respectively. The resulted optical spectra are shown in Figure 4.15(a). It can be seen

that for the film sputtered at 30 W, no absorption peak could be observed at 850 nm. However for films sputtered at 50 W, 60 W and 80 W, absorption peaks started to present in the 790–1100 nm region. With a power of 90 W, the film showed a rather different UV-Vis-NIR spectrum compared to those sputtered at lower powers. Compared to the film sputtered at 30 W, for films sputtered at 50 W, 60 W and 80 W the transmittance at 550 nm show a general increase from 67.5% to 77.7%, 82.3% and 80.6%, while at the same time the transmittance at 850 nm decreased from 84.1% to 75.4%, 74.4% and 68.8%, respectively. For the film sputtered at 90 W, the transmittance at 550 nm increased to 77.5% and the transmittance at 850 nm decreased to 77.7% relative to the 30 W sample. However, the shape of the spectrum shows a clear difference compared to others, which will be further discussed below. It can also be seen in Figure 4.15(c) that the average transmittances in the 390–700 nm range and 790–1100 nm range showed similar trends, i.e. an increase of transparency in the visible range with stronger absorption in the NIR range. From this optical performance, it looks like the film sputtered at 80 W gives the best optical properties, but the sputtering target started to show small cracks when the films were sputtered at 80 W and 90 W, which is perhaps due to the limited thermal conductivity of this target. Therefore, for the rest of study, 60 W was used as an effective and safe choice of sputtering power. The XRD results (Figure A.3, Appendix A) show that the films are all amorphous and the SEM results (Figure A.4, Appendix A) show that the films sputtered at powers below 80 W are still highly uniform.

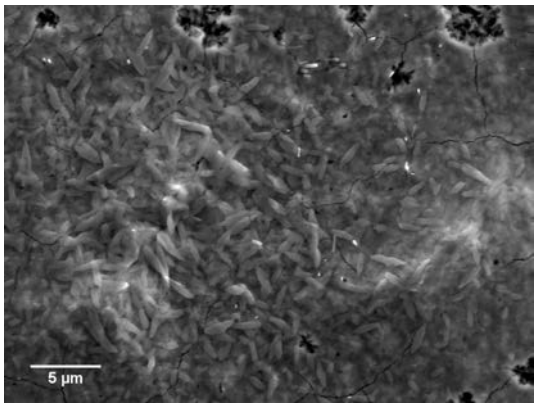
From Figure 4.15(d), it can be seen that the higher the power, the thicker the film is. The thickness of the film increased from 1000 nm to 3000 nm as power increased from 50 W to 80 W. This is because higher power generates more Ar ions and creates more collision events. Besides, high power gives the Ar ions more kinetic energy, and thus leads to higher penetration depth, a deeper collision cascade inside the target and thus generates more knocked-out surface atoms. Moreover, there would be more kinetic energy would be transferred to the removed atoms, which would thus have higher probability of reaching the surface of the substrate and form a stronger adhesion with the base.



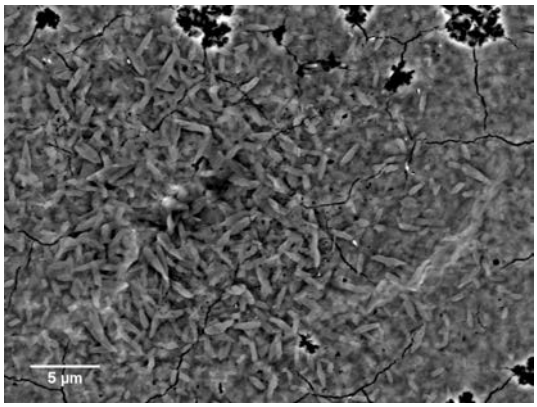
(a) SE image at low magnification.



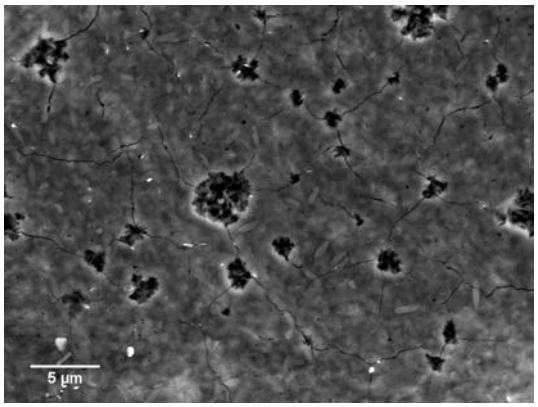
(b) SE image at high magnification.



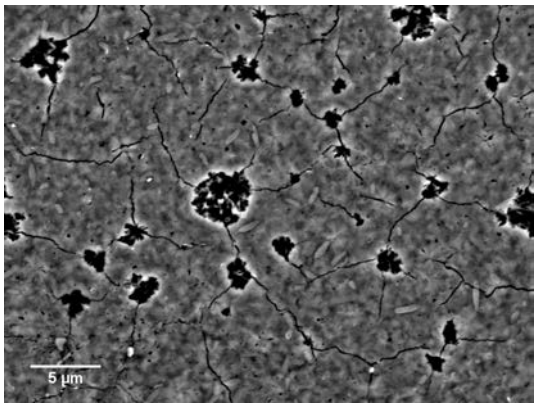
(c) Needle-shape features shown in SE image.



(d) BSE image of the needle-shape features.



(e) Cracks on the surface shown in SE image.

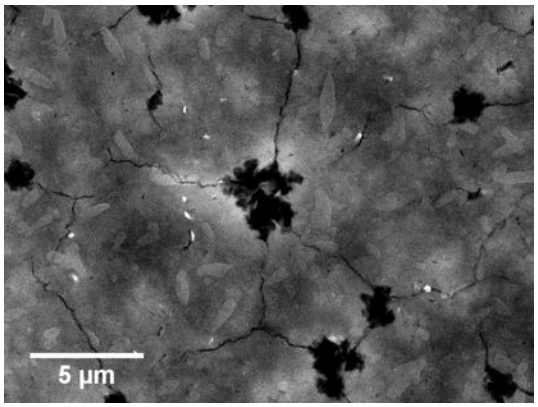


(f) BSE image showing the cracks.

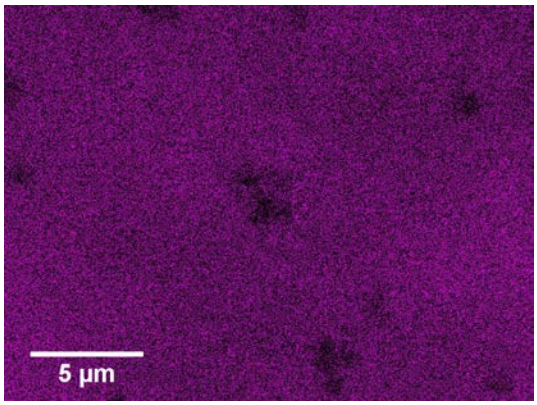
Figure 4.16: SEM images of the film deposited at 90 W in Ar from the $Cu_2P_2O_7$ target.

For the film sputtered at 90 W, SEM imaging shows a surface morphology different from all the other films. As shown in Figure 4.16, at lower magnification, the SEM image (Figure 4.16(a)) shows plenty of bumps on the surface, mostly with a 3-fold

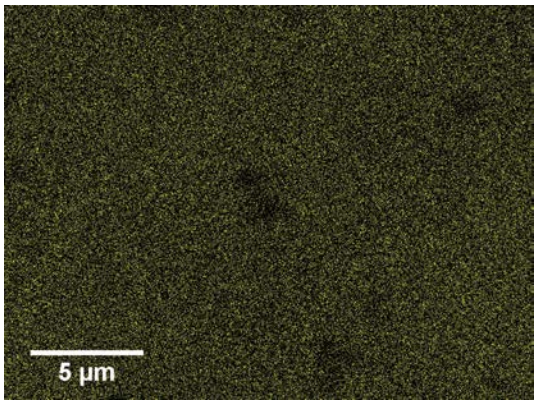
or 4-fold symmetry. At higher magnification (Figure 4.16(b)), voids on the surface in between these bumps can be seen more clearly. The size of the voids (black) are mostly between 500 nm – 2 μm. As the magnification is further increased, one can see needle-shaped areas (Figure 4.16(c)) on the surface, which showed more obvious contrast in the back-scattered electron images (Figure 4.16(d), 4.16(f)), indicating there might be a difference in average atomic mass in these areas compared to the rest of the films.



(a) SE image of the studied area.



(b) P map.



(c) Cu map.

Figure 4.17: EDS maps of the film deposited at 90W from pure $Cu_2P_2O_7$ target in Ar gas.

To further investigate variations in phase composition in the film deposited at 90 W, high resolution EDS analysis was carried out. From the EDS elemental maps for Cu, P, O, C and Al (Figure 4.17) no contrast could be seen in the needle-shaped phase while there is clearly a difference in the BSE images. Further point/local EDS

analysis did not show any detectable chemical difference in these two regions either.

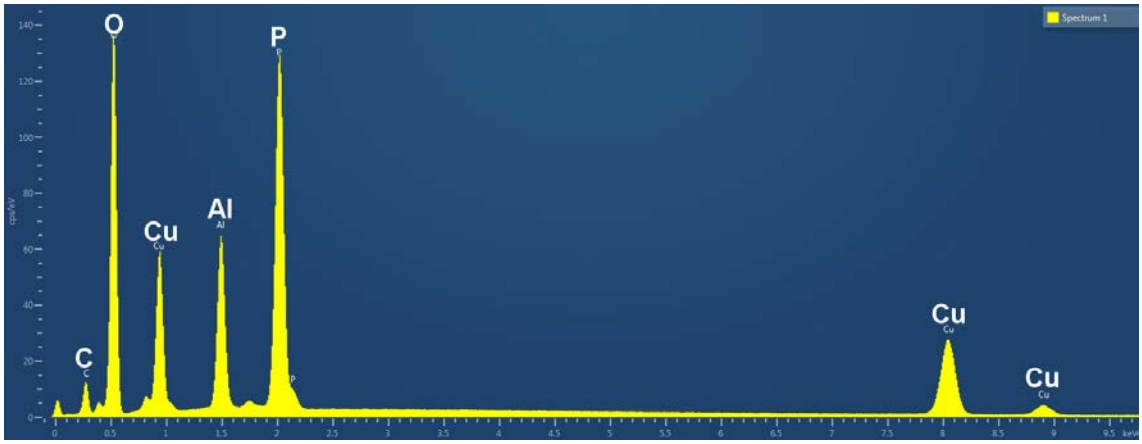


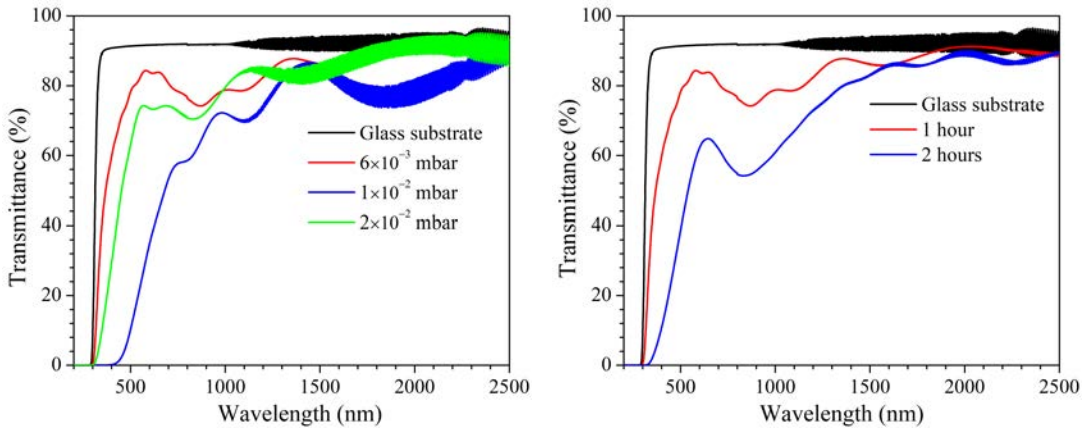
Figure 4.18: EDS spectrum (0–9.7 keV) of the film deposited at 90W from pure $Cu_2P_2O_7$ target in Ar gas.

After the electron beam has been scanning the same area for a few seconds, small bubbles started to appear from the edges of the cracks in the image (Figure 4.16(e), 4.16(f)). One plausible explanation for this is that the small bubbles were actually created by trapped water, and the needle-shape areas are the hydrated compounds, and that is why EDS mapping could not show any difference in composition because hydrogen cannot be detected by EDS. A possible explanation for the existence of the hydrated phase is that the sample has a much higher phosphorous content (Figure 4.15(d)) which could easily attract water vapour given phosphorous oxides are mostly hygroscopic [26]. This could also explain the formation of cracks and voids on the surface. It is likely that when the film was taken out from the sputtering chamber it did not contain any hydrated compound, but after being exposed to air for some time the film started to react with water molecules in the air and generated hydrated products. The formation of the new phase modified the local lattice structure and thus created a structural mismatch between the hydrated and non-hydrated parts and generated strains that led to the development of cracks, voids and bumps on the surface. In the SEM images, small bubbles were appearing from these hydrated regions. In fact, the shape of the voids on the surface resembles that of an ink droplet on a paper. It is worth mentioning that no Ar peaks (2.96 keV) could be found in

the EDS spectra (Figure 4.18), which rules out the possibility of the bubbles being Ar gas trapped in the film.

At this stage in the project, it had become clear that adding extra phosphorous into the target would produce films with high phosphorous contents, which could enable me to explore how films with high phosphorous content would behave which could further verify the speculation on the hygroscopic behavior.

4.3.1.4 Sputtering pressures / durations



(a) Transmittance spectra of films deposited at different pressures.

(b) Transmittance spectra of films deposited for different times.

Figure 4.19: Properties of films deposited from pure $Cu_2P_2O_7$ target in Ar gas at room temperature and a power of 60 W (2.96 W/cm^2) with different sputtering pressures and durations.

Apart from the sputtering power, the effects of different sputtering pressures and durations have also been explored. In Figure 4.19(a), it can be seen that with higher gas pressure during sputtering, the films become less transparent in the visible range while not showing much change in the NIR range, which is even further from the desired shape of the spectrum. If the pressure is too low, the sputter rate would be too low (or the plasma cannot be sustained at all) and thus make film deposition less efficient. Therefore, for the rest of the study, 6×10^{-3} was used as the sputtering pressure unless otherwise stated. For films sputtered for longer times (Figure 4.19(b)), the absorption in NIR range increased, yet was accompanied by a significant decrease of transparency in the visible range in this case.

4.3.2 $Cu_2P_2O_7$ / P_2O_5 target + Ar gas

In this section, films sputtered from the $Cu_2P_2O_7$ / P_2O_5 target with mol ratio 1:1 will be discussed. The reason that this mol ratio was chosen is because from the previous results, films with Cu/P ratio of 1.7 (Figure 4.11(d)) have been made at substrate temperature of 200 °C, so to produce films with an ideal Cu/P ratio of 1, a significant amount of extra phosphorous needs to be added to the target, especially for films deposited at high substrate temperatures. However, compared to the films sputtered from the pure copper pyrophosphate target, these films showed very different behavior. Various sputtering parameters were used to deposit thin films, including: RF power from 30 to 90 W (power densities: 1.48–4.44 W/cm^2), substrate temperatures from room temperature (20 °C) to 400 °C, post-annealing temperatures from 200 to 400 °C for films deposited at room temperature. Most of the films showed a consistent and uniform surface when they were first taken out from the sputtering chamber, but once they were in contact with the air, the surface started to react and crack quickly. In general after around 5 hrs the films would deliquesce into liquid droplets as shown in Figure 4.20.



Figure 4.20: Picture of the film deposited from $Cu_2P_2O_7$ / P_2O_5 target after 5 hrs in the air. The film was deposited at room temperature using RF power of 30 W (1.48 W/cm^2) for 1hr. Scale of the image: 36 × 18 mm.

This shows that these films made from target that contains a higher P content are highly hygroscopic, and react with the water molecules rapidly once they are exposed to air. A series of optical microscopy images have been taken to show the development of cracks on the surface of a typical film (Figure 4.21). These images recorded the

transformation of the film surface from 3 mins to 30 mins after being taken out from the chamber. It can be seen that after only 3 mins, the film has already split into several pieces due to the reaction, and some pieces on the surface slowly disappeared under the optical microscope during the observation period (red arrow in the figure). The darker bits are the remained film while the lighter pathways in between are the cracks on the surface, which widened as time increased.

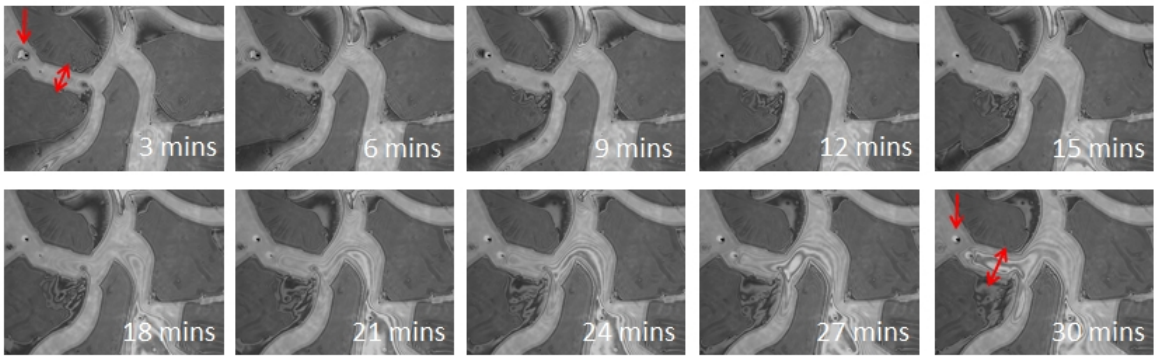


Figure 4.21: Optical microscopy images showing the transformation of film surface over time. The film was deposited at room temperature using RF power of 30 W (1.48 W/cm^2) for 1hr. Scales of each image: 1.8 mm × 1.3 mm.

Because the films reacted and became droplets quickly, it is difficult to measure their optical spectra, chemical composition and structure. Only for the films that did not fully react could these measurements be carried out, and the results are shown in Figure 4.22. The only films that did not turn into droplets were either post-annealed at temperature of 400 °C or deposited at substrate temperatures equal or above 200 °C. For the sample post-annealed at 400 °C (labelled 'annealing' in Figure 4.22), the stability in air could be explained by the fact that the boiling point of phosphorous pentoxide is 360 °C (at 1 atm), and only above this temperature could the major hygroscopic component of the film be evaporated. Below this annealing temperature, phosphorous pentoxide could not be removed and would stay in the films and kept the films hygroscopic as observed. The films post-annealed at 300 °C or below started to react with water a few minutes once they were taken out from the furnace. For films that were deposited at substrate temperatures of 200, 300 and 400 °C (the last two are labelled 'substrate' in Figure 4.22), the reason that they remained stable is

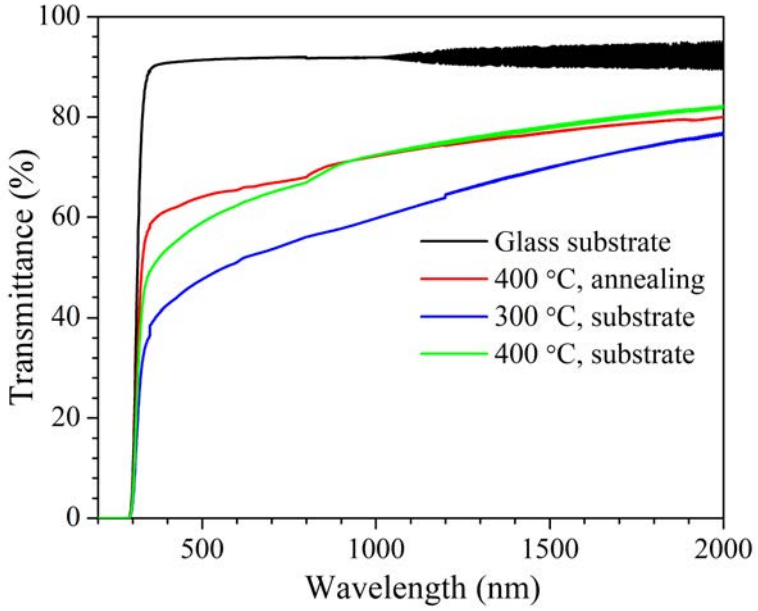
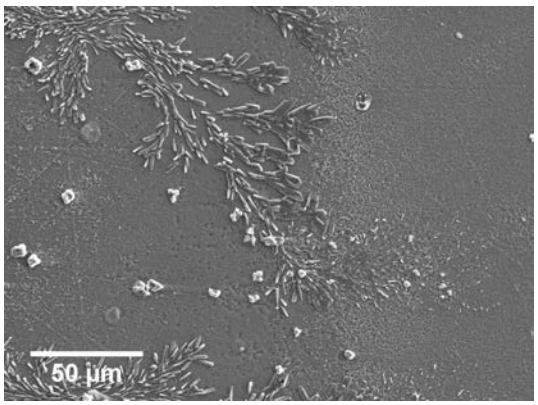


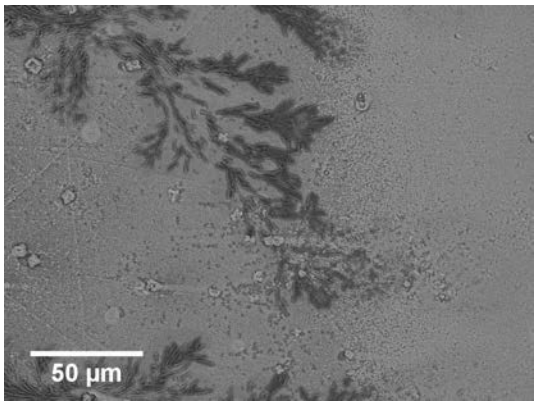
Figure 4.22: Transmittance spectra of films deposited and processed at several different conditions from the $Cu_2P_2O_7$ / P_2O_5 target (substrate temperatures: 300 °C, 400 °C, post-annealing temperature: 400 °C; power: 30 W (1.48 W/cm^2) for all three samples shown here).

probably because during the sputtering process the pressure inside the chamber is much lower than atmospheric pressure, and reduced the boiling point of phosphorous pentoxide from 360 °C to below 200 °C. In terms of their optical performance, all of the films are not very transparent and showed no absorption in the NIR range, as shown in Figure 4.22.

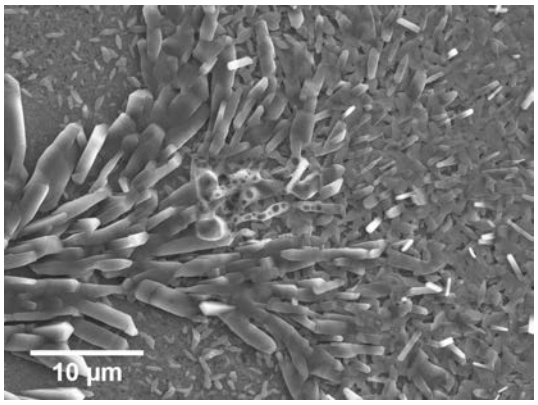
SEM analysis have been carried out on some of the films. The SEM images show that the film made by the P loaded target formed uneven structure compared to the generally smooth surface of the films deposited from the pure $Cu_2P_2O_7$ target. Dendritic features were found on the film deposited at a substrate temperature of 300 °C (Figure 4.23). The EDS maps (Figure 4.24) on the same area show that the 'stem' of the dendrite is made of P rich components (darker area in the BSE image). In fact, after a few minutes under the electron beam (around 3–5 minutes), the stem part started to react and change its shape. By shifting the mapping area in Figure 4.24 for ∼10 μm, one could easily see the difference before and after reaction (Figure 4.25).



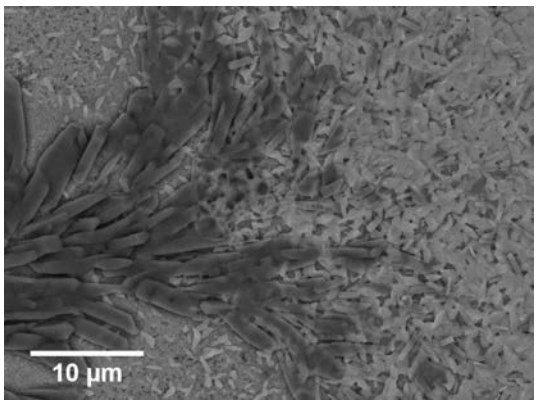
(a) SE image showing the dendritic features on the film.



(b) BSE image of the film.



(c) SE image of the dendritic structure at higher magnification.

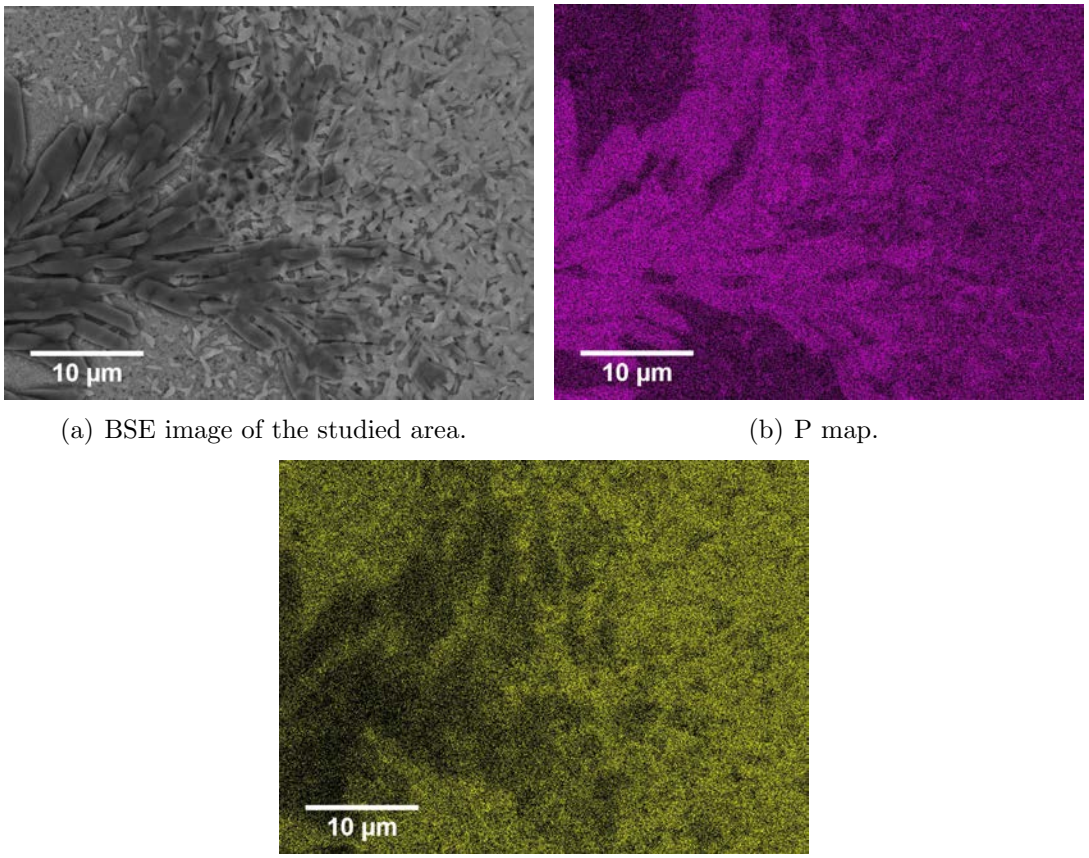


(d) BSE image of the film.

Figure 4.23: SEM images of the film deposited at substrate temperature of 300 °C from $Cu_2P_2O_7$ / P_2O_5 target in Ar gas.

In the SEM images one can also see spherically-shaped (or 'flower bud' shaped) features on top of the dendrites (Figure 4.26).

By performing EDS mapping, it could be seen that the spherical features have different chemical composition than the dendrites. In the spherical regions, both copper and phosphorous maps showed strong contrast while in the dendrite region only the phosphorous maps showed clear difference from the substrate (Figure 4.27). In order to understand the chemical difference between these two regions more clearly, linescans were performed, as shown in Figure 4.28. It can be seen from the counts per second (cps) subfigure that few counts of Cu could be detected from the dendritic area. Similar counts of Cu and P were obtained from the spherical area. In terms of



(a) BSE image of the studied area.

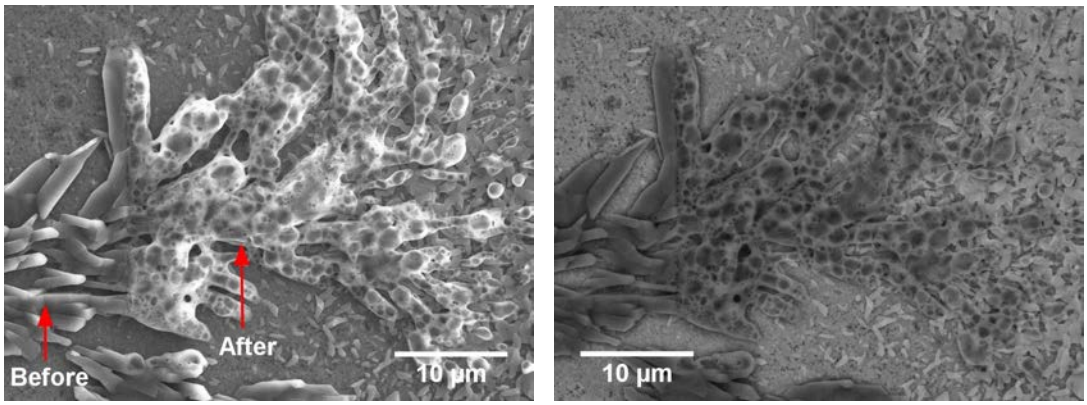
(b) P map.

(c) Cu map.

Figure 4.24: EDS maps of the film deposited at substrate temperature of 300 °C from $Cu_2P_2O_7$ / P_2O_5 target in Ar gas.

the rest of the film, neither Cu nor P signals were strong, which implies that there is very thin or almost no film outside the areas of dendrites and spheres. By calculating the atomic percents of elements from the cps values, one could see the Cu/P ratio of the spherical areas is close to 1 in most of the places. Very little damage showed in the spherical area compared to the dendrites after the sample was exposed to the electron beam for a few minutes (Figure 4.29).

For the sample deposited at a substrate temperature of 200 °C, similar phenomena were detected. Different areas with different chemical compositions were detected, as shown in Figure 4.30. The copper are aggregated only in the spherical features, while the phosphorous also exist in the 'matrix' part (similar to the dendritic part described in Figure 4.27). The shapes of the features and and the chemical distribution can be



(a) SE image of the shifted area with red arrows showing the contrast before and after reaction.

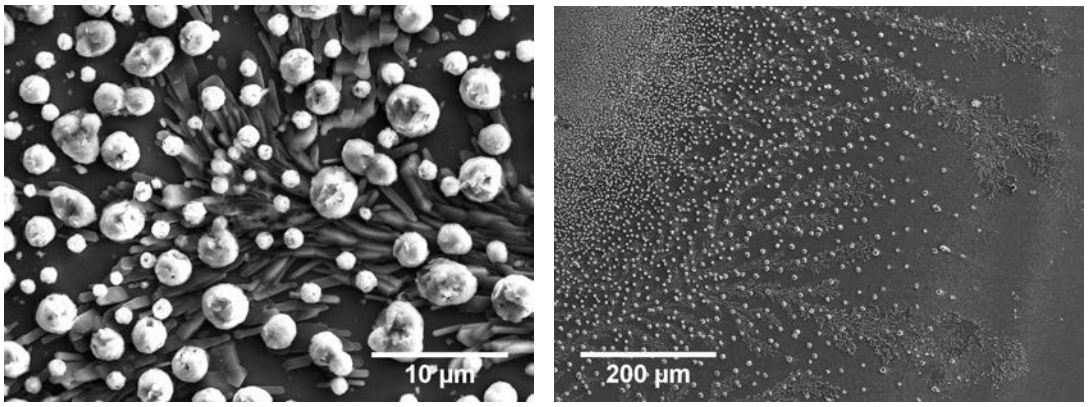
(b) BSE image of the shifted area.

Figure 4.25: SEM images of the same area in Figure 4.24(a) but shifted 10 µm after reaction with electron beam (accelerating voltage: 10 kV).

seen more clearly in the maps at higher magnification (Figure 4.31).

Like the sample deposited at 300 °C, here, the copper rich area showed little change after exposure to electron beam compared to the phosphorous rich area, which indicates that the presence of copper might be crucial for the sample's stability under the electron beam.

Although the films did not show ideal optical properties, they showed great potential as amperometric sensors for water. Traditionally, an amperometric sensor is made of an electrolysis cell that would quantitatively and continuously absorb water entering into the system and will then electrolyze the water into hydrogen and oxygen. The system then measure the electrolysis current to obtain the amount of water in the environment. P_2O_5 thin films have long been a popular choice as the absorbent layers due to their high water affinity [27, 28]. However, this thin layer of phosphorous pentoxide is usually manufactured by pasting the substrate with H_3PO_4 syrup and electrolyzing it afterwards until it is dry. The process of drying can take up to several days, sometimes even weeks. The results above show that instead of applying paste and drying for a long period of time, one can produce this highly water-sensitive layer by sputtering, and could easily deposit a protective layer on top if needed. The vacuum system provides a natural protection for the

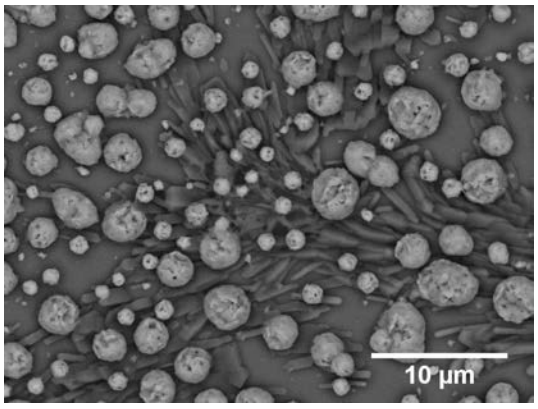


(a) SE image showing the 'flower buds' and dendrites features.

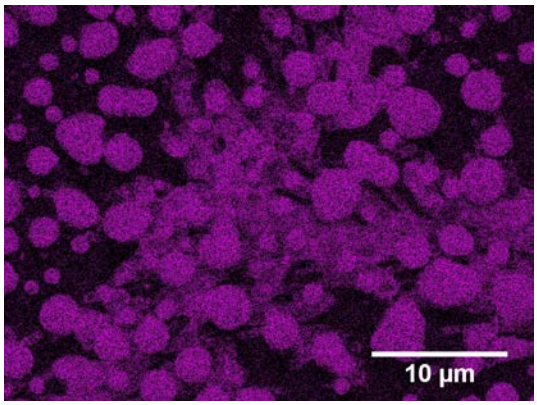
(b) SE image at lower magnification.

Figure 4.26: SEM images of the film deposited at a substrate temperature of 300 °C from $Cu_2P_2O_7$ / P_2O_5 target in Ar gas.

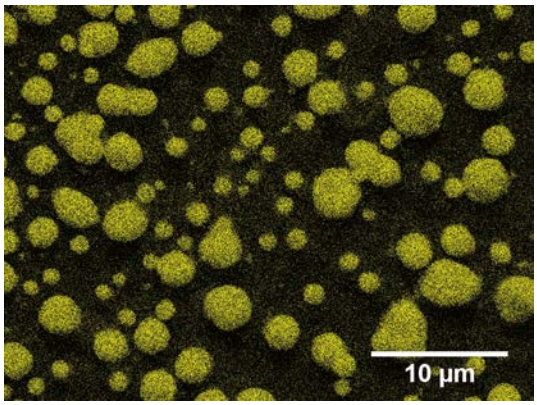
hydroscopic layer and even allows manufacturers to do all the assembling in-situ without having any contact with the atmosphere. However, as the main purpose of the thesis is to make NIR absorbing films that are stable in the air, research on these hygroscopic P loaded films were not further pursued in this study.



(a) BSE image of the studied area.



(b) P map.



(c) Cu map.

Figure 4.27: EDS maps of the film deposited at a substrate temperature of 300 °C from $Cu_2P_2O_7$ / P_2O_5 target in Ar gas.

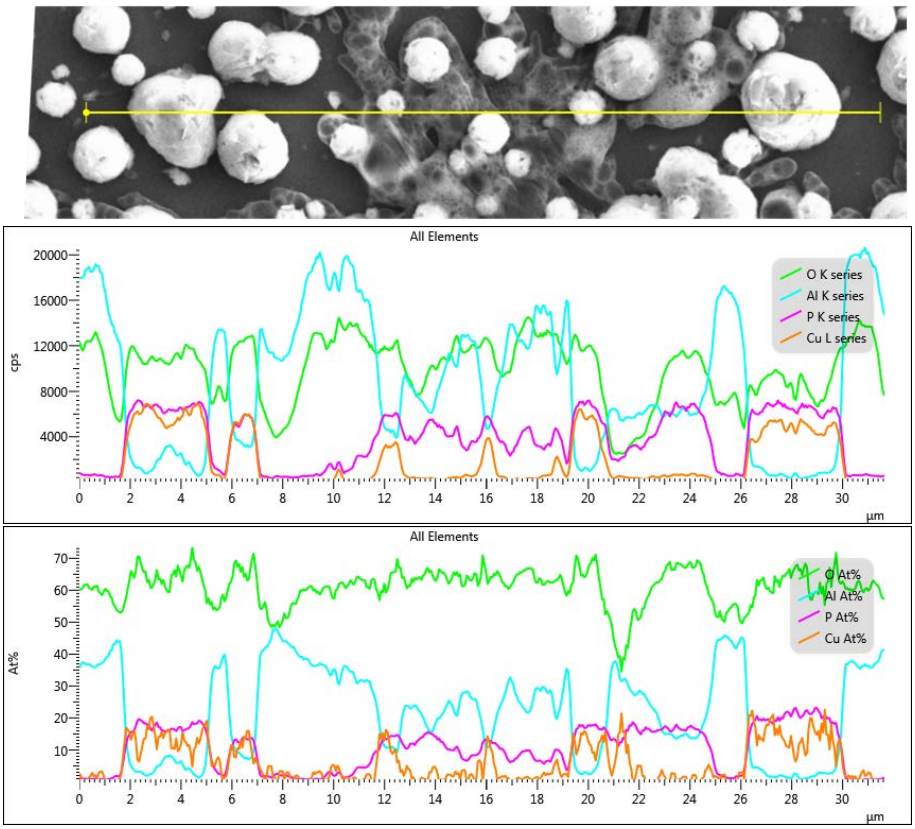
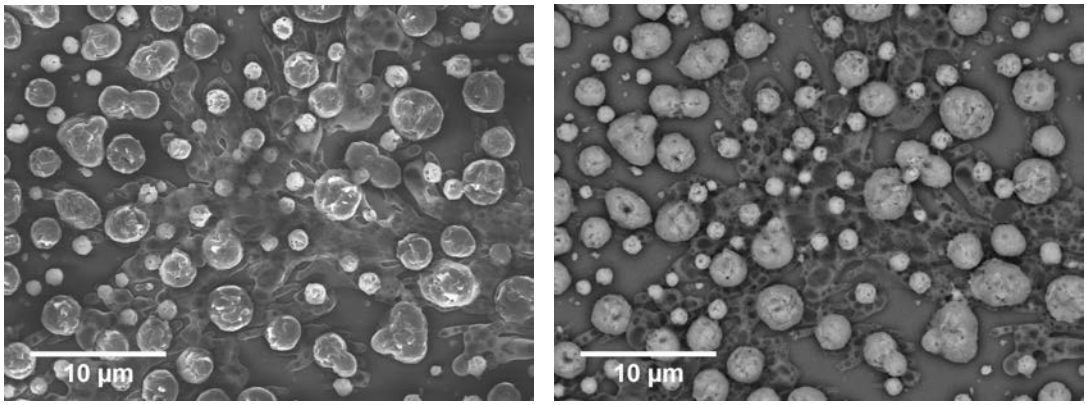
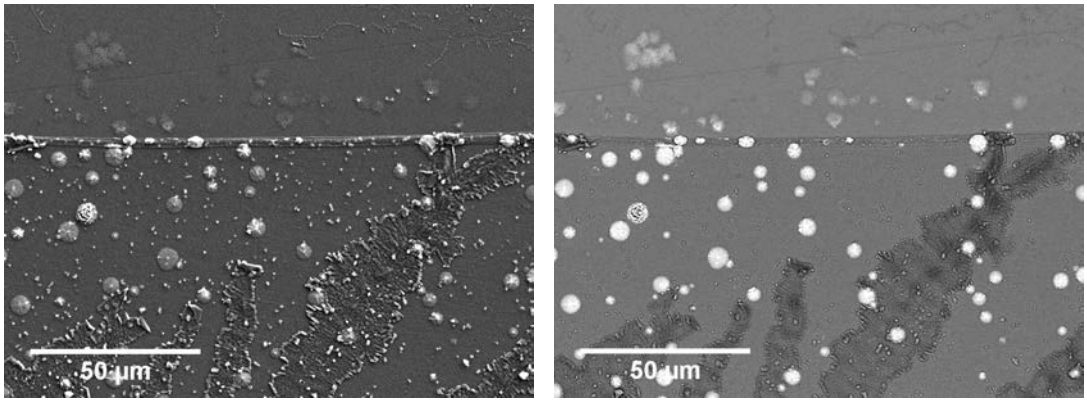


Figure 4.28: EDS line scan on the film deposited at a substrate temperature of 300 °C from $Cu_2P_2O_7$ / P_2O_5 target in Ar gas. The graph includes the scan region (top), cps scan result (middle) and at% scan result (bottom).



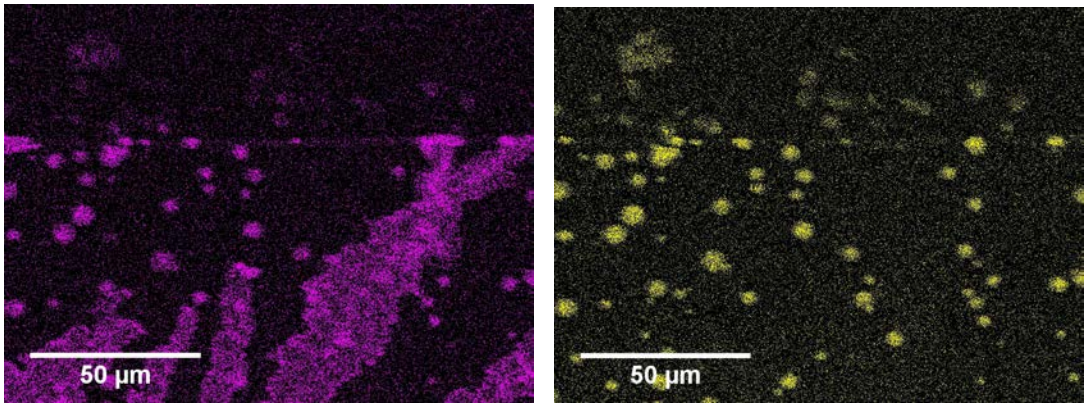
(a) SE image. (b) BSE image.

Figure 4.29: SEM images of the film deposited at a substrate temperature of 300 °C after reaction with the electron beam (accelerating voltage: 10 kV).



(a) SE image of the studied area.

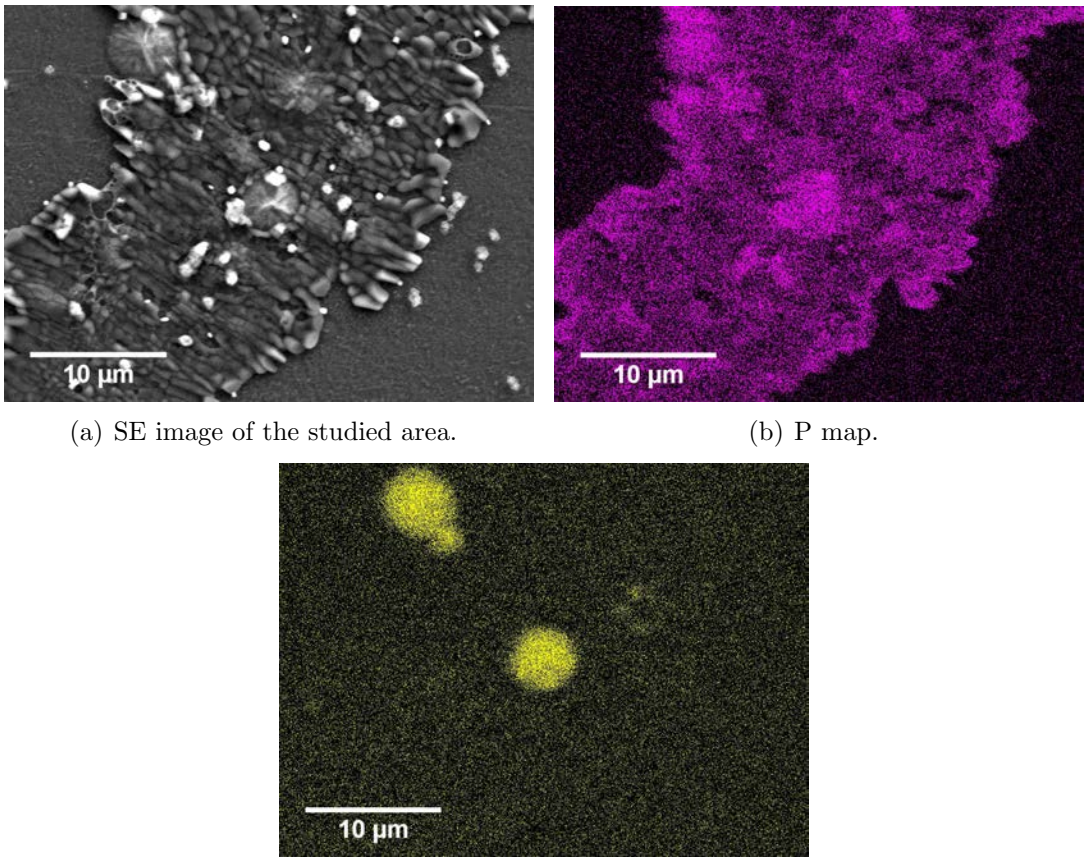
(b) BSE image of the studied area.



(c) P map.

(d) Cu map.

Figure 4.30: EDS maps of the film deposited at a substrate temperature of 200 °C from $Cu_2P_2O_7$ / P_2O_5 target in Ar gas.

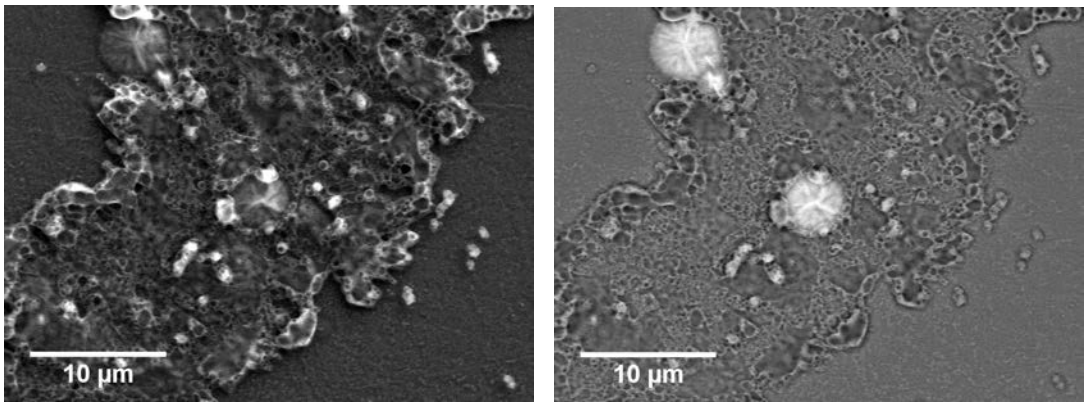


(a) SE image of the studied area.

(b) P map.

(c) Cu map.

Figure 4.31: EDS maps (high magnification) of the film deposited at a substrate temperature of 200 °C from $Cu_2P_2O_7$ / P_2O_5 target in Ar gas.



(a) SE image.

(b) BSE image.

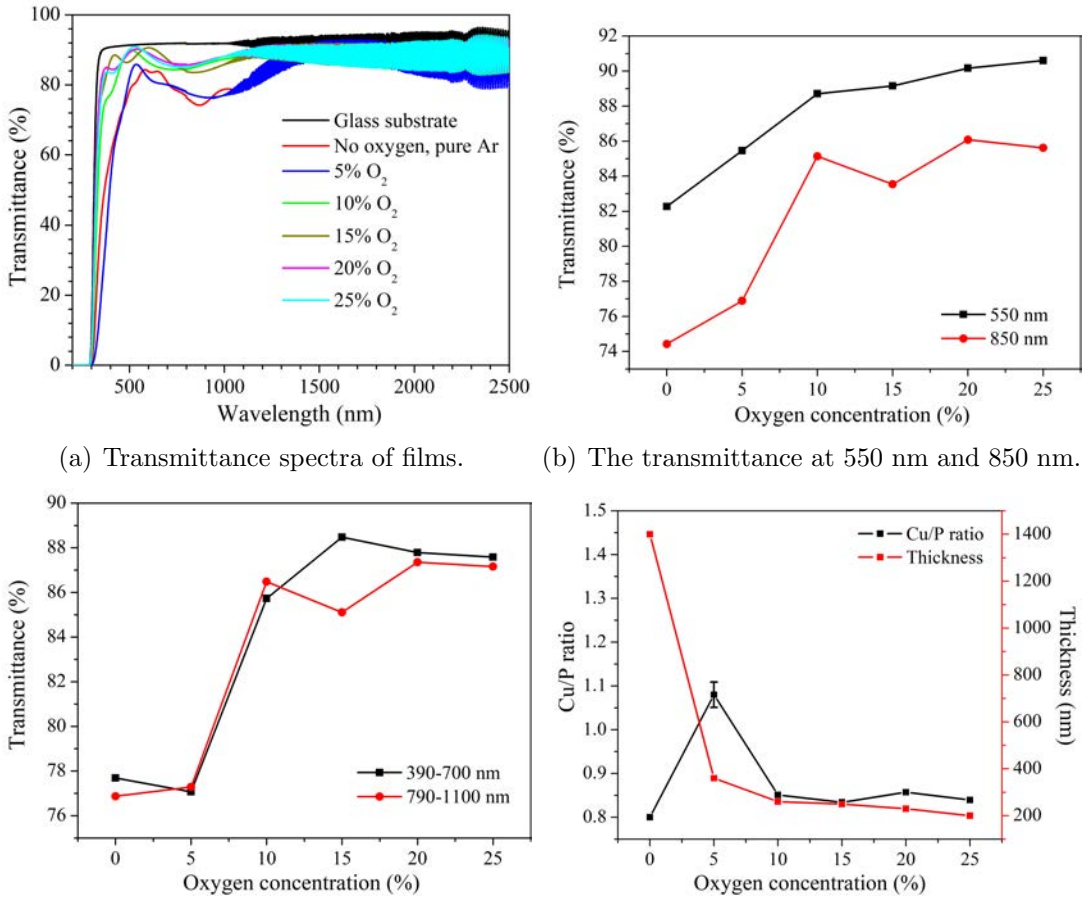
Figure 4.32: SEM images of the film deposited at a substrate temperature of 200 °C after reaction with electron beam (accelerating voltage: 10 kV).

4.3.3 $Cu_2P_2O_7$ target + Ar / O_2 gas

Another important consideration in the sputtering of copper pyrophosphate is that non-stoichiometry can not only happen to the phosphorous, but also the oxygen content, especially in this case where relatively high concentration of oxygen is required to form the $Cu_2P_2O_7$ phase. To investigate whether the oxygen content has an influence on the films performance, Ar mixed with O_2 gas was used for sputtering under different conditions.

The relationship between the oxygen percentage and the optical performance was first investigated. From the studies above, optimised power and pressure parameters have been defined, so these films were deposited at 60 W (2.96 W/cm^2) at room temperature for 1 hr, with sputtering pressure of 6×10^{-3} mbar. The reason for choosing room temperature is that it makes film with Cu/P ratio closest to the stoichiometric value (Figure 4.11(d)). The resulting optical spectra are shown in Figure 4.33(a). The spectrum of the film deposited in 5% O_2 / Ar gas did not show much difference from the one deposited in pure Ar, but for the films sputtered in gas with higher oxygen content (10%, 15%, 20% and 25%), the spectra showed broader windows in the visible range but the absorption peaks also shift toward shorter wavelengths, close to the visible range. Although this shift is not favourable, it will be shown later that it can be controlled simply by changing the film thickness.

From Figure 4.33(b), it can be seen that compared to the film sputtered in pure Ar gas, the transmittance at 550 nm increased from 82.3% to 85.5%, 88.7%, 89.2%, 90.2% and 90.6% for samples sputtered with 5%, 10%, 15%, 20% and 25% oxygen, respectively. The transmittance at 850 nm increased from 74.4% to 76.9%, 85.1%, 83.5%, 86.1% and 85.6% for these samples, respectively. One major reason for the increase of transmittance at both wavelengths is probably the reduction of thickness shown in Figure 4.33(d). Meanwhile, the average visible and NIR transmittance also show considerable enhancement as the oxygen concentration increases in the sputtering gas, though here the differences between the visible and NIR transmittance are still small for most of the samples.



(a) Transmittance spectra of films.

(b) The transmittance at 550 nm and 850 nm.

(c) The average transmittance in the ranges of 390–700 nm and 790–1100 nm.

(d) Cu/P ratios and thicknesses of films. The Cu/P ratio error bar of the 5% sample is calculated from the ratio values of multiple sites on one film.

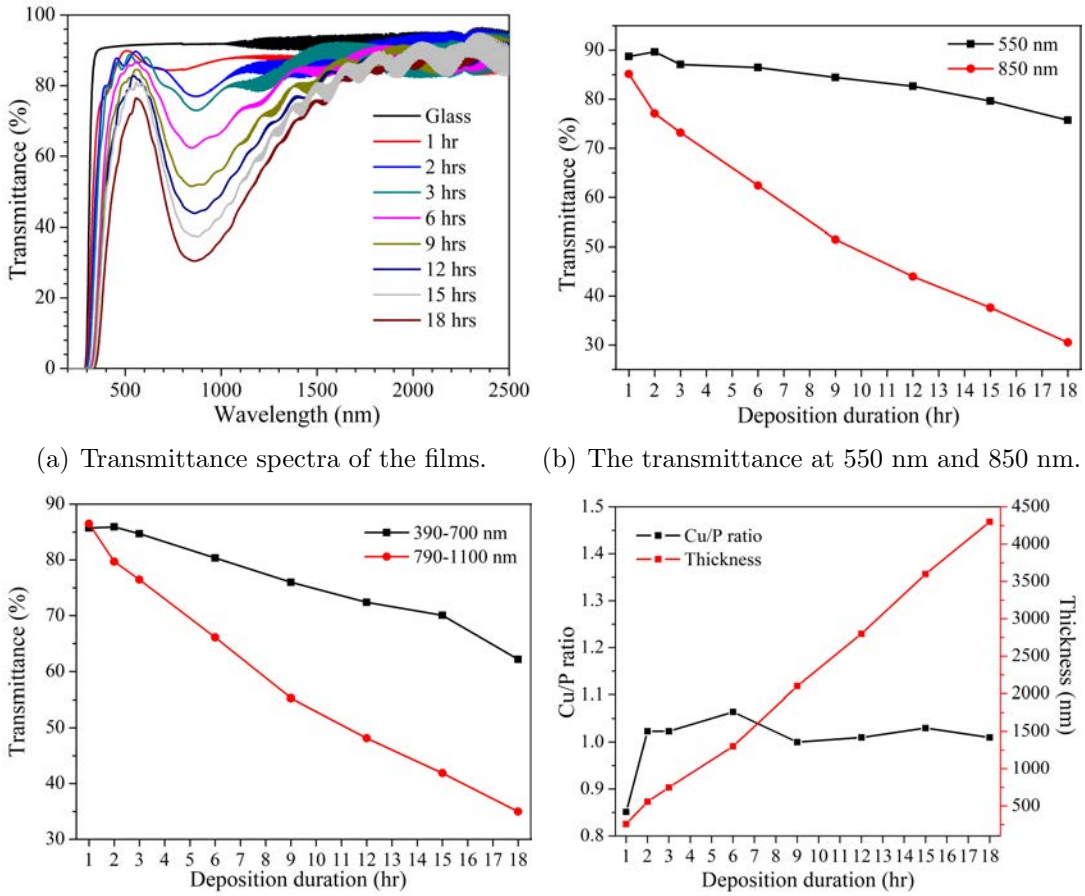
Figure 4.33: Properties of films deposited from the pure $Cu_2P_2O_7$ target in Ar / O_2 gas with different amounts of O_2 (60 W, room temperature).

In fact, it is interesting to see in Figure 4.33(d) that the introduction of oxygen drastically reduced the thickness of the film. There are several possible reasons for this. Firstly, oxygen ion that carries negative charge (O^-, O_2^-) would move towards the substrate while the argon ions and the positive oxygen ions (O^+, O_2^+) are accelerated towards the target. The high energy negative oxygen ions could thus contribute to re-sputtering of the deposited film [29]. It is also possible that while the oxygen ions are moving in the reverse direction to the rest of the plasma, the collision between these two groups of ions could reduce the sputter yield. Besides, in this study the total flow rate of the gas remained the same, meaning the higher the

oxygen flow rate was, the smaller the argon flow rate must be, which would further reduce the average sputter yield. Moreover, the introduction of oxygen might affect the microstructure, bonding and chemical composition (especially the oxygen content) of the deposited thin film, which are all connected with the thickness. Similar oxygen-induced reduction in thickness has been reported by previous research on the sputtering of other oxide films as well [30].

Figure 4.33(d) shows that by adding 5% O_2 to the sputtering gas, the Cu/P ratio increased from 0.8 to about 1.1. By adding more O_2, the Cu/P ratios of the deposited films drop back to between 0.8 and 0.9. The SEM micrographs (Figure A.6, Appendix A) show that the films all have uniform surfaces. The XRD results (Figure A.5, Appendix A) show that the films deposited with different levels of oxygen are all amorphous.

Even though the films showed absorption near the target NIR range, the absorption peaks are still not strong enough. In order to increase the absorption in the NIR range, longer sputtering times were used to increase the thickness of the film to counteract the effect of O_2 in the sputtering gas reducing film thickness. In this part of the project, samples from three oxygen percentages, 10%, 15% and 20%, were studied. Figure 4.34 shows the relationship between the thickness of film and the optical performance for samples sputtered in 10% O_2 / Ar gas. It can be seen that as the sputtering duration increased, the absorption in the NIR range became stronger as well. The transmittance at 850 nm showed a relatively linear decrease from 85.1% to 30.5% as the sputtering time increased from 1 hr to 18 hrs, while at 550 nm, in the visible range, only showed a comparatively small decrease from 88.7% to 75.8%. The film sputtered for 18 hrs showed absorbance over 60% at 850 nm given that the average transmittance of glass is 91.3% in the 390–1100 nm range. The average transmittance in the 790–1100 nm range also showed a significant decrease from 86.5% to 35.0% as the sputtering duration increased, while the transmittance in the 390–700 nm range only decreased from 85.7% to 62.2%. Figure 4.34(d) shows the expected linear correlation between the thickness of the film and the deposition duration. It can be seen in Figure 4.34(a) that by merely



(a) Transmittance spectra of the films.

(b) The transmittance at 550 nm and 850 nm.

(c) The average transmittance in the ranges of 390–700 nm and 790–1100 nm.

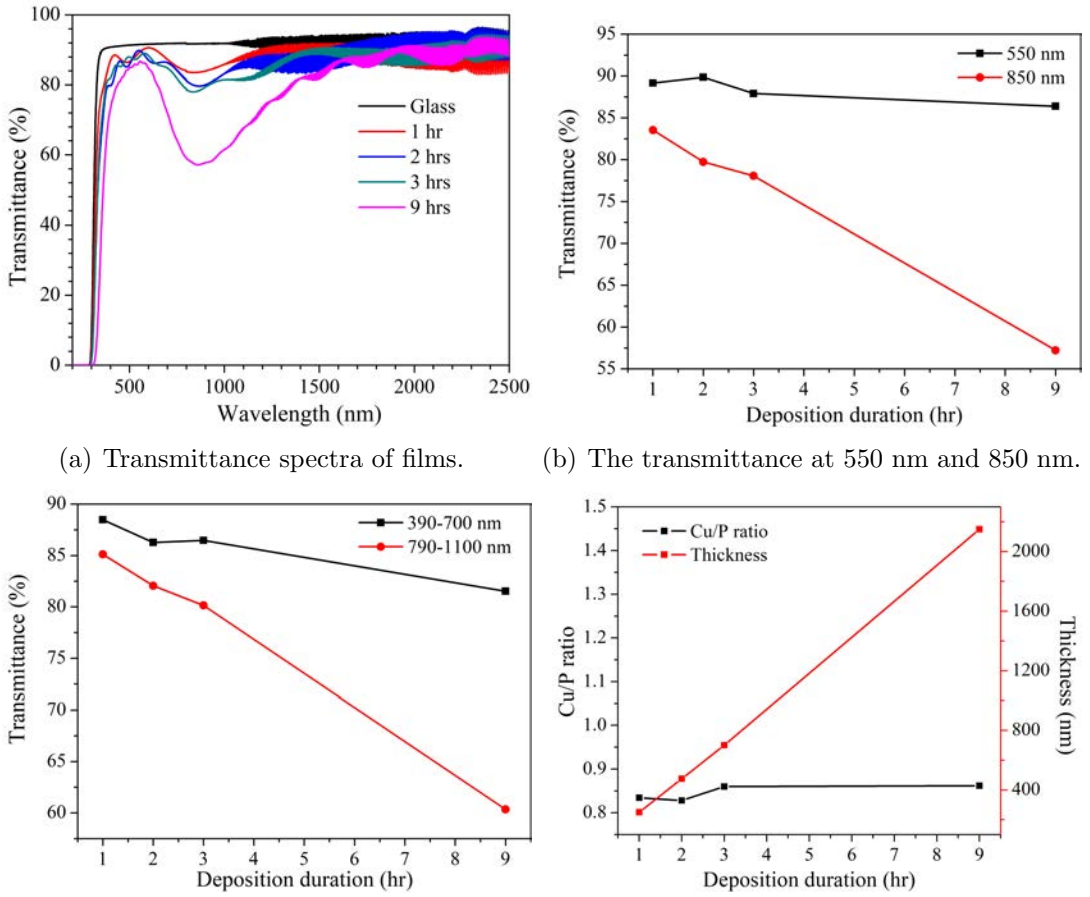
(d) Cu/P ratios and thicknesses of the films.

Figure 4.34: Properties of films deposited from the pure $Cu_2P_2O_7$ target in 10% O_2 / Ar gas for different times (60 W, room temperature).

increasing the sputtering duration, i.e. the thickness of the film, the shift of the absorption peak towards visible range mentioned in Figure 4.33(a) disappeared. In fact, similar phenomenon could be detected for films made with 15% and 20% of oxygen as well, which will be shown later (Figures 4.35(a) and 4.36(a)). This is probably because for samples with small sputtering durations, the thickness of which are much smaller than the target NIR wavelength (over 790 nm), the films can only interact with light of smaller wavelength. However, that problem does not exist for thicker films.

Figure 4.34(d) shows that all of the films have Cu/P ratios around 1 (0.8–1.1), meaning that the films produced are all relatively stoichiometric. The SEM results

(Figure A.8, Appendix A) show that all of the films have highly uniform surfaces. The XRD results (Figure A.7, Appendix A) show that the films are all amorphous.



(a) Transmittance spectra of films.

(b) The transmittance at 550 nm and 850 nm.

(c) The average transmittance in the ranges of 390–700 nm and 790–1100 nm.

(d) Cu/P ratios and thicknesses of films.

Figure 4.35: Properties of films deposited from the pure $Cu_2P_2O_7$ target in 15% O_2 / Ar gas for different times (60 W, room temperature).

For films sputtered in 15% O_2 / Ar gas, the results are shown in Figure 4.35. Here the films were sputtered for 1 hr, 2 hrs, 3 hrs and 9 hrs, respectively. The transmittance at 850 nm decreased from 83.5% to 57.2% as the time increased, yet the transmittance at 550 nm remained in the range 85%–90% with little change from 89.2% to 86.4%. The average transmittance in the 790–1100 nm range decreased from 85.1% to 60.3% as the duration increased from 1 to 9 hrs, while the average transmittance in the 390–700 nm decreased only from 88.5% to 81.5%. It can be found that the *gap* between the average transmittance in 390–700 nm range and 790–

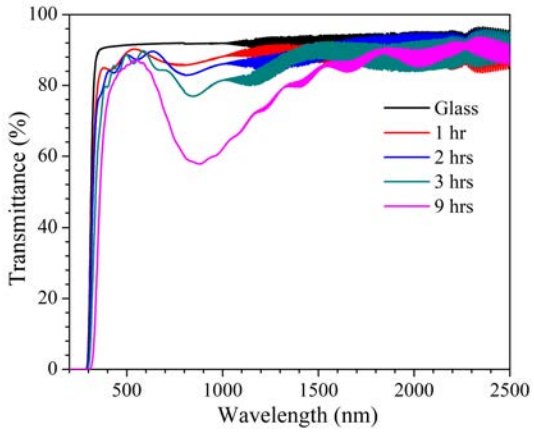
1100 nm range for the 9 hrs sample made with 15% O_2, is very close to that (the *gap* value) of the 9 hrs sample made with 10% O_2. However, for the 9 hrs sample made with 15% oxygen, the average transmittance in both visible and NIR regions is around 5% higher than that of the 10% oxygen sample. These two films have nearly the same thickness, meaning that thickness is not the reason for the difference in their transparency. The reason will become clearer later.

Figure 4.35(d) shows that the films deposited for different times are highly stoichiometric and have good consistency in the Cu/P ratio. The XRD (Figure A.9, Appendix A) and SEM (Figure A.10, Appendix A) results show that the films made with 15% O_2 are amorphous and highly uniform.

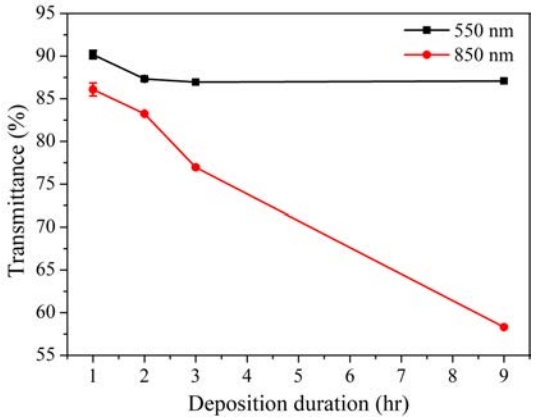
For films sputtered in 20% O_2 / Ar gas, the influence of longer sputtering duration is presented in Figure 4.36(a). In this series, the films were sputtered for 1 hr, 2 hrs, 3 hrs and 9 hrs, respectively. Similar to the case of 15% oxygen, the transmittance at 850 nm decreased from 86.1%($\pm$0.8%) to 58.3% as the sputtering duration increased from 1 hr to 9 hrs, while the transmittance at 550 nm decreased only from 90.2%($\pm$0.5%) to 87.1%. For the average transmittance in the range of 390–700 nm, the value reduced from 88.2%($\pm$0.2%) (1 hr) to 72.2% (9 hrs) while for the range of 790–1100 nm, the corresponding value decreased from 87.4%($\pm$0.5%) to 61.1%. As can be seen in all of the three cases demonstrated (10%, 15% and 20% O_2), the thicker the film, the bigger the separation between the average visible and NIR transmittance values becomes, and so does the difference between the transmittance at 550 nm and 850 nm. For the 9 hrs sample in this batch, the average transmittance in both target visible and NIR range is very close to that of the 9 hrs sample made with 15% O_2.

EDS results show little fluctuation in the chemical composition of film as the deposition time changed (Figure 4.36(d)). Once again, linear correspondence was obtained between the thickness of film and the deposition duration. The XRD (Figure A.11, Appendix A) and SEM (Figure A.12, Appendix A) results show that the films made with 20% O_2 are amorphous and highly uniform.

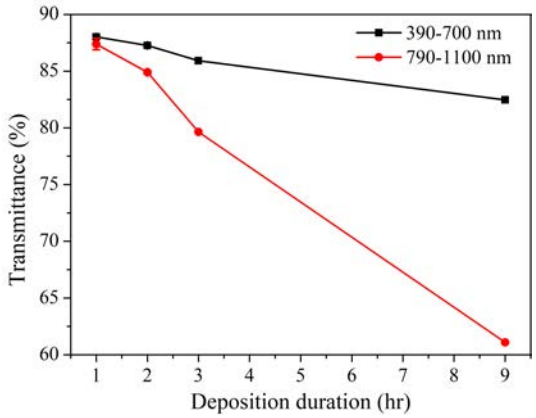
In Figure A.11, one could see a shift in the XRD amorphous hump for samples made with oxygen, similar to the shift seen in Figure A.3 for samples deposited with



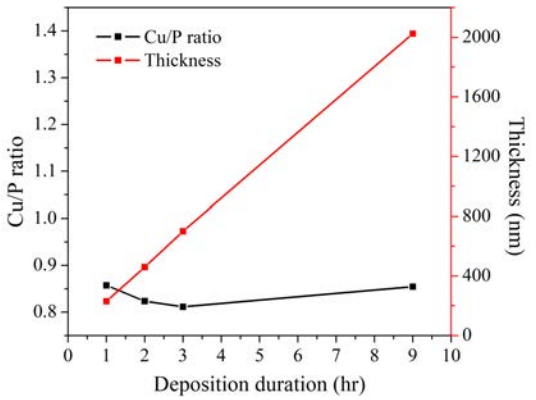
(a) Transmittance spectra of films.



(b) The transmittance at 550 nm and 850 nm.



(c) The average transmittance in the ranges of 390–700 nm and 790–1100 nm.



(d) Cu/P ratios and thicknesses of films.

Figure 4.36: Properties of films deposited from the pure $Cu_2P_2O_7$ target in 20% O_2 / Ar gas for different times (60 W, room temperature). Error bars measured from the optical spectra of multiple samples are included for the 1 hr and 2 hrs sample in subfigures b and c. Some of the error bars might be too small to be easily seen in these graphs.

power of 50 W or more. Although amorphous thin films have no long-range order and are macroscopically isotropic, the X-ray amorphous pattern is a fingerprint of the short-range order [31]. The shift of the peak towards a lower angle suggests that the average inter-atomic distance is larger in the film. By comparing the deposition conditions and properties of the films in these two graphs, we can find that this shift towards a lower angle happens when the deposition rate is high (above 16 nm/min). It has been previously reported that the deposition rate could affect the diffusion and relocation of atoms during sputtering [32]; in turn, this can affect the bonding process

and thus the average inter-atomic distance. A good way to study this would be to use simulation techniques, such as molecular dynamics, in order to model the sputtering process and the impacts of deposition rate on the short-range order of atoms [33, 34].

Images of some selected films are shown in Figure 4.37. As can be seen as the oxygen content in the sputtering gas increases, the deposited film changed colour from light brown to green then to light blue. The light brown colour is similar to that of CuO/Cu_2O films, while the light blue colour is close to that of the starting copper pyrophosphate powder. The green colour is a mixture of yellow/brown and blue. This result is reflected by the change in the optical spectra shown previously. The change in colour also indicates that there might be a change in chemical states. For films sputtered with lower oxygen content, the light brown colour could be due to many reasons such as the generation of oxygen vacancies that made the film more metallic, while the green colour indicates an intermediate state of the transition from brown to blue (fully oxidized). To further understand the chemical states of the films, XPS studies have been carried out on some of the samples.



Figure 4.37: Pictures of (a) glass substrate, (b) film sputtered with 5% O_2, (c) film sputtered with 10% O_2, (d) film sputtered with 15% O_2, (e) film sputtered with 20% O_2. All of the films shown here were sputtered at RF power of 60 W (2.96 W/cm^2) at room temperature.

4.3.3.1 Assessment of reproducibility

The reproducibilities of samples have also been examined in this study. The error bars for the optical results of the 1 hr and 2 hrs samples made with 20% oxygen are shown in Figure 4.36(b) and 4.36(c). Each of the error bars are calculated from the measurement of multiple samples from separate sputtering experiments using the same conditions. The relatively small error bars, varying from 0.1% to 0.8%, show the high reproducibility of the films and the presented results. In fact, not only the transmittance values at 550 nm and 850 nm or the average visible and NIR transmittance, but the entire UV-Vis-NIR spectra of the films also show a high degree of consistency in shape and values (Figure 4.38).

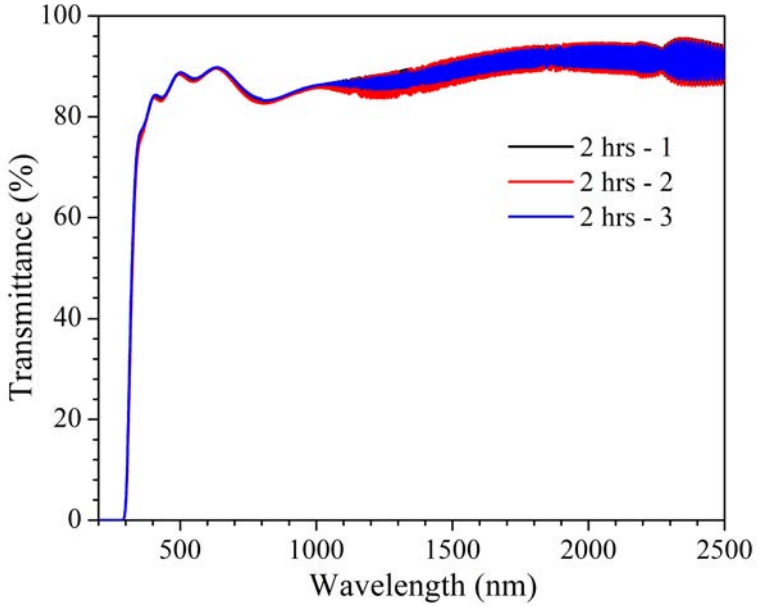


Figure 4.38: Transmittance spectra of three different samples deposited under the same conditions (20% O_2, 2 hrs, $Cu_2P_2O_7$ target).

4.3.3.2 Environmental stability

The environmental stability of the film deposited for 18 hrs with 10% O_2 was studied by leaving the film in an air environment for 90 days (temperature: 20 °C, no direct exposure to sunlight). The results of the optical spectra before and after the 90-days period are shown in Figure 4.39.

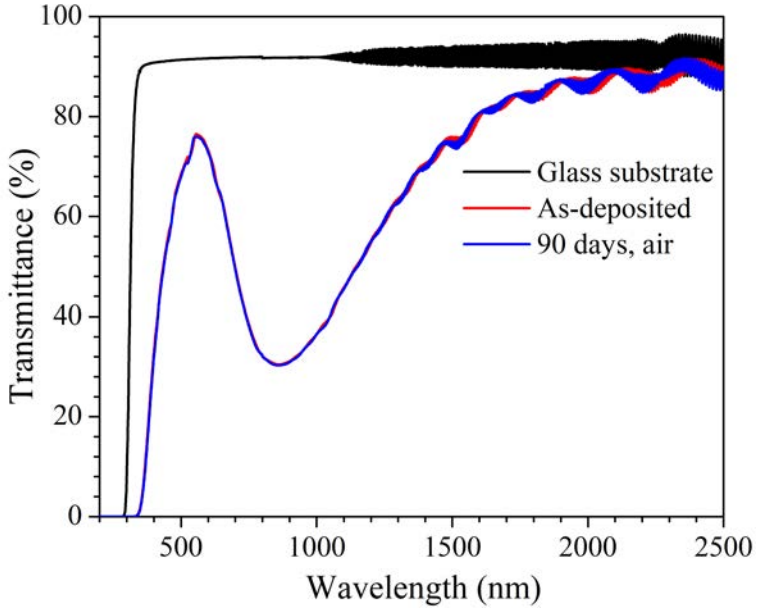


Figure 4.39: Transmittance spectra of the as-deposited film and after 90 days of exposure to the air. The film was sputtered with 10% O_2 for 18 hrs from the $Cu_2P_2O_7$ target.

As the result shows, there is little difference between the spectra before and after the 90-days exposure, demonstrating a high environmental stability over this testing period.

4.3.3.3 XPS studies of $Cu_2P_2O_7$ thin films

XPS analysis have been carried out to study both the target and thin films. Figure 4.40 shows the XPS spectrum from the target. Since there is no adventitious carbon peak for the etched area, the spectrum is calibrated using the Fermi level. In the spectrum, one can see the shake-up satellites due to the excitation of electrons to bound states. According to the literature, the strong satellite peaks are evidence for the existence of Cu^{2+} ions [35]. The binding energies of the reported satellite peaks for divalent Cu are near 938–947 eV [36–38], there are usually several Gaussian-Lorentzian components in these satellite features [35]. For the $Cu_2P_2O_7$ target, two components were assigned as the satellites of divalent Cu at 942.1 and 945.8 eV, as shown in the deconvoluted spectrum (Figure 4.40). For the Cu $2p_{3/2}$ peak, it is known to be asymmetric even in many pure copper compounds and thus is generally fitted

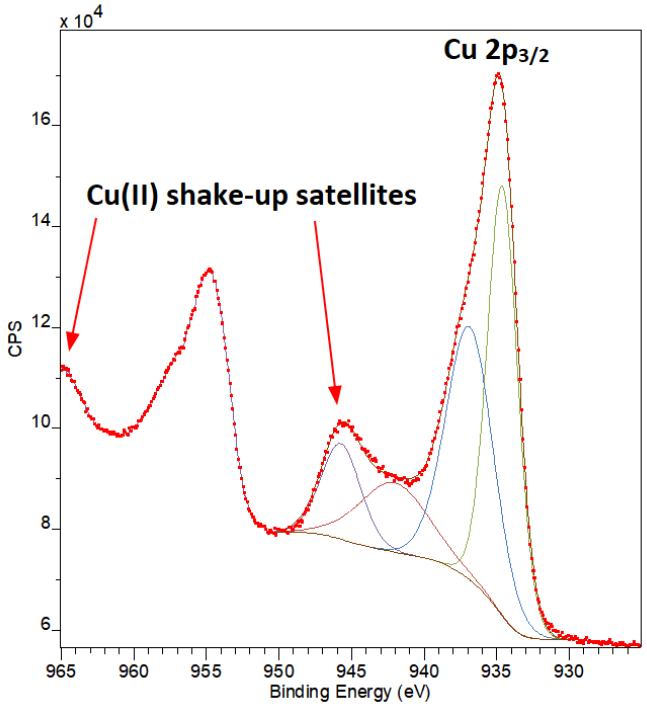


Figure 4.40: XPS spectrum of the $Cu_2P_2O_7$ target.

using multiple components [35]. The two components used to fit the Cu $2p_{3/2}$ peak here are at 934.6 (main peak) and 936.9 eV.

Figure 4.41 shows the deconvoluted XPS spectrum of the film deposited from the $Cu_2P_2O_7$ target with 10% O_2 for 9 hrs. The spectrum is calibrated using the Fermi level. The components at 935.2 (main peak) and 936.6 eV are assigned to $Cu_2P_2O_7$ while the one at 933.1 eV is assigned to CuO (black-arrowed). This is because the peak separation between the 935.2 and 933.1 eV components is consistent with the previous data reported for the gap between the main Cu $2p_{3/2}$ peaks of copper phosphate and copper(II) oxide [35]. The Cu^{2+} satellite can be separated into two components here as well, at 944.6 and 946.6 eV. Although to achieve an overall Cu/P ratio that is close to 1 as observed in EDS, the copper pyrophosphate environment here might be non-stoichiometric, i.e. as $Cu_{1-x}PO_y$.

In order to study how different oxygen levels during sputtering affected the oxidation states of the deposited films, similar deconvolution process with constraints on peak separations and FWHM were applied to the XPS spectra from

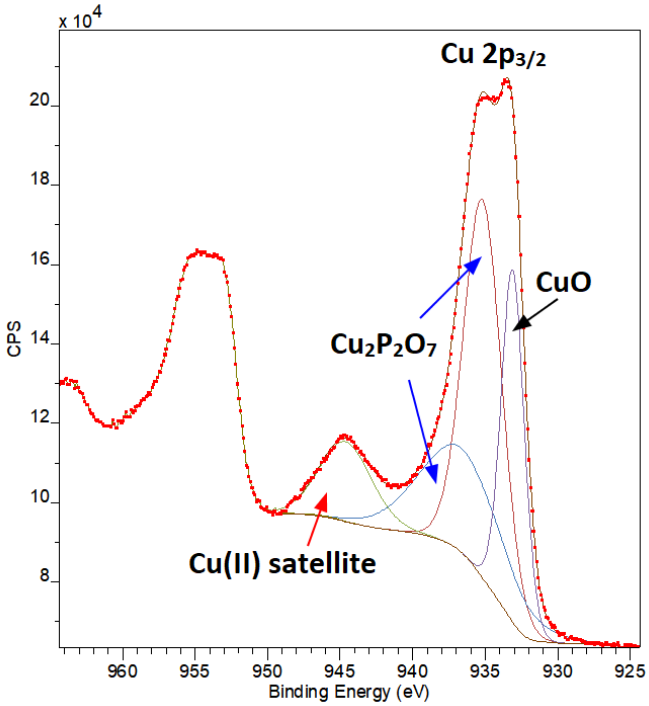


Figure 4.41: XPS spectrum of the film deposited from the $Cu_2P_2O_7$ target with 10% O_2 for 9 hrs (60 W, room temperature).

films made with 15% and 20% O_2 ($Cu_2P_2O_7$ target, 9hrs), as shown in Figures 4.42 and 4.43. Both of the spectra are calibrated using the Fermi level. The three components of the Cu $2p_{3/2}$ peak of the 15% O_2 sample are at 936.5 eV, 935.1 and 933 eV, respectively. The first two are assigned to $Cu_2P_2O_7$ while the third one is assigned to CuO (black-arrowed). The position values show high consistency with the sample made with 10% oxygen. In terms of the 20% O_2 thin film, the two components assigned to $Cu_2P_2O_7$ are at 935.1 (main peak) and 936.5 eV. The one assigned to CuO is at 933.1 eV (black-arrowed). The position values of the 20% O_2 sample are also highly consistent with that of the specimens made with 15% and 20% O_2.

However, by comparing the spectra of these samples, one can clearly see the variation in chemical environments, particularly the amount of CuO chemical environment in each sample. The film made with 10% oxygen has larger CuO component (chemical environment) than that of the 15% oxygen sample, and the

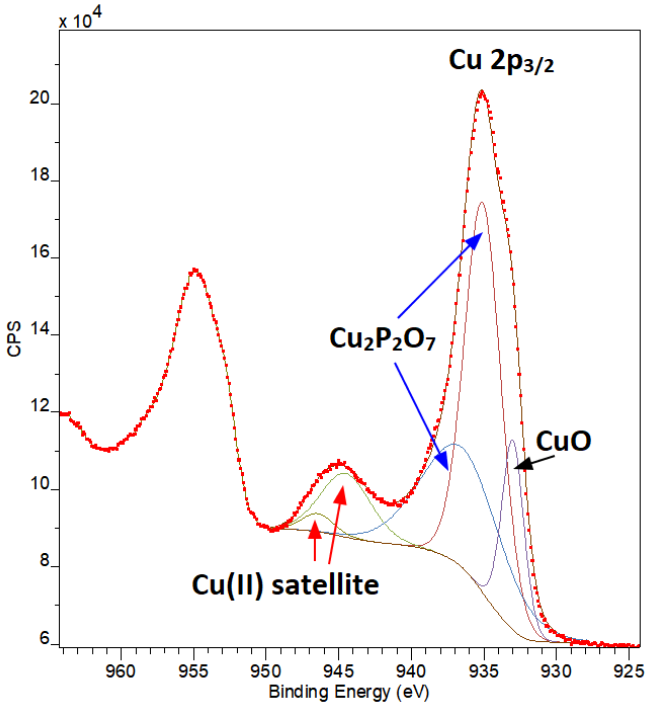


Figure 4.42: XPS spectrum of the film deposited from the $Cu_2P_2O_7$ target with 15% O_2 for 9 hrs (60 W, room temperature).

CuO component of the 15% O_2 sample is larger than that of the 20% O_2 specimen. This could thus explain the 5% difference between the transmittance of the 10% O_2 sample and the 15% O_2 sample given CuO thin films are usually not very transparent in the visible and NIR range [39], in fact most of them appear black or dark brown [24]. The changes in chemical states observed here are also consistent with the colours of the films shown in Figure 4.37, where the films change from light brown (highest CuO environment) to green (medium CuO environment) then to light blue (least CuO environment and mostly copper pyrophosphate). Futhermore, it can be seen that the shapes of both Cu $2p_{3/2}$ peak and Cu^{2+} satellites of the deposited films are closer to that of the $Cu_2P_2O_7$ target (Figure 4.40) as the amount of oxygen increases in the sputtering gas.

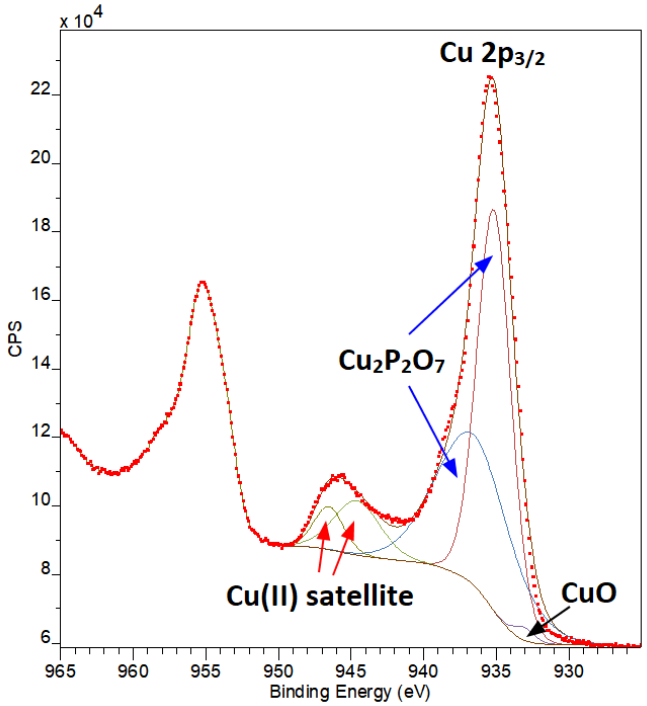


Figure 4.43: XPS spectrum of the film deposited from the $Cu_2P_2O_7$ target with 20% O_2 for 9 hrs (60 W, room temperature).

4.4 Discussion

Solution-based techniques such as spin-coating are commonly used for making traditional organic NIR absorbing thin films. A distinct advantage of room temperature sputtering over solution-based thin film production techniques is its ability to produce films with high uniformity, which is crucial for many optical applications. The uniform surface would provide a smooth interface when it comes to making multi-layer device. Compared to high temperature solution-based techniques such as spray pyrolysis, room temperature sputtering offers a more energy-efficient route and allows the deposition onto plastic substrates that could potentially be important for flexible applications. Moreover, the fact that many TCOs and window coating companies are now using sputtering as their manufacturing approach means that the infrastructure should already be available to incorporate copper pyrophosphate into their production.

In contrast to TCOs, the absorption peak of $Cu_2P_2O_7$ is in a different range of

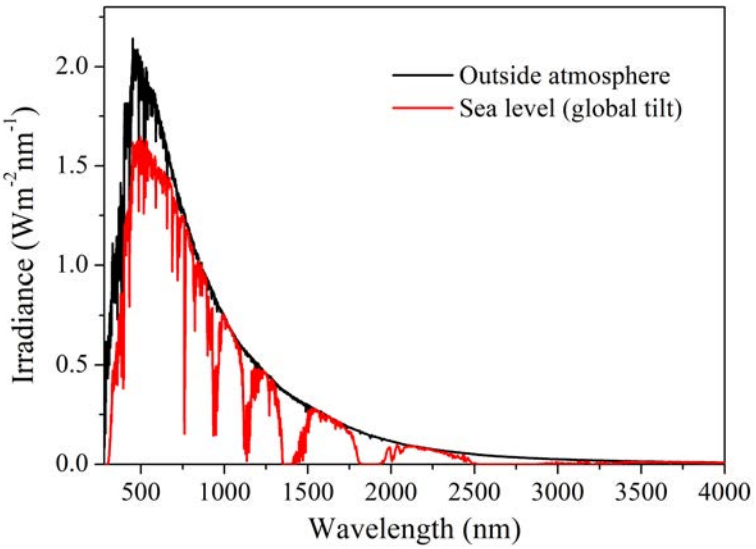


Figure 4.44: Solar irradiation spectra. Data originally from American Society for Testing and Materials (ASTM) [40]. Global tilt meaning the spectrum includes the radiation from not only solar disk but also sky diffusion and diffusion from ground reflection on a south facing surface tilted 37° from the horizontal.

wavelength. The plasma oscillations in TCOs usually reflects the irradiance with wavelength above 1300 nm (Figure 4.45), but $Cu_2P_2O_7$ thin films cover the 790–1100 nm region which contains a significant amount of NIR solar radiation energy. If we consider standard solar irradiation (Figure 4.44), the whole near-infrared (790–2500 nm) direct irradiance power is 415 W/m^2 while the direct irradiance power between 790 and 1100 nm is 227 W/m^2, nearly 60% of the total power. With $Cu_2P_2O_7$ thin film (18 hrs), the irradiance power (790–1100 nm) could be reduced to 78 W/m^2, calculated using Equation (4.1).

$$W_t = \sum_{i=790}^{1099} W_i T_i \Delta\lambda \tag{4.1}$$

where W_t is the overall amount of power that transmitted through the sample, λ is the wavelength, W_i and T_i are the solar irradiance and the transmittance of the sample at a particular wavelength respectively, $\Delta\lambda$ is the step size of the spectrum which is 1 nm in this case. Here, the left Riemann sum is used to approximate the integral of the irradiance (Equation (4.2)) as the step sizes for the measurements of optical spectra are finite.

$$W_{t-i} = \int_{790}^{1100} W(\lambda)T(\lambda)d\lambda \tag{4.2}$$

W_{t-i} refer to the integral power that transmitted through for a continuous spectrum, $W(\lambda)$ and $T(\lambda)$ refer to solar irradiance and transmittance of the sample as functions of wavelength respectively.

149 W/m^2, calculated from Equation (4.3) assumes there is no reflectance, is absorbed by the $Cu_2P_2O_7$ thin film. W_a is the total amount of power absorbed by the sample.

$$W_a = \sum_{i=790}^{1099} W_i(1 - T_i)\Delta\lambda \tag{4.3}$$

This means 66% of the solar irradiance in the range of 790–1100 nm could be blocked by films of the performance I have demonstrated in this work. Considering a flat surface with size of 80 m^2 uniformly covered by $Cu_2P_2O_7$ coated glass, the total irradiance power that could be blocked by $Cu_2P_2O_7$ thin film is about 12 kW (around three times higher than the power consumption of an average household central air conditioner during the hotter months [41]). In contrast, a commercial ITO coated glass (Figure 4.45) can only block 41 W/m^2 with an overall transmittance of 82% in the 790–1100 nm range. Thus, TCO and $Cu_2P_2O_7$ thin films could work together as compensation for each other in different wavelength ranges to achieve a high blocking rate across the entire NIR spectrum (790–2500 nm).

Meanwhile, an ideal shape of a 'perfect transmittance spectrum' has also been presented in Figure 4.45 as reference. So far I have found that to make $Cu_2P_2O_7$ films with spectra close to the ideal shape, factors including thickness of the film and oxygen percentage of the sputtering gas are crucial. Other factors such as chemical doping and distortion of lattice geometry could also affect the broadening of the absorption peak according to previous literature [5].

Compared to the current organic NIR-absorbing materials on the market, copper pyrophosphate shows many advantages. Typical NIR-absorbing organic materials such as naphthalocyanine and mixed-valence ruthenium complexes have

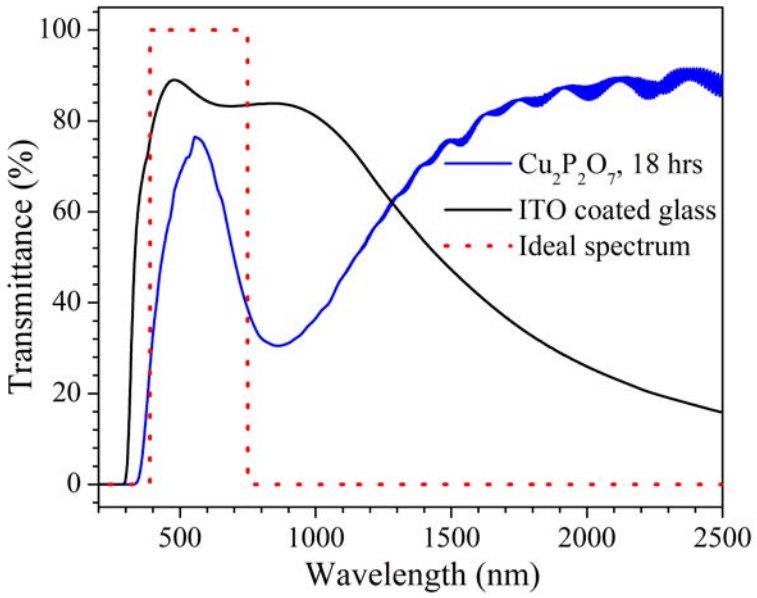


Figure 4.45: Transmittance spectra of a $Cu_2P_2O_7$ film (18 hrs, 10% oxygen, pure $Cu_2P_2O_7$ target), an ITO coated glass and an ideal sample.

decomposition temperatures lower than 400 °C [4, 42], $Cu_2P_2O_7$ instead has a thermal decomposition temperature up to 1050 °C [12] which is ideal for many space and military applications. Besides, photo-absorbing organic materials in general have many issues with chemical- and photo- stability according to previous research [43, 44], either due to reaction with air/H_2O or decomposition/polymerization reactions induced by light. Moreover, the low cost (∼USD 2 / kg [45]) of copper pyrophosphate (compared to that of naphthalocyanine [46]) would greatly facilitate the establishment of a manufacturing process. The light green or blue colours of the sputtered films are also favourable for many architectural applications.

4.4.1 $Cu_2P_2O_7$ + TCOs: A prototype

As a trial of getting closer to the 'perfect transmittance spectrum', a prototype was made integrating commercial ITO film and copper pyrophosphate thin film using the strategy as presented. The commercial ITO coated glass was obtained from Sigma Aldrich ®[47], of which the spectrum was showed in Figure 4.45. The copper pyrophosphate thin film was sputtered with 20% oxygen for 18 hrs from a $Cu_2P_2O_7$ target. The spectrum of the double-layered coating is shown in Figure 4.46.

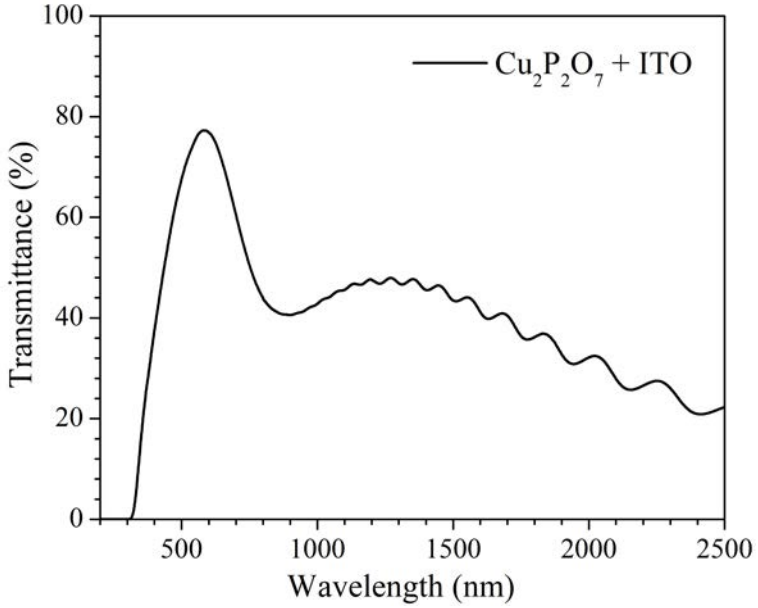


Figure 4.46: Transmittance spectrum of a double-layered coating combining a $Cu_2P_2O_7$ film (18 hrs, 20% oxygen, pure $Cu_2P_2O_7$ target) and an ITO film deposited on glass.

Although this is only a prototype with plenty of room for future improvement, the double-layered coating already showed a much wider and better coverage over the entire NIR range (790–2500 nm) than ITO itself. However, being aware that the spectrum is also affected by interference between multiple reflections at different interfaces is important. In order to better control the impact, further simulation is required in the future to maximise the visible transmittance and minimise the NIR transmittance.

4.5 Conclusion and suggestions for future work

In this chapter, the process of making efficient and low-cost NIR-absorbing $Cu_2P_2O_7$ thin films has been introduced. The films have up to 62% of absorbance at 850 nm while maintaining 85% of transmittance at 550 nm. The thin film can absorb 66% of total solar irradiance in the wavelength range of 790–1100 nm. Multiple microscopic and analytical tools such as XRD, (FE-)SEM, EDS and XPS have been applied to study the structure and chemistry of the thin films. A prototype of NIR

double-layered coating containing copper pyrophosphate and ITO was also made and tested. Compared to traditional organic dyes, these copper pyrophosphate films have high stability against thermal, chemical and photonic influences. Besides, given the low-temperature processing it requires, it could be easily incorporated into many applications including flexible devices. It is hoped that this technology could open up new markets for this material to further applications including low-emissivity windows, military camouflage devices and perhaps even transparent solar cells.

In terms of future work, it would be worth doing more optimization of the thin film as well as further exploration on the device side. Previously, the effects of doping have been studied in powdered copper pyrophosphate [5]. It would be interesting to see how different dopants would affect the optical performance of $Cu_2P_2O_7$ thin films. Besides, as previously discussed, sputtered films with high phosphorous content might be good candidates for amperometric water sensors. Other methods of making this particular thin film other than sputtering could also be investigated. Regarding devices such as transparent solar cells, the HOMO/LUMO properties of the films needs to be measured in order to find the right materials for the compact layer and hole transport layer. Last but not least, interesting magnetic properties have also been reported before for powder copper pyrophosphate [48], it might be worth looking at how thin film systems would behave differently from the powder system.

Bibliography

[1] J. Fabian, H. Nakazumi, and M. Matsuoka, Chemical Reviews **92**, 1197 (1992), ISSN 0009-2665.

[2] S. Daehne, U. Resch-Genger, and O. S. Wolfbeis, *Near-infrared dyes for high technology applications*, vol. 52 (Springer Science & Business Media, 2012), ISBN 9401151024.

[3] C. T. Riley, J. S. Smalley, J. R. Brodie, Y. Fainman, D. J. Sirbuly, and Z. Liu, Proceedings of the National Academy of Sciences **114**, 1264 (2017), ISSN 0027-8424.

[4] D. K. Ng, Y.-O. Yeung, W. K. Chan, and S.-C. Yu, Tetrahedron letters **38**, 6701 (1997), ISSN 0040-4039.

[5] F. Norindr, Thesis, Southampton University (2009).

[6] D. R. Rosseinsky and R. J. Mortimer, Advanced Materials **13**, 783 (2001), ISSN 0935-9648.

[7] A. Boltasseva and H. A. Atwater, Science **331**, 290 (2011), ISSN 0036-8075.

[8] Sigma Aldrich (2018), URL `https://www.sigmaaldrich.com/catalog/product/aldrich/344699?lang=en&region=GB`.

[9] Alfar Aesar (2018), URL `https://www.fishersci.co.uk/shop/products/copper-ii-pyrophosphate-hydrate-p2o7-43-5-48-5-2/p-7059008`.

[10] D. Noguchi, Y. Kawamata, and T. Nagatomo, Japanese journal of applied physics **42**, 5255 (2003), ISSN 1347-4065.

[11] Y. Abe, N. Itadani, M. Kawamura, K. Sasaki, and H. Itoh, Japanese Journal of Applied Physics **46**, 777 (2007), ISSN 1347-4065.

[12] C. E. Bamberger, E. Specht, and L. M. Anovitz, Journal of the American Ceramic Society **80**, 3133 (1997), ISSN 0002-7820.

[13] C. B. Carter and M. G. Norton, *Ceramic materials: science and engineering* (Springer Science & Business Media, 2007), ISBN 0387462716.

[14] C. P. Liu and G. R. Jeng, Journal of Alloys and Compounds **468**, 343 (2009), ISSN 0925-8388.

[15] Y.-H. Sun, W.-H. Xiong, and C.-H. Li, Transactions of Nonferrous Metals Society of China **20**, 624 (2010), ISSN 1003-6326.

[16] H.-C. Lai, H.-H. Tsai, K.-Y. Hung, and H.-P. Feng, Journal of Intelligent Material Systems and Structures **26**, 1050 (2015), ISSN 1045-389X.

[17] R. M. German, Critical reviews in solid state and materials sciences **35**, 263 (2010), ISSN 1040-8436.

[18] M. Brett and R. Parsons, Journal of Vacuum Science & Technology A: Vacuum, Surfaces, and Films **4**, 423 (1986), ISSN 0734-2101.

[19] V. Kobrinsky, A. Rothschild, V. Lumelsky, Y. Komem, and Y. Lifshitz, Applied Physics Letters **93**, 113502 (2008), ISSN 0003-6951.

[20] M. Surmeneva, R. Surmenev, V. Pichugin, A. Ivanova, I. Grubova, M. Chaikina, I. Khlusov, A. Kovtun, and M. Epple, in *Strategic Technology (IFOST), 2012 7th International Forum on* (IEEE), pp. 1–4, ISBN 146731773X.

[21] J. G. Speight, *Lange's handbook of chemistry*, vol. 1 (McGraw-Hill New York, 2005).

[22] Sigma Aldrich (2019), URL `https://www.sigmaaldrich.com/catalog/product/sial/214701?lang=en&region=GB`.

[23] C. Niveditha, M. J. Fatima, and S. Sindhu, Journal of The Electrochemical Society **163**, H426 (2016), ISSN 0013-4651.

[24] T. K. Wong, S. Zhuk, S. Masudy-Panah, and G. K. Dalapati, Materials **9**, 271 (2016).

[25] R. E. Honig, *Vapor pressure data for the more common elements* (David Sarnoff Research Center, 1957).

[26] N. N. Greenwood and A. Earnshaw, *Chemistry of the Elements.* (1984).

[27] F. Keidel, Analytical Chemistry **31**, 2043 (1959), ISSN 0003-2700.

[28] H. Huang, P. K. Dasgupta, and S. Ronchinsky, Analytical Chemistry **63**, 1570 (1991), ISSN 0003-2700.

[29] J.-H. Xu, B. Moon, and K. Rao, Journal of materials research **10**, 798 (1995), ISSN 2044-5326.

[30] C. Chananonnawathorn, S. Pudwat, M. Horprathum, P. Eiamchai, P. Limnontakul, C. Salawan, and K. Aiempanakit, Procedia engineering **32**, 752 (2012), ISSN 1877-7058.

[31] H. E. Fischer, A. C. Barnes, and P. S. Salmon, Reports on Progress in Physics **69**, 233 (2005), ISSN 0034-4885.

[32] A. Barranco, A. Borras, A. R. Gonzalez-Elipe, and A. Palmero, Progress in Materials Science **76**, 59 (2016), ISSN 0079-6425.

[33] M. H. Shapiro, Radiation Effects and Defects in Solids **142**, 259 (1997), ISSN 1042-0150.

[34] S.-P. Ju, C.-I. Weng, J.-G. Chang, and C.-C. Hwang, Surface and Coatings Technology **149**, 135 (2002), ISSN 0257-8972.

[35] M. C. Biesinger, Surface and Interface Analysis **49**, 1325 (2017), ISSN 0142-2421.

[36] Z. Ai, L. Zhang, S. Lee, and W. Ho, The Journal of Physical Chemistry C **113**, 20896 (2009), ISSN 1932-7447.

[37] K. H. Yoon, W. J. Choi, and D. H. Kang, Thin Solid Films **372**, 250 (2000), ISSN 0040-6090.

[38] S. Lee, N. Mettlach, N. Nguyen, Y. Sun, and J. White, Applied Surface Science

206, 102 (2003), ISSN 0169-4332.

[39] K. Mageshwari and R. Sathyamoorthy, Materials Science in Semiconductor Processing **16**, 337 (2013), ISSN 1369-8001.

[40] ASTM (2018), URL https://rredc.nrel.gov/solar/spectra/am1.5/.

[41] Air conditioning (2019), URL http://energyusecalculator.com/electricity_centralac.htm.

[42] Z. Y. Wang, J. Zhang, X. Wu, M. Birau, G. Yu, H. Yu, Y. Qi, P. Desjardins, X. Meng, and J. P. Gao, Pure and applied chemistry **76**, 1435 (2004), ISSN 1365-3075.

[43] F. C. Krebs and K. Norrman, Progress in Photovoltaics: Research and Applications **15**, 697 (2007), ISSN 1062-7995.

[44] R. S. Sanchez and E. Mas-Marza, Solar Energy Materials and Solar Cells **158**, 189 (2016), ISSN 0927-0248.

[45] $Cu_2P_2O_7$ Price (2018), URL https://yuyinchem.en.made-in-china.com/productimage/ZCQxITXvHGWU-2f1j00fwDENyczLlbn/China-Copper-Pyrophosphate-Cupric-Pyrophosphate-Cu2p2o7-CAS-10102-90-6.html.

[46] Sigma Aldrich, *Naphthalocyanine*, URL https://www.sigmaaldrich.com/catalog/product/aldrich/381896?lang=en&region=GB.

[47] Sigma Aldrich (2019), URL https://www.sigmaaldrich.com/catalog/product/aldrich/703192?lang=en&region=GB.

[48] O. Janson, A. Tsirlin, J. Sichelschmidt, Y. Skourski, and H. Rosner, arXiv preprint arXiv:1011.5393 (2010).

Chapter 5

Conclusion and Suggestions for Future Work

At the beginning of this thesis, two concerns, economical and NIR performance, were raised regarding the current TCO leader ITO. In response to that, research has been carried out around these two issues.

In terms of the cost of indium, Si-doped ZnO films have been made and tested as a low-cost replacement for ITO with promising electrical and optical properties. The research started by focusing on the chemical and structural properties of the sputtering target. The Si content of the target obtained from the EDS study is within the optimal range of Si concentration reported in previous research. The thin film studies started by following the traditional route of an empirical search for the optimal conditions of making a conducting and visibly transparent thin film. However, this traditional approach does not offer adequate information on the change in microstructures and chemistry inside the film and why the properties show certain changes. In the following part of the thin film research, in-depth studies on as-deposted SiZO films grown on MgO substrates (substrate temperature: 200 °C) and films post vacuum annealed at different temperatures (400 and 550 °C) were carried out using advanced microscopic techniques, including texture XRD, TKD, HR-TEM, STEM etc. Hall effect measurements show that the resistivity decreased from 3.6×10^{-1} Ωcm to 6.7×10^{-3} Ωcm and 3.9×10^{-3} Ωcm for samples annealed at 400 °C and 550 °C. The XRD results showed that all of the films are c-axis oriented. However,

GPA analyses on the HR-TEM images point out that the grains in the as-deposited sample are not perfectly aligned. This is further supported by the broad XRD rocking curve of the as-deposited film. The texture XRD results reveal that the out-of-plane alignment improved after annealing, with the FWHM of rocking curve reduced from 9° to 5° and 3° for the 400 and 550 °C samples respectively. Enhancement in in-plane alignment has also been observed in the annealed films according to the TKD results. Two preferred in-plane orientations between the SiZO film and MgO substrate were found to develop during the annealing process. EDS results show that the annealing process had little affect on the Si/Zn ratio in the films. The Si/Zn ratios in these films are higher than that of the target, showing a preferred deposition of Si. Although the Si contents in the films are well above the equilibrium level shown in the SiO_2-ZnO phase diagram, no precipitation/phase separation could be detected. The improvement in out-of-plane alignment and the reduction in grain boundary misorientations were assigned as two of the reasons for the increase in electron mobility and may also help reduce the concentration of electron localizing defects that would contribute to the observed increase in carrier concentration. However, arrays of nano-pores were observed in the annealed films from STEM and Fresnel imaging, suggesting that creep damages may have occurred due to the presence of high temperature and internal tensile stress field. To avoid creep damage, some suggestions have been listed for future researchers.

Despite the fact that TCOs are often used as coatings to reduce heat gain / heat loss by blocking thermal irradiation in the NIR range, their incomplete coverages of reflection in the NIR range misses out most of the irradiation in the range of 790–1100 nm, which composes nearly 60% of the solar NIR irradiance. To resolve this issue, $Cu_2P_2O_7$ thin films have been proposed and made, for the first time, for the absorption of irradiance in the 790–1100 nm range. In the first part of this study, the absorption properties of the powder was confirmed by measuring its total reflectance spectrum. XRD measurements were used to determine the phases of hydrated and dehydrated compounds. After that, a process of making sputtering targets with no post-sintering shrinkage and cracking was designed and tested. In terms of the

production of thin films, films deposited from a pure $Cu_2P_2O_7$ target in Ar gas show high visible transparency yet little absorption in the NIR range. EDS results show that some of the films possess a high Cu/P ratio that might be the reason for the lack of NIR absorption. Therefore, a batch of films were made from a $Cu_2P_2O_7/P_2O_5$ (mol ratio: 1:1) target in Ar gas. However, most of the films were highly hydrophilic and interacted with the water in the air once they left the chamber. Another reason for the lack of NIR absorption might be the deficiency of oxygen in the films given the large ratio of oxygen in the desired compound. To test that, films were deposited from a $Cu_2P_2O_7$ target in Ar/O_2 with different percentages of oxygen. As a result, the ones deposited with 10%, 15% and 20% oxygen all exhibited higher absorption in the 790–1100 nm range, with up to 62% of absorbance at 850 nm while keeping 85% of transmittance at 550 nm. The film deposited for 18 hrs with 10% of oxygen can absorb 66% of total solar irradiance in the 790–1100 nm range. SEM and EDS results show that these films are highly uniform and stoichiometric. XRD results reveal the amorphous nature of the films. XPS data suggests that with higher oxygen ratio in the sputtering gas, the sputtered films contain the chemical characteristics of more copper phosphate and less copper oxide. This is consistent with the change in the film's colour. In the end, a prototype of coating combining a copper pyrophosphate thin film and commercial ITO was made and it shows a desired blockage of NIR light over the full 790–2500 nm range.

In short, this work has explored the ways and challenges of making low-cost and highly efficient inorganic NIR coating by carrying out in-depth studies on SiZO films and designing the process of making $Cu_2P_2O_7$ thin films. So what is next for Si doped ZnO thin films, $Cu_2P_2O_7$ thin films and inorganic NIR coatings that integrate TCOs and $Cu_2P_2O_7$?

For Si doped ZnO thin films, there are a few things that would be useful to study for both scientific and commercial interest:

1) Study of the influence of a single grain boundary would help us better understand how changes in grain alignment would affect the electrical conductivity, which is particularly useful for the study of polycrystalline films grown on glass substrates.

One way to investigate that is to deposit epitaxially-grown thin films on bi-crystal substrates with different grain boundary orientations [1, 2].

2) Given the structural changes observed in this thesis, it would be interesting to examine the in-plane alignment, out-of-plane alignment and the nano-defects of SiZO films grown on other single crystal substrates.

3) Measurement of the concentration of oxygen vacancies is important not only for better understanding of doping mechanisms inside the thin films, but would also help point out the direction for increasing the amount of effective dopants.

4) Co-doping with either cations or anions might help further increase the conductivity of SiZO films. This has been shown previously by Rashidi *et al.* using fluorine as an extra dopant to enhance the performance of sprayed SiZO films [3].

In terms of $Cu_2P_2O_7$ thin films, despite the high NIR absorption rate the films show here, I believe that this is only a beginning and there are a few things future research should focus on for further optimization and applications:

1) Thickness. As shown previously, the NIR absorption efficiency increases as the films become thicker due to the increased interaction between film and the incoming light. It is true that one could persist in increasing the thickness of the film to achieve greater NIR blocking effect, however eventually this would come down to a balance between the NIR performance, sacrifice of the visible transparency, the time/labour/materials each film costs and the needs of the applications. For each of the many potential applications of this coating, it is an issue that requires careful decisions made by the producers and end users.

2) More studies on the environmental stability of the film in different types of ambience. In this study, the environmental stability of one of the films has been shown. However, the singular environmental setting used for this study means the result cannot cover the stability of the films in other types of environments e.g. high humidity, which could be important depending on the locations of the end use. One way, though, to ensure a longer lifetime of the film is to seal the coated glass with another layer of glass on top to avoid direct contact with the ambience (similar to the design of laminated glass).

3) Doping of the thin films. According to Norindr [4], Zn doped copper pyrophosphate powder also exhibits promising NIR blocking effects. Therefore, it might be worth testing such idea on the manufacture of thin films.
4) Applications. As said before, the NIR absorbing capability of the thin film suggests that the film might be a good candidate for transparent solar cell, with matching electron transport layer and hole transport layer. The magnetic properties of the thin film is also worth exploring according to previous research on $Cu_2P_2O_7$ powder [5].

As for the inorganic NIR coating that could cover the full 790–2500 nm range, a double-layered prototype has been made and tested in this thesis. As technology progresses for TCOs and $Cu_2P_2O_7$ thin films, it is expected that the optimization of the NIR coating will follow. A few ideas, though, are listed as follows:
1) Combining doped ZnO film with CuPO film. Although still not as good as ITO, it might be worth trying to deposit $Cu_2P_2O_7$ on top of some commercial doped ZnO coated glasses. This is a quick and relatively easy trial of making truly low-cost double-layered NIR coatings.
2) *In-situ* depositions of both the TCO and $Cu_2P_2O_7$ layers. The prototype shown in this thesis was made by the deposition of $Cu_2P_2O_7$ on a commercial ITO coated glass. However, if one could deposit the TCO layer and the $Cu_2P_2O_7$ layer *in-situ* without any exposure to the air in between the productions of these two layers, it could avoid the contamination that might be induced at the interface.
3) Deposition on plastic substrates. As mentioned previously, one of the advantages of room temperature sputtering used for the deposition of $Cu_2P_2O_7$ here is that it allows the deposition on plastic substrates that are vulnerable to high temperatures, though the low temperature processing makes it more challenging to produce a highly conductive TCO layer [6–8], which requires further research for optimization. A coating on plastic substrate has the advantages of portability, flexibility for storage and may open up the markets for possible flexible devices.

Bibliography

[1] C. Dark, M. Kilburn, G. Hammerl, C. Schneider, J. Mannhart, and C. Grovenor, in *Journal of Physics: Conference Series* (IOP Publishing), vol. 43, p. 272, ISBN 1742-6596.

[2] S. B. Lee, S. J. Yoo, Y.-M. Kim, J.-G. Kim, and H. N. Han, Scientific reports **6**, 26493 (2016), ISSN 2045-2322.

[3] N. Rashidi, A. T. Vai, V. L. Kuznetsov, J. R. Dilworth, and P. P. Edwards, Chemical Communications **51**, 9280 (2015).

[4] F. Norindr, Thesis, Oxford University (2009).

[5] O. Janson, A. Tsirlin, J. Sichelschmidt, Y. Skourski, and H. Rosner, arXiv preprint arXiv:1011.5393 (2010).

[6] Sigma Aldrich (2019), URL `https://www.sigmaaldrich.com/catalog/product/aldrich/703192?lang=en&region=GB`.

[7] Sigma Aldrich (2019), URL `https://www.sigmaaldrich.com/catalog/product/ALDRICH/749796?lang=en&region=GB&cm_sp=Insite-_-prodRecCold_xviews-_-prodRecCold5-4`.

[8] Sigma Aldrich (2019), URL `https://www.sigmaaldrich.com/catalog/product/aldrich/639303?lang=en&region=GB`.

Appendices

Appendix A

SEM and XRD results of $Cu_2P_2O_7$ Thin Films

A.1 Post-deposition annealing

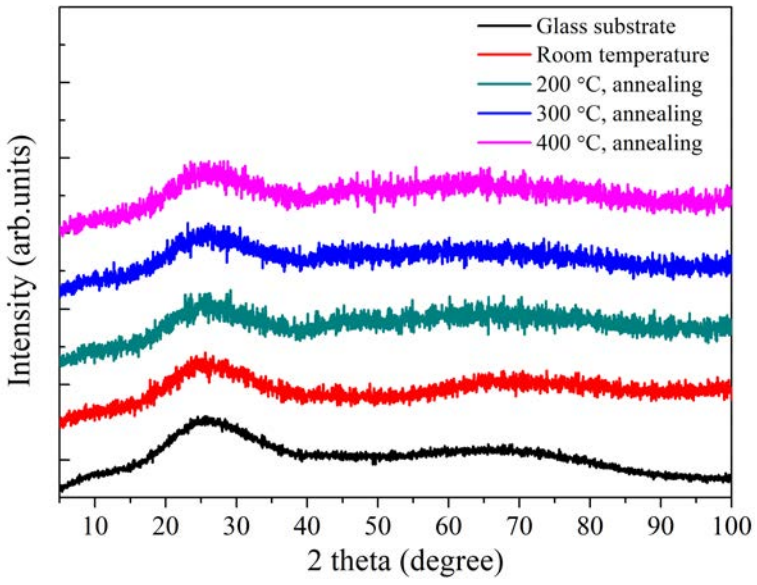
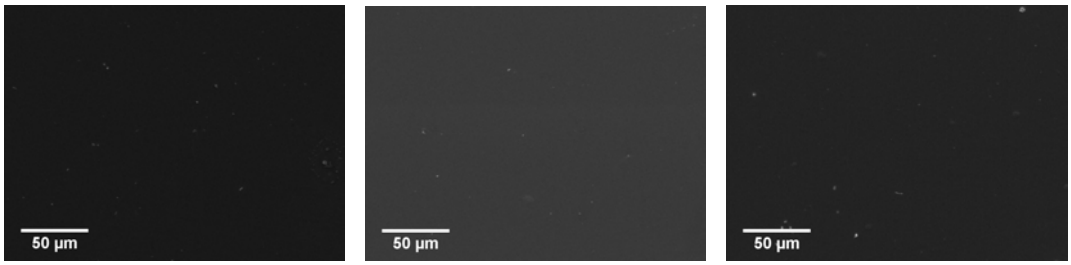


Figure A.1: XRD spectra of films deposited from pure $Cu_2P_2O_7$ target in Ar gas and post-annealed at different temperatures.



(a) Thin film post-annealed at 200 °C.

(b) Thin film post-annealed at 300 °C.

(c) Thin film post-annealed at 400 °C.

Figure A.2: SEM images of selected films deposited from pure $Cu_2P_2O_7$ target in Ar gas and post-annealed at different temperatures.

A.2 RF power

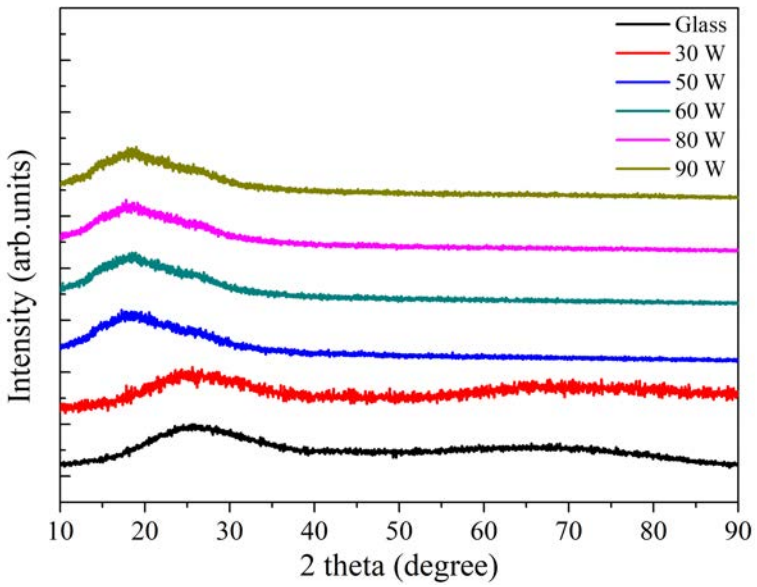
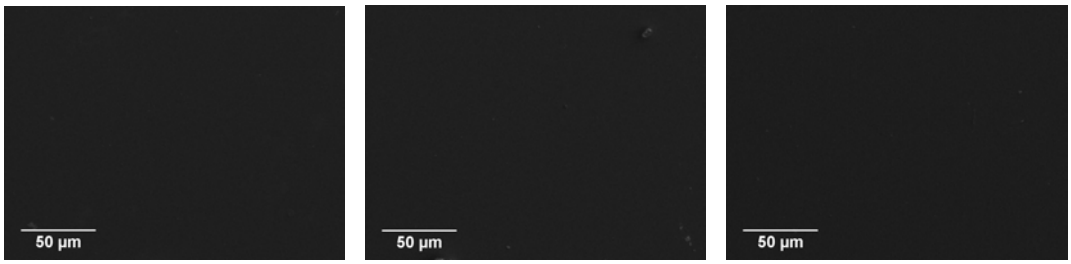


Figure A.3: XRD spectra of films deposited from pure $Cu_2P_2O_7$ target in Ar gas with different powers.



(a) Thin film deposited at 50 W. (b) Thin film deposited at 60 W. (c) Thin film deposited at 80 W.

Figure A.4: SEM images of (selected) films deposited from pure $Cu_2P_2O_7$ target in Ar gas with different powers.

A.3 Oxygen content

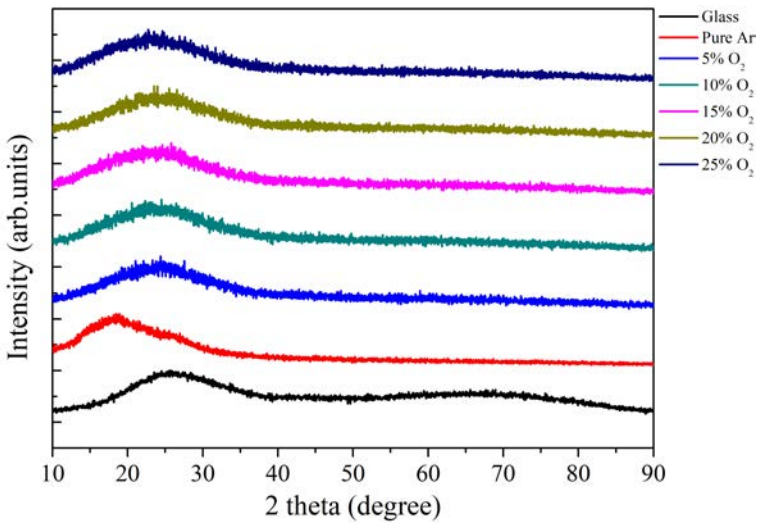
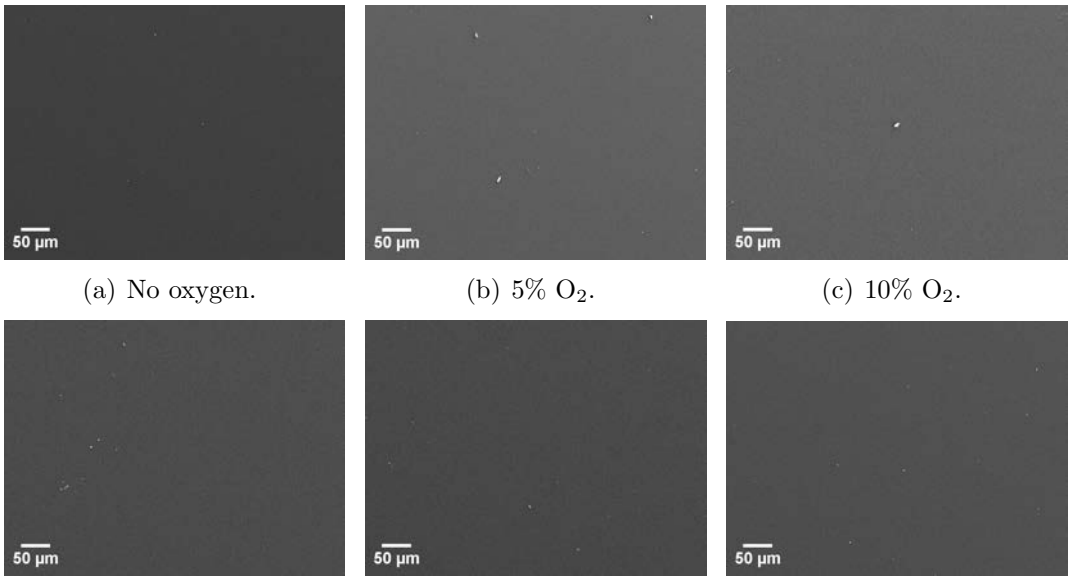


Figure A.5: XRD spectra of films deposited from the pure $Cu_2P_2O_7$ target in Ar / O_2 gas with different amounts of O_2.



(a) No oxygen. (b) 5% O_2. (c) 10% O_2.

(d) 15% O_2. (e) 20% O_2. (f) 25% O_2.

Figure A.6: SEM images of films deposited from the pure $Cu_2P_2O_7$ target in Ar / O_2 gas with different amounts of O_2.

A.4 10% oxygen

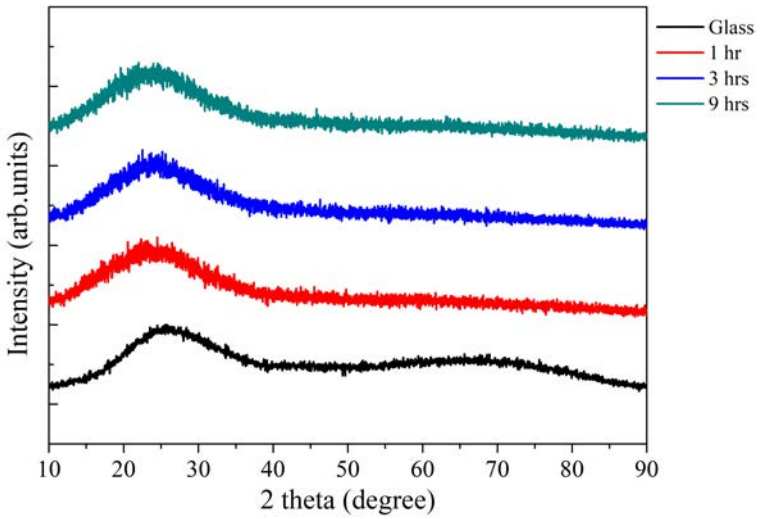
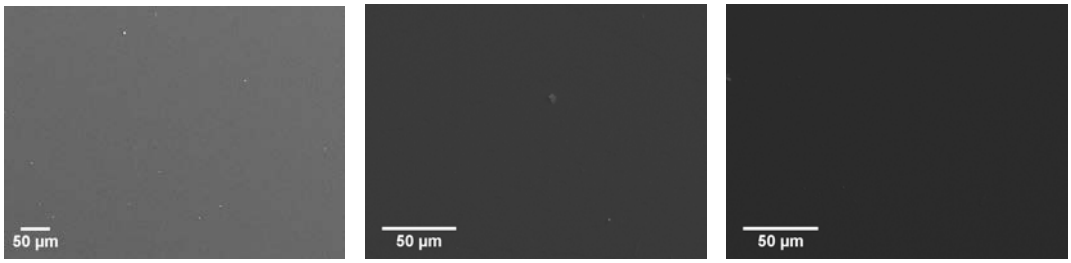


Figure A.7: XRD spectra of selected films deposited from the pure $Cu_2P_2O_7$ target in 10% O_2 / Ar gas for different times.



(a) 3 hrs. (b) 9 hrs. (c) 18 hrs.

Figure A.8: SEM images of selected films deposited from the pure $Cu_2P_2O_7$ target in 10% O_2 / Ar gas for different times.

A.5 15% oxygen

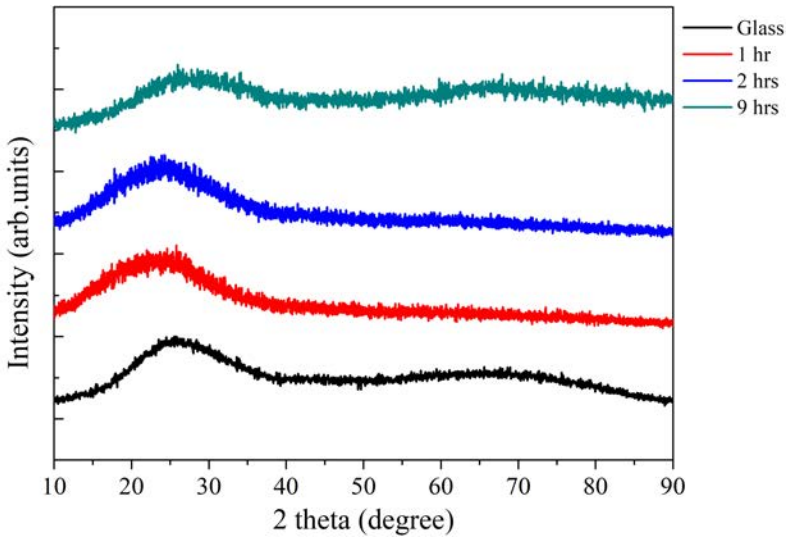
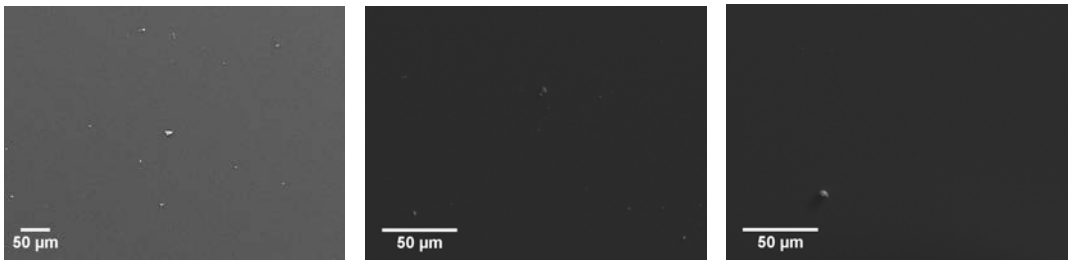


Figure A.9: XRD spectra of selected films deposited from the pure $Cu_2P_2O_7$ target in 15% O_2 / Ar gas for different times.



(a) 2 hrs. (b) 3 hrs. (c) 9 hrs.

Figure A.10: SEM images of films deposited from the pure $Cu_2P_2O_7$ target in 15% O_2 / Ar gas for different times.

A.6 20% oxygen

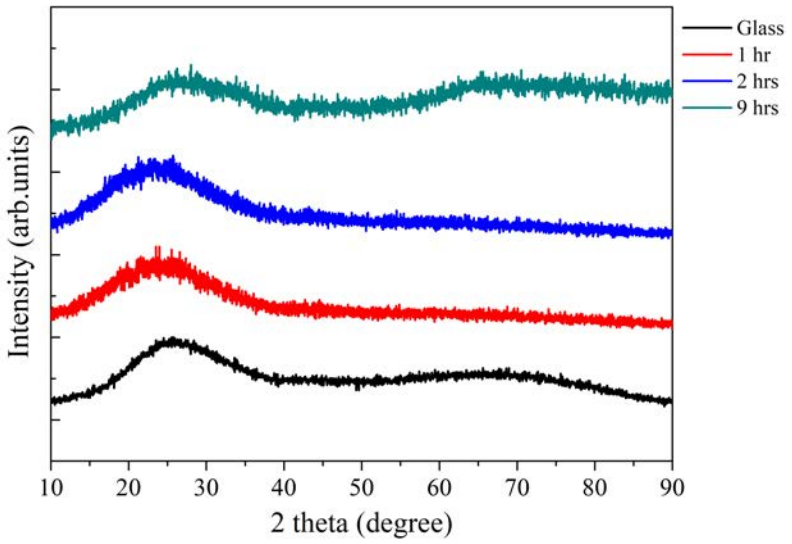
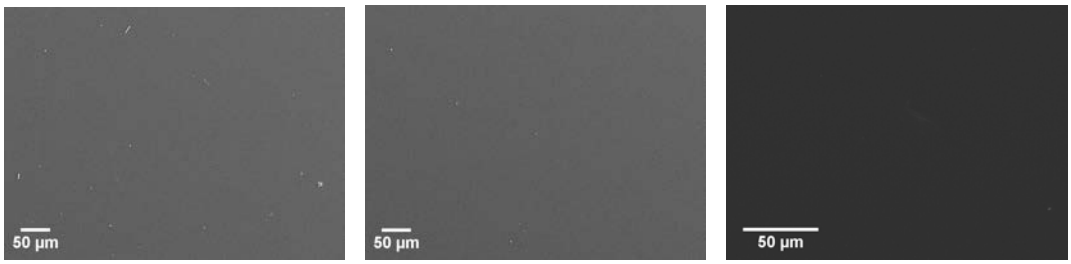


Figure A.11: XRD spectra of selected films deposited from the pure $Cu_2P_2O_7$ target in 20% O_2 / Ar gas for different times.



(a) 2 hrs. (b) 3 hrs. (c) 9 hrs.

Figure A.12: SEM images of films deposited from the pure $Cu_2P_2O_7$ target in 20% O_2 / Ar gas for different times.

Appendix B

Quality Control Document

To better manage the production process, a quality control document has been used since the beginning of this work. For each sputtering session, the date of the session, the information about the substrate and the target, the details of the sputtering process including the on and off time of pumps, heater and plasma are required to be written down. Any further analysis that has been carried out on the sample such as XRD, SEM were written in a separate table as shown. Any issues of the instrument were recorded in the 'Notes and Comments' area.

Quality Control Document:

Metric	Value	
Experiment ID		
Operator		
Date (dd/mm/yyyy)	/ /	
Time, Operation Start	:	
Substrate Material		
Target		
Target Composition		
Target Size		Inch
Turbo Pump Power, Pre Sputtering		%
Time Turbo Pump On	:	
Heater Temperature (Set Point)		°C
Heater Power		%
Time Heater On	:	
Gas type		
Pressure, Pre Sputtering		mbar
Turbo Pump Power During sputtering		%
Plasma Power		W
Reflected Power		W
Time Plasma On	:	
Pressure, During Sputtering		mbar
Sputtering Duration		h
Time Plasma/Gas Off	:	
Time Heater Off	:	
Time Turbo Pump Off		
Time/Temp Chamber Open	:	°C
Time, Procedure Finished	:	

Analysis	Date

Notes and Comments: